

# VIMS observations of Saturn's infrared aurorae

A thesis submitted for

*Doctor of Philosophy*

At the University of Leicester

By James Blake (MPhys)

Department of Physics and Astronomy

2017

# Abstract

James Blake

## *VIMS observations of Saturn's infrared aurorae*

The  $\text{H}_3^+$  infrared aurorae of Saturn were analysed using the Cassini Visual and Infrared Mapping Spectrometer (VIMS) to produce two studies of the emission above the limb. The first, following Stallard et al. (2012a), was a case study of the peak altitude of the southern auroral emission above the limb. The results showed that the measured peak emission altitude is dominated by the alignment of the auroral curtain with the limb, and that accounting for this alignment issue results in a peak intensity altitude of  $1215 \pm 119$  km above the 1 bar level. In the second study, a new projection technique mapped the  $\text{H}_3^+$  limb emissions with respect to latitude, altitude and local time. This technique enabled a statistical analysis of the average latitude-altitude structure of the auroral intensity, temperature and density using 511 observations from the years 2005-2010. For the northern auroral oval, the peak emission altitude was found to be  $1333 \pm 152$  km above the 1 bar level, the average temperature for the peak emission layer was  $549^{+34}_{-12}$  K and the nadir column density was  $1.6^{+3.6}_{-0.9} \times 10^{15} \text{ m}^{-2}$ . Likewise for the southern auroral oval, the peak emission altitude was  $1225 \pm 193$  km, the average temperature was  $585^{+6}_{-29}$  K and the nadir column density was  $6.2^{+0.4}_{-0.3} \times 10^{15} \text{ m}^{-2}$ . The peak emission latitude was found to be  $74^\circ \pm 1^\circ$  for both hemispheres, though the southern auroral emission was found to have a wider latitudinal distribution than the north. The north-south asymmetry in the magnetic field strength was used to explain the hemispheric differences in these properties. Pressure scale height analysis of  $\text{H}_3^+$  revealed that in both hemispheres, the  $\text{H}_3^+$  altitudinal distribution is controlled by its production and loss mechanisms and not gravity.

.

# Acknowledgements

I would like to extend a heartfelt thanks to my research group, RSPP, for their support and guidance. Most particularly to the three people who have quite literally taught me everything I know about  $\text{H}_3^+$  and infrared auroras; Dr Tom Stallard, Dr Henrik Melin and Dr James O'Donoghue. Henrik, thank you for your unfathomable patience and kindness, for taking the time to listen to me and going out of your way to help me even when that meant putting my problems before your own. James, thank you for the advice and daft sense of humour! I miss you now that you're in the states as I miss the days where the three of us were in F66 together, I imagine always will. Last but not least, Tom, where do I start? You made all of this possible and I'm going to carry what I've learned from you for the rest of my life. You have been my mentor, my colleague and my friend. I am hugely grateful for the opportunities and experiences you've given me over the last few years and I hope someday that I'll have the opportunity to work with you again.

A huge thank you to my family for their unyielding patience and support over the years; whether it was helping me move house or supporting me during the write up of this thesis, I needed you and you were there for me. I am also immensely grateful to the STFC and the UK tax payers for funding this PhD and supporting me financially during my research.

Lastly, I would like to thank Michael Perry, Melissa McHugh and Liam Harris. The three of you have been a rock for me throughout and have saved me from breaking when things became difficult. I can only hope I've been half as good a friend as you've all been for me. I have grown and changed in many ways over the course of my PhD, much of this I think can be attributed to you three.

To end this in the finest of RSPP traditions, pub anyone?

*For Mike, Mel and Liam*

# Contents

List of Figures.....	x
List of Tables.....	xi
List of Terms.....	xv

<i>Chapter/Section</i>	<i>Page</i>
<b>Chapter 1 Introduction and description of Saturn.....</b>	<b>1</b>
1.1 Saturn's interior.....	1
<i>1.1.1 Motions of plasma in the magnetic field.....</i>	<i>5</i>
<i>1.1.2 The magnetosphere and the solar wind.....</i>	<i>10</i>
1.2 The upper atmosphere.....	11
1.3 Influences on the ionosphere.....	17
<i>1.3.1 Photoionisation.....</i>	<i>17</i>
<i>1.3.2 Loss mechanisms.....</i>	<i>20</i>
<i>1.3.3 The ring rain.....</i>	<i>20</i>
<i>1.3.4 Enceladus.....</i>	<i>22</i>
1.4 The main auroral oval.....	24
<i>1.4.1 The magnetospheric origins of the aurorae.....</i>	<i>26</i>
<i>1.4.2 Hydrogen atomic and molecular emission.....</i>	<i>32</i>
<i>1.4.3 The infrared emission, production and loss of H<sub>3</sub><sup>+</sup> .....</i>	<i>33</i>
<i>1.4.4 Auroral morphology and intensity in the UV and IR.....</i>	<i>35</i>

1.4.5 Atmospheric temperatures.....	41
1.4.6 Atmospheric ion densities.....	44
1.4.7 Altitudinal structure of $H_3^+$ emission.....	45
1.5 Infrared spectroscopy.....	48
1.5.1 The vibration and rotational energy states.....	50
1.5.2 Emission bands and ro-vibrational transitions.....	54
1.6 Research Questions.....	56
<b>Chapter 2 The VIMS instrument.....</b>	<b>58</b>
2.1 The Cassini mission.....	58
2.2 The VIMS instrument.....	60
2.3 The scanning mechanism and observations.....	64
2.4 Calibration.....	65
2.5 The VIMS team.....	68
<b>Chapter 3 Data and spectral processing.....</b>	<b>69</b>
3.1 The $H_3^+$ emission as viewed by VIMS.....	69
3.2 Extraction the $H_3^+$ emission spectrum.....	73
3.2.1 Additional sources of emission.....	73
3.2.2 Bin subtraction.....	76
3.2.3 Selectively sampling appropriate regions.....	80
3.2.4 The observed spectra.....	81
3.3 Poor data.....	86
3.4 Generating the backplanes and filtering the data.....	88

3.4.1	<i>The NASA navigational team</i> .....	88
3.4.2	<i>Filtering and purification of the data</i> .....	88
	<b>Chapter 4 The effects of alignment on peak emission altitude</b> .....	<b>92</b>
4.1	The altitudinal profiling in Stallard et al. (2012a).....	92
4.2	The data set.....	95
4.3	Calculating emission as a function of altitude.....	102
4.3.1	<i>Sampling smaller regions</i> .....	106
4.3.2	<i>Measuring the alignment</i> .....	111
4.4	Results.....	113
4.4.1	<i>The distribution of emission</i> .....	115
4.5	Discussion.....	117
	<b>Chapter 5 Intensity mapping of the infrared aurorae</b> .....	<b>121</b>
5.1	The aims of a statistical auroral study.....	121
5.2	The observations.....	123
5.3	The projection process.....	126
5.3.1	<i>Selecting the pixels</i> .....	126
5.3.1.1	<i>The polygon clipping procedure – 3D</i> .....	129
5.3.1.2	<i>The spreading functions</i> .....	130
5.3.2	<i>Pixel Filtration and noise reduction</i> .....	134
5.3.3	<i>Projecting into three dimensions – making the maps</i> .....	134
5.3.4	<i>Extraction of the H<sub>3</sub><sup>+</sup> emission</i> .....	138
5.4	Results.....	141
5.4.1	<i>The intensity map</i> .....	141

5.4.2	<i>Testing the gaussian fits</i> .....	144
5.4.3	<i>Altitude and latitude profiles of <math>H_3^+</math> emission</i> .....	145
5.5.1	The shell subtraction model.....	150
5.5.2	Line of sight corrected intensity profiles.....	152
5.6	Discussion.....	155
5.6.1	<i>North-South asymmetry</i> .....	155
5.6.2	<i>Comparisons with other measurements and models</i> .....	156
	<b>Chapter 6 Temperatures and densities of the infrared aurorae</b> .....	<b>160</b>
6.1	The challenges of temperature and density analysis.....	160
6.2	The partition function.....	162
6.3	Generating model spectra.....	164
6.4	Calculating temperatures.....	167
6.5	The wavelength shift.....	168
6.6	Results: temperature maps and profiles.....	169
6.7	Calculating densities.....	175
6.8	Line of sight corrected density profiles.....	178
6.9	The scale height.....	181
6.10	Discussion.....	183
6.10.1	<i><math>H_3^+</math> Temperature comparisons</i> .....	184
6.10.2	<i><math>H_3^+</math> Density comparisons</i> .....	185
6.10.3	<i>The effect of scale height</i> .....	189
	<b>Chapter 7 Conclusions and future work</b> .....	<b>190</b>
7.1	The effect of limb alignment on peak emission altitude.....	190

7.2 Auroral intensities.....	190
7.3 Auroral temperatures.....	191
7.4 Auroral densities.....	192
7.5 The north-south asymmetry.....	193
7.6 Pressure scale height and H <sub>3</sub> <sup>+</sup> altitudinal structure.....	194
7.7 Future developments.....	194
7.7.1 <i>Mapping the body emissions</i> .....	194
7.7.2 <i>Broadening the data set</i> .....	195
7.7.3 <i>Constraining models</i> .....	195
<b>Bibliography</b> .....	<b>196</b>

# List of Tables

	<i>Page</i>
1.1 H <sub>3</sub> <sup>+</sup> and H <sub>2</sub> temperature measurements.....	43
2.1 The VIMS yearly wavelength shift.....	67
3.1 Spectral bins and their wavelength bandwidths.....	75
3.2 Bin subtraction factors.....	79
4.1 Peak emission altitudes.....	113
5.1 Number of observations from each year (for the statistical study).....	125
6.1 Fit coefficients of the H <sub>3</sub> <sup>+</sup> partition function (Miller et al., 2013).....	163
6.2 Scale heights of H <sub>3</sub> <sup>+</sup> .....	182

# List of Figures

	<i>Page</i>
1.1 Gas giant internal structure.....	2
1.2 Saturn's magnetosphere.....	3
1.3 Particle motion in a converging B field.....	5
1.4 Mirror points and pitch angles.....	8
1.5 Saturn's upper atmospheric emissions, figure 7.19 of West et al. (2009).....	13
1.6 STIM model results for Saturn's upper atmosphere, Moore et al. (2009).....	16
1.7 Neutral density and temperature profiles, figure 1 of Galand et al. (2011).....	18
1.8 Electron density profiles, figure 9 of Galand et al. (2009).....	18
1.9 Electron density profiles, figure 3 of Galand et al. (2011).....	19
1.10 Artists impression of ring rain.....	21
1.11 Latitudinal $H_3^+$ intensity profile affected by ring rain.....	22
1.12 Examples of auroral images (Hubble, UVIS and VIMS).....	25
1.13 Auroral emission mechanisms.....	25
1.14 Co-rotation enforcement currents, figure 1 Cowley and Bunce (2003).....	26
1.15 The Dungey cycle.....	27
1.16 Polar ionosphere currents.....	29
1.17 The Dungey and Vasyliunas reconnection lines.....	30
1.18 UV auroral morphology, figure 1 (a) and (k) Clarke et al. (2005).....	36
1.19 Infrared, ultraviolet and visible aurora comparison at Saturn.....	38
1.20 Ultraviolet aurorae examples.....	39

1.21 Infrared aurorae examples.....	40
1.22 Altitudinal ion densities and volume emission rates (Tao et al., 2011).....	45
1.23 Observations of Stallard et al. (2012a).....	46
1.24 Altitudinal intensity profile of Stallard et al. (2012a).....	47
1.25 The $H_3^+$ molecule.....	49
1.26 $H_3^+$ vibrational energy states.....	51
1.27 $H_3^+$ rotational energy states.....	52
1.28 $H_3^+$ energy transitions.....	53
1.29 The $H_3^+$ emission spectrum change with temperature.....	55
2.1 The VIMS instrument.....	62
2.2 VIMS optical path.....	63
2.3 An example VIMS observation.....	65
2.4 VIMS spectral bins.....	66
3.1 Model $H_3^+$ spectrum.....	70
3.2 Model $H_3^+$ spectrum as resolved by VIMS and SPEX.....	71
3.3 The effect of the wavelength shift.....	72
3.4 Extracting $H_3^+$ emission.....	77
3.5 Extracting methane emission.....	78
3.6 Reflected sunlight in VIMS observations.....	80
3.7 Thermal emissions in VIMS observations.....	81
3.8 $H_3^+$ spectra model-observation comparison.....	83
3.9 VIMS spectra from different sources.....	84
3.10 Example of poor data.....	87

4.1 The observations of Stallard et al. (2012a).....	93
4.2 Altitudinal intensity profile of Stallard et al. (2012a).....	94
4.3 Observations used in the alignment study.....	97-100
4.4 The polygon clipping procedure – 1D.....	103
4.5 Altitudinal profile development and comparison with Stallard et al. (2012a).....	105
4.6 Sampling the $H_3^+$ emission above the limb.....	107
4.7 Sampling the $H_3^+$ emission on the planet.....	109
4.8 Peak emission altitude plotted against alignment with the limb.....	112
4.9 Contour plot of altitudinal intensity profiles.....	114
4.10 Combine altitudinal intensity profiles for alignments better than $4^\circ$ .....	116
5.1 Spacecraft locations of 511 observations.....	124
5.2 Polygon clipping procedure – 3D.....	128
5.3 The spreading function.....	131
5.4 Examples of poor observations.....	133
5.5 Latitude-altitude data density.....	136
5.6 Latitude-local time data density.....	137
5.7 Extracting $H_3^+$ emission from the latitude-altitude map.....	139-140
5.8 The $H_3^+$ intensity map.....	142
5.9 Altitudinal $H_3^+$ intensity profiles.....	147
5.10 Latitudinal $H_3^+$ intensity profiles.....	149
5.11 The shell subtraction model.....	151
5.12 Line of sight corrected altitudinal $H_3^+$ intensity profiles.....	153
5.13 Altitudinal ion densities and volume emission rates (Tao et al., 2011).....	157

5.14 Comparison of data and model altitudinal $H_3^+$ intensity profiles.....	158
6.1 Model of $H_3^+$ spectra at 400 K and 600 K.....	164
6.2 Temperature calculation – bin ratio groups.....	165
6.3 Yearly bin ratio – temperature profiles.....	168
6.4 The $H_3^+$ temperature map.....	170
6.5 Altitudinal $H_3^+$ intensity and temperature profiles.....	172-173
6.6 Cross section of a sector of a frustrum.....	174
6.7 Altitudinal volumetric $H_3^+$ density profiles.....	176
6.8 Line of sight corrected altitudinal $H_3^+$ density profiles.....	179-180
6.9 Altitudinal ion density profiles (Tao et al., 2011).....	186
6.10 Altitudinal atmospheric temperature profile (Tao et al., 2011).....	187
6.11 Altitudinal ion density and ion temperature profiles (Moore et al., 2009).....	188
6.12 Comparison of altitudinal $H_3^+$ density profiles to models.....	189

# List of terms

**VIMS** – The **V**isual and **I**nfrared **M**apping **S**pectrometer instrument aboard the Cassini spacecraft.

**1 bar level** – a global isobaric pressure surface at 1 bar ( $10^5$  Pa) used as a reference point for analysing the upper atmosphere of Saturn. Typically used in this thesis to refer to an altitude of 0 km in Saturn's atmosphere.

**Integration time** – the length of time the VIMS instrument spends collecting light for each pixel. This number varies between observations

**Observation** – a complete image compiled by the VIMS instrument consisting of an array of pixels in two dimensions. Each observation is saved as an individual file of intensities as well as separate file containing the SPICE kernels for that observation.

**Pixel** – An element of an observation that contains the total intensity of emission over the full spectral range (all spectral bins) of VIMS as observed for VIMS' field of view during the allotted time of the pixel's integration (integration time).

**Spectral bin** – The emission collected by a single charged couple device in the VIMS detector array. Each spectral bin has a wavelength bandwidth which it observes.

**Spectel** – A pixel as viewed in one spectral bin.

**SPICE kernels** – The ephemeris of the observation such as the date and time of the observation as well as spacecraft viewing geometry and trajectory. This information is used for each observation to determine the location of the body of Saturn within the observation's field of view. The kernels are also used to determine the field of view (in terms of latitude, altitude, local time etc) of each pixel in an observation. For a more detailed definition of each kernel please refer to Section 2.5.

**NAIF** – NASA **N**avigational and **A**ncillary **I**nformation **F**acility

# Chapter 1

## *Introduction and Description of Saturn*

At an orbital distance of 9.5 astronomical units Saturn is the sixth planet of our solar system. Saturn was first observed with a telescope by Galileo Galilei in 1610, a discovery which he later related to Marc Wessler in 1613 in his work “*Istoria e dimostrazioni intorno alle macchie solari e loro accidente*” or as it is more commonly known in English “*Letters on Sunspots*”. In the four centuries since, the gas giant Saturn has been the focus of a wide array of studies and treatises. With the advent of spacecraft missions in more recent decades, such as Pioneer 11, the Voyager missions and Cassini-Huygens, our knowledge of the Kronian system has been vastly improved from Galileo’s initial idea of a planet with handles. Famous for its spectacular ring system, we now know that Saturn is primarily comprised of hydrogen and helium with an overall planetary mass of  $5.683 \times 10^{26}$  kg, and much like Jupiter, has a fast rotation rate with one day lasting approximately 10.6 terrestrial hours. It is, however, significantly less dense and somewhat smaller than Jupiter, with a density of  $687 \text{ kg m}^{-3}$  (lower than that of water) and a radius of 58,232 km compared to Jupiter’s density of  $1,326 \text{ kg m}^{-3}$  and radius 69,911 km.

### Section 1.1 Saturn’s interior

Saturn has an internally driven magnetic field generated by a fluidic dynamo within a layer of metallic hydrogen in the planetary core (Russell et al., 1993). The first measurements of Saturn’s magnetosphere (the region over which the planet’s magnetic field is dominant) were made in 1971 during a flyby by Pioneer 11 spacecraft. It has been subsequently discovered to be the second largest magnetosphere in our solar system (the first being Jupiter’s). Measurements from Pioneer 11, Voyager 1 and Voyager 2 all showed the Kronian dipole axis to be very closely aligned with the rotational axis (within 0.1 degrees) and to be also highly axisymmetric, further measurements from the Cassini spacecraft later confirmed this (Southwood and Kivelson, 2007). The axis of this dipole moment is almost perfectly aligned with the rotational axis (to within 1 degree of latitude) rendering the magnetic essentially axisymmetric. It has also been observed to be hemispherically asymmetric due to the quadrupole moment strengthening the magnetic field in the north and weakening the field in the south thus offsetting the centre of the dipole moment northward of the planetary core (Dougherty et al., 2005, Gombosi et al., 2009).

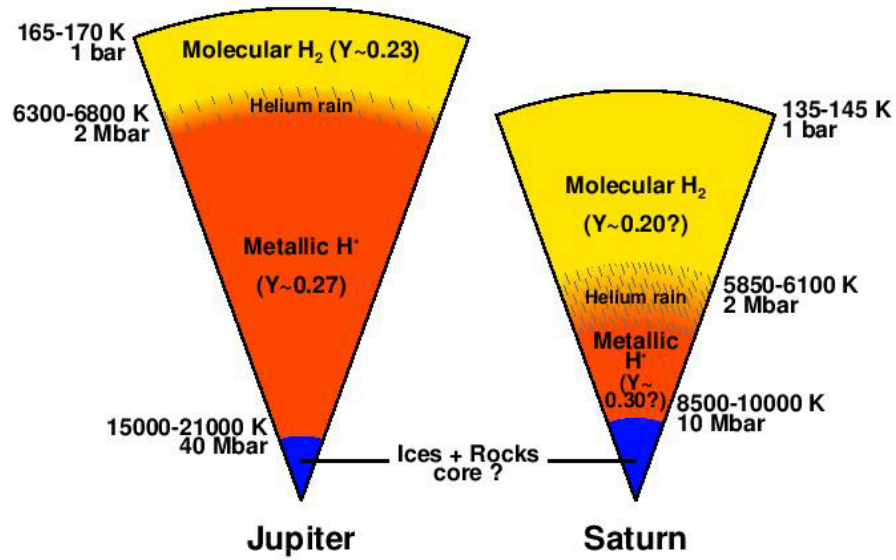


**Figure 1.1:** A schematic representation of the interiors of Jupiter and Saturn from Guillot and Gautier (2015). The temperatures are estimated using homogeneous models. The sizes and composition of the central dense cores of both planets are very uncertain. The convection of the metallic hydrogen outside the core is thought to be responsible for the generation of the magnetic field of both planets.  $Y$  is the mixing ratio of hydrogen-helium.

Though the internal structure of the giant planets is yet largely unknown, models have been developed based on the size, mass, composition and gravitational field strength of these worlds. In Figure 1.1, one such model is shown (Guillot and Gautier, 2015) for Jupiter and Saturn. This model shows a large region of metallic hydrogen outside of a solid core. It is suggested that this region outside the core is more fluid as shown in Figure 1.1 and therefore capable of transporting charged material, thereby creating currents. The generation of the magnetic field is fundamentally similar to an electrical current travelling through a long wire, which generates a magnetic field in accordance with Ampère's Law;

$$\mathbf{B} = \frac{\mu_0 \mathbf{I}}{2\pi r}, \quad (1.1)$$

where  $\mathbf{B}$  is the magnetic field strength (Tesla or  $\text{N}\cdot\text{A}^{-1}\cdot\text{m}^{-1}$ ),  $\mathbf{I}$  is the current strength (A),  $r$  is the radial distance from the wire (m) and  $\mu_0$  is the permeability of free space ( $4\pi \times 10^{-7} \text{ T}\cdot\text{m}\cdot\text{A}^{-1}$ ). Whilst significantly more complex than a simple current in a long straight wire or solenoid, the convective motions of charged material generate the magnetosphere of Saturn. The nature of this field can be described by the effects that it has on a charged particle using the Lorentz equation;

$$\mathbf{F} = q(\mathbf{E} + \mathbf{v} \times \mathbf{B}), \quad (1.2)$$

where  $F$  is the force exerted on a charged particle (N),  $q$  is the charge of said particle (C), the vector  $E$  is the electric field strength ( $\text{Vm}^{-1}$ ), the vector  $v$  is the velocity ( $\text{ms}^{-1}$ ) of the charged particle and the vector  $B$  is the magnetic field strength at the location of the charged particle. From the measurements of the magnetic field taken by Pioneer 11 and Voyager 1 it was determined that Saturn's magnetic field is largely dipolar with a quadrupole component that is far smaller in its contribution than those of Jupiter and Earth. The ratio of the strength of the quadrupole moment to the dipole moment is 0.07 as compared to 0.14 in the terrestrial field. Saturn's quadrupole moment has however been cited as the cause of the field strength asymmetry between the northern and southern magnetic hemispheres (Gombosi et al., 2009).

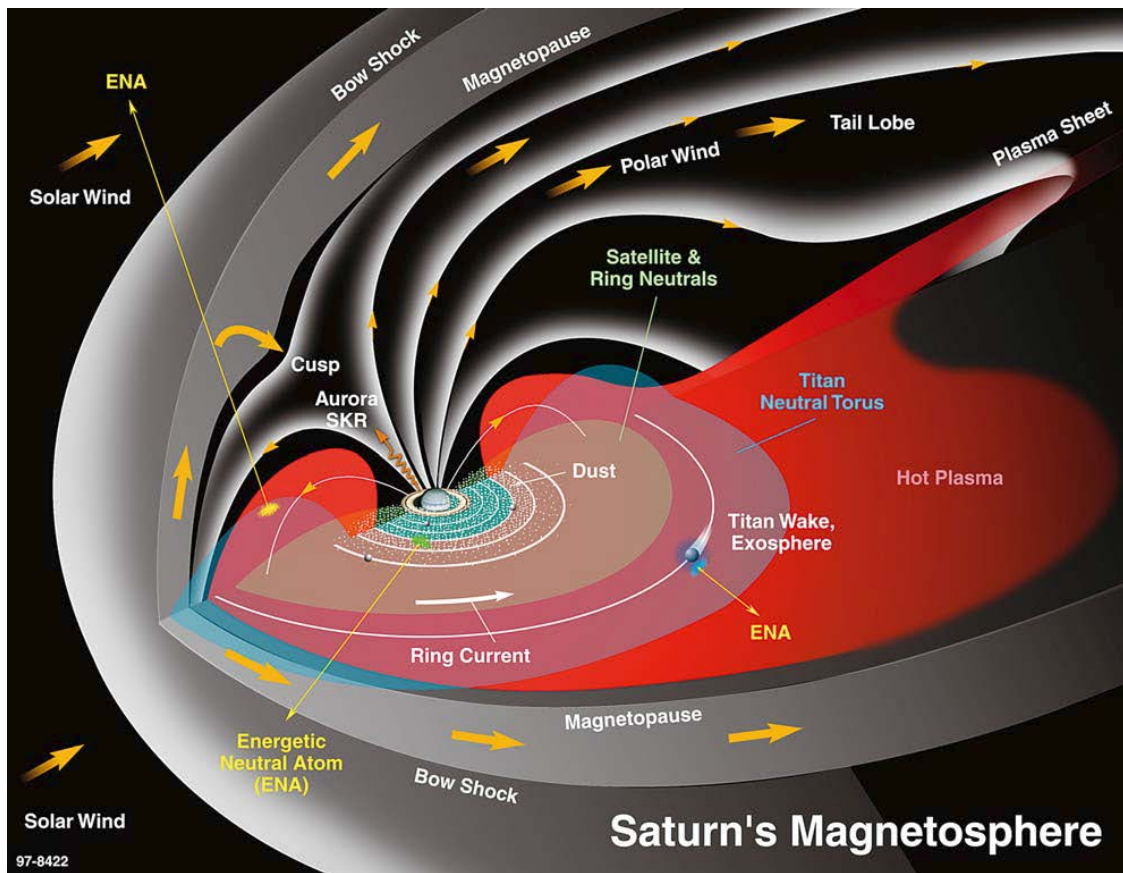


**Figure 1.2:** A schematic of the magnetosphere of Saturn is taken from Krimigis et al. (2004).

As shown in Figure 1.2 the resultant magnetosphere generated by this core dynamo has a structure that extends far beyond the atmosphere of the planet. The edge of the Kronian magnetosphere, the stand-off distance of the magnetopause at the sub solar point varies between 16 and 27  $R_s$  with the average being 22  $R_s$ , the location of the magnetopause serves as a proxy for the changeable solar wind pressure (Krimigis et al., 2007) which will feature in later

sections. On the night-side of the planet is a magnetotail which consists of two lobes, the northern lobe has a magnetic field which points away from the planet and the southern lobe conversely points towards the planet. Reconnection events occur at both the subsolar point of the magnetosphere as well as in the magnetotail as will be detailed in Section 1.4.1.

Much of the particle population residing in Saturn's magnetosphere consists of neutral species sources from the rings and the satellite Enceladus. These neutrals are highly abundant and surround the planet in a cloud of hydrogen species, water molecules and their dissociative products. The magnetosphere is said to be dominated by this neutral population, which is unsurprising when one considers that in the inner magnetosphere the ratio of the number of neutrals to the number of ions is approximately sixty to one. Due this balance of the different populations, the volume of Saturn's magnetosphere can be considered to be made of a weakly ionised relatively dense gas. The ions and electrons within this gas constitute the magnetospheric plasma population and in Saturn's inner magnetosphere are largely dominated by corotation much like Jupiter, however, due to a weaker field strength there are also elements of the magnetosphere that bear resemblance to that of Earth's largely convection driven magnetospheric system. The magnetosphere is predominantly a dipole with an orientation opposite to that of Earth. The strength of Saturn's magnetic field is approximately  $21\mu\text{T}$  at the equatorial ionosphere; which correlates with a magnetic dipole moment of  $4.6 \times 10^{18} \text{ Tm}^{-3}$  (Gombosi et al., 2009, Belenkaya et al., 2011). Much like the terrestrial magnetosphere, the solar wind has significant influence on the dynamics of the Kronian magnetosphere. The structure and regions of the magnetosphere will be discussed further in Section 1.3 and 1.4 within the context of their influence on Saturn's upper atmosphere and aurorae.

### Section 1.1.1 Motions of plasma in the magnetic field

In the following sections, the ionosphere will be discussed in terms of different latitudinal and magnetospheric regions. One aspect that will be covered in these regions is the differences in the plasma that precipitated from the magnetosphere. This section will give brief overview of the most common form of particle acceleration and precipitation present throughout most of the magnetosphere.

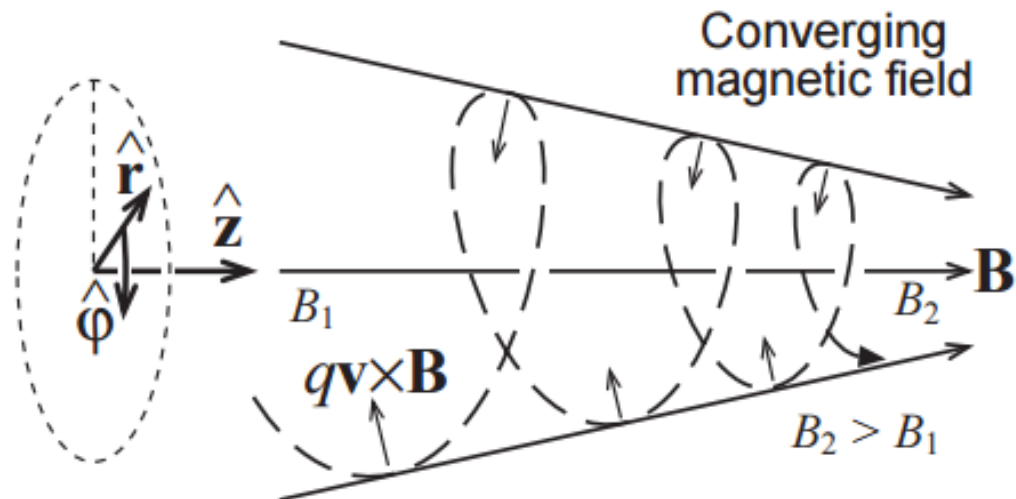


**Figure 1.3:** Taken from figure 1.6 of the lecture notes from course 4319 Space Plasmas, taught by Professor Steve Milan at the University of Leicester. Shown on the left is the cylindrical coordinate system used to describe the gyromotions of the charged particle  $q$ . The field lines  $\mathbf{B}$  are shown as solid line arrows and the motion of the charged particle along them is shown as the dashed line arrow. The smaller arrows pointing inward represent the vector of the Lorentz force of equation 1.2.

The properties of a magnetic field are generally defined in terms of the effect the field would have on a charged particle as per equation 1.2; the Lorentz force. Using this equation it can be seen that a charged particle will gyrate around a field line with a frequency (gyrofrequency) defined by:

$$\omega_c = \frac{|q|B}{m} \quad (1.3),$$

and a gyroradius (also known as a Larmor radius) as defined by:

$$r_L = v_{\perp} / \omega_c \quad (1.4)$$

Where  $\omega_c$  is the gyrofrequency,  $q$  is the charge of the particle of mass  $m$  traversing a magnetic field line of strength  $B$ . Taking this forward in a cylindrical coordinate system shown in Figure 1.3 consisting of radial distance of the particle from the field line  $r$ , the azimuthal angle  $\varphi$  of the particle around the field line and the polar angle  $z$  (the position of the particle along the field line) we can express the velocity of the plasma particles as follows:

$$\mathbf{v} = (v_r, v_\varphi, v_z) \quad (1.5)$$

Where  $v_z$  is equivalent to the particle velocity parallel to the field line  $v_{\parallel}$  and  $v_\varphi$  is equivalent to the negative of the particle velocity perpendicular to the field line  $-v_{\perp}$ . As the particle travels along the field line the strength of the magnetic field changes, increasing with polar angle (towards the poles).

$$\text{div } B = \frac{1}{r} \frac{\partial}{\partial r} (r B_r) + \frac{1}{r} \frac{\partial B_\varphi}{\partial \varphi} + \frac{\partial B_z}{\partial z} \quad (1.6)$$

As the magnetic field lines converge towards the poles the field strength increases, thereby creating a  $B$  field gradient in the  $z$  direction which allows us to define the field as follows:

$$\frac{1}{r} \frac{\partial}{\partial r} (r B_r) = -\frac{\partial B_z}{\partial z} \quad (1.7)$$

$$\frac{\partial}{\partial r} (r B_r) = -r \frac{dB(z)}{dz} \quad (1.8)$$

$$B_r = -\frac{r}{2} \frac{dB(z)}{dz} \quad (1.9)$$

Since the field strength is varying with  $z$  so too must the force exerted on the charged particle, in this case an electron  $e$  ( $q=e$ ):

$$F_z = -e v_\varphi B_r = e v_{\perp} B_r \quad (1.10)$$

$$F_z = -\frac{e v_{\perp} r}{2} \frac{dB}{dz} \quad (1.11)$$

Substituting in for  $B_r$  to ensure everything is in terms of  $z$ :

$$F_z = -\frac{e m v_{\perp}^2}{2 q B} \frac{dB(z)}{dz} = -\frac{m v_{\perp}^2}{2 B} \frac{dB(z)}{dz}, \quad (1.12)$$

which can also be written as:

$$m \frac{dv_z}{dt} = -\frac{m v_{\perp}^2}{2 B} \frac{dB(z)}{dz}. \quad (1.13)$$

Finally the mass  $m$  can be cancelled on both sides and  $v_z$  with can be replaced with  $v_{\parallel}$  to produce:

$$\frac{dv_{\parallel}}{dt} = -\frac{v_{\perp}^2}{2B} \frac{dB(z)}{dz} \quad (1.14)$$

Rearranging further allows us to convert  $dz/dt$  into  $v_{\parallel}$  which is useful given equation 1.16, 1.17 and 1.18 as we can express everything only in terms of the perpendicular velocity  $v_{\perp}$  in equation 1.19.

$$v_{\parallel} dv_{\parallel} = -v_{\perp}^2 \frac{dB}{B} \quad (1.15)$$

$$d(v_{\parallel}^2) = 2v_{\parallel} dv_{\parallel} \quad (1.16)$$

$$v^2 = v_{\perp}^2 + v_{\parallel}^2 = \text{constant} \quad (1.17)$$

$$d(v_{\parallel}^2) = -d(v_{\perp}^2) \quad (1.18)$$

Substituting in  $v_{\perp}$  and integrating gives equation 1.19 which can be rearrange to show equation 1.20.

$$\ln(v_{\perp}^2) = \ln(B) + \text{constant} \quad (1.19)$$

$$\frac{v_{\perp}^2}{B} = \text{constant} \quad (1.20)$$

This is known as the *first adiabatic invariant*, which can also be expressed as equation 1.21. The particle's magnetic moment  $\mu$  (equation 1.21) can be used to describe how gradients in the field strength along the field direction will affect the particle's motion. When conserved, it requires the parameters of the system such as the magnetic field strength and direction to change slowly as seen by the particle such that the changes over a single gyration of the particle are small compared to the initial state of the field (hence the term adiabatic). The cyclical motions come from the gyration of a particle around the central magnetic field line which it is traversing.

$$\mu = \frac{mv_{\perp}^2}{2B} \quad (1.21)$$

The significance of this is that as the field strength increases, the parallel velocity of the charged particles decreases until it eventually reaches a point where the charged particle is reflected back. This is referred to as the magnetic mirror point and is defined not by the type of charged particle (its mass or charge) nor even the kinetic energy but rather the pitch angle  $\alpha$ .

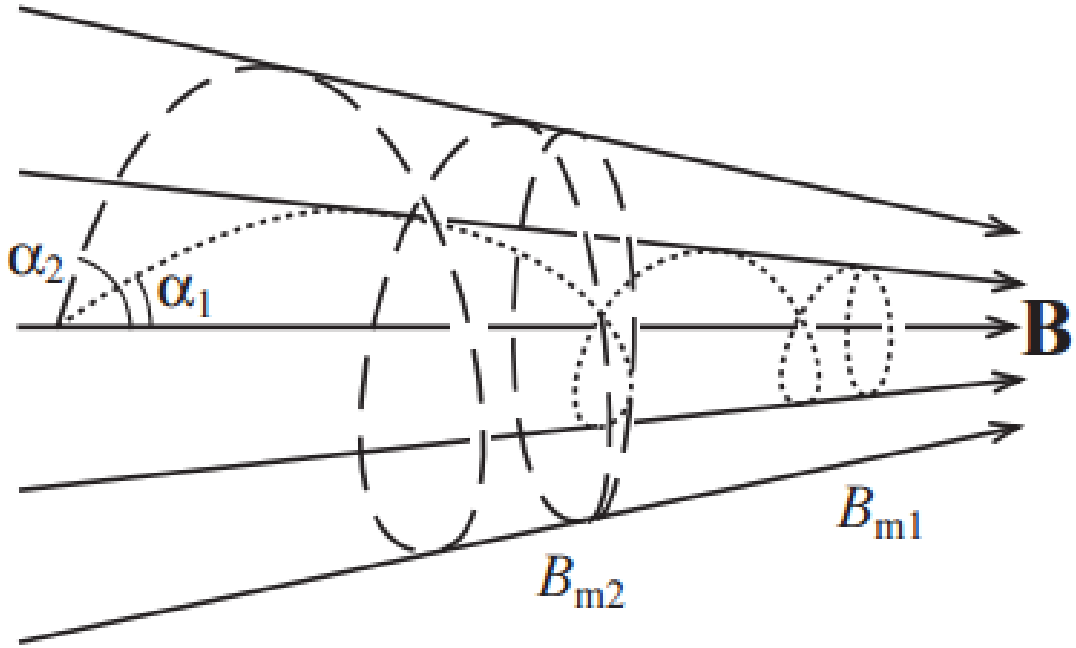


**Figure 1.4:** Taken from figure 1.8 of the lecture notes from course 4319 Space Plasmas, taught by Professor Steve Milan at the University of Leicester. This figure shows the motions of two charged particles with different pitch angles  $\alpha_1$  (dotted line) and  $\alpha_2$  (dashed line) as they travel along converging field lines (solid arrows) and are magnetically reflected and field strengths  $B_{m1}$  and  $B_{m2}$  respectively.

The first adiabatic invariant arises when particles - in this case electrons - undergo cyclical motions over timescales which are fast with respect to the timescales of the variations that the particle encounters (temporally or spatially) in the electromagnetic fields that control the particle's motion.

$$\tan(\alpha) = \frac{v_{\perp}}{v_{\parallel}} \quad (1.22)$$

$$v_{\parallel} = v \cos(\alpha) \quad v_{\perp} = v \sin(\alpha) \quad (1.23)$$

$$\frac{v_{\perp}}{B} = v^2 \sin^2(\alpha) = \text{constant} \quad (1.24)$$

Where  $\alpha$  is the particle pitch angle (the angle made between the direction of the particle's velocity and the central magnetic field line) and  $B_m$  is the magnetic field strength at which the particle will reflect (or mirror point). Two pitch angles and their corresponding mirror points are shown for two charged particles as an example in Figure 1.4.

$$\frac{\sin^2(\alpha)}{B} = \frac{\sin^2(\alpha)}{B_m} = \frac{1}{B_m} \quad (1.25)$$

$$B_m = \frac{B}{\sin^2(\alpha)} \quad (1.26)$$

If there is no electric field parallel to the magnetic field, provided the magnetic field does transfer energy to or from the particle and change its kinetic energy  $W$ , said kinetic energy must remain constant. Given the following equation 1.27 from Kivelson and Russell (1995):

$$W = \frac{1}{2} m(v_{\perp}^2 + v_{\parallel}^2) = \frac{1}{2} m v_{\parallel}^2 + \mu B = \text{constant}, \quad (1.27)$$

in order for the kinetic energy to remain constant as the perpendicular velocity increases, the parallel velocity decreases. Once the magnetic field strength is high enough as the particle nears the planet, the parallel velocity reduces to zero after which the particle reverses course after reflecting from this mirror point. With a smaller pitch angle like  $\alpha_1$  in Figure 1.4, the parallel velocity component is much greater than the perpendicular and therefore the charged particle requires greater field strength  $B_{m1}$  to reflect it and the particle with pitch angle  $\alpha_2$ . This motion of plasma in the magnetic field is generally true for the closed field lines (both ends of the field line connected to the planet) in Saturn's magnetosphere

If the mirror point is within the atmosphere, it is very likely the particle will be lost either to precipitation or charge exchange. If an electron with a higher kinetic energy precipitates, it will require a much greater number of collisions before it loses enough energy to be thermalized with the surrounding atmosphere. Thus, typically, the electrons with higher energies (hard electrons) will penetrate deeper into the atmosphere than those with lower energies (soft electrons). Particle precipitation will become important in Sections 1.3 and 1.4 as it is a mechanism by which plasma from the magnetosphere can enter the atmosphere and therefore represents a manner in which these two systems interact. There are other forms of plasma processes which are present only in specific regions of the magnetosphere; of these, those most pertinent to the generation of the auroral emissions are discussed in Section 1.4.

### Section 1.1.2 The magnetosphere and the solar wind

It is important to consider that the magnetosphere of the Saturn is situated in a much larger external magnetic structure, the heliosphere, or more commonly, the magnetic field of the Sun and the solar wind. The solar wind consists of hydrogen/helium based plasma ejected from the corona (due to coronal expansion) of the Sun at velocities of  $300\text{-}800\text{ km s}^{-1}$ , which is neutral overall as it also contains a mix of electrons, protons and alpha particles (Cowley, 1996). This magnetic field and plasma structure permeates the entirety of the solar system and is hence referred to as the interplanetary magnetic field (IMF).

As described in Kivelson and Russell (1995) the spatial variability of the coronal expansion, coronal mass ejections as well as the rotation of the sun causes, in turn, a variation in the speed of the solar wind flows. This then results in high velocity plasma catching up to slower plasma creating regions of compression and rarefaction. Since the solar wind flows radially outwards from the sun, these compressions form “the Parker spiral” in the solar equatorial plane which corotates with the Sun (Gosling and Pizzo, 1999); for visual reference this has been likened to water being sprayed out of a rotating sprinkler. These variations in plasma density and field strength result in a variable pressure on the magnetosphere of Saturn, the consequences of which will be discussed in Section 1.4.

## Section 1.2 The upper atmosphere

For the purposes of auroral study, the regions of Saturn's atmosphere that are of greatest interest are the thermosphere and the ionosphere within it, which are both largely encompassed in this thesis by the general term "upper atmosphere". The thermosphere is typically characterised by a steep temperature gradient with the base of the region being a temperature minimum. This temperature gradient is born from energy input from solar photons, with the greatest deposition rate at the highest altitudes (lowest energy photons) and the smallest rate at the lower altitudes (high energy photons). Alternatively, as with Nagy et al. (2009), both the thermosphere and the upper atmosphere can be defined as the region of the atmosphere above the homopause at Saturn. The homopause can be defined by examining the two regions above and below this boundary, which can be characterised in terms of chemical behaviour and populations, as well as dominance of eddy diffusions and molecular diffusion. Where eddy diffusion is dominant below the homopause, a region known as the homosphere, the atmosphere is chemically uniform as all species have the same scale height due to constant convection; thus the lower atmosphere has a diverse mix of hydrocarbons and other heavier molecular species such as methane (as compared to the lighter species of hydrogen and helium). The homopause denotes the boundary where eddy diffusion and molecular diffusion are equal, and above this point molecular diffusion dominates, hence this upper atmosphere is differentiated according to the individual pressure scale heights of each particular chemical species wherein hydrogen (both atomic and molecular) as well as helium are the dominant species. The pressure scale height is the altitude range over which the pressure of a gas decreases by a factor of  $e$  (2.718) and is derived from ideal the ideal gas law (equation 1.28) under conditions of hydrostatic equilibrium as well as the definition of density:

$$PV = nRT \quad (1.28)$$

$$\rho = \frac{nM}{V} \quad (1.29)$$

$$\frac{dP}{dz} = -\rho g \quad (1.30)$$

Where  $P$  is the pressure (pascal),  $V$  is the volume of the gas ( $\text{m}^3$ ),  $n$  is the number of particles,  $R$  is the gas constant and  $T$  is the temperature (kelvin),  $M$  is the molecular mass,  $\rho$  is the density,  $g$  is the acceleration due to gravity ( $\text{ms}^{-2}$ ) and  $z$  is the altitude (m). Rearranging equation 1.29 for  $V$  and substituting into equation 1.28 gives the pressure in terms of molecular mass and density in equation 1.31:

$$P = \frac{\rho RT}{M} \quad (1.31)$$

Rearranging equation 1.31 for density and substituting into the equation 1.29 (hydrostatic equilibrium) yields equation 1.32:

$$dP = -\rho g dz = -\left(\frac{MPg}{RT}\right) dz \quad (1.32)$$

This can be rearranged to expressed in a form that can be integrated with pressure on the left hand side and altitude on the right as shown in equations 1.33 and 1.34

$$\frac{dP}{P} = -\left(\frac{Mg}{RT}\right) dz \quad (1.33)$$

$$\int_{P_0}^P \frac{dP}{P} = -\int_{z_0}^z \frac{Mg}{RT} dz \quad (1.34)$$

Integrating between the limits of  $P_0$  and  $P$  for pressure and  $z_0$  and  $z$  for altitude (equation 1.34) gives equation 1.35. Using the law of subtracting logarithms and taking the exponential of both sides give equation 1.36.

$$\ln(P) - \ln(P_0) = -\frac{Mg}{RT}(z - z_0) \quad (1.35)$$

$$P = P_0 e^{-\frac{Mg}{RT}(z-z_0)} \quad (1.36)$$

In order to decrease the pressure by a factor of e, which can also be expressed as a power of e, the altitude range must be equal to  $H$  as follows in equation 1.37 given a constant  $T$ .

$$H = \frac{RT}{Mg} \quad (1.37)$$

This breaks down at lower altitudes (i.e. in the stratosphere and troposphere – also regarded as the lower atmosphere), the emissions of which can be seen in Figure 1.5, as circulation currents override the distribution by gravity.

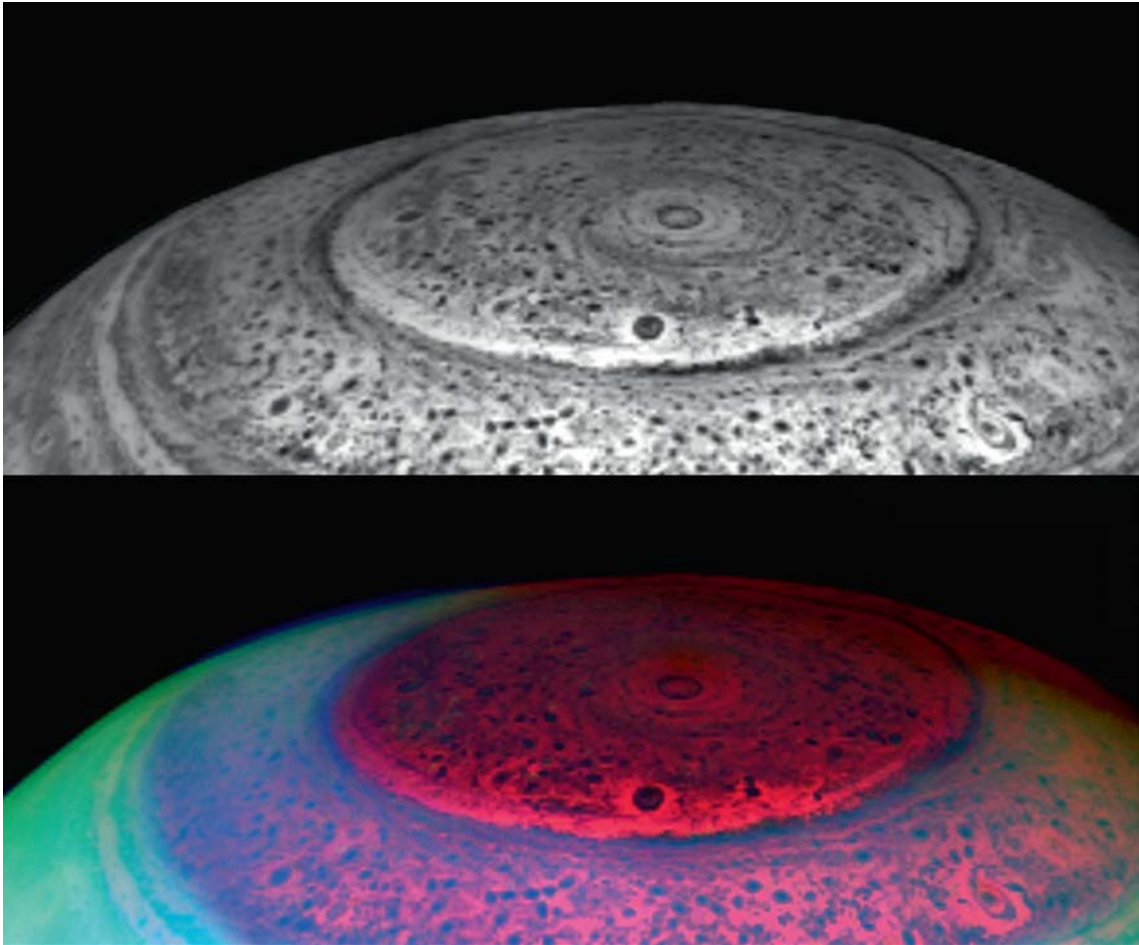


**Figure 1.5:** Figure 7.19 of West et al. (2009) showing the infrared emission of Saturn's Southern Pole from the upwelling thermal radiation at  $5.1 \mu\text{m}$  revealing the cloud structure in silhouette in the upper panel. This radiation is shown in red in the lower image, with the reflected sunlight from the overlying hazes in blue ( $3.1 \mu\text{m}$ ) and green ( $4.1 \mu\text{m}$ ).

The upper atmosphere of Saturn can be considered to have two major chemical components; a neutral population and a charged population. These two groups are linked together throughout the Kronian atmosphere via the interchange of energy from collisional interactions. The regions of the atmosphere where significant populations of ions and thermal free electrons ( $<1\text{eV}$ ) present is what we refer to as the ionosphere (Schunk and Nagy, 2000); it is the layer of the atmosphere where neutral species are ionised by incident EUV solar radiation or energetic particle precipitation. It is also in this layer of the atmosphere that the auroral emissions are primarily generated, as discussed in Section 1.4. One of the most important aspects of the ionospheric system is the location and size of the electron populations. From various studies and models it has been made apparent that there is significant latitudinal variation of both the ion and electron populations in the upper atmosphere and hence ionosphere of Saturn. The distribution of these ions, electrons and neutrals with altitude is shown below in Figure 1.6 from Moore et al. (2009) for the latitude  $30^\circ \text{N}$ .

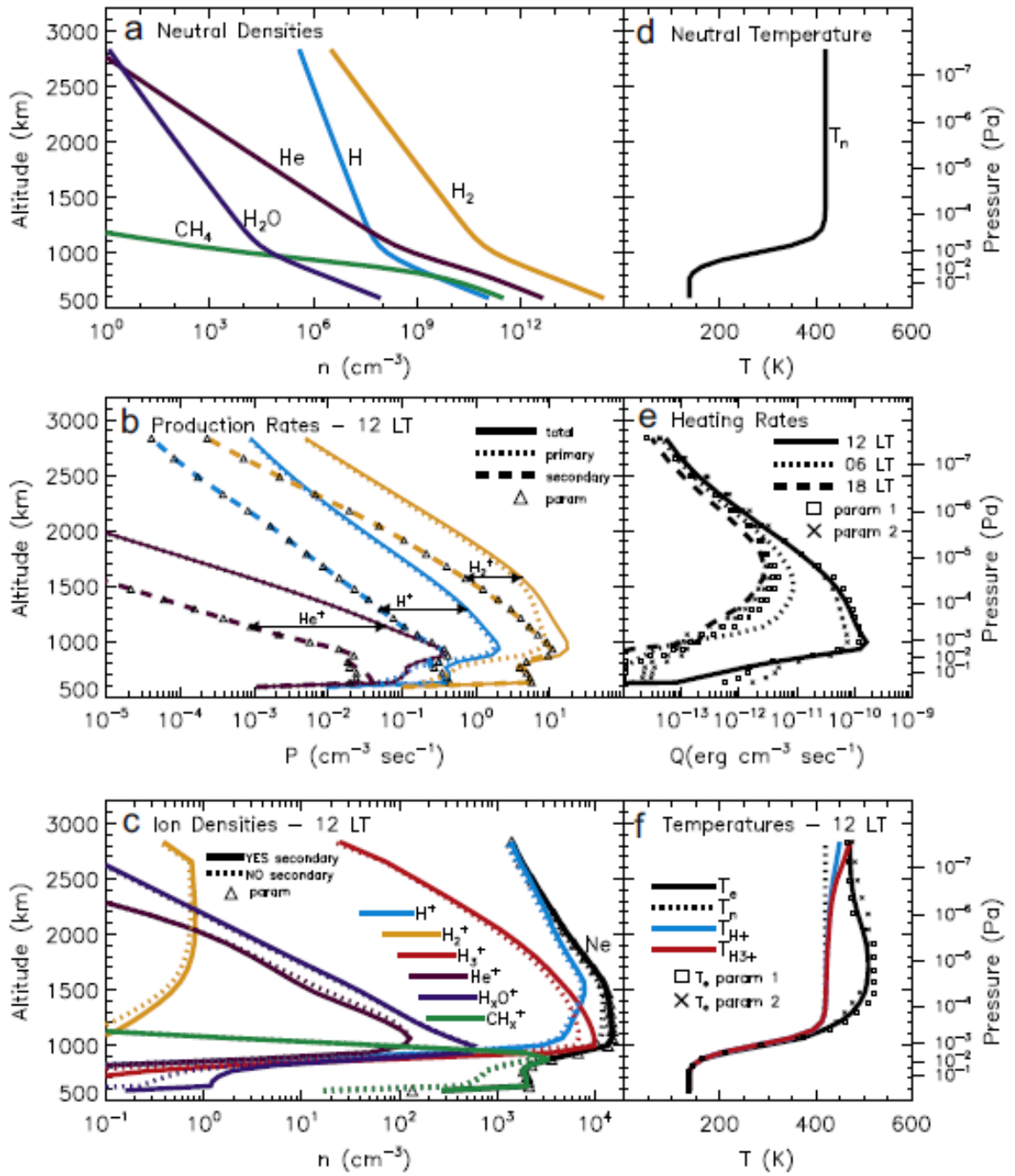


**Figure 1.6:** (on previous page) Figure 1 of Moore et al. (2009), the results from the Saturn Thermosphere Ionosphere Model for 30° N using TIMED/SEE solar maximum conditions during the Saturn equinox. (a) Background neutral densities. (b) Primary (dotted), secondary (dashed), and total (solid) production rates at local noon for  $H^+$ ,  $H_2^+$ , and  $He^+$ , where the  $H^+$  production is the sum of direct photoionization of H and dissociative photoionization of  $H_2$ . The triangles represent secondary production rates. (c) Ion and electron densities at local noon. Solid curves represent calculations that have accounted for secondary production, while dotted curves represent calculations that have not. Triangles give the electron densities that result from the parameterizations of the secondary production rates. (d) Background neutral temperature. (e) Thermal electron heating rates at local noon (solid line), dawn (dotted line), and dusk (dashed line). In addition, the cross and square symbols represent heating rates estimated from two different parameterizations. (f) Ion and electron temperatures at local noon. The cross and square symbols correspond to electron temperatures that have been derived using the two different parameterizations of the electron heating rates.

This model was based on the response of the atmosphere to photo-ionisation (the removal of an electron from an atom or molecule by an energetic photon) caused by the influx of solar photons. Their model shows most of the ion populations peaking in density around 1000 km above the 1 bar pressure surface commonly used in analysis for Saturn's atmosphere for a reference point. The neutral populations decrease consistently with altitude and have densities that are several orders of magnitude greater than those of the ions. The population densities of the neutrals decrease at a rate commensurate to their scale heights with the heavier species decreasing in density faster than the lighter species. This altitudinal distribution of temperature and density of the neutral populations is similarly characterised in the work of Galand et al. (2011) in Figure 1.7 for the auroral latitude of 78° S.

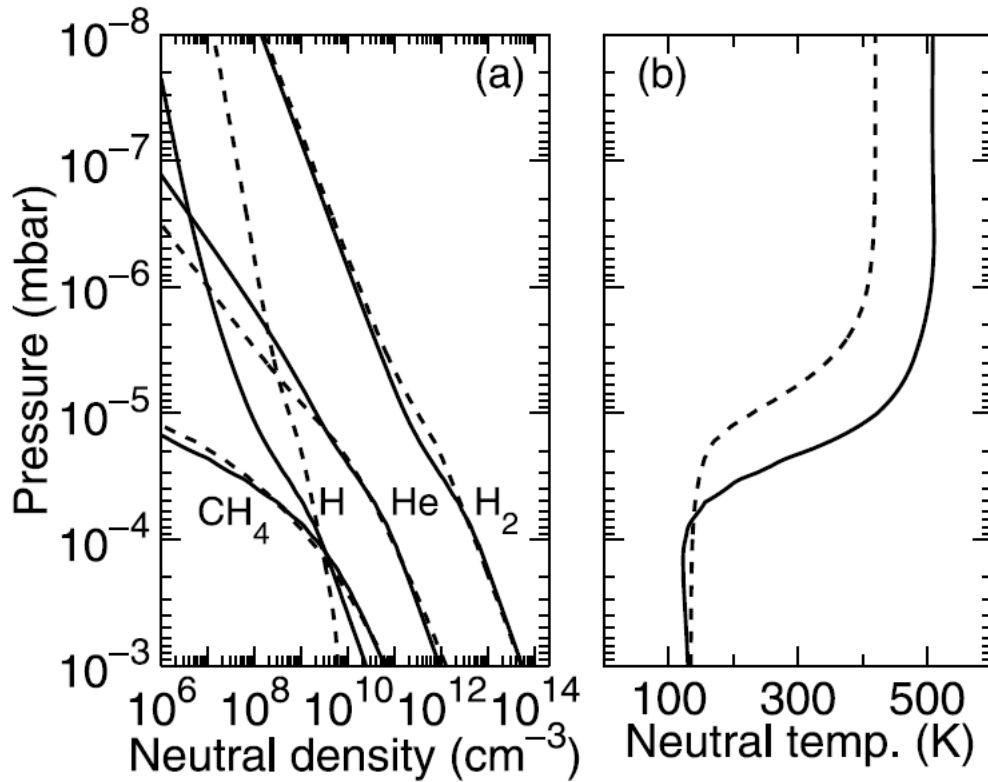


**Figure 1.7:** figure 1 of Galand et al (2011) showing the density of the neutral populations (a) and the neutral temperature (b) with altitude. The neutrals density profiles shown as solid black lines are based on the solid black temperature profile from the STIM model using an exospheric temperature of 510 K, whereas the dashed profiles are based on the temperature profile of Moses et al. (2000) with an exospheric temperature of 420 K.

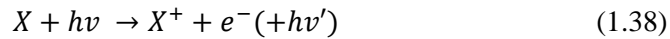
The ionosphere of Saturn has several sources and sinks for its constituent ion and electron populations such as photoionisation and particle precipitation that can both increase the plasma population or quench it depending on the source. As such, Section 1.3 which will cover the ionosphere in much greater detail has been subdivided into sections devoted to each identified influence including: photoionisation (Section 1.3.1), particle precipitation from the rings (Section 1.3.2), the Enceladus plasma torus responsible for the secondary oval as well as the Enceladus auroral spot (Section 1.3.3). The mechanisms that generate the main auroral oval have been separated out into Section 1.4 as they are the most pertinent to this thesis.

### Section 1.3 Influences on the ionosphere

In this Section, the various influences on the ion and electron populations are discussed with the exception of those relating to the main auroral oval (as they are most pertinent to the subject of this thesis they have been reserved for discussion in Section 1.4). The first influence is photoionisation that occurs globally on the dayside as a result of solar influx (Section 1.3.1). before discussions of loss mechanisms (Section 1.3.2), the ring rain (Section 1.3.3), the plasma torus and auroral spot from Enceladus (Section 1.3.4).

#### Section 1.3.1 Photoionisation

The photoelectron population arises from the electron absorption of extreme ultraviolet (EUV) photons from solar irradiance (as described in Schunk and Nagy, 2000). The distribution of this population of electrons has been examined in Galand et al. (2011) as demonstrated in Figure 1.8 and 1.9. The generalised reaction that produces the ions of Figure 1.6 is given in reaction 1.38 for a neutral species  $X$ .



This reaction requires that the photon ( $h\nu$ ) have an energy that is equal to or greater than the ionisation energy to remove the electron from  $X$  (for example, if  $X$  were hydrogen, the requisite energy would be 13.6 eV). A higher energy photon would be able to ionise an atom or molecule  $X$  and then scatter a new photon  $h\nu'$  at a lower energy. The altitude of this reaction is dictated by the depth to which EUV solar photons can penetrate. Galand et al. (2009) modelled the distribution of electrons from photoionisation for 30° north and found a similar peak electron density altitude (Figure 1.8); note though that the vertical structure of the observations was not expected to be observed in the model profiles as the model did not contain any processes that would produce such sharp layers.

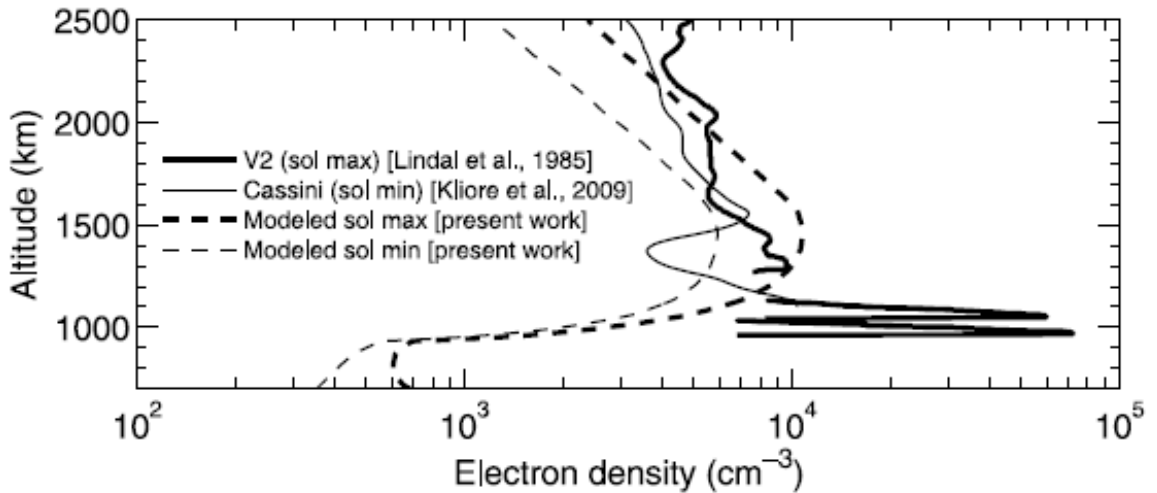


**Figure 1.8:** figure 9 from Galand et al. (2009), the electron density variation with altitude as observed in the Voyager 2 radio occultation analysed in Lindal et al. (1985) (thick solid black line), as observed in the Cassini radio occultation analysed in Kliore et al. (2009) (thin solid line) as well as the modelled profiles from Galand et al. (2009) for solar maximum (thick dashed line) and solar minimum (thin dashed line).

In the thermosphere the dominant ion produced by photoionisation is the long lived  $H^+$  (Galand et al., 2011). This ion can be lost through the reaction with vibrationally excited  $H_2$  ( $\nu > 4$ ) to produce the ion  $H_2^+$ . The ion  $H_2^+$  is also a component in the reaction to produce the molecule  $H_3^+$  which is the emissive species that is the focus of this thesis as described in Section 1.4.1. The distribution of this ion at lower latitudes has been modelled in the works of Moore et al. (2009) as shown in Figure 1.6. Local time variations in the electron population have been observed using radio occultations taken of the upper atmosphere at latitudes close to the equator and these show a diurnal variation in the electron density, to the point of creating an asymmetry in the population with respect to dawn and dusk (Moore et al., 2010). There is also a significant local time variation in the ion population. At sunrise the  $H_3^+$  population builds at a rate that is far more rapid than  $H^+$  or  $H_2^+$ , as these two ions are quickly lost to the production of  $H_3^+$  (Moses and Bass, 2000, Galand et al., 2009). Conversely, the same  $H_3^+$  population deteriorates after dusk due to the process of recombination and a lack of photoionisation. This process not only produces ions but also free electrons as part of the ionospheric plasma. It was observed in the radio occultations from Cassini that there was a peak in the electron density in the altitude range of 1800-2900 km above the 1 bar level as well as a secondary peak in the range of 1150-1800 km above the 1 bar level (Nagy et al., 2006).

Photoelectrons are not the only free electrons that interact with the ionosphere as shown in Figure 1.9 from Galand et al. (2011). There are also electrons that precipitate into the

atmosphere from the magnetosphere. These electrons and their interactions with the ionosphere/thermosphere of Saturn will be discussed in Sections 1.3.4, 1.3.5 and 1.4.

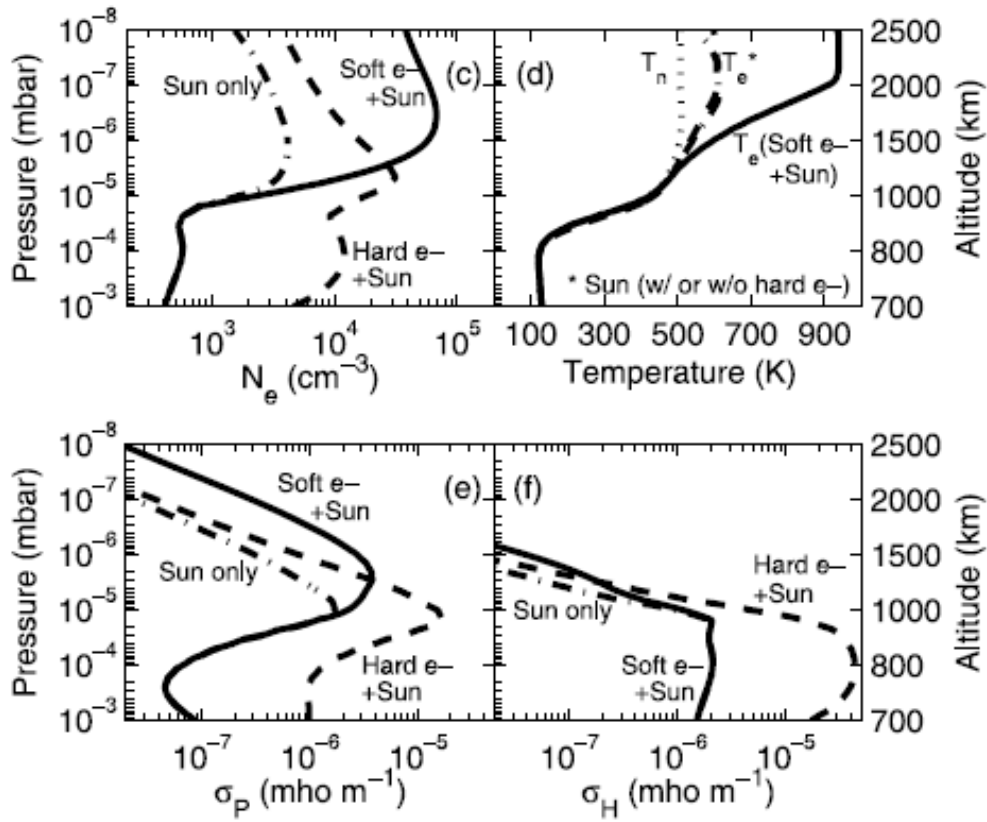


**Figure 1.9:** Figure 3 of Galand et al. (2011) showing the secondary electron densities (c) from STIM (Saturn Thermosphere-Ionosphere Model) calculations at 78 S latitude, at noon (for a solar zenith angle of 78), at equinox, during solar minimum, for the soft electron case [auroral electrons ( $E_m = 500\text{eV}$ ,  $Q_0 = 0.2 \text{ mW m}^{-2}$  + photoelectrons)] (dashed line), the hard electron case [auroral electrons ( $E_m = 10 \text{ keV}$ ,  $Q_0 = 0.2\text{mW m}^{-2}$ ) + photoelectrons)] (dash-dotted line). Likewise, the temperatures of the secondary electrons (d), the Pedersen conductivity (e) and the Hall conductivity are plotted for the same conditions as (c).

### 1.3.2 Loss mechanisms

Production mechanisms are not the only process involved in ionosphere, there are also loss mechanisms which need to be taken into account as well. These mechanisms account for ion-neutral reactions such as: the charge exchange between  $H^+$  and vibrationally excited  $H_2$  (McConnell et al., 1982, Moses et al., 2000, Moore et al., 2010), forced vertical motions of the plasma (McConnell et al., 1982, Majeed and McConnell, 1991) and water inflow (Connerney and Waite, 1984, Majeed and McConnell, 1991, Moses and Bass, 2000, Moore et al., 2006) and electron-ion recombination (included in all models). It has been noted that there is a mid-latitude dip in both the electron and  $H_3^+$  density; this was found to be due to the inflow of water from both the rings and Enceladus described in both models (Connerney and Waite, 1984, Moore et al., 2006, 2010) and shown indirectly in observations (O'Donoghue et al., 2014); described in Section 1.3.4.

### Section 1.3.3 Ring Rain

O'Donoghue et al. (2013) observed a significant variation in the  $H_3^+$  population (an IR active species which will be discussed in detail in Section 1.4) in the form of latitudinal bands of brightening between the latitudes  $30^\circ$  and  $50^\circ$  in both hemispheres. This was interpreted as a direct consequence of water ion precipitation from the rings which has since been dubbed “ring rain”, an artist's impression of which is shown in Figure 1.10. Cassini observations of the rings of Saturn have revealed a water-product atmosphere surrounding them; this atmosphere consists of icy grains which are partially ionised by the UV solar irradiance. In the region of the rings where the centrifugal forces from the motions of the icy grains balance with the gravitational pull of Saturn the rings are described as being unstable. It is from this region that trapped ions such as  $O_2^+$  and  $O^+$  as well as water molecules are able to stream down magnetic field lines mapping to gaps in the rings and precipitate into the atmosphere (an artist impression of which is shown in Figure 1.10). When they reach the atmosphere, they consume the electron and ion populations in a process known as quenching which was posited in Connerney (1986). Thus the latitudinal regions that map magnetically to the gaps in the rings exhibit a brightening of  $H_3^+$  emission in the form of a global latitudinal band as compared to the latitudinal bands either side which map to the rings (as shown in the intensity profile of Figure 1.11). The presence of neutral water at these latitudes also leads to the depletion of the  $H^+$  population as well as the  $e^-$  population, therefore molecular ions (such as  $H_3^+$ ) become more dominant, at least in the late morning to early afternoon sector (Moore et al., 2006).

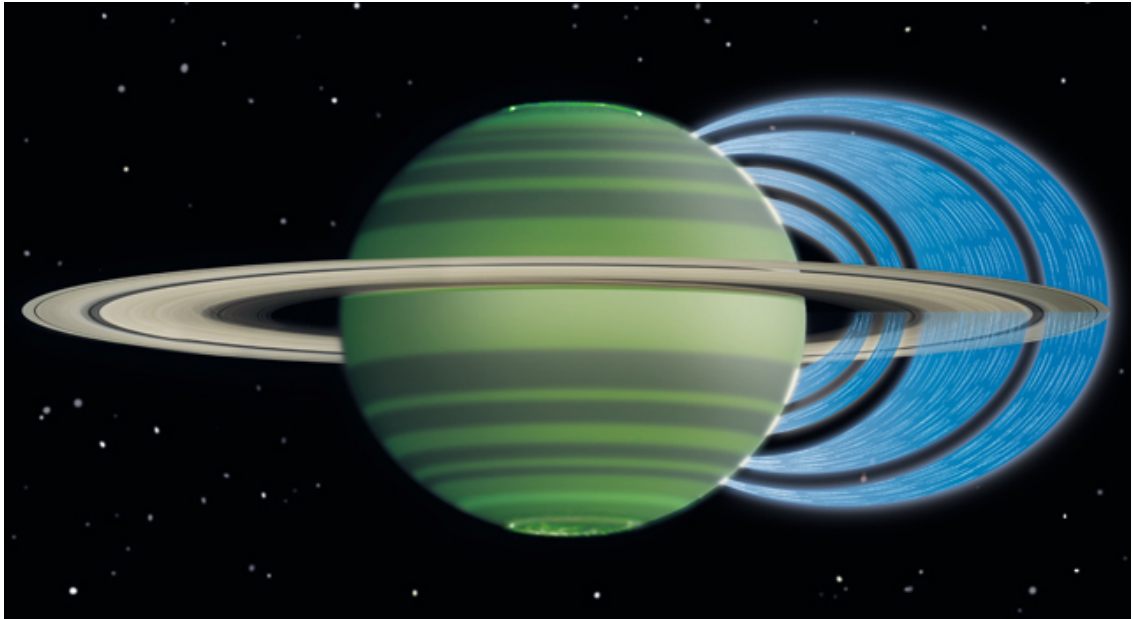


**Figure 1.10:** An artist's impression of the precipitation of ions into the upper atmosphere of Saturn; created as part of a press release in association with the work of O'Donoghue et al. (2013). Image credits to NASA/JPL-Caltech/Space Science Institute/University of Leicester.

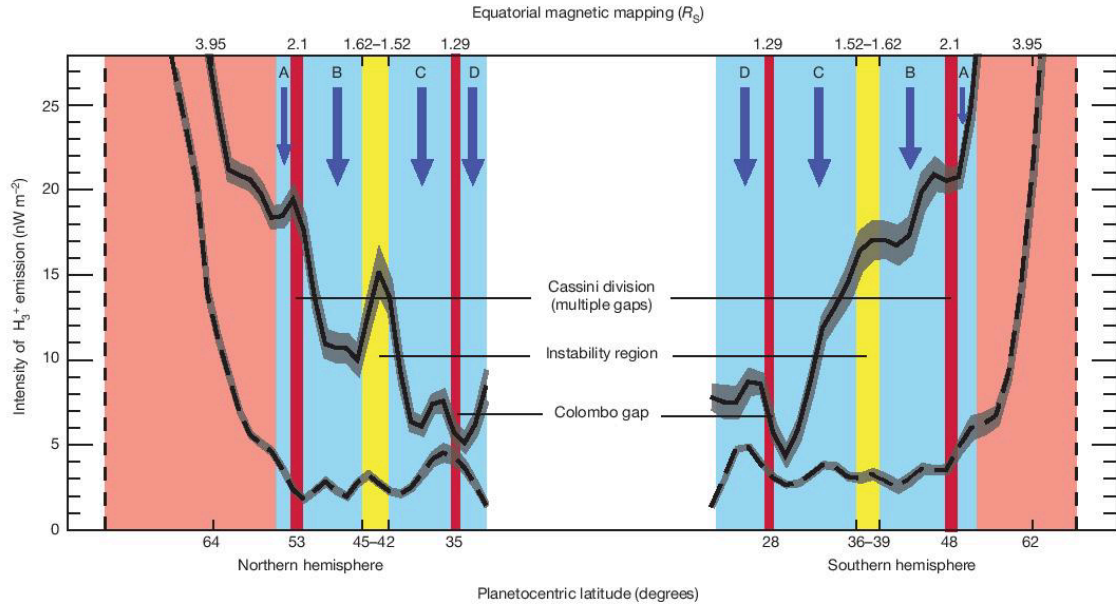


**Figure 1.11:** Figure 2 of O’Donoghue et al. (2013) showing the variation in  $H_3^+$  IR emission intensity for two emission lines  $3.953 \mu\text{m}$  (black line) and  $3.622 \mu\text{m}$  (dashed black line) as a function of latitude long Saturn’s noon meridian. The bottom horizontal axis shows the planetocentric latitudes whilst the top axis shows the planetocentric equatorial distances that these latitudes map to magnetically. The latitudes have been colour coded into bands, with the blue regions denoting latitudes which map to rings and are subject to water influx, the red bands map to gaps in the rings, the yellow to the instability region (where the Keplerian velocity of the rings is close to the rotational velocity of the magnetic field) and remaining regions are shaded pink.

### Section 1.3.4 Enceladus

Enceladus, a moon of Saturn orbiting at a distance of approximately  $4 R_s$ , ejects neutral material into the space around it through cryovolcanism. Photoionisation of this material loads ionised mass onto the magnetic field lines in that region. The mass loading of the field lines located around Enceladus leads in turn to the precipitation of plasma into the atmosphere, enhancing the ionospheric plasma population and triggering auroral emission akin to that described in Section 1.4 focused in an auroral spot at the footprint of the magnetic field lines which map to Enceladus. Heretofore, this auroral spot has only been seen in the ultraviolet (Pryor et al., 2011).

The process of mass loading by Enceladus occurs across its entire orbit, and as a consequence of this, the neutral species that are present in the induced plumes can be ionised and form a plasma torus within the magnetosphere of Saturn (Melin et al., 2009, Smith et al., 2010), the

majority of which is in the range of 3-6  $R_s$ , and migrates outwards due to the centrifugal force. The flow of plasma and the motion of the magnetic field lines in this region gives rise to another phenomenon known as the secondary auroral oval (denoted as separate from the main auroral oval in Section 1.4). Radial outward motion of the plasma creates a current that must be closed with bipolar field aligned currents with the downward currents flowing into the polar regions and upward currents flowing equatorward (Cowley and Bunce, 2003). The Enceladus plasma torus maps magnetically to this secondary auroral oval, which has a brightness which is roughly 25% the brightness of the main auroral oval, and is identified a broad region of emission at  $\sim 62^\circ$  N and  $\sim 58^\circ$  S (Stallard et al., 2008, Stallard et al., 2010). A similar process is also responsible for the generation of Jupiter's main auroral oval which is on average 100 times brighter than Saturn's main oval. The extent to which this process happens at Saturn is far weaker than at Jupiter due to a weaker plasma torus; the expulsion of neutrals from Enceladus' plume results in mass loading at a rate of approximately 350 kg/s (Hansen et al, 2006) whereas the pick-up rate from Io's atmosphere is one tonne per second (Herbert et al, 2008).

#### 1.4 The main auroral oval

One of the key features of the ionosphere and the main focus of this thesis is Saturn's main auroral oval (examples of which are in Figure 1.9). This section contains a short summary of published research that is relevant to the context of this thesis. Auroral emissions represent an interaction region between a planet's atmosphere, magnetosphere and proximal space environment, as well as – for the infrared aurora – the thermal characteristics and dynamics of the atmosphere. Unlike Jupiter, where the main auroral oval is created by the breakdown in corotation within the Jovian magnetosphere generating corotation enforcement currents, Saturn has an auroral oval more akin to that of Earth, in that it lies on an open-closed field line boundary (Bunce et al., 2008, Cowley and Bunce, 2003, Clarke et al., 2009). In subsequent research, it has since been shown that the solar wind, much like the terrestrial aurorae, has a significant impact on the aurorae of Saturn. By contrast, Jupiter's aurorae are dominated by sources internal to its magnetosphere (Clarke et al., 2009). The first few parts of this section will cover the mechanisms that drive the Saturn's aurorae in more detail as well as the chemical and molecular processes involved in the generation of the infrared auroral emissions. To begin with, the primary mechanism of auroral generation, particle precipitation, is explained in Sections 1.4.1-1.4.3. The later Sections 1.4.4-1.4.6 will address the morphology, dynamics and physical properties of the aurora. There are three types of auroral emission that have been observed at Saturn; the Ultraviolet emission, the Visible emission and the Infrared emission (Melin et al., 2007). Of these three emission types, the emission mechanisms for which are shown in Figure 1.13, the Infrared and Ultraviolet are the two that have been studied in the greatest detail, largely because the visible emission is generally drowned out on the dayside by reflected sunlight at the same wavelengths. For the infrared and ultraviolet aurorae there are windows in the emission of different species that enable us to view the auroral emission at all local times with relatively minor interference from other sources of emission. This will be covered in detail in later sections.

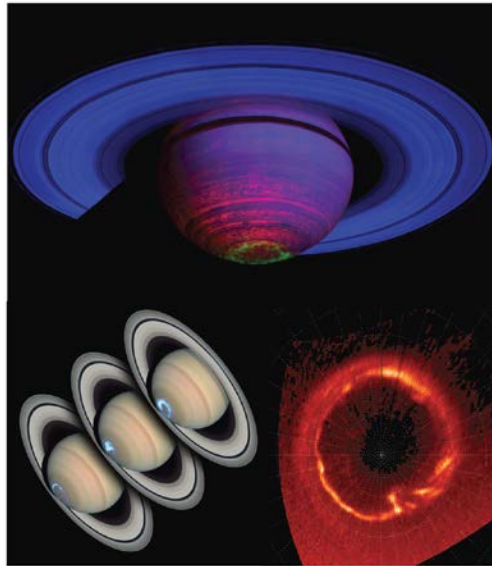


**Figure 1.12:** from figure 1 of Bunce et al. (2012) an image of Saturn in the infrared displaying Saturn's dynamic auroral oval (top) as viewed by Cassini VIMS, Hubble Space Telescope observations of the Ultraviolet aurora (left) showing the evolution of Saturn's main auroral oval from the quiescent state to a highly active state in response to a high pressure region from the solar wind (from lower left to upper right) as well as a Cassini UVIS observation of main oval. These images show Saturn's main aurora oval to be circular in morphology and varying in intensity with time.

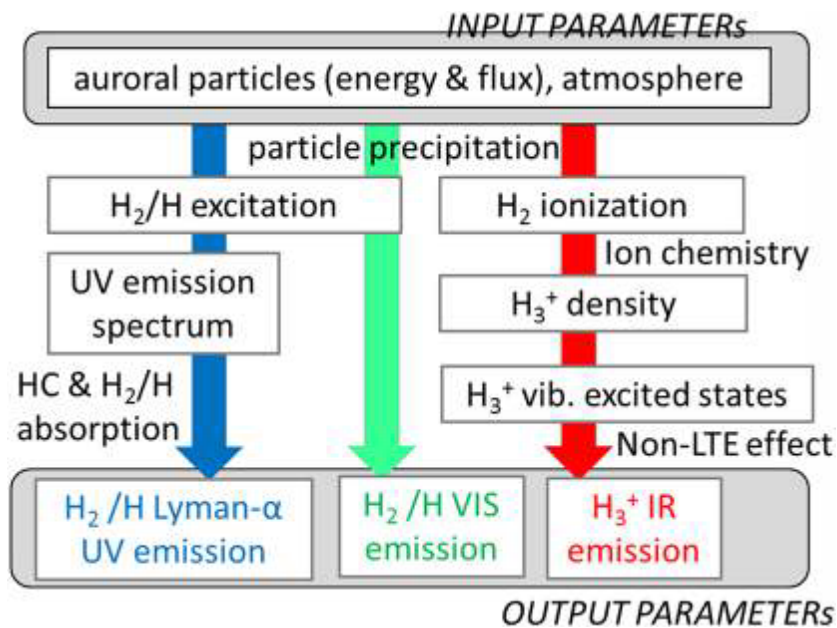


**Figure 1.13:** Figure 9 of Badman et al. (2009) showing a flowchart of the auroral processes at Saturn after particle precipitation into the  $H_2$  dominated atmosphere.

### 1.4.1 The magnetospheric origin of the aurorae

The origin of Saturn's main auroral oval has been subject to discussion in a variety of different published literature. Some suggested that, like its fellow gas giant Jupiter, Saturn's main auroral oval would be generated by what is referred to as corotation enforcement currents. As described in Andre et al. (2008), the region inside of  $3 R_s$  the magnetic field and the plasma populations are rigidly corotating with the planet and the magnetic field lines. The ionosphere exerts a viscous torque on the magnetic field lines, dragging them round with the planetary rotation. This corotation holds true so long as the magnetic field energy density dominates over the kinetic energy of the plasma and forces the plasma to be confined to the field lines. However, as the field strength and therefore the magnetic energy decreases with distance there is a point, known as the Alfvén point, where these forces balance. Beyond this Alfvén point and away from the body of the planet, the balance between the magnetic energy density and the kinetic energy of the plasma shifts, and the plasma dominates. As the plasma orbits the planet, the centrifugal forces cause it to diffuse radially outwards resulting in a current (Figure 1.14). This current must be closed as (since we do not observe a build-up of plasma in the outer magnetosphere) along the field lines, hence a strong circuit of electric currents also known as Hill currents (Hill, 1979) force plasma to travel along the field lines in the directions shown in Figure 1.14.

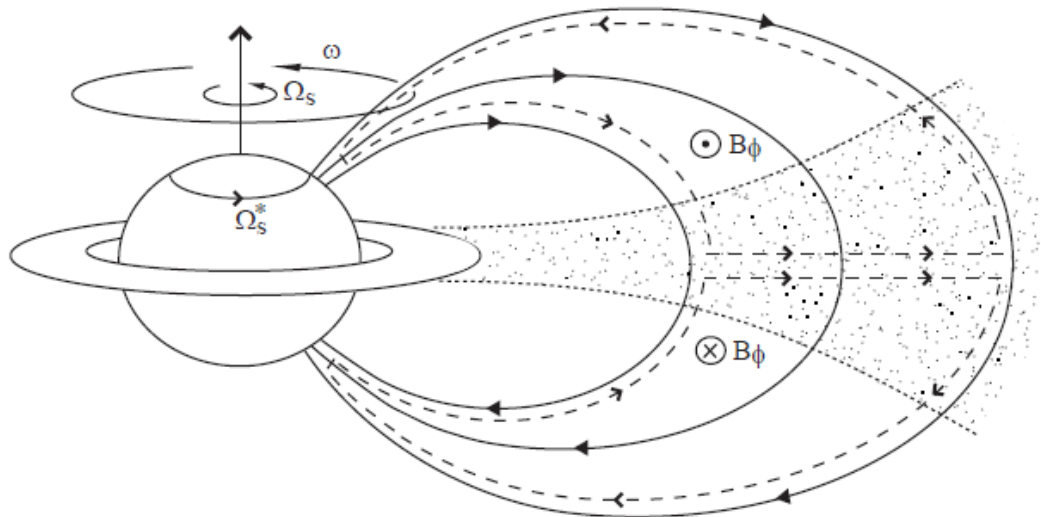


**Figure 1.14:** From figure 1 of Cowley and Bunce (2003) showing the corotation enforcement currents (dashed lines), the plasma torus (shaded region) and the azimuthal magnetic fields arising from the current system  $B_\phi$ .

Cowley and Bunce (2003) showed that the field aligned currents associated with this system force the plasma into corotation; which is why they are referred to as corotation enforcement currents. However, they also showed that these currents are both too weak to generate the

aurorae of Saturn (they only amount to approximately  $10 \text{ nA m}^{-2}$ ). Not only are they too weak, but the magnetic field lines on which these currents lie map to the wrong latitudes in Saturn's ionosphere; at around 20 degrees colatitude as compared to the main auroral oval, which is generally located at a colatitude of 15 degrees. Instead of these currents, it has been subsequently found that the auroral regions are associated with the open closed field line boundary (OCFLB) much like the terrestrial aurora.

At distances greater than  $14 R_S$  the outer magnetosphere extends out to the magnetopause; a boundary which defines the edge of Saturn's magnetic field, the average location of which is  $22 R_S$  at the sub-solar point (Gombosi et al., 2009). The magnetic field lines in this region can be mapped to high latitudes (specifically the polar and auroral regions). At these latitudes there are purely planetary field lines where both ends are connected to Saturn (closed flux) and field lines where one end is connected to the planet and the other extend out into the solar wind (open flux); these different types of field lines shown in Figure 1.15 form part of the Dungey cycle at Saturn.

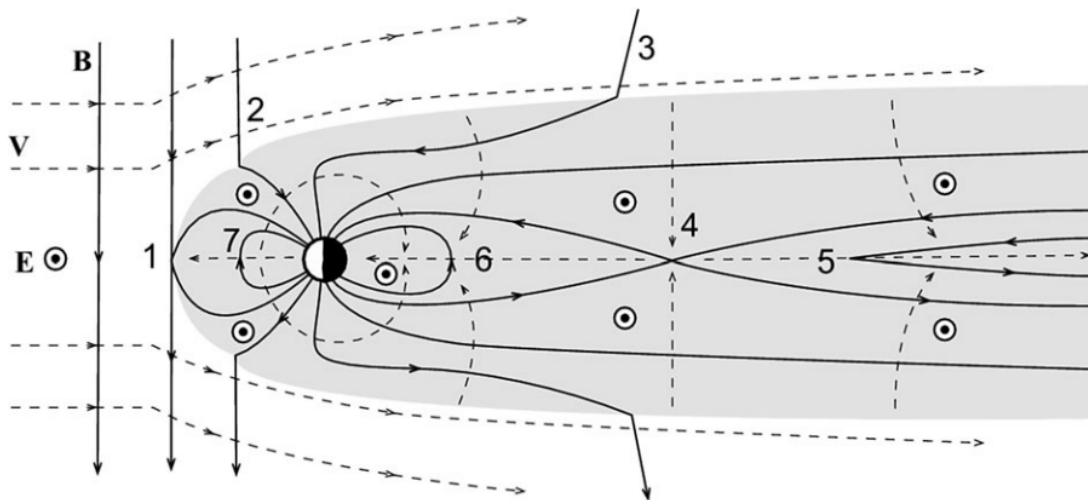


**Figure 1.15:** A representation of the Dungey cycle at Earth in stages in the x-y plane where x is the ecliptic Sun-Earth line (left to right) and y is the direction perpendicular to the ecliptic plane (bottom to top), from Seki et al. (2007), courtesy of Steve Milan. Where the solid arrows represent magnetic field lines  $\mathbf{B}$  (the straight ones on the left are those of the Interplanetary Magnetic Field – IMF – and the rest are connected to Saturn as part of its magnetosphere). The dashed arrows represent the motion of the field lines  $\mathbf{V}$  and the circumpunct is used to represent the electric field  $\mathbf{E}$  (which is pointed out of the x-y plane shown here). The grey shaded region represents the planetary magnetosphere (the region over which the planet's magnetic field is dominant).

Using Figure 1.15 as a guide we see that the Dungey cycle begins with the Interplanetary Magnetic Field (IMF) impacting on a magnetosphere with a  $B_y$  component that is in opposition; for Saturn where the magnetic field lines are oriented north-south the IMF  $B_y$  component would need to be northward. Under these circumstances, reconnection can occur at point (1), creating newly “opened” field lines where one end is attached to the planet (one in the north and one in the south) and the other end stretches out into interplanetary space. The flow of the solar wind pulls the solar wind portion of the field line anti-sunwards through (2) and (3) until it forms part of the magnetotail. Once in the magnetotail, two open field lines (one from the northern lobe of the tail and one from the southern) can reconnect (4) forming a closed planetary field line and a new purely interplanetary field line. The new IMF line (5) is distorted and stressed; it continues flowing to the right where it will eventually rejoin the solar wind flow. The new closed planetary field line is also stressed and so flows and relaxes planetward (6). The cycle is closed as this planetary field line flows around the planet through the dawn sector (for Saturn) to the dayside (7).

Reconnection events in the magnetotail accumulate plasma and electrons from the solar wind and accelerate this energetic population towards the planet, where those electrons and ions with a pitch angle within the loss cone will precipitate and be lost to the upper atmosphere (Kivelson and Russell, 1995). As a consequence of this, there is a change in the electron densities in the auroral and polar upper atmosphere of Saturn (Galand et al., 2011). It is the open-closed field line boundary (marked by the blue line in Figure 1.16) that this cycle forms that has been cited as the primary source of precipitating electrons that generate the main auroral oval (Bunce et al., 2012).

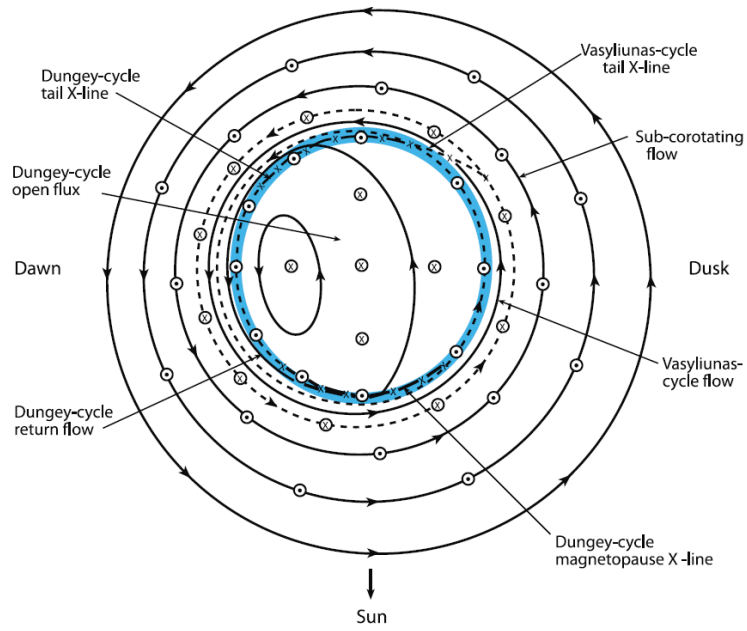


**Figure 1.16:** From Bunce et al. (2012) and Cowley et al. (2004a), a schematic depicting the various plasma flows in Saturn's northern polar ionosphere as well as the associated field-aligned current patterns. The upward directed field-aligned current pattern is shown as the shade blue region.

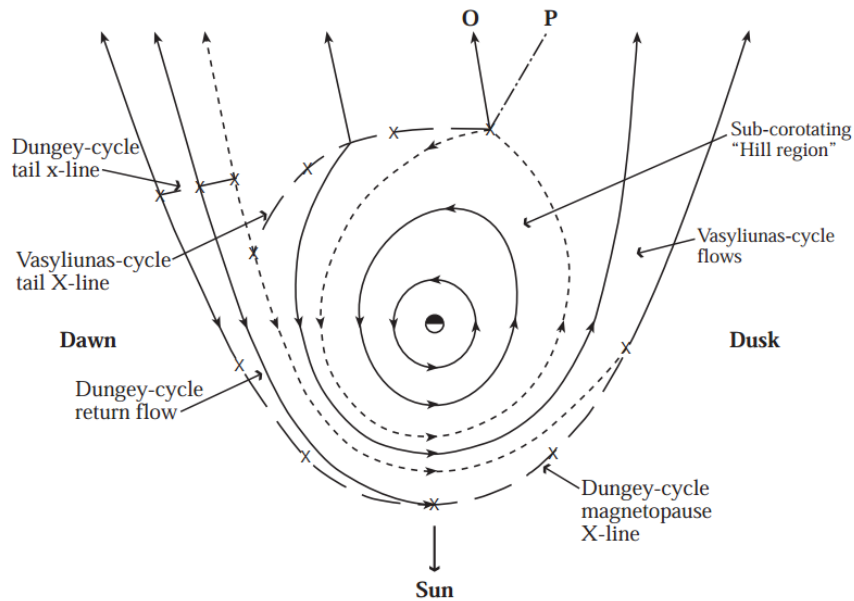


**Figure 1.17:** A sketch of the plasma flows in the equatorial plane of Jupiter’s magnetosphere depicting the reconnection lines of both the Vasyliunas and Dungey cycle from Badman and Cowley (2007) and Cowley et al. (2003). Also marked on this diagram is the location of the sub corotating Hill region. The flows at Saturn are essentially the same. As described in Cowley et al. (2003), the solid lines with arrows show plasma stream lines, while dashed lines with arrows show streamlines which separate flow regions with differing origins and characteristics as indicated. The reconnection lines are shown using dashed lines whereby “X”s indicate X-type reconnection lines, while the solid line marked “O” indicates the O-type line of the Vasyliunas-cycle plasmoid which is ejected down-tail (which is a streamline). The dot-dashed line marked “P” is the outer boundary of the plasmoid, which asymptotes to the dusk tail magnetopause.

Inside of the outermost boundary of the magnetosphere is a region of sub-corotating plasma that forms part of the Vasyliunas cycle (Figure 1.17). The Vasyliunas cycle, first described in Vasyliunas (1983) has been succinctly explained in Badman and Cowley (2007) as follows; Vasyliunas suggested that mass-loaded flux tubes in the outer corotating region will generally be radially restrained on the dayside by the solar wind dynamic pressure, but may then stretch out down-tail as they rotate into the dusk sector, eventually pinching off to form a tailward propagating plasmoid. The mass loading inflates the flux tubes around dusk, these flux tubes then flow into the magnetotail where they are pinched off to form plasmoids. The reconnection line for this process is marked in Figure 1.17 as the “Vasyliunas cycle tail x-line”. The mass-reduced closed portions of these flux tubes then return to the dayside via dawn, where they

again become mass loaded by radial diffusion from the inner regions and stretch out once more as they rotate into the dusk sector. This is the process that we refer to as the Vasyliunas cycle, and reconnection events from this process as well as the Dungey cycle are thought to be responsible for diffuse auroral enhancement via the injection of hot plasma which circles round to the dawn sector (Cowley, 2005).

#### 1.4.2 Hydrogen atomic and molecular emission

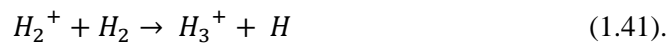
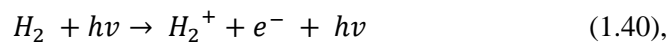
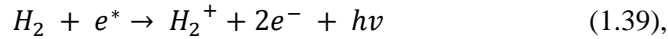
As described in Badman et al. (2015), ultraviolet and visible photons are produced when electron-excited hydrogen molecules and atoms are de-excited from their energised states into their ground level states. For the gas giants Jupiter and Saturn these transitions are predominantly the H Lyman  $\alpha$  emission line (triggered by an electron exciting to the  $n=2$  level de-exciting to the  $n=1$  level by emitting a UV photon) and the H<sub>2</sub> Lyman-Werner emission lines (which involves molecular transitions from either the Lyman electronic state B or the Werner electronic state C down to the ground electronic state X). The excited states mainly receive their energy from collisions with electrons that have precipitated from the magnetosphere. The altitudinal depth of these emissions can be measured by determining the degree of absorption from both H<sub>2</sub> molecules for wavelengths less than 120 nm and hydrocarbon species such as methane for wavelengths less than 130 nm; the extent to which this absorption occurs is wavelength dependent and hence can be calculated by comparing wavelengths that are affected by absorption with others that are not. The ratio of these two groups, also known as the colour ratio, is therefore directly related to the altitude of the emission and can be used to derive the altitudinal location of the auroral emission (Kurth et al., 2009).

At Saturn, the primary energy range of the electrons that generate the ultraviolet aurorae has been estimated at 10-18 keV (Gustin et al., 2009) and 5-30 keV (Gerard et al., 2009), the penetration depth of which is very close to or above the methane homopause. Based on the radiated power of 10-30 GW from the UV auroral emissions, it is suggested that the energetic input of the precipitating electrons stands at 100-300 GW (Gerard and Singh, 1982). This, in turn, indicates a significant degree of heating occurring in the auroral regions due to energy deposition from the precipitating electrons. Further, in the case where the precipitating electrons ionise atmospheric neutrals, secondary thermal electrons are produced and released into the thermosphere, further increasing the local plasma population as well as affecting the production/recombination rate of H<sub>3</sub><sup>+</sup> as described in Section 1.4.3.

The altitude of peak auroral UV emission has been measured by Gerard et al. (2009). They conducted a statistical study from a series of 836 images of the night side auroral emission as observed by the Hubble Space Telescope (HST). This study measured the average peak emission to be  $1145 \pm 305$  km. Spectral analysis showed that the prevailing temperature in the measured night side limb was 400 K. This study concluded that the peak brightness of H and H<sub>2</sub> emission was in the range of 900-1300 km above the 1 bar pressure level. From the study of Melin et al. (2009) it is shown that to a good approximation, the UV and IR emissions are synonymous in the main auroral oval and one can be considered a good proxy for the other in terms of latitude and local time, in spite of the differences between their production methods.

### 1.4.3 The IR emission, production and loss of $H_3^+$

Aurorae have been seen on several planets besides Earth and in Geballe et al. (1993) it was shown that, like Jupiter, Saturn has an infrared aurora emitted by the molecular species  $H_3^+$ . The molecule  $H_3^+$ , also known as the trihydrogen cation, is produced in a two-step reaction. The first step is the production of  $H_2^+$ , which can be achieved by ionising  $H_2$  either with an energetic UV photon (reaction 1.39) or an energetic electron collision (reaction 1.40), this  $H_2^+$  rapidly reacts with remaining  $H_2$  molecules to form  $H_3^+$  (reaction 1.41).



Destruction of  $H_3^+$  can come in multiple forms, the first of which is dissociative recombination with a free electron leading to the production of either a combination of atomic and molecular hydrogen (reaction 1.42) or purely atomic hydrogen (reaction 1.43). Alternatively  $H_3^+$  can be destroyed through collisions with a neutral species  $X$  (reaction 1.44). This reaction is highly efficient for any species  $X$  that has a higher proton affinity than  $H_2$  (Flower, 1990); examples of which include  $CH_4$  and  $C_2H_2$ .



There are significant differences between the infrared aurorae of the gas giants; the first is the intensity of Saturn's main oval, which is of the order of one hundred times weaker than that of Jupiter. A second difference is the relative altitude of the auroral peak emission layer; at Jupiter, the peak emission layer lies beneath the homopause, in a region where there is a significant population of hydrocarbons that consumes  $H_3^+$  via protonation (reaction 1.44), as compared to Saturn where the peak emission layer is above the homopause (Stallard et al., 2012a), such that  $H_3^+$  can only be destroyed by dissociative recombination (reactions 1.42 and 1.43). Below the homopause  $H_2^+$  reacts quickly with hydrocarbons and is therefore lost before it can generate the  $H_3^+$  population (Kim and Fox, 1994, Moses and Bass, 2000, Achilleos et al., 1998), this

contributes toward the “drop-off shoulder” in the infrared emission that occurs at the homopause boundary. Both of these production and loss mechanisms, or lack thereof, are particularly important with regard to the infrared aurora as it changes the chemical populations of the ambient atmospheric layer and hence the density of the emissive species  $\text{H}_3^+$ . As such, the Kronian aurorae are an excellent and accessible diagnostic tool for examining large scale magnetospheric phenomena, atmospheric behaviour and characteristics as well as solar wind dynamics. These factors have been studied at length in a diverse variety of literature, of which a relevant sample has been detailed below.

Across the body of Saturn, the main source of ionisation is EUV solar irradiance, which can generate a large amount of  $\text{H}_3^+$  in the upper atmosphere on a global scale via photo-ionisation (though this amount is relatively much smaller per unit area), though only on the day side. In the Polar Regions however, most  $\text{H}_3^+$  is generated by electrons accelerated down magnetic field lines and into the upper atmosphere. The precipitation of these electrons leads to the ionisation of the local neutral molecular hydrogen population and to the generation of an IR auroral emission through the process described above. In this region of the ionosphere (at a latitude of approximately  $75^\circ$ ) there is an increase in the population of vibrationally excited  $\text{H}_2$  ( $v \geq 4$ ), which results in the more efficient removal of  $\text{H}^+$  through the process of charge exchange,  $\text{H}_2(v \geq 4) + \text{H}^+ \rightarrow \text{H}_2^+ + \text{H}$  (Cravens et al., 1987), thus increasing the production of  $\text{H}_3^+$  via reaction 1.41.

The altitude of the bright  $\text{H}_3^+$  emission is governed by the ionisation rate, which is controlled by aspects of the auroral mechanism such as the pitch angle and the energy of the precipitating electrons. The  $\text{H}_3^+$  intensity is governed by both the temperature of the surrounding atmosphere and the density of the  $\text{H}_3^+$  population in that region. The resultant  $\text{H}_3^+$  population has a lifetime of around 10 minutes and as such is able to thermalize with the surrounding neutral atmosphere through collisions, where it establishes a quasi-local thermal equilibrium with the neutral atmosphere (Melin et al., 2011). Through the transfer of energy in collisions with neutrals, the  $\text{H}_3^+$  population reaches higher molecular energy levels (higher temperatures) they are able to transit through forbidden ro-vibrational energy transitions and emit photons in the near infrared spectrum, thus generating the IR aurorae. As  $\text{H}_3^+$  absorbs energy from the surrounding atmosphere and radiates it out to space through these IR emissions, the molecule plays a significant role in the cooling of Saturn’s upper atmosphere; this property has come to be termed “the  $\text{H}_3^+$  thermostat” at Jupiter (Miller et al., 2010). The emissions constitute a spectrum which we can use to measure properties such as the temperature. The particulars of these different transitions and the manner in which they can be analysed is discussed in Sections 1.5, 1.5.1 and 1.5.2.

For the UV emission, shown in Figure 1.40 and 1.41, the emission is triggered by the excitation of H and H<sub>2</sub>. Unlike the IR emission, this does not involve a series of chemical reactions but rather the inelastic collision between precipitating electrons and primarily H<sub>2</sub> (Gustin et al., 2009, 2012 and 2013). The collision excites the H<sub>2</sub> molecule into higher rotational-vibrational-electronic states, from which the molecule de-excites by emitting UV photons. The UV emission of H<sub>2</sub> is attenuated by CH<sub>4</sub> which absorbs wavelengths smaller than 1350 Å. As the density of CH<sub>4</sub> decreases with altitude, it can be used to ascertain the altitude of UV emissions using the colour ratio technique described in Section 1.4.2. The altitude of the UV emission is determined by the energy of the precipitating electrons; higher energy electrons will require a greater number of collisions to dissipate their energy and some electrons may have enough energy to trigger ionisation which in turn leads to energetic secondary electrons (Figure 1.6 and Figure 1.9); which may also stimulate UV emission.

#### Section 1.4.4 Auroral morphology and intensity in the UV and IR

Variations in auroral emission intensity as well as morphology have been observed in response to the solar wind conditions (Clarke et al., 2005, 2009, Cray et al., 2005, Bunce et al., 2005a, Badman et al., 2005). At Saturn the solar wind ram pressure (the pressure on the magnetosphere from the solar wind plays a significant role in combination with the orientation of the IMF (Bunce et al., 2012). Shock-compression fronts such as corotating interaction regions (CIRs) have been shown to reduce the size of the auroral oval and increase the intensity, in effect creating auroral “storms” that are associated with this change in the pressure on the magnetosphere. In contrast, in the terrestrial magnetosphere bursts of reconnection activity are dominated by the orientation of IMF but the solar wind ram pressure plays a much smaller role (Kivelson and Russel, 1995); the reason for this difference in influence has been put down to the difference in scale of the Saturn and Earth’s respective magnetospheres (Bunce et al., 2012). The orientation of the IMF changes on relatively similar timescales at both Saturn and Earth (from 10 minutes to approximately an hour), and similarly the production rates of open flux on the dayside, also known as dayside reconnection voltages are of the same order (around 20kV for rarefactions of the solar wind, and 200kV for compressions). However, as explained in Bunce et al. (2012), the amount of open flux in Saturn’s magnetotail is much larger (~50GWb) than at Earth (~0.5GWb) and hence the growth phase of these sub-storm like events at Saturn could be of the order of 1 week rather than the 1 hour at Earth. Hence, Saturn’s magnetotail would be less sensitive to the orientation of the IMF than Earth. Though compression induced reconnection is much rarer for Earth’s magnetotail (Boudouridis et al., 2003), it is essentially the modus operandi for Saturn on the nightside.

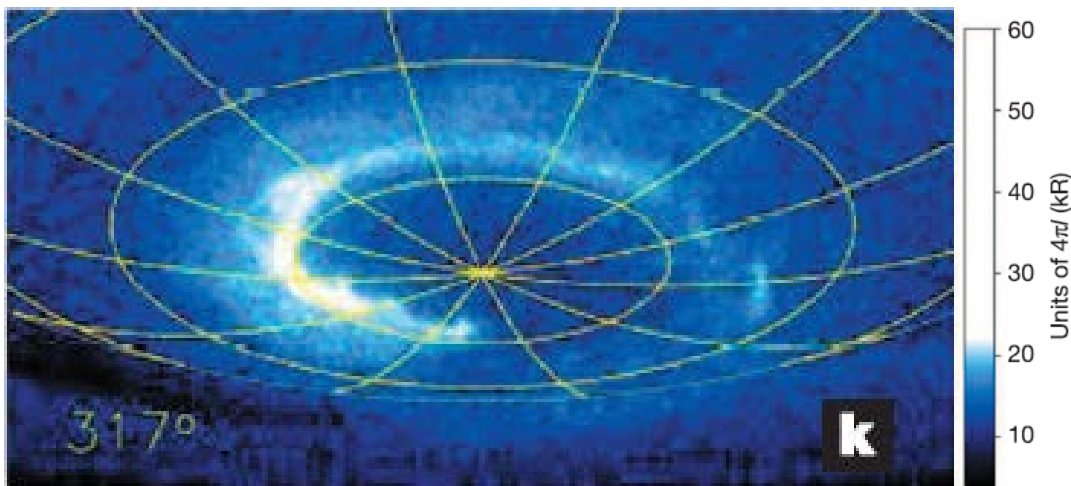
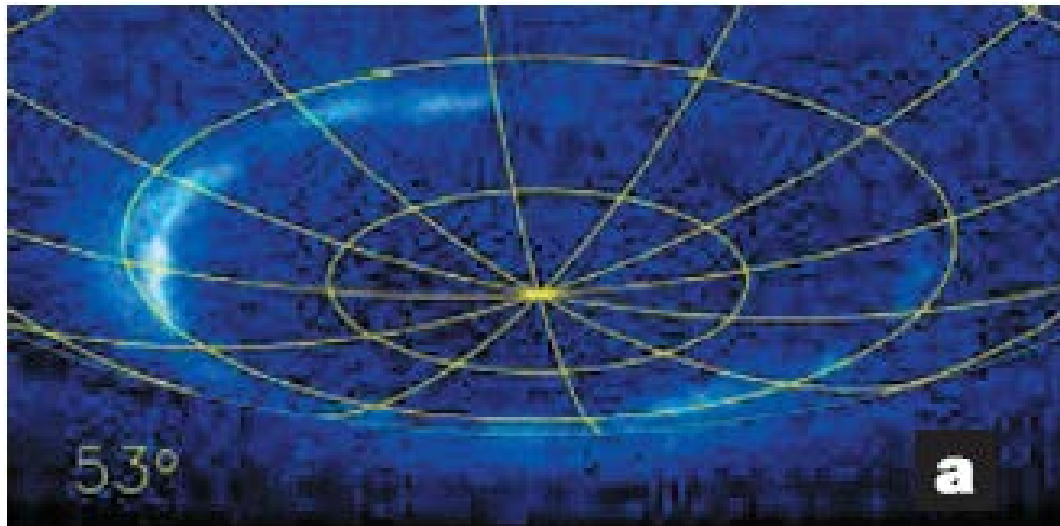


**Figure 1.18:** Figure 1 (a) and (k) of Clarke et al. (2005) showing the southern auroral of Saturn as observed by the Space Telescope Imaging Spectrograph (STIS) instrument on the Hubble Space Telescope (HST) on the 8<sup>th</sup> (a) and 28<sup>th</sup> of January 2004. The numbers in each panel are the central meridional longitude in degrees in the Saturn Longitude System. Saturn north is up in each frame with the latitude and longitude plotted at every 10° and 30° respectively. Each frame is made from the combination of two clear images (total exposure time of 540s) taken in one HST orbit. The units of intensity are kilorayleighs (kR), the scale of which is shown in the colour bar at the bottom right.

The UV main auroral oval varies dynamically between oval (Figure 1.18 top) and spiral morphologies (Figure 1.18 bottom), (Clarke et al., 2005). The auroral emission sometimes intensifies and broadens towards the poles in response to solar wind compressions, with some small bifurcations being reported in the main oval (Radioti et al., 2011a, Badman et al., 2013); see Figure 1.20. The average morphology of  $H_3^+$  aurorae has been examined by Badman et al. (2011). Using a data set of 96 observations taken at high latitude between the years 2006 and

2009 by the Visual and Infrared Mapping Spectrometer (VIMS) aboard the Cassini spacecraft, they measured the main oval to be at 74-75 ° latitude on the day side and 73° latitude on the night side for both the north and south auroral ovals. The location of these main ovals (both IR and UV) has been observed to oscillate by 1-2° latitude (Nichols et al., 2008, 2010b). Melin et al. (2011) analysed simultaneous IR and UV observations of the aurora using VIMS and UVIS aboard Cassini. They showed that the emission from multiple species H, H<sub>2</sub> and H<sub>3</sub><sup>+</sup> are morphologically identical in the main auroral oval at approximately 73° latitude (north and south); as shown in Figure 1.19 and discussed further below. There was also an equatorward arc in the UV predominantly emitted by atomic hydrogen species as well as a poleward arc in the both the UV and IR emitted by H<sub>2</sub> and H<sub>3</sub><sup>+</sup> respectively. This information is pertinent to this thesis as it signifies that any information derived from the statistically averaged auroral morphology of the H<sub>3</sub><sup>+</sup> emission may only be considered analogous to the UV in the main oval. Lamy et al. (2013) analysed a wide series of observations from a diverse suite of instruments on Cassini's remote sensing palette including VIMS, UVIS, the Radio and Plasma Wave Science instrument (RPWS) and the Ion and Neutral Camera (INCA). From this multitude of data they found that there is typically a circumpolar quasi circular main auroral oval in both the IR and UV between 70 and 72 degrees in each hemisphere as well as intermittent emission between 75 and 82 degrees and 0600-1600 local time on the dayside. A faint arc of emission fixed in local time was observed between latitudes of 68 and 70 degrees and the longitudes of dawn and dusk on the day side. Overall, these different measurements suggest a degree of fluctuation in the peak auroral emission latitude as different studies have provided a range of 70-75° latitude for each hemisphere (a range which is larger than the observed latitudinal width of the main auroral oval).

For Jupiter, Clarke et al. (2004) showed that for the main auroral oval the IR and UV emissions were in very strong agreement, however outside of the main oval there are significant differences. Melin et al. (2011) also showed that the UV and IR main auroral ovals of Saturn are likewise collocated; Figure 1.19 shows three (spectrally) very different auroral arcs which have likely arisen from different particle precipitation energies which have deposited their energies at different altitudes. Since H<sub>3</sub><sup>+</sup> is formed by a chemical reaction of ionised H<sub>2</sub> and the surrounding neutral H<sub>2</sub> populations, and emission does not occur until the molecule has thermalized with its surroundings, unlike the UV emission there is a lag between the ionisation by particle precipitation and the IR emission. Furthermore, the lifetime of the H<sub>3</sub><sup>+</sup> molecule is dependent on the electron density of the surrounding atmosphere (Badman et al., 2015) which lends the H<sub>3</sub><sup>+</sup> emission an altitudinal dependency. Lastly, given that the lifetime of the H<sub>3</sub><sup>+</sup> ion is about 10 minutes at Saturn (Melin et al., 2011), it is likely that this population can experience horizontal transport in the thermosphere and therefore generate a more diffuse aurora in

comparison to the UV (Tao et al., 2013, Radioti et al., 2013a). The effects of these factors on auroral morphology can be seen in Figures 1.15 and 1.16 which show the UV emission predominantly in the dawn sector and confined to the main auroral oval, whereas the IR emission is much broader and sometimes extends into the regions poleward of the main oval.

Stallard et al. (2007) observed a significant difference between the IR and UV emissions at polar latitudes (latitudes higher than the auroral ovals) insofar as the IR emission is notably more abundant across the polar region with a greater relative brightness as compared with the UV emission which is weak to the point of being undetectable (thus far). This polar emission has been seen to take the form of patchy regions across the pole, localised bright spots, extended arcs of emission as well as, in a few cases, infilled areas of emission that are brighter than the main oval at latitudes between  $82^\circ$  and the pole, as can be seen in Figure 1.21 (b, c, i and j) from Badman et al. (2011). Broad infilling of this region has also been interpreted as the result of a large scale reconnection event in the magnetotail as a result of compression from the solar wind (Cowley et al., 2005, Badman et al., 2005, Stallard et al., 2012a). It is thought that the compressions close open field lines in the magnetotail which map to the region poleward of the main oval where they deposit plasma and energy.

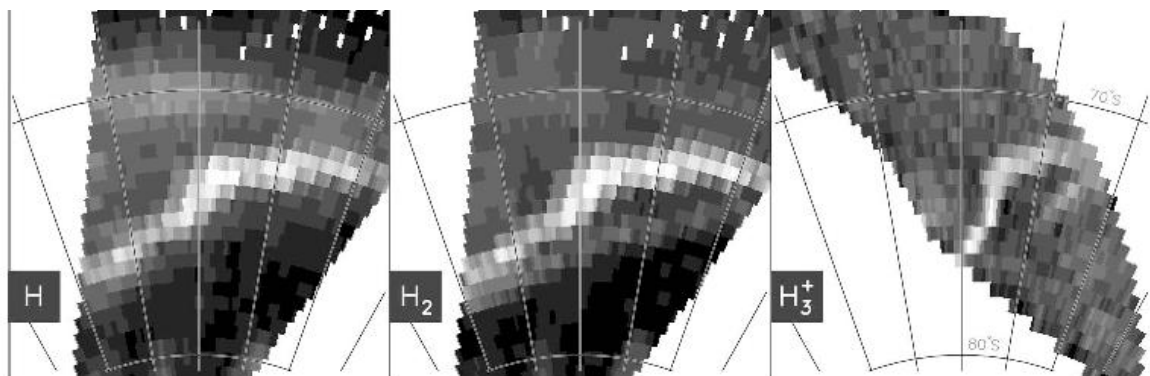


**Figure 1.19:** Figure 2 from Melin et al. (2011) showing latitude-longitude projections of the H Lyman  $\alpha$  and H<sub>2</sub> Lyman Werner UV emissions as well as the H<sub>3</sub><sup>+</sup> IR emissions as observed by the Cassini UVIS and VIMS instruments on day 254 of 2008. This figure demonstrates that for the UV and IR emissions are collocated in the main auroral oval.

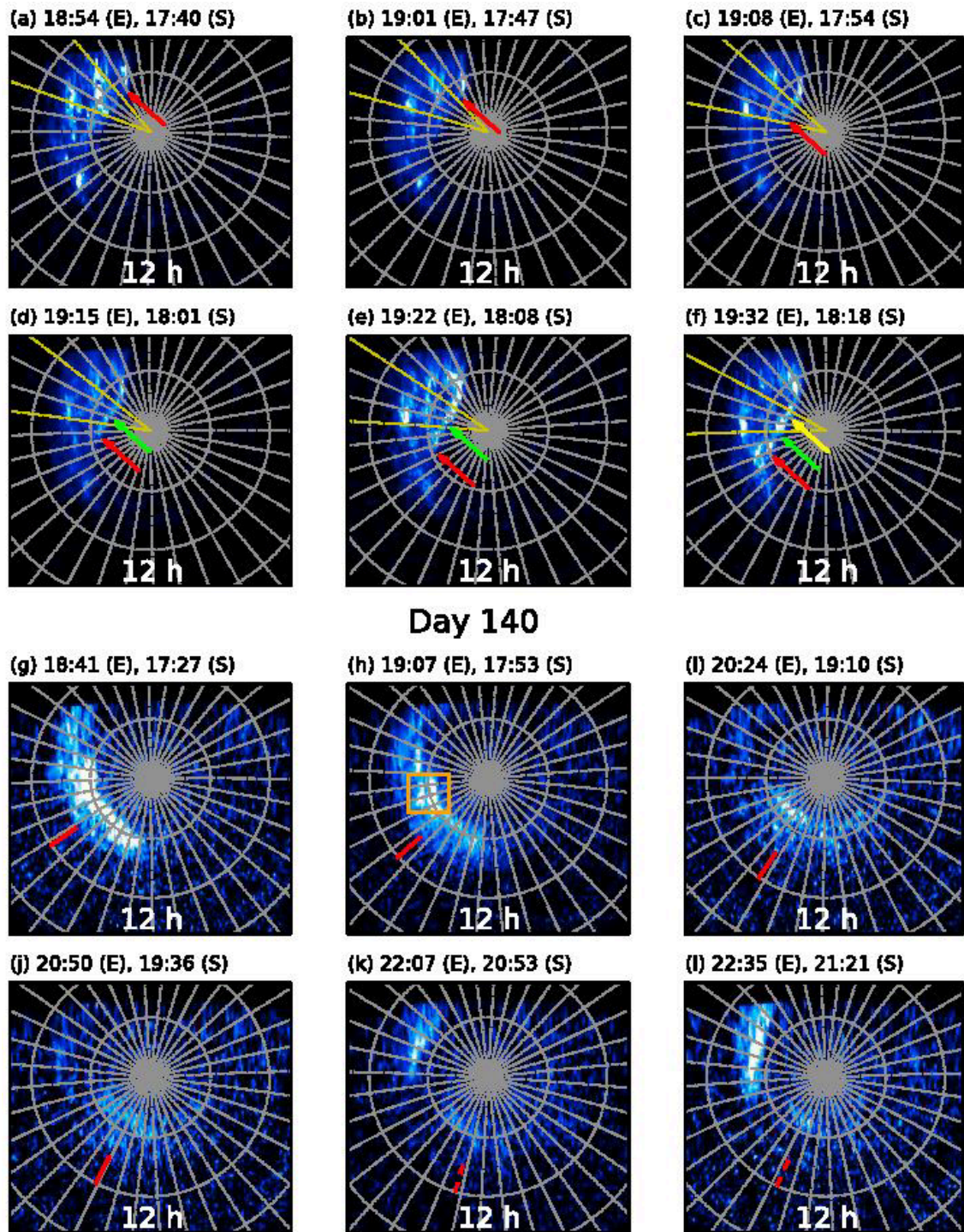
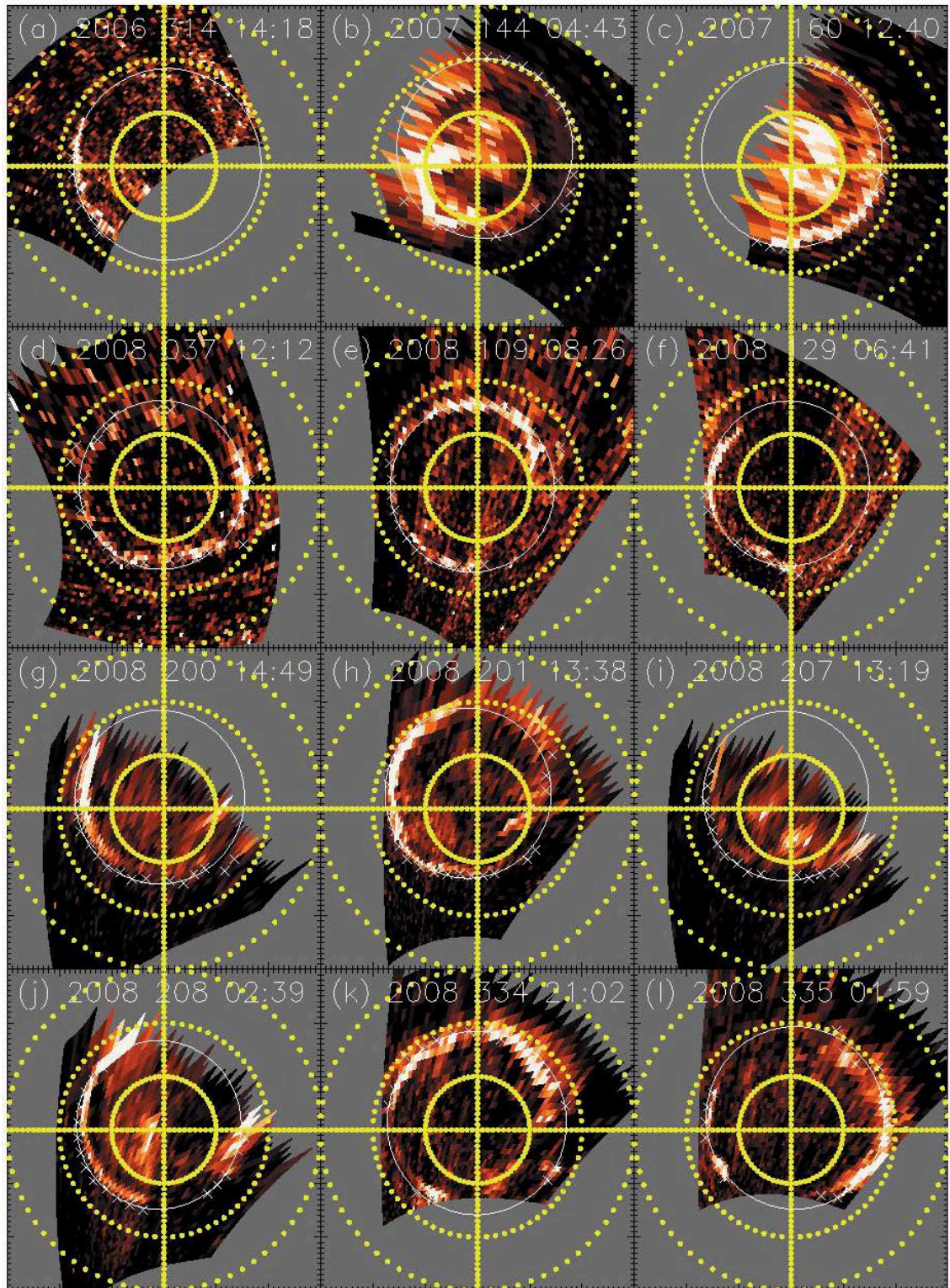


**Figure 1.20:** Figure 1 from Nichols et al. (2014) showing multiple projections of Hubble Space Telescope observations of Saturn's ultraviolet aurora taken on day 95 (a-f) and day 140 (g-l) of the year 2013. These observations demonstrate the dawnside bright arc of UV aurora, in contrast with the IR aurora which encircle the planet (Figure 1.16). Despite this difference in global morphology, the emission in the main auroral arc for both the IR and UV is collocated.



12

**Figure 1.21:** (previous page) Figure 1 from Badman et al. (2011) images of the northern aurora of Saturn obtained from the Cassini VIMS instrument, with the date and start time of each observations printed above each image. Each image has been projected to an altitude of 1000 km above the 1 bar level and shows a wide diversity of auroral morphologies. The yellow lines mark the noon-midnight and dawn-dusk meridians.

#### Section 1.4.5 Atmospheric Temperature

As the upper atmosphere of Jupiter has been seen to be in quasi-thermal equilibrium (Miller et al., 1990) and given the similarities in chemical composition and atmospheric dynamics, Saturn's upper atmosphere has been largely assumed to also be in this state. Melin et al. (2007) measured  $\text{H}_3^+$  temperatures of  $380 \pm 70$  K and  $420 \pm 50$  K in the southern main auroral oval and the remaining southward polar regions respectively from multiple observing campaigns using the spectrometer CGS4 at the United Kingdom Infrared Telescope (UKIRT). This study also showed a significant variability in the line emission intensity of  $\text{H}_3^+$ , to explain this, Melin et al. (2007) invoked the variability of the column density of  $\text{H}_3^+$ .

In Lam et al. (1997) it was shown that there was an inverse relationship (99% anti-correlation) between the number density  $N(\text{H}_3^+)$  and the temperature  $T(\text{H}_3^+)$  at Jupiter. In Miller et al. (1994)  $\text{H}_3^+$  had been regarded as a "thermostat" molecule such that the excitation of the molecule and subsequent IR radiation into space offset increased heating from particle precipitation (the deposition of energy from electrons precipitating into the atmosphere). In Melin et al. (2007) however, they showed that the infrared emission of  $\text{H}_3^+$  did not have an inverse relationship between  $T(\text{H}_3^+)$  and  $N(\text{H}_3^+)$  after the measured  $\text{H}_3^+$  temperatures from observations in the year 1999 and 2004 were the same but the  $N(\text{H}_3^+)$  measurements were different. They found that though there was increased particle precipitation in 2004, the increase in the cooling from  $\text{H}_3^+$  was not sufficient to offset the heating from this particle precipitation.

O'Donoghue et al. (2016) used the ground based 10m W. M. Keck telescope to observe the regions of the aurorae in both the north and the south simultaneously in April of 2013 (for Saturn this means a northern spring and a southern autumn). Their average measurements of the  $\text{H}_3^+$  temperature yielded  $404 \pm 13$  K for the northern dayside and  $460 \pm 17$  K for the southern dayside. O'Donoghue et al. (2016) noted that the southern auroral region appears to be on average 56 K hotter than its northern counterpart over the course of the 2 hours of observations. This was attributed to the north-south asymmetry in the magnetic field strength leading to a greater total heating rate in the south. This heating arises from resistance encountered by electrical currents (such as those in Section 1.4.1) driven through the ionosphere from the

magnetosphere transferring energy into atmosphere; noted as the most important energy input for the polar upper atmosphere (the auroral oval and the poleward regions both north and south) in Cowley et al. (2004).

Koskinen et al. (2013) used solar occultations of the exosphere (altitudes greater than 1900 km above the 1 bar level) at a variety of latitudes (14.2°-66.1° north and 38°-73.5° south) using the Cassini UVIS instrument to measure both the temperature and density of H<sub>2</sub> in this region. Their findings showed that the temperature ranges from 370 – 540 K ( $\pm 20$  K). This study was subsequently followed up by Koskinen et al. (2015), which used a wider variety of stellar and solar occultations from the same instrument between the years 2004 and 2015. Their revised measurements of the exospheric temperature provided a new range of 380 – 590 K. They noted that the temperature seemed to increase nearer the poles; it was thought this was likely due to auroral heating processes (such as the dominant Joule heating and minor particle precipitation). These results, along with a few others are shown in Table 1.1; the range of values shown here indicates significant temporal and spatial variability owing to the large differences between various temperature measurements. The consensus among the other measurements shows a temperature range of 400 to 600 K, with the measurement of 800 K from Festou and Atreya (1983) as a potential outlier.

Author/Paper	Year of Data	Latitude Range	Altitude range /Species/Spectra	Temperature (K)
Festou and Atreya (1983)	1981	36° N	1540 km - H <sub>2</sub> - UV	800
Smith et al. (1983)	1981	29.5° N	1100 km - H <sub>2</sub> - UV	400
Miller et al. (2000)	1998 (Stallard et al., 1999)	Southern Polar Region	CI - H <sub>3</sub> <sup>+</sup> - IR	600
Melin et al. (2007)	1999, 2004, 2005	Southern Main Oval	CI - H <sub>3</sub> <sup>+</sup> - IR	380 ± 70
		Southern Polar Region		420 ± 50
Melin et al. (2011)	2008	70-74° South	1100 km - H <sub>3</sub> <sup>+</sup> - IR	440 ± 50
				420 ± 85
Lamy et al. (2013)	2009	65-90° South	1150 km - H <sub>3</sub> <sup>+</sup> - IR	430 ± 88
				392 ± 98
O'Donoghue et al. (2014)	2011	68-80° North	CI - H <sub>3</sub> <sup>+</sup> - IR	527 ± 18
		68-80° South		583 ± 13
O'Donoghue et al. (2016)	2013	Northern Aurora		404 ± 13
		68-82°	1400 km - H <sub>3</sub> <sup>+</sup> - IR	
		Southern Aurora		460 ± 17
		68-72°		
Koskinen et al. (2013)	2004-2015	66° N - 73.5° S	>1900 km - H <sub>2</sub> - UV	370-540 ± 20
Koskinen et al. (2015)	2004-2015	41° N - 69° S	>1900 km - H <sub>2</sub> - UV	380-590

**Table 1.1:** (previous page) measurements of the temperature (for  $\text{H}_2$  and  $\text{H}_3^+$ ) of the upper atmosphere of Saturn for various latitudes and time periods. All altitudes are expressed in terms of kilometres above the 1 bar level. According to Figure 1.8, the thermosphere should correspond to an altitude range of 800-1500 km above the 1 bar level and the exosphere to altitudes greater than 1500 km. The variation in these measurements indicates both temporal and spatial variability in the temperature of the upper atmosphere.

In terms of models of Saturn's atmosphere Moore et al. (2009) examines the altitudinal density and temperature structure of  $\text{H}_3^+$ . Moore et al. (2009) calculated an altitudinal structure for the  $\text{H}_3^+$  temperature profile (Figure 1.6) which seems to rise from 200K to 400K between 500 and 1000 km above the 1 bar level; this subsequently stabilises and only increases very gradually at higher altitudes. We will compare this structure with our measurements in later Chapter 6.

#### Section 1.4.6 Atmospheric ion densities

Along with the temperature measurements mentioned in Section 1.4.5, O'Donoghue et al. (2016) also measured the column densities (the total number of molecules along the line of sight per unit area) to be  $7.7 \pm 2.3 \times 10^{15} \text{ m}^{-2}$  for the northern dayside and  $1.5 \pm 0.7 \times 10^{15} \text{ m}^{-2}$  for the southern dayside as well as intensities that range from 0.1 to 0.5 watts  $\text{m}^{-2} \text{ str}^{-1}$ . Although these figures show the southern aurora to have a lower column density, it worth noting that Melin et al. (2011) measured a column density of  $7 \pm 1 \times 10^{15} \text{ m}^{-2}$  for the southern aurora in 2008, which suggest some margin of variability in the auroral ion column density. Moore et al. (2009) derives a peak density of  $\text{H}_3^+$  at 1000 km above the 1 bar level (shown in Figure 1 of their paper); with a peak density of  $10^4 \text{ cm}^{-3}$  ( $10^6 \text{ m}^{-3}$ ). Tao et al. (2011) used their model of the auroral regions of Saturn to produce altitudinal profiles of ion density and volume emission rates for various ionic species, as shown in Figure 1.22. A noticeable feature of the altitudinal profiles is the rapid decay of the  $\text{H}_3^+$  population below an altitude of 800 km, which is in keeping with the location of the homopause mentioned in Section 1.2.1. Figure 1.22 also makes it explicitly clear what effect an increase in the energy of the precipitating electrons has on the population of various ion species; in particular for  $\text{H}_3^+$  this means a lowering of the peak ion density altitude. According to this model the peak  $\text{H}_3^+$  volumetric density should be of the order of  $10^{10}$  to  $10^{11} \text{ m}^{-3}$ .

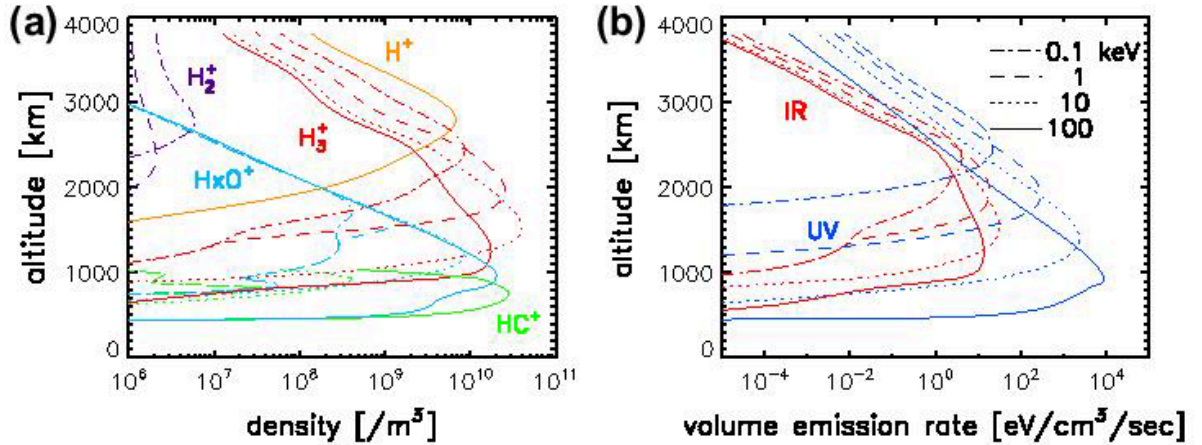


**Figure 1.22:** from Figure 8 of Tao et al. (2011) showing for various species the altitudinal ion density profiles and volume emission rates for various precipitating electron energies; 0.1 keV (dot dashed), 1 keV (dashed), 10 keV (dotted) and 100 keV (solid).

#### Section 1.4.7 Altitudinal structure of $\text{H}_3^+$ emission

Whilst the morphology studies in Section 1.4.4 have provided a guideline for measurements like overall brightness and those in Section 1.4.5 have provided temperature, it is only Stallard et al. (2012a) that has provided information on the altitudinal variation of infrared auroral intensity. In Stallard et al. (2012a), nine observations taken in 2006 by the VIMS instrument shown in Figure 1.23, yielded a peak auroral emission altitude at 1155 ( $\pm 25$ ) km above the 1 bar level. They used a histogram technique to collate the emission from multiple auroral observations into altitudinal bins, thereby producing an altitudinal profile shown in Figure 1.24. This altitudinal study was the first of its kind for the IR emission, and when compared to the analysis of the altitudinal UV emission profile (purple dot dashed line in Figure 1.24) of Gerard et al. (2009) posited that, for the peak emission in the main auroral oval, both the IR and UV emissions are both generated by the same energetic particles. However it was noted that though the peak emission altitudes were very similar for both emission types, the IR auroral emission had a much narrower distribution than the UV (Stallard et al., 2012b). This was attributed differences in the production of both aurorae, as the IR emission can only come from  $\text{H}_3^+$  which is produced by the reaction of  $\text{H}_2$ , the UV emission on the other hand can come from both  $\text{H}_2$  and  $\text{H}$ ; simple scale height considerations show that the  $\text{H}$  population will extend to much higher altitudes and therefore the UV emission will be broader in its distribution as soft electrons that deposit their energies at higher altitudes are able to stimulate the UV emission from  $\text{H}$  atoms (contributing to the  $\text{H}$  Lyman  $\alpha$  UV emission at higher altitudes). The work of Stallard et al. (2012a) will be discussed in much greater detail in Chapter 3.

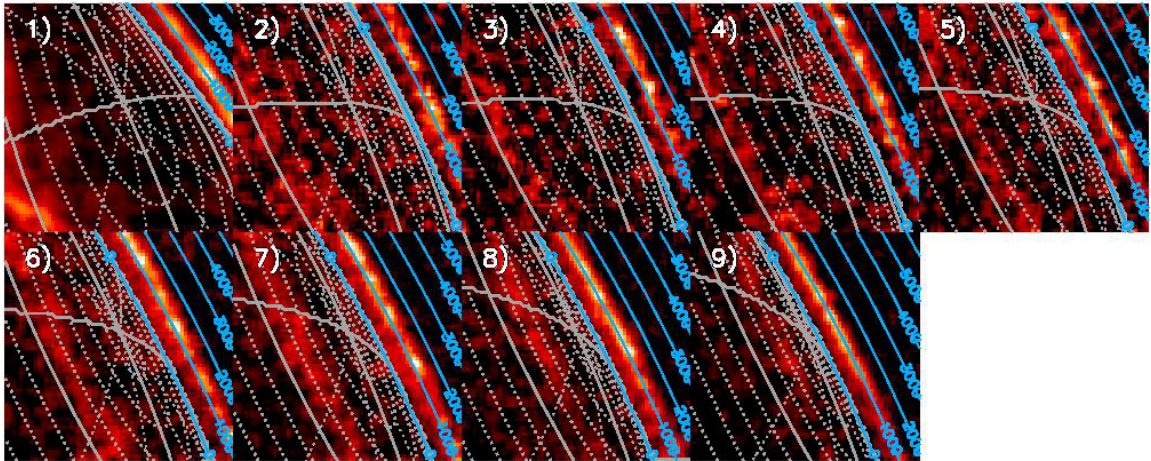


**Figure 1.23:** Figure 1 from Stallard et al. (2012a) showing the nine observations and the auroral curtains therein that were used in this study. Each of these observations was selected for the auroral emission both above the limb of the planet and on the body of the planet. Only images 2-5 were used to make the emission profile in Figure 1.19, as the others were found to have a larger latitudinal difference between the limb and the auroral oval of more than  $1.5^\circ$  of latitude.

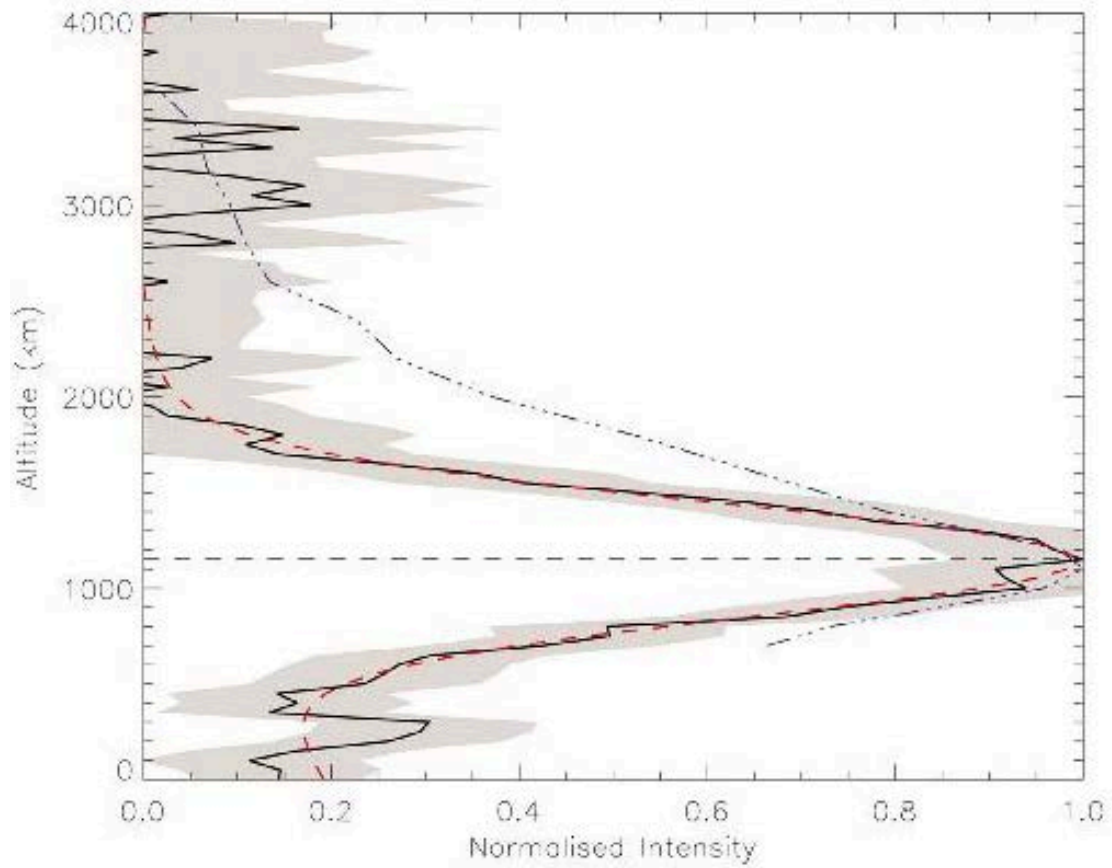


**Figure 1.24:** Figure 2 from Stallard et al (2012a) showing their measured average altitudinal intensity profile (solid black line) and its associated fit (red dashed line) as well as the altitudinal profile of the UV emission (purple dot dashed line) from Gerard et al (2009). This shows the peak emission for the IR profile of Stallard et al. (2012a) and the UV profile of Gerard et al. (2009) to have approximately the same altitude; though the IR emission decays with altitude at a faster rate than the UV emission.

## Section 1.5 Infrared Spectroscopy

As explained in Section 1.4.5, at Jupiter, due to the scale of the  $\text{H}_3^+$  molecular lifetime,  $\text{H}_3^+$  is able to thermalize with the surrounding neutral atmosphere above the homopause and establish Quasi Thermal Equilibrium (Miller et al., 1990, Miller et al., 2013), which we assume is also true at Saturn. The result of this excitation is a series of ro-vibrational transitions that emit predominantly in the 3-5  $\mu\text{m}$  wavelength range (Miller et al., 1990). The transition between these energy states is what generates the  $\text{H}_3^+$  infrared emissions. These transitions and the nature of the spectra that result will be explained in Sections 1.5.1 and 1.5.2.

Due to the nature of quantum mechanics, many aspects of atoms and molecules are quantised, these include: the rotational angular momentum, the projection of the rotational angular momentum onto the molecular axis (the axis around which the molecule is symmetrical) and vibrational energy. As such, molecules have discrete energy levels for both rotation, which is based on the quantisation of angular momentum of the electrons, and vibration which is based on the quantisation of the angular momentum of the molecule as well as the vibrational mode.

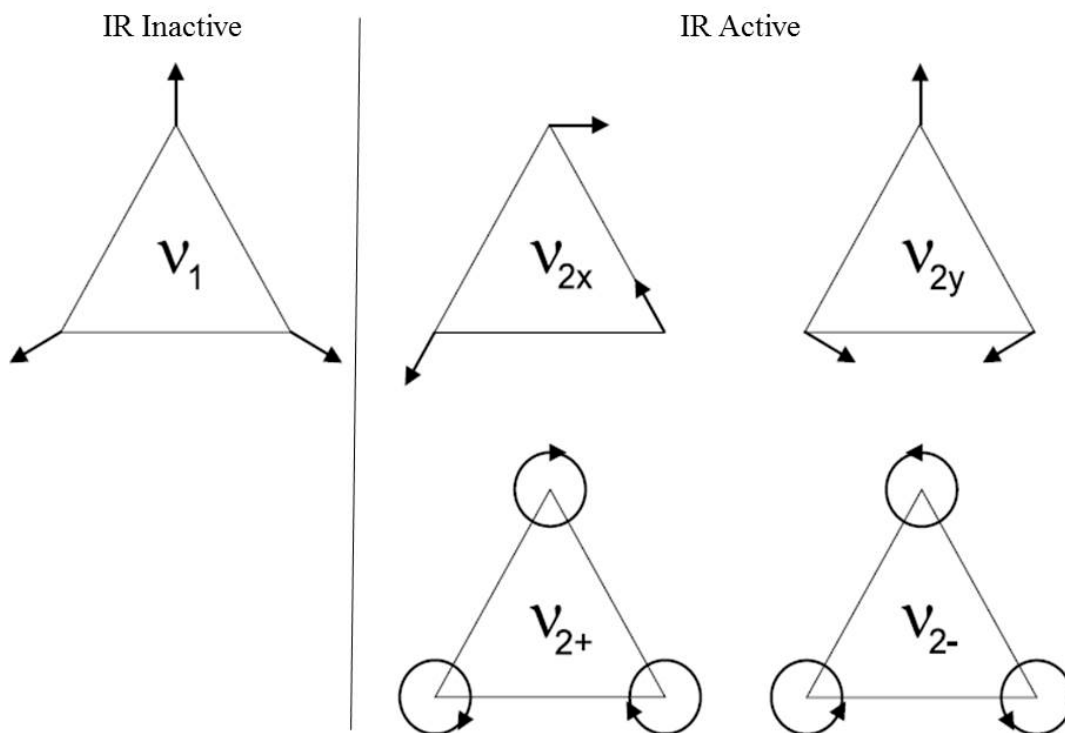


**Figure 1.25:** Each triangle represents an  $\text{H}_3^+$  molecule where each vertex represents a hydrogen nucleus and the edges between them are the bonds of the molecule. The symmetrical oscillation (breathing motion) from the vibrational mode  $\nu_1$  shown above does not result in any emission as the molecular magnetic moment is not altered and as such is described as being infrared-inactive. However, the asymmetric oscillation of the  $\nu_2$  vibration mode does result in a change of dipole and hence leads to emission, i.e. it is infrared active. The degenerate modes  $\nu_{2x}$  and  $\nu_{2y}$  refer to the fact that the oscillations of the H atoms are such that there is a dipole moment in either the x direction (left to right) for  $\nu_{2x}$  or the y direction (bottom to top) for  $\nu_{2y}$ . The degenerate modes  $\nu_{2+}$  and  $\nu_{2-}$  arise from the phase of spin motions (angular momentum) of the H atoms such that the net spin is either positive (clockwise) for  $\nu_{2+}$  or negative for  $\nu_{2-}$  (anti-clockwise). Note that the vibrational mode  $\nu_1$  only has a vibrational component whereas the  $\nu_2$  mode has both vibrational oscillations as well as rotational oscillations (denoted by the circular arrows in modes  $\nu_{2+}$  and  $\nu_{2-}$ ).

### Section 1.5.1 The vibrational and rotational energy states

The vibrational states of a molecule are born from the position and motion of the atoms within it which are described by the degrees of freedom of the molecule (derived from number of nuclei). For each vibrational state there is a quantum numbers that is used to describe it, the vibrational angular momentum  $l$ . This quantum number can take the value of combinations of the vibrational mode quantum numbers  $\nu_1$  and  $\nu_2$ , which are shown in Figure 1.25. The  $\nu_1$  mode is referred to as the “normal” mode, which results in a symmetrical expansions and contraction of all the bonds in unison. Since the only transitions that can trigger emission are those which result in a change of the molecular magnetic dipole moment, this normal mode does not result in any emissions and is therefore infrared inactive. On the other hand, the asymmetrical motion of the doubly degenerate vibrational mode  $\nu_2$  does trigger a change in the magnetic dipole moment of the molecule is therefore infrared active and produces a spectrum of emissions. The  $\nu_2$  mode is split into two levels of degeneracy which is shown in Figure 1.25, this degeneracy comes from the motion of the protons as they oscillate in different directions which gives  $\nu_{2x}$  and  $\nu_{2y}$ , and from combinations of these two modes in different phases we get  $\nu_{2+}$  and  $\nu_{2-}$ . Both of these  $\nu_1$  and  $\nu_2$  modes can be combined as is shown in Figure 1.26 to form multiple quantised energy states.

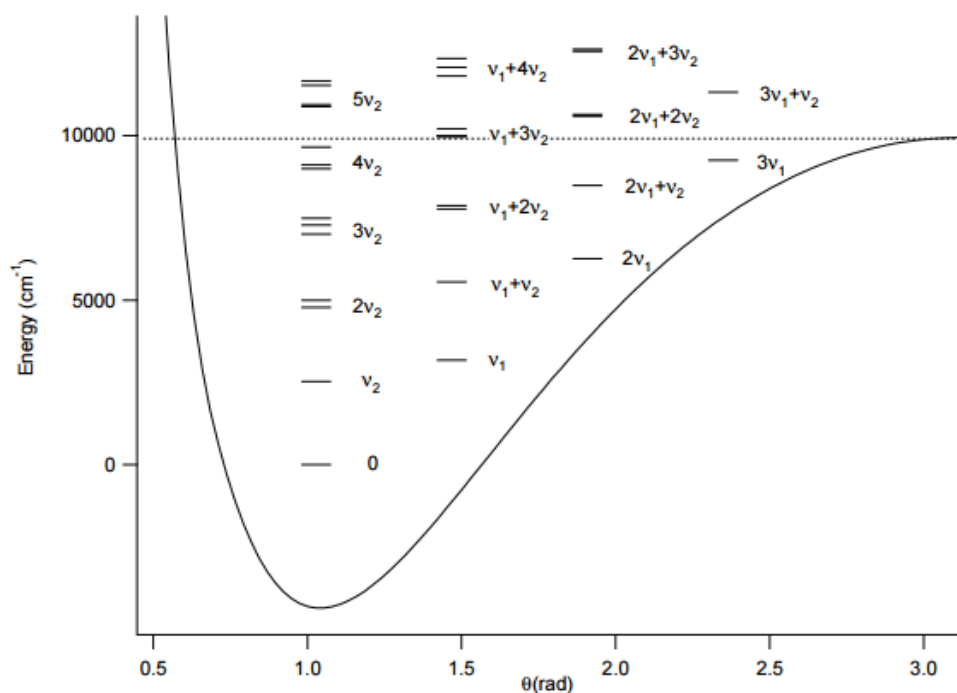


**Figure 1.26:** From Mccall (2001), plot of the different vibrations energy states of the  $\text{H}_3^+$  molecule. The plot also shows a one dimensional slice of the potential energy surface. The dashed line represents the dissociation energy; energy inputs leading to energy levels above this threshold will break the bonds between the atoms. The state marked 0 is the ground state of the molecule, note that it is higher than the potential surface; this is due to the anharmonicity of the potential energy curve. As described in Banwell and McCash (1994) the anharmonicity of the potential means that the energy of molecule in the ground state, also referred to as the equilibrium oscillation, is not equal to the minimum energy of the potential energy curve as its asymmetry means that the bonds of the molecule can oscillate in one direction more than another. This means that the molecule oscillates around this equilibrium point; this makes the ground state energy greater than the bottom of the potential curve as it has additional oscillation frequency terms (please see page 61 of Banwell and McCash, 1994, for reference).

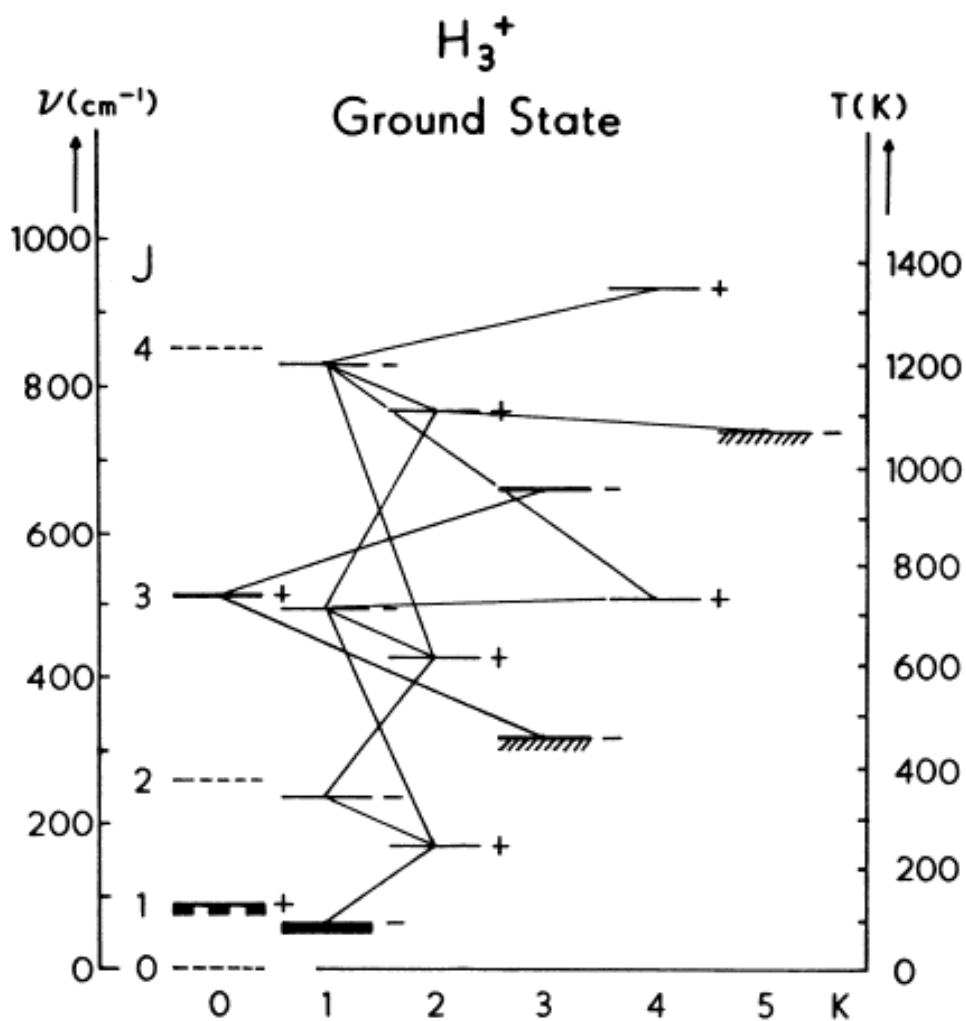


**Figure 1.27:** A plot of the rotational energy levels found in the  $\text{H}_3^+$  vibrational ground state (vibrational energy level 0 in Figure 1.21).  $J$  is the rotational angular momentum and  $k$  is the projection of  $J$  onto the molecular axis. The forbidden rotational transitions are shown as lines connecting the different energy levels. This figure is taken from Pan and Oka (1986).

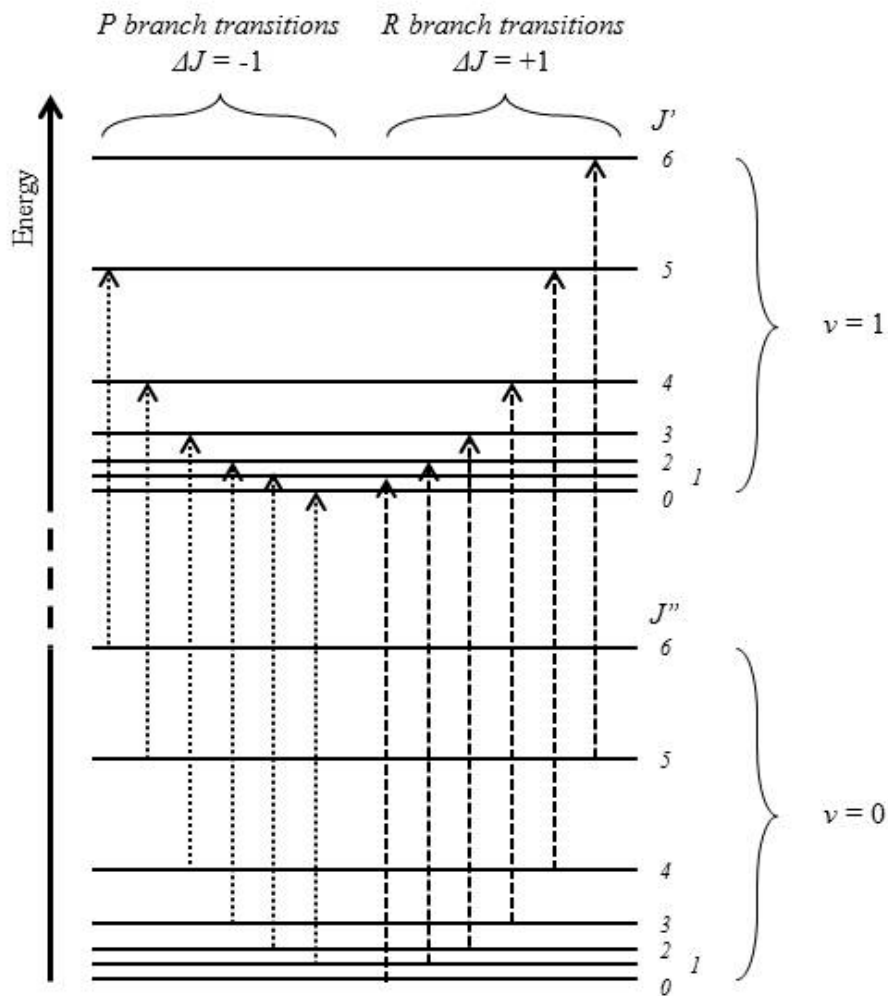


**Figure 1.28:** A selections of low energy excitations from the vibrational ground state to the first vibrational energy level. The degeneracy of the vibrational states due to rotation allows for a wider spectrum of wavelengths to be emitted.

From the laws of quantum mechanics, all transitions must obey a series of selection rules. These selection rules however do assume ideal symmetry in a molecule, which is inevitably not always the case as the molecule distorts and as it rotates;  $\text{H}_3^+$  has been described as “floppy”. As such, there are a series of transitions that are referred to as being “forbidden” since they disobey these selection rules. As these molecular transitions are a combination of change in both rotational and vibrational energy levels, we refer to them as ro-vibrational transitions. The selections rules for these forbidden transitions are shown in equations 1.45 and 1.46 (from Pan and Oka, 1986):

$$\Delta J = 0, \pm 1 \quad (1.45)$$

$$\Delta k = 0, \pm 1, \pm 2, \pm 3 \quad (1.46)$$

where quantum number  $J$  is the motional angular momentum, and  $k$  is a signed quantum number derived from the projection of  $J$  onto the molecular axis (an axis around which any rotation or reflection of the molecule does not result in any structural changes, i.e. the molecule is the same before and after). Each vibrational energy state  $l$  degenerates into more states with quantum numbers  $J$  and  $k$  as shown in Figure 1.27. Hence, though there may be two discrete vibrational energy states, there is further variation within these states engendered by the various rotation states within the molecule, this leads to several different bands of available transitions (Figure 1.28) which are based on the rotational transitions as explained in Banwell and MacCash (1994) the details of which are laid out in Section 1.5.2.

### Section 1.5.2 Emission bands and ro-vibrational transitions

The changes in the rotational state lead to different bands of emission from the same transitions of vibrational states (Figure 1.28). These bands are denoted by letters which correspond to specific changes in the rotational state (see equation 1.47). Due to the selection rules of the forbidden transitions as detailed in Pan and Oka (1986), the only bands that are emitted from  $H_3^+$  are P, Q and R as they correspond to the  $J$  rotational state changes -1, 0 and +1 respectively.

$$\begin{array}{ccc} \Delta J = & -1 & 0 & +1 & \\ & P & Q & R & \end{array} \quad (1.47)$$

As can be seen from Section 1.5.1 there are a wide variety of energy transitions available to the  $H_3^+$  molecule. Many of these transitions have been put into groups according to specific behaviours, the first of which is the fundamental band; a series of transitions which denote where the molecule has been excited up to the first vibrational energy level of  $\nu_2$  and transits from this to the ground state ( $\nu_2 \rightarrow 0$ ). This is the most common transition as it is the first energy level filled when the  $H_3^+$  population receives energy input. This also has the effect of making the transitions in this band the most intense. The hot band transitions involve excitation to the second vibrational energy level ( $2\nu_2 \rightarrow 0$ ) and as such are less common due to the fact the first vibrational energy level must be full before the second can be populated. This band has garnered its name from the fact that it requires higher temperatures and therefore energy inputs to populate. Overtone transitions are simply transitions between vibrational energy levels greater than or equal to two; a transition that moves between two or more vibrational energy states. As the resultant emissions from the hot band transitions are weaker than those from the

fundamental band, these overtone emissions are weaker than both the above for the same reason.

In this thesis we are only concerned with a very select subset of emissions from this diverse spectrum, specifically the fundamental transitions in the 3-4  $\mu\text{m}$  as they are the brightest, most ubiquitous and well within the range of wavelengths observable by VIMS. This can be seen in Figure 1.29 which shows an  $\text{H}_3^+$  emission spectrum at a temperature of 500 K (black) and 600 K (red). Figure 1.24 clearly demonstrates that the energy of all of these emission lines is determined by the temperature of the  $\text{H}_3^+$  molecule; as the emission lines are brighter at 600 K than they are at 500 K. Hence, the greater the temperature of the ambient atmosphere, the more energy each collision will impart thus generating a larger population of excited molecules which in turn promotes a greater number of transitions (thus increasing the intensity of each emission line).

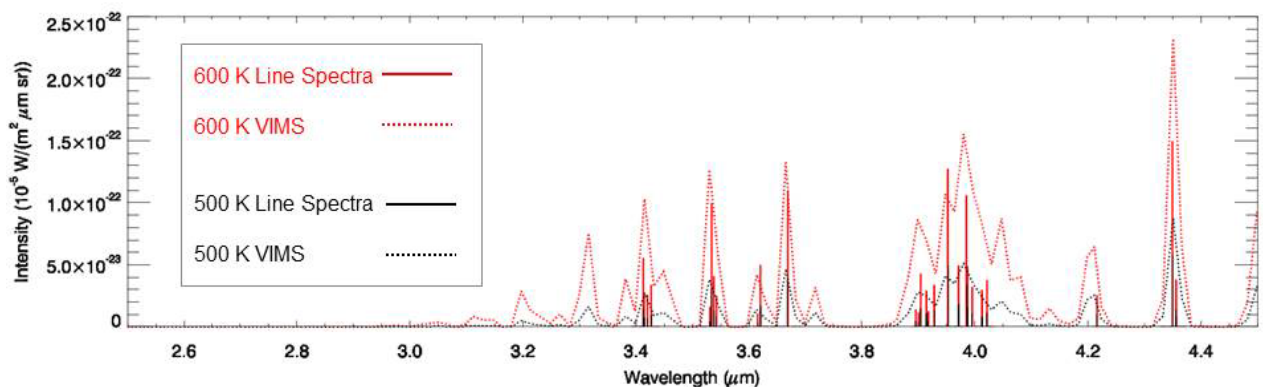


**Figure 1.29:** A plot of  $\text{H}_3^+$  fundamental emission lines between 1.8 and 5  $\mu\text{m}$ , created using the line model of Neale et al. (1996) shown in black with the partition function and associated coefficients from Miller (2010). The red dashed line denotes the spectrum that would be seen by VIMS given the shape of its spectral bins and spectral resolving power. Note that though the majority of the emissions lines are at wavelengths greater than 3  $\mu\text{m}$ , there are other emission bands at shorter wavelengths such as around 2  $\mu\text{m}$ , however, as demonstrated by this Figure, they are comparatively very weak and as such are not used in this thesis.

## Section 1.6 Research Questions

The  $\text{H}_3^+$  infrared aurorae represent the interface between the magnetosphere and the atmosphere of Saturn. The properties of the aurorae such as morphology, intensity, temperature and density are all heavily affected by the dynamics of both the atmospheric and magnetospheric systems and hence are an excellent tool for characterizing their interactions and analysing properties of both systems. In the pursuit of characterising these interactions, the primary research goal of this thesis was to examine the  $\text{H}_3^+$  emissions in the infrared aurorae, both spatially and spectrally to discern such properties and thus contribute to the wider knowledge of atmospheric and magnetospheric science at Saturn; or in other words “*what is the atmospheric response to the particle precipitation in the auroral atmosphere?*”

To begin with, the first consideration was for the altitudinal variation of the auroral emission. This aspect is heavily related to a number of variables such as particle precipitation energy, the temperature of the local neutral population, the conductivity of the atmosphere in this region both for ions and electrons as well as the presence or absence of other species such as hydrocarbons. As explained in Sections 1.4.4 and 1.4.7, there are different morphology and altitude measurements of the peak auroral emission intensity. In Stallard et al. (2012a) they measured the alignment of the auroral curtain (Figure 1.18) with the limb to ensure that the altitudinal profiles did not contain line of sight bias, however they did not analyse the effects of the variation of alignment. Thus, in order to discern whether variations in the altitudinal distribution of IR emission was caused by line of sight bias or from actual altitudinal fluctuations, the first goal of the research in this thesis was to examine the altitudinal profiles of the IR auroral emission and how they vary with alignment (Chapter 4). In studying this we can get a much better understanding of the nature of the altitudinal variation and variability of  $\text{H}_3^+$  emission in Saturn’s aurora as well as all the system variables that are intrinsically related to its production, and thereby establish whether or not the VIMS data set is a viable tool for measuring the peak emission altitude.

From the previous studies into the morphology of the infrared aurorae (Stallard et al., 2012a, Badman et al., 2011, Lamy et al., 2013) as observed by VIMS, it was apparent that many of them have focused on case studies of small groups of high sub-spacecraft latitude observations. Largely due to the fact that this position affords a far better viewing geometry of the entire auroral oval as well as potentially positioning the auroral oval on the limb of the planet. There are a large number of VIMS observations that have been taken at equatorial sub-spacecraft latitudes that have remained as yet untouched in the study of the auroral emissions; this is unsurprising in light of the poor alignment of the auroral curtain with the limb that is typical of these observations with this viewing geometry. In Chapter 4 we look at whether the altitude is

varying or if the different altitudes retrieved are merely down to line of sight bias. The study of altitudinal variation in the aurora of Chapter 4 enables a wider set of VIMS observations to be used in a broad scale statistical study through the development of a projection technique as shown in Chapters 5 and 6. This projection technique also provides the average latitude and local time distribution of the  $\text{H}_3^+$  emission as well as  $\text{H}_3^+$  temperatures and densities. Hence, the primary goals of this broad scale statistical study were to examine the properties of  $\text{H}_3^+$  intensity, temperature and density with respect to the dimensions of latitude, altitude and local time over a large number of observations. Specifically, this thesis will focus on what the time averaged conditions for these different variables, i.e.:

- “What are the average latitudinal and altitudinal distributions of the  $\text{H}_3^+$  IR emission?”
- “What are the average temperature and densities of  $\text{H}_3^+$  in the aurora?”
- “Do these properties change with altitude or latitude?”
- “Are these properties different for each hemisphere?”

Producing time averaged measurements and profiles of these properties is the best way to answer these research questions, and the results of which can subsequently be used to feed models of the atmosphere, the magnetosphere, current sheet systems and the ionosphere. They can also be used as a baseline comparison for all past and future measurements of these properties of the  $\text{H}_3^+$  emission in Saturn’s infrared aurorae.

## Chapter 2

### *The VIMS instrument*

In this thesis, all research has been conducted using data collected from the Visual and Infrared Mapping Spectrometer (VIMS) aboard the Cassini spacecraft. This Chapter (as well as Chapter 3) contains details of the scientific goals and technical specifications of the VIMS instrument, followed by an explanation of how  $\text{H}_3^+$  and methane emissions are extracted and processed from the raw data. Finally, this chapter will also cover techniques that provide profiles of the spatial distribution of these emissions, the results of which will be discussed in subsequent chapters.

#### Section 2.1 The Cassini Mission

Launched on the 15<sup>th</sup> of October 1997, the Cassini mission to Saturn has produced a profound collection of measurements and observations of the planet, its rings and moons, as well as the surrounding space environment. Fitted with a diverse suite of instrumentation, the Cassini orbital spacecraft has the capability to analyse targets over a broad region of the electromagnetic spectrum. Of specific interest to this thesis is the data collected by the Visual Infrared Mapping Spectrometer (VIMS); as its name implies, VIMS provides spectral imaging in the visible and the near infrared wavelength range. VIMS is part of an instrument palette that also contains other optical instruments including the Ultraviolet Imaging Spectrometer (UVIS), the Composite Infrared Spectrometer (CIRS) and the Imaging Sub System (ISS). Note that though CIRS observes in the infrared, its wavelength range is 7-1000  $\mu\text{m}$  which is outside of the range of wavelengths of  $\text{H}_3^+$  emission lines and hence this instrument is not used in this thesis. The Cassini mission has a wide range of scientific goals which these instruments were designed to achieve. As these instruments share the same pallet, it is possible for them to operate simultaneously and with some orbits being specifically designed to target specific parts of Saturn and the surrounding system. There are some observations collected by the VIMS instrument that were primary (taken with viewing geometries aimed at targets meant for VIMS to analyse) and others that are rider observations (targets meant for other instruments, but also observed with VIMS).

The VIMS instrument has a defined set of scientific goals, a detailed explanation of which can be found in Brown et al (2004). To summarise these goals very briefly, during the flyby of Jupiter, the VIMS instrument aimed to collect data on the chemical and dynamical makeup of the atmosphere as well as the properties of certain moons, the Jovian rings and the Io plasma

torus. Upon arrival and orbital insertion into the Saturnian system, the VIMS instrument aimed to investigate chemical and dynamical processes in the atmosphere of Saturn and its satellites (such as Titan), as well as the surface compositions of some of Saturn's icy satellites. As explained in the introductory chapter of this thesis, the Infrared Auroral process at Saturn arises from an interaction between the atmosphere and magnetosphere of Saturn which, in turn, drive a chemical process that leads to auroral emission. The VIMS instrument addresses this scientific aim using one of the two channels contained within VIMS, specifically the infrared channel; herein referred to as the VIMS-IR channel (just as the visible channel is referred to as the VIMS-VIS channel). As the VIMS instrument is in orbit around Saturn, it is able to obtain significantly better spatial resolution than a ground based telescope, and hence is better suited to studying fields of research interest as auroral morphology. Thus, the VIMS-IR data forms the core of all the research contained within this thesis – VIMS-VIS data is not used as its wavelength coverage does not contain the desired  $\text{H}_3^+$  emission lines. The following is technical specification which explains how VIMS functions and how we extract information from its observations.

## Section 2.2 The VIMS instrument

The VIMS infrared channel has a spectral coverage of 0.85-5.1  $\mu\text{m}$  and consists of a series of components, as shown in Figure 2.1. First is the fore optics; a 23cm Ritchey-Chrétien telescope (the name of this particular arrangement of primary mirror and secondary mirror) operating at f/3.5 (this f/ratio is known as the focal ratio and is equal to the effective focal length divided by the aperture width), which is equipped with a secondary mirror that can be scanned in two orthogonal directions. This results in a scan of a  $64 \times 64$  mrad scene (field of view) across a  $0.2 \times 0.4$  mm entrance slit. This entrance slit is then, in turn, coupled to a classical grating spectrometer using an f/3.5 Dall-Kirkham collimator (which narrows the beam of incumbent light by aligning the motions of the photons in one direction with lenses).

The spectrometer utilises a triply-blazed diffraction grating whose blaze angles have been designed to compensate for the steep drop in intensity of the solar spectrum toward longer wavelengths. Blazing is a process by which the surface of a material is cut into a series of saw tooth ridges of a consistent size (width, depth and blazing angle); light reflected from a blazed surface will be diffracted at an angle that is dependent on both the wavelength of the light and the width of each blazed ridge. The grating in VIMS is blazed in three separate zones to enable the performance of the spectrometer to be more evenly distributed over the 0.8 – 5.0  $\mu\text{m}$  spectral region, thus yielding a more uniform signal to noise ratio. Though the groove spacing is the same for the entire grating (27.661/mm), the three regions are blazed at different angles, calibrated to wavelengths of 1.3, 3.25 and 4.25  $\mu\text{m}$  each covering 20, 40 and 40%, respectively of the area of the grating. The light dispersed by the grating is imaged onto a  $1 \times 256$  array of InSb (Indium Antimonide) detectors using an f/1.8, all-reflective, flat field camera. Each of these detectors is calibrated to a specific and unique wavelength range of width 16.6 nm. In order to take a measurement of the internal thermal background radiation (generated by both the VIMS instrument and the rest of Cassini) and the current that is naturally present in the detectors when they are not irradiated, the VIMS instrument also incorporates a shutter to block light from the fore optics. The optical path through the instrument of incumbent emissions is shown in Figure 2.2, where the light follows a series of stages, first [1] is the emission from the source (Saturn) entering the instrument and subsequently reflecting off of the primary mirror. This is followed by [2] a second reflection from the secondary mirror which is able to move in two orthogonal directions and reflect light onto a slit of dimensions 0.2 by 0.4 mm. The light is subsequently fed into [3] an f/3.5 Dahl-Kirkman Collimator after which it illuminates a blazed diffraction grating [4] where it is dispersed into its constituent spectral components before finally being imaged the detector [5] by an f/1.8 flat field camera. The detector output is fed

into the Signal Processor Sub Assembly where it is packaged into an observation to be transmitted back to Earth.

Each detector has dimensions  $200 \times 103 \mu\text{m}$  and is arranged within a linear array in the IR focal plane such that each one produces a monochromatic image of the instrument slit which is read by two FET multiplexers (a device that selects one of its digital inputs and forwards it on in a single line) to feed the full spectrum image generated by this collective of detectors to the VIMS command and data processing units. The multiplexers handle 128 detectors each, they are also “Inter-digitated” such that each multiplexer reads the signal from every other detector along the array. This was a failsafe, so that should one multiplexer fail, the instrument would not lose coverage from half (on one side) of the detector array. The VIMS instrument also has a passive coolant system much like that of the Galileo Near-Infrared Mapping Spectrometer (NIMS); the “ancestor” instrument for VIMS. The passive coolant system is necessary to maintain detector dark current (the current within the detector when the shutter is closed) within the range of tolerance for observations at Saturn (the detector must be cooled to 60 K or less, and will become inoperable for observing above 77 K). Further reductions of stray thermal radiation come from four order-sorting filters which are mounted over the detector array. This works by preventing light with wavelengths outside of a specific range from interfering with detectors that are not calibrated to them (this helps reduce the presence of artefacts within observations).

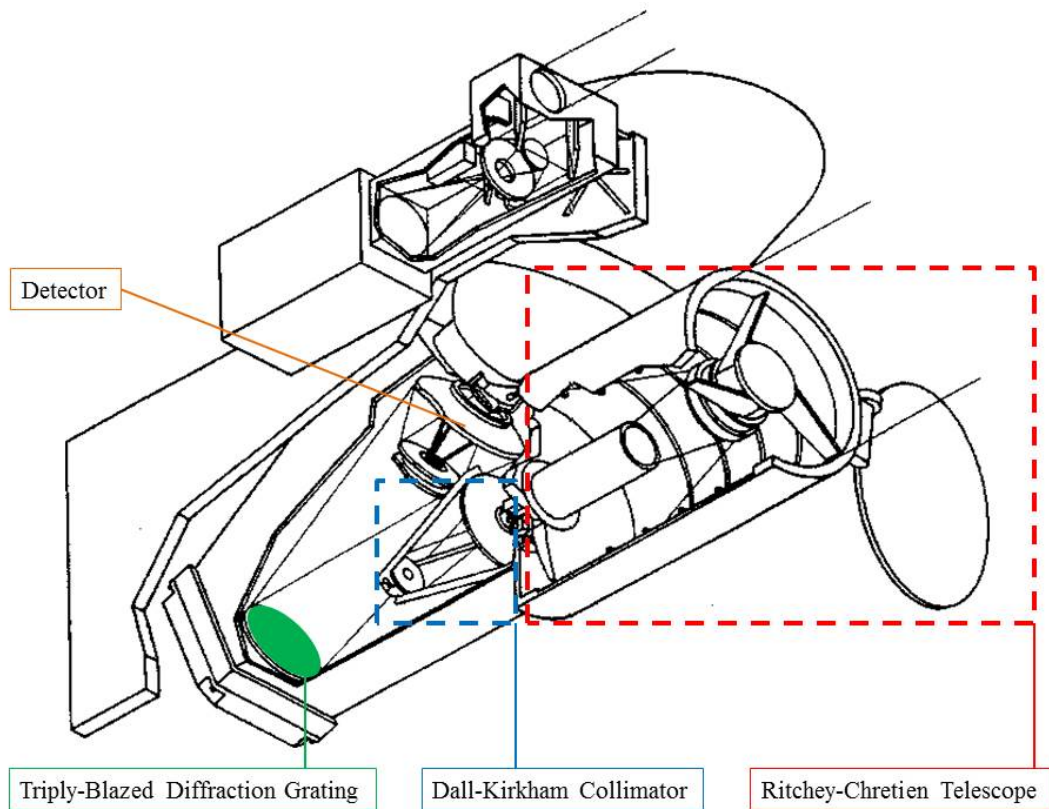


**Figure 2.1:** A wire frame schematic of both the infrared and visible channels in the VIMS instrument aboard the Cassini spacecraft as seen in the Brown (2004) paper. Key parts of the instrument are highlighted: the Ritchey-Chretien telescope (red), the Dall-Kirkham collimator (blue), the triply blazed diffraction grating (green) and the detector (orange).

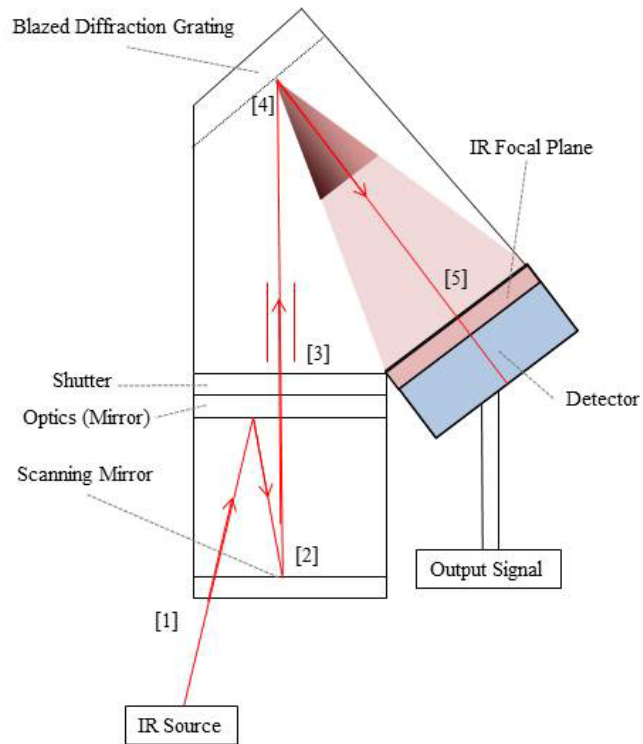


**Figure 2.2:** A simplified schematic of the VIMS – IR channel with a ray diagram (shown in red) to demonstrate the light path through the instrument (based on the operation description in the white paper Brown et al., 2004).

### Section 2.3 The scanning mechanism and observations

In order to generate a two dimensional image across 256 spectral bins (each pixel is a composite of 256 spectral bins, each of which corresponds to one of the aforementioned detectors, hence, in this thesis, a collection of collocated spectral bins will be called a pixel, the individual components of which will be referred to as spectels), VIMS is equipped with a secondary mirror which can scan in two orthogonal directions. For each observation the “cross track” data is acquired by scanning the secondary mirror in a “whiskbroom mode” (much like sweeping a path, VIMS sweeps its field of view from left to right, perpendicular to the path of Cassini’s motion, then moves to the next row and repeats the sweep). The “along path” data is acquired either by passively using the spacecraft drift (like the VIS channel) or by sweeping the secondary mirror in the remaining orthogonal direction. In this fashion, the observations are put together row by row, pixel by pixel as shown in Figure 2.3 where each pixel is formed through the process described by Figure 2.2. The speed at which this process is accomplished is dependent on the integration time selected for the observation; the number of milliseconds that VIMS will collect data for each pixel. The observation shown in Figure 2.3 had an integration time for each pixel of 320 ms, which amounts to approximately 22 minutes for the entire observation. This factor can be important when considering how temporally variant the data in an observation may be. The longer the integration time, the greater the time difference between the first pixel collected and the last. Hence, observations with longer integration times may be unsuitable for studies involving the rapid temporal evolution of phenomena. Likewise, observations with shorter integration times will be subject to a smaller signal to noise ratio than those with longer integration times, and will thus be unsuitable for studies of weak emission sources.

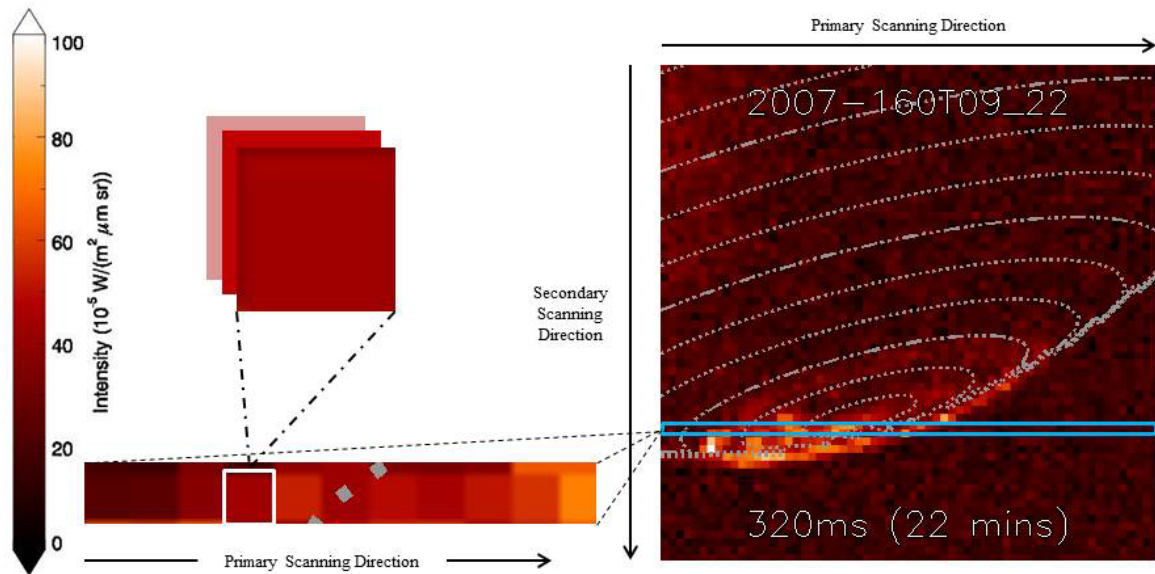


**Figure 2.3:** A complete observation such as the one shown (above and right) is compiled by scanning pixel by pixel along the primary scanning direction (as labelled), once this row is complete the next row in the secondary direction is scanned, left to right. Each individual pixel is a composite of multiple spectral bins or spectels.

#### Section 2.4 Calibration

Before launch, each of the VIMS channels were calibrated separately – VIS in Italy and IR at NASA’s Jet Propulsion Laboratory (JPL) – before they were subsequently integrated at JPL. There were multiple aspects to the ground calibration work. The first was spectral calibration which gave a specification of the wavelength position and band pass for each VIMS spectral bin as a function of temperature. The VIMS-IR response was measured to be identical across the full field of view to within approximately 1 nanometre over the range of temperatures tested. Radiometric testing was conducted by measuring emissions from within the instrument as well as the currents that are consistently present in the detector array; this is referred to as detector dark current subtraction (dark because the shutter is closed during this process). Geometric testing was necessary in order to ensure the emissions were incident on the detectors in the intended manner, without aberrations or distortions from the path the light has travelled through the instrument; this is known as “flat-fielding”. Lastly, polarimetric testing was conducted to account for the effects of any polarisation arising from the diffraction grating. Much of this calibration has been redone since, using solar emissions as well as a laser diode to ensure the measurements would be consistent both pre and post launch.

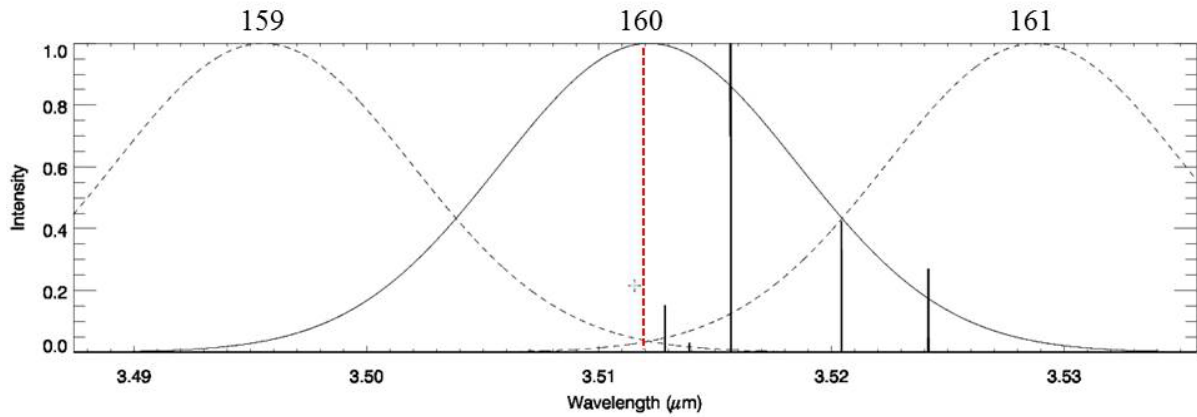


**Figure 2.4:** A plot of the spectral lines present in bin 160 whereby the observed intensities are shown as the vertical solid black lines. The overarching curve is the Gaussian as calculated for bin 160 at a temperature of 500 Kelvin and the two dashed curves either side are the Gaussians for bin 159 (left) and 161 (right). The red dashed line marks the central wavelength of bin 160 (which corresponds to the peak of the gaussian at 3.512  $\mu\text{m}$ ). Note that the emission lines have been normalised to the intensity of the brightest line in order to best display their position alongside the gaussian distributions of the spectral bins.

Figure 2.4 shows the spectral bin 160 - which has a central wavelength of 3.512  $\mu\text{m}$ . The full width half maximum (FWHM) of the overarching Gaussian is the wavelength bandwidth 16.6nm of bin 160. Each spectral bin has a shape similar to those in Figure 2.4, though the emission lines contained within them are different. During the Cassini mission, it was found that the central wavelengths of the spectral bins have been shifting gradually with time. The current conjecture for the reason behind this shift is that the plastic fixtures and fittings in the instrument may have deformed with time due to the rotation of the spacecraft. Since this rotation has been consistent across the entire mission of Cassini, all parts would be affected in a similar and consistent manner, thus changing the optical arrangement of the instrument in the linear fashion that has been observed. This shift in wavelength is an important component to consider as it will affect which bins the  $\text{H}_3^+$  emission lines are located in as well as the amount of absorbed emissions bleeding between bins. The shift in the central wavelength has been measured for each year of the Cassini mission, and is shown for the years 2012-2014 in Table 2.1.

Year	Shift from original calibration in nm $\pm$ 0.1 nm
2004/5	0.0
2006	1.8
2007	3.0
2008	4.1
2009	5.2
2010	6.1
2011	6.9
2012	7.7
2013	8.4
2014	9.0

**Table 2.1:** Shows the annually averaged shift in the central wavelength of the spectral bins with respect to the original calibration for the duration of the mission.

There are also calibrations that are required during the generation of each and every VIMS observation. As with any kind of detector, there is always a degree of background fluctuation. Some of these fluctuations are systematic, in that they are caused by effects such a temperature change of the entire detector array. Others however, are more random in nature and may be endemic to random fluctuations within individual detectors. To remove systemic fluctuations, with each row that VIMS scans, it takes data for an additional pixel at the end which is used for background subtraction of the detector dark current and IR emissions within the instrument. This is accomplished by closing the shutter so that the emissions internal to the instrument can be measured and subtracted from the emissions which are external to the instrument; which in turn is part of a process called “dark current subtraction”. So for a  $64 \times 64$  array, at the end of each row, VIMS will scan an extra 65<sup>th</sup> pixel whilst the shutter is closed, which is then used to calibrate the relevant row and subtract background fluctuations that consistently affect the entire detector array, thereby reducing any observable influence of internal emissions remaining in the instrument. This initial calibration is applied to the data when downloaded from the VIMS instrument system. This cannot, however, account for the random background fluctuations. Hence, we have devised our own methods of dealing with these remaining fluctuations which will be discussed in Chapters 4, 5 and 6.

## Section 2.5 The VIMS team

It is important to note that all VIMS observations are processed by a team whose key members are largely at the University of Arizona and the Jet Propulsion Laboratory (NASA). It is this team of people that take the raw data collected by VIMS and put together files for each observation that contains not only the emissions from Saturn but also the space craft navigational data which can be used to derive the VIMS field of view as well as the location of the planet in an observation. We refer to these files as the SPICE kernels which are defined as follows:

- S kernels: Spacecraft ephemeris (position) as a function of time
- P kernels: Planet/Satellite/target body ephemeris (within the VIMS observation) as a function of time
- I kernels: Instrumental VIMS description of kernel such as field of view, shape or orientation of the observation etc.
- C kernels: Pointing data – the orientation and “look” direction of VIMS.
- E kernels: what the VIMS observation was meant for (e.g. looking at the aurora).

These kernels have then been fed to a series of programs created by Dr Henrik Melin (University of Leicester) which calculates the location of the 1bar pressure surface as well as the value of such variables as latitude, longitude and altitude for each pixel in a VIMS observation (see Chapter 3 Section 3.4). This data is saved for each VIMS observation and has been used extensively in this study. It must be noted that this data has been inherited for the work in this thesis and all credit for it must go to Dr Henrik Melin and the VIMS team. More details on the VIMS team can be found on their website: <http://wwwvims.lpl.arizona.edu/>.

## Chapter 3

### *Data and Spectral processing*

#### Section 3.1 The $\text{H}_3^+$ emission as viewed by VIMS

In every VIMS observation there are multiple sources of IR emission, each of these has their own spectral signature. As discussed in Chapter 2, Figure 2.4, sometimes there is an overlap in the spectral profiles of these different signatures, which signifies that for some spectral bins, there is more than one emissive component that needs to be accounted for. Hence, in the process of analysing the emissions of the  $\text{H}_3^+$  molecule it is important to be able to identify and remove light from other sources (such as reflected sunlight, thermal emissions from deeper in the atmosphere and methane fluorescence). The infrared emission spectrum of  $\text{H}_3^+$  is very well understood as it has been intensively studied under laboratory conditions (Oka, 1992) and modelled with *ab-initio* calculations (Neale et al., 1996, Miller et al., 2010) to characterise its behaviour. Figure 3.1 shows how some emission lines of  $\text{H}_3^+$  are relatively brighter than others (compare those around 4  $\mu\text{m}$  to those below 3.5  $\mu\text{m}$ ). These relative intensities change with temperature (see Figure 1.29) as at higher temperatures, higher energy levels are easier to populate with the greater availability of energy. This change of wavelength emission intensity is a very well understood and documented phenomenon, as such it is entirely possible to measure the temperature of an  $\text{H}_3^+$  population from its infrared emissions; provided the observing spectrometer has a high enough spectral resolution. This technique will be discussed in Chapter 6.

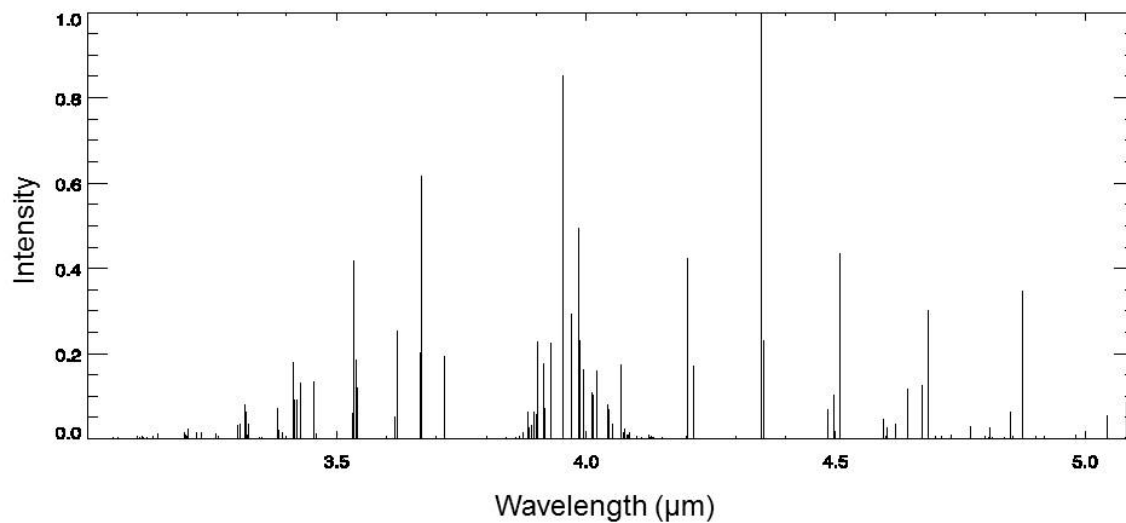


**Figure 3.1:** A model  $\text{H}_3^+$  spectrum between 3.0 and 5.1  $\mu\text{m}$  at 440 kelvin; normalised to the maximum intensity for the purpose of clarity.

The Gaussian of bin 160 (3.512  $\mu\text{m}$ ) in Figure 3.2 shows the resolution of a VIMS spectral bin which covers multiple emission lines, each spectral bin is therefore a composite of different emission lines that fall within its spectral range. These lines are affected by the Gaussian nature of the bin (which is generated by the manner in which each calibrated bin absorbs radiation from spectral lines around the wavelength the detector is calibrated for). Those wavelengths closest to the centre of the bin experience the least reduction in absorption, whereas those near the edge of the bins' limits experience far greater reduction as shown in Figure 3.2. When we consider the emission of a bin, the spectral resolution of VIMS means that we can only examine the summation of all the emission lines within the spectral range of a bin. As such, it is important to note the distinction between spectral line intensity and spectral bin intensity; the former is the intensity of a single  $\text{H}_3^+$  emission line, whereas the latter is the collective emission of multiple as seen by the detector for an individual bin. The emission lines present within bin 160 are also shown as viewed by the Spex instrument. The reason the emission lines are displayed as they would be observed by Spex is to demonstrate the difference between VIMS and a ground based instrument. Compared to other ground-based IR spectrometers, Spex is a medium to low resolution instrument, and yet it vastly outperforms VIMS in terms of resolving individual emission lines. This is an important feature to note for future reference, since it must be taken into account when considering any kind of calculations that rely on the intensity of specific emission lines (such as temperature measurements); VIMS has a significantly weaker spectral resolution. To compare the two instruments directly, Spex has a resolving power of around  $R = 2000$  whereas VIMS-IR has a resolving power of around  $R = 400$ ; hence the difference in the full width half maximum on the Gaussians in Figure 3.2.

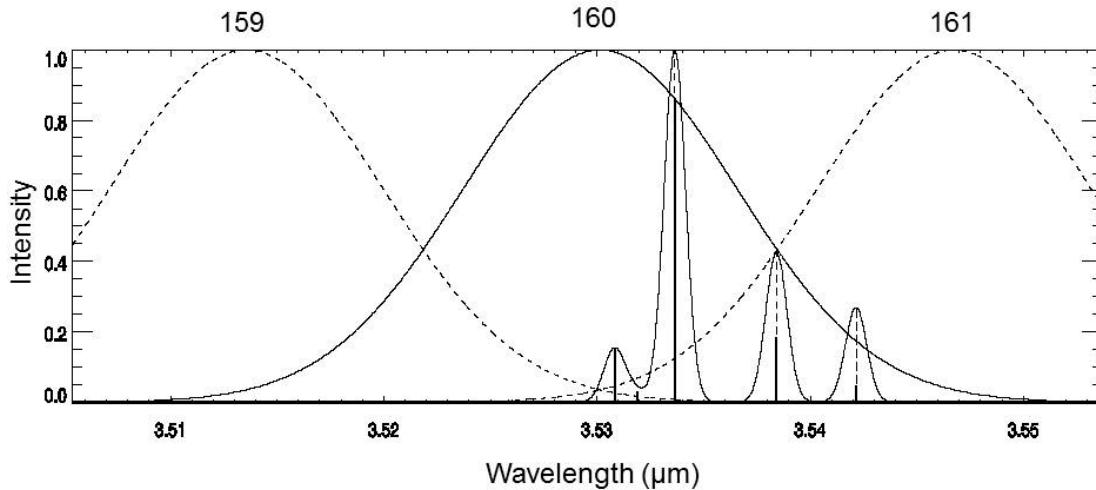


**Figure 3.2:** A plot of modelled spectral lines present in bin 160 whereby the intensities are shown as the vertical solid black lines with the extent of the original line intensities marked by the vertical dashed lines (the intensities have been normalised to make it easier to see everything on the same scale). The overarching curve is the Gaussian as calculated for bin 160 at a temperature of 500 Kelvin and the two dashed curves either side are the Gaussians for bin 159 (left) and 161 (right). The narrower Gaussians denote the emission lines as would be resolved by the Spex instrument. The Spex instrument of NASA's infrared telescope facility has a wavelength resolution of approximately  $0.5 \times 10^{-7}$  and has been added to this plot to compare the wavelength resolution of VIMS with a ground-based instrument. There is some small degree of variability around the emission lines (due to random thermal fluctuations between molecules) however this fine scale variation is not tangible with the wavelength resolution of VIMS-IR. Note that the point at which the gaussians of bins 160 and 161 meet with the emission line at approximately  $3.538 \mu\text{m}$  is coincidence only.

As described in the calibration section of Chapter 2, with the bin shift moving the central wavelength of each detector, the Gaussian also moves and thus the detector absorption of individual spectral lines also changes year-by-year. In other words, the shift in the centre of the bins means a shift in the centre of the Gaussian distribution of the bin, and hence a change in the strength of different wavelengths within that spectral bin (as demonstrated in Figure 3.3). It can also mean that a bin which was previously dominated by emissions from one light source can begin to show spectral signatures from another light source. With the severity of this effect compounding year on year, it is something which must be accounted for when comparing the same spectral bins in observations from different years, in the interest of spectral accuracy.

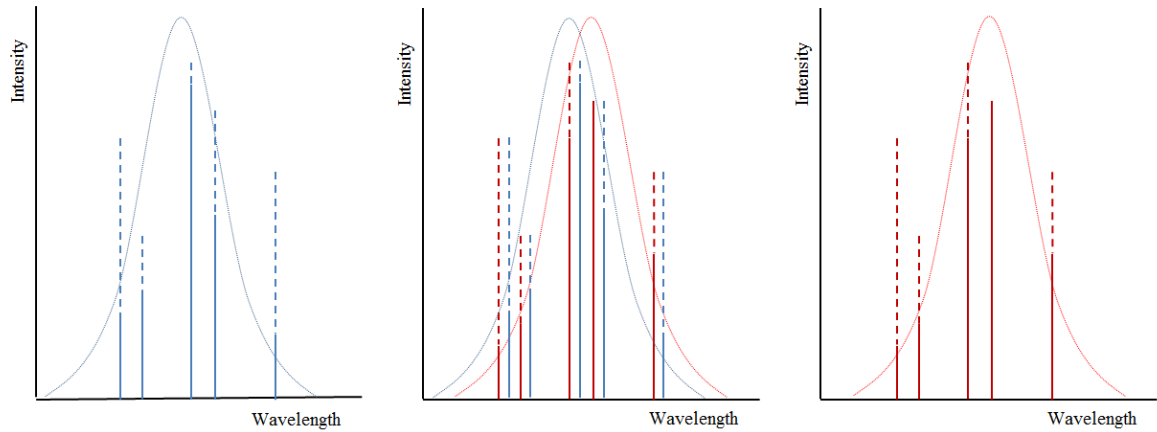


**Figure 3.3:** An exaggerated drawn plot of what happens to different spectral lines within in a bin, should the central wavelength of the bin be moved. The blue lines represent the gaussian profile and emission lines as observed by a single spectral bin for one year, the red equivalents represent the same parameters in the following year after the wavelength shift has occurred. Note how the Gaussian is centred on a new wavelength and the observed intensities of each emission line have completely changed.

## Section 3.2 Extracting the $\text{H}_3^+$ emission spectrum

A pure  $\text{H}_3^+$  signal cannot be immediately measured as there are other light sources in the Saturn's atmosphere;  $\text{H}_3^+$  is not the only infrared active molecule. Further, the emission lines are only present in certain spectral bins; the aurorae are visible in some spectral bins and not others. Hence, when selecting wavelengths for analysis, we choose spectral bins where the  $\text{H}_3^+$  emissions are bright and other emissions are dim. In this manner it is fairly simple to target specific spectral bins based on the strength of the observable  $\text{H}_3^+$  emission, as compared to the background emissions. Further, it also allows for the selective subtraction of bins that contain solely reflected sunlight and thermal emission from those that also have the auroral emission; such that the auroral signal is left behind whilst the influence of the reflected sunlight and thermal emissions is neutralised.

### 3.2.1 Additional sources of emission

There are several different groups of emissions to consider when analysing observations of Saturn (not to mention that there are emissive orders within those groups themselves; such as the Q and R branches in the  $\text{H}_3^+$  emission spectrum). These groups are divided in this thesis into predominantly four categories: sunlight, methane,  $\text{H}_3^+$  and thermal emissions (the emissions of  $\text{H}_3^+$  are isolated as distinct parameters as it is the subject of study in this thesis and methane is a constraining factor on the population of  $\text{H}_3^+$ ). The sunlight category refers to the Infrared component of the light reflected from various parts of the atmosphere including tropospheric hazes and various cloud decks – this sunlight spectral signature can be seen in blue in Figure 3.4. Studying this reflected sunlight in comparison to a pure solar spectrum would enable the derivation of how much solar energy has been imparted on the atmosphere; this in turn is a useful component in the study and modelling of atmospheric dynamics. The thermal category comes from emissions originating throughout the atmosphere from non  $\text{H}_3^+$  species that have become vibrationally excited either due to heating from one source or another (e.g. solar influx or the internal heat of Saturn). These emissions have made it beyond the outer layers of the atmosphere to radiate out into space and can be used to measure aspects such as the mixing ratios of various species (one such example is acetylene and ethane as described in Fletcher et al., 2016). This information is vital to determining the chemistry of the atmosphere as well as the dynamics, a sample of this signature is displayed in red in Figure 3.5.

Methane fluorescence occurs in the wavelength range 3.2-3.4  $\mu\text{m}$  (coincident with some  $\text{H}_3^+$  transitions), comes from a layer of methane that peaks in density around 600 km above the 1bar

pressure level. Fluorescence is a process by which a molecule is excited to a higher vibrational level and converts the excess vibrational energy into kinetic energy (heating) via collisions with other neutrals, thereby making a ‘radiationless’ transition to the lowest degenerate state of the higher vibrational energy level, after which it transits down to the ground state by emitting in the IR a series of emission lines known as the fluorescence spectrum. This spectrum offers insight into the distribution of methane and hence the location of the homopause as previously described in Section 1.2.1 of Chapter 1, which is an important structural parameter in the context of giant planetary atmospheres (Drossart et al., 1999). Whilst these different spectral signatures offer a variety of opportunities for scientific study, it is primarily the  $\text{H}_3^+$  emission that we are interested in and as such we need methods of isolating this emission from the others. The first of these techniques is a process called bin subtraction, described Section 3.2.2, which removes the contribution of the non-  $\text{H}_3^+$  emission from our spectra to leave behind the  $\text{H}_3^+$  emission. Selective sampling is covered in Section 3.2.3 and simply involves choosing which parts of an observation to work with so as to minimise the potential contribution of unwanted spectral signatures. Lastly, in Section 3.2.4, we discuss the bin selection mentioned at the start of this section which involves choosing spectral bins that have strong contributions from  $\text{H}_3^+$  emission lines and weak contributions from everything else.

In this thesis, we commonly refer to VIMS spectral bins by their bin number as opposed to their wavelength range. For the sake of reference, Table 3.1 has been included to show the range of each bin that has been used in the studies of Chapters 4-6 as well as their central wavelengths as of 2005.

VIMS Bin	Central Wavelength ( $\mu\text{m}$ )	Bandwidth - FWHM ( $\mu\text{m}$ )	Signatures present
148	3.31619	0.016101	M/S/T
153	3.39872	0.016034	H/M/S/T
160	3.51284	0.015977	H/S/T
162	3.54664	0.016282	S/T
165	3.59610	0.01714	H/S/T
167	3.63085	0.017796	S/T
168	3.64853	0.018106	H/S/T
170	3.68283	0.018609	S/T
179	3.83472	0.018952	S/T
183	3.89859	0.023959	H/S/T
184	3.91478	0.020077	H/S/T
185	3.93069	0.020349	H/S/T
186	3.94762	0.020577	H/S/T
187	3.96375	0.020771	H/S/T
189	3.99672	0.021054	H/S/T
190	4.01280	0.021179	S/T
200	4.18299	0.022139	H/S/T
202	4.21120	0.022002	S/T
207	4.29650	0.021439	S/T
209	4.33280	0.021204	H/S/T

**Table 3.1:** The VIMS spectral bins used in the studies of Chapters 4, 5 and 6 along with: the central wavelength (the peak of the Gaussian that constitutes the spectral bin), the bin bandwidth (FWHM of the Gaussian) and the spectral signatures contained within that bin (where H stands for  $\text{H}_3^+$  emissions, S for reflected sunlight, T for thermal emissions and M for methane fluorescence).

### Section 3.2.2 Bin Subtraction

To demonstrate the workings and benefits of subtracting unwanted spectral signatures, Figure 3.4 and 3.5 were constructed. The bin subtraction process begins by selecting a pair of bins that both have the emissions sources that need to be removed and are relatively close in wavelength range, where one bin contains the emission that you are trying to isolate and one does not. By considering locations within the observation that do not have the desired emissions, say the auroral  $H_3^+$  emission in the case of Figure 3.4, we are able to sample these spectral bins in regions where there is only the unwanted spectral signatures. By scaling the bin without the  $H_3^+$  to match the other in this region we can subtract out the other emission sources. In Figure 3.4 the “ $H_3^+$ ” bin selected is bin 209; it has been referred to as an “ $H_3^+$ ” bin due to the fact that there are strong  $H_3^+$  emission lines within this bin, as can be seen by the presence of the auroral oval on the body of the planet in Figure 3.4 [2] and [4]. Conversely, however, bin 207 (Figure 3.4 [3]) does not have any strong  $H_3^+$  emission lines and hence the auroral oval is absent from the image. Whilst these two bins are different in  $H_3^+$  emission, they are quite similar in sunlight and thermal emissions; the thermal emissions on the body of the planet are co-located in both [2] and [3] (shown in [1] as red and as a brighter green in the same region for [2] and [3]). Although both of these bins contain reflected sunlight, the intensity of this emission is somewhat stronger in bin 207 than 209, and as such must be scaled to match so that the thermal emission can be removed without overcompensating and thus destroying the  $H_3^+$  that we are trying to extract; this scaling was found to be an average factor of 0.8 for these bins using the above technique across the VIMS data set. The result of this subtraction is that [4] now displays the auroral emission more clearly, since the background emission has been removed from the bin, leaving behind  $H_3^+$  emission. This process can also be conducted for other emission sources besides  $H_3^+$  such as methane, as demonstrated in Figure 3.5 which follows the same sequence of steps as Figure 3.4. Here, sunlight and thermal emission are significantly brighter in bin 153 as this bin contains no methane fluorescence lines; when this bin is scale by 0.45 and subtracted from bin 148, the resultant image shows only the methane fluorescence on the limb.

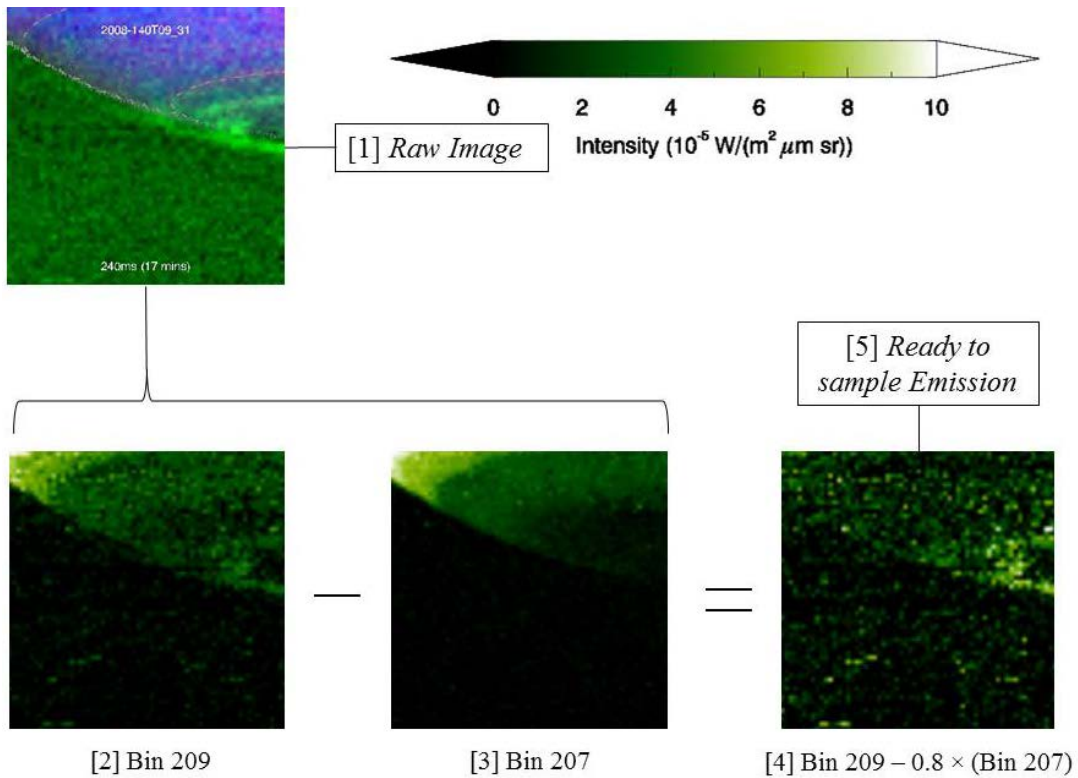


**Figure 3.4:** Shown above is observation 2008-140T09\_31 as a combination of multiple bins with the thermal emission from bin 255 (central  $\lambda = 5.10680 \mu\text{m}$ ) in red, reflected sunlight from bin 1 (central  $\lambda = 0.88421 \mu\text{m}$ ) in blue and the combination of a range of  $\text{H}_3^+$  rich spectral bin 209 in green [1]. The observation is also displayed in spectral bin 209 (central  $\lambda = 4.33280 \mu\text{m}$ ) [2], bin 207 (central  $\lambda = 4.29650 \mu\text{m}$ ) [3] and the result of bin 207 multiplied by 0.8 and subtracted from bin 209 [4]. The first image [1] was created to demonstrate the location of the sunlight on the body of the planet (and hence show the reason why this observation requires subtraction). Images [2], [3] and [4] are all scaled to the same maximum intensity such that the effects of the sunlight subtraction are immediately observable when comparing bin 209 before [2] and after [4] subtraction. The images [2] to [4] are displayed in colour scale ranging from green to black for their respective bins.

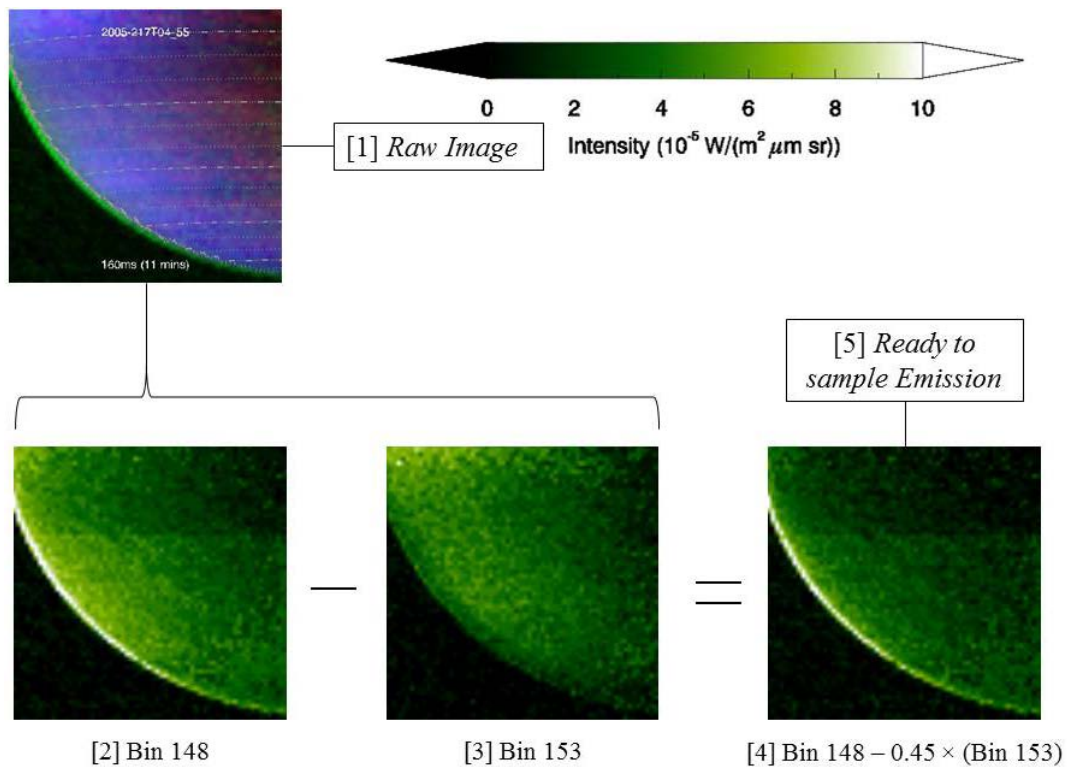


**Figure 3.5:** Similar to Figure 3.4, the set of images above are from the same observation 2005-217T04\_55 [1] shown in the methane bin 148 (central  $\lambda = 3.31619 \mu\text{m}$ ) [2], bin 153 (central  $\lambda = 3.39872 \mu\text{m}$ ) [3] and bin 153 multiplied by 0.45 and subtracted from bin 148 [4].

As the central wavelengths of each spectral bin have been shifting with each successive year of the Cassini mission, the subtraction factors are constantly changing. Whilst the subtraction factors derived for each pair of auroral/non-auroral bins (see Table 3.2) works well when using the VIMS data set to only examine intensities (as is so in Chapter 4), they are limited in their capacity to function for spectral analysis in pursuit of properties such as temperature and density (Chapter 6). As such, it was necessary to measure an average subtraction factor for each year rather than the entire data set. This is discussed in Chapter 6 Section 6.5.

Bin Pair ( $H_3^+$ /background)	Subtraction factor
153/148	0.45
160/162	0.7
165/167	0.7
168/170	0.7
202/200	0.75
209/207	0.8

**Table 3.2:** A list of  $H_3^+$ /background bin pairs and their subtraction factors as used in Chapter 4.

### Section 3.2.3 Selectively sampling appropriate regions

Extraction of the background emission signatures (Section 3.2.4) across a wide range of wavelengths requires an understanding of the different observation geometries available to VIMS. The observations, shown Figures 3.6/3.7 (a)-(c) are a good example of why this is important. They demonstrate that it would be futile to attempt to extract an auroral  $H_3^+$  emission spectrum from the observation in Figure 3.6 (c) as there are no aurorae present in this observation. Likewise, if we were trying to isolate the thermal emissions shown in Figure 3.7 it would be significantly easier to only sample the night side of the planet to avoid to reflected sunlight in Figure 3.6.

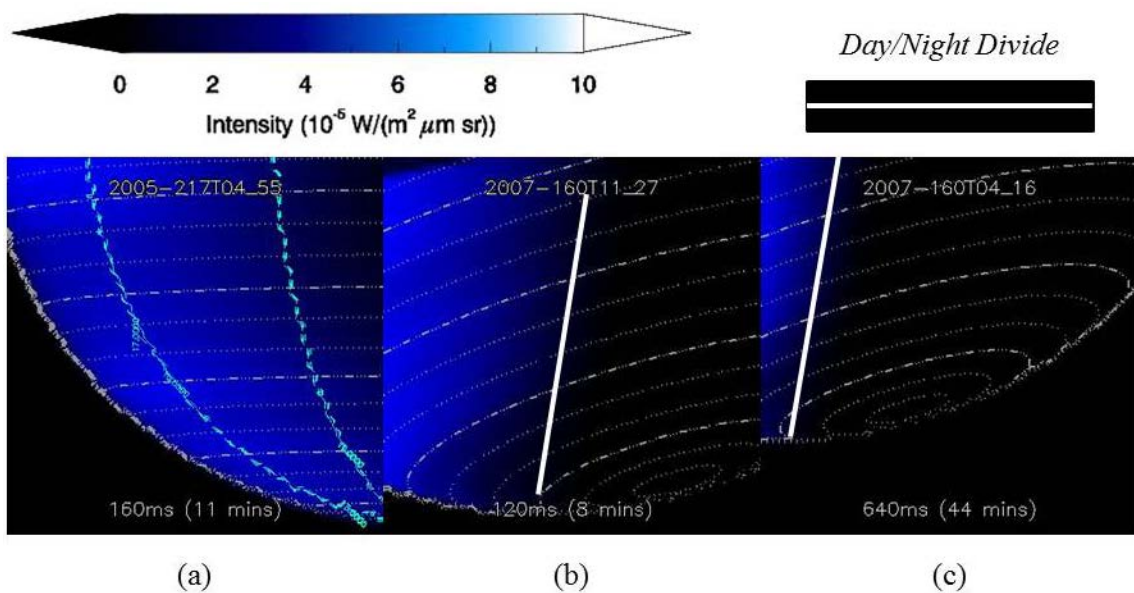


**Figure 3.6:** Three observations shown only the emission in bin 1, which is dominated by reflected sunlight. The dashed blue lines in (a) mark the region which was sampled to create the blue spectral profile in Figure 3.9 to demonstrate the spectral signature of reflected sunlight. The solid white lines in (b) and (c) delineate the day/night boundary (dawn in both cases).

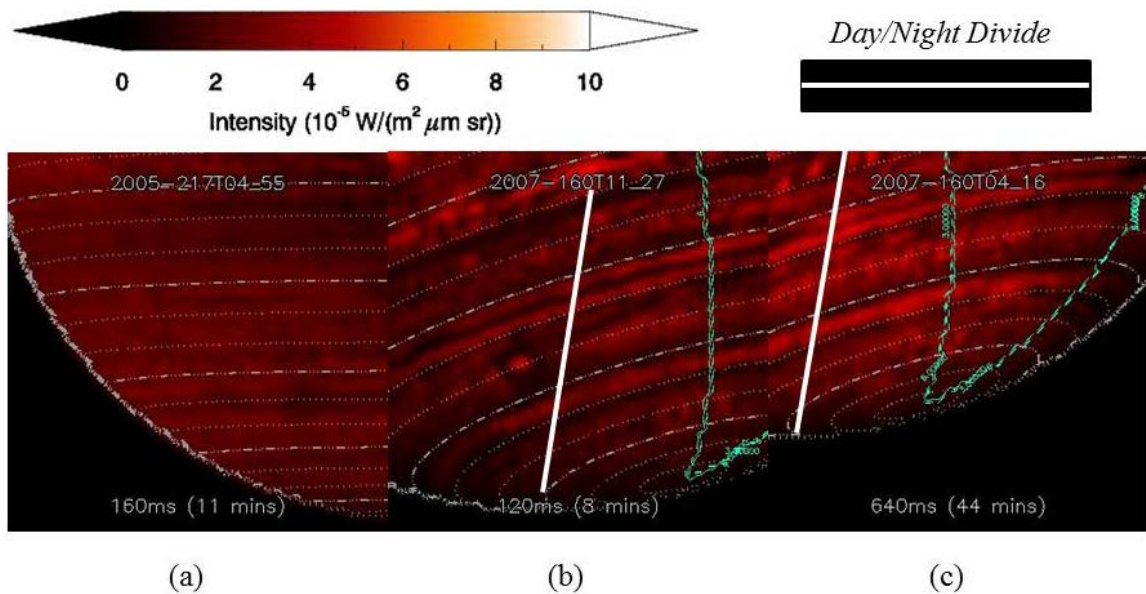


**Figure 3.7:** The same three observations from Figure 3.6 shown in bin 255. The blue dashed lines in (b) and (c) mark the boundary of the region sampled to create the red thermal profile in Figure 3.9. The solid white lines, as in Figure 3.6, mark the dawn day/night boundary. Note that (a) was not sample for the thermal emission as in Figure 3.6 (a) it can be seen that this observation is entirely on the dayside of the planet.

#### Section 3.2.4 The observed spectra

Whilst Section 3.2.3 explains that there are spatial regions where different types of emission (such as reflected sunlight) are dominant, this Section shows that the signatures also have wavelength regions in the spectrum where they are dominant. By using the method of identifying appropriate regions to sample as described in Section 3.2.3, Figure 3.9 was created to examine these wavelengths bands for different emission sources. For reflected sunlight the pixels between 06:30 and 10:00 (in sub solar local time) of observation 2005-217T04\_55 were sampled (the dayside body of the planet). An average intensity of every included pixel was taken across all spectral bins, the result of which is the blue profile in Figure 3.9, where it can be seen that the reflected sunlight is dominant at wavelengths shorter than 3.2  $\mu\text{m}$ . Likewise, the thermal emissions were sampled between 03:00 and 06:00 in observations 2007-160T11\_27 and 2007-160T04\_16, shown as the red profile in Figure 3.9. This profile demonstrates that thermal emissions are dominant at wavelengths longer than 4.4  $\mu\text{m}$ ; this wavelength marks the beginning of the black body radiation curve for Saturn. To obtain the methane fluorescence the dayside limb above the 1 bar level of the limb up to an altitude of 1000 km was sampled from observation 2005-217T04\_55. This created the yellow profile visible between 3.2 and 3.4  $\mu\text{m}$  in Figure 3.9. Lastly, the  $\text{H}_3^+$  signature was sampled from a sequence of observations (2007-

160T13\_28, 2007-160T12\_40, 2007-160T08\_28, 2007-160T05\_04, 2007-160T04\_16) in the region between 300 and 1200 km above the 1 bar level at auroral and polar latitudes (greater than  $67^\circ$ ), this profile is shown in purple in Figure 3.8 and 3.9. Multiple observations were used to increase the number of pixels sampled and to reduce the noise in the  $H_3^+$  profile. Despite this averaging still contained some fluctuations from the random background noise as can be seen when comparing the sample (purple)  $H_3^+$  profile to the model in Figure 3.8. Hence, it was necessary to sample the emission above altitude of 4000 km, where measured signal was only the background noise, take an average of this emission for each spectral bin across all included pixels and subtract it from the averages in the  $H_3^+$  spectral profile. This was done to each observation individually before taking the mean of the five different profiles as the background noise level varies between observations.

As  $H_3^+$  cannot survive for long in regions of the atmosphere below the homopause (see Section 1.4 of Chapter 1), it is mostly emissions from above the homopause that we observe at Saturn. These emissions escape attenuation by methane absorption; which renders the lower atmosphere “dark” between wavelengths of 3.4 and 4.4  $\mu\text{m}$  (Figure 3.9). Hence the emissions are still very bright for a specific selection of  $H_3^+$  spectral lines, which is why only certain wavelengths tend to be examined for the purpose of isolating and characterising the  $H_3^+$  emissions in the analysis of observations (as the lower atmosphere appears to be dark due to the absorption). This can be seen in the  $H_3^+$  profile in Figure 3.8, which shows an intensity plot of the VIMS spectral bins both from sampling observations above the limb (purple) and modelling the  $H_3^+$  as it would be resolved by VIMS (red).

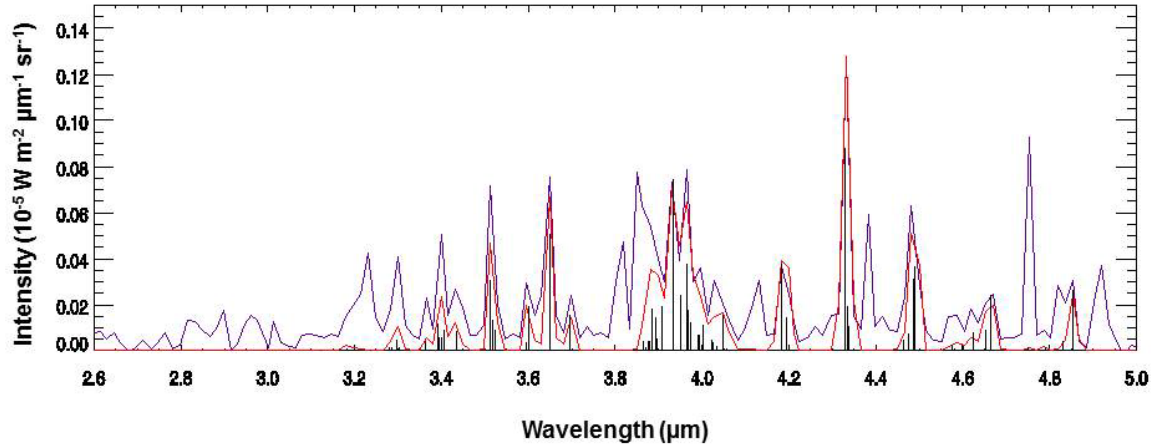


**Figure 3.8:** A plot comparing the model spectrum of  $H_3^+$ , shown in red, with the  $H_3^+$  emission sampled from a sequence of observations (2007-160T13\_28, 2007-160T12\_40, 2007-160T08\_28, 2007-160T05\_04, 2007-160T04\_16) shown in purple. The  $H_3^+$  emission lines present in this range are marked by the vertical black lines. Note the deviations between the sampled (purple) and modelled (red) profiles is due to the fact that the sampled profile contains instrumental noise as well as contributions from other emission sources (such as thermal emissions and methane fluorescence).

Looking at the wavelength range of 3.2-4.5  $\mu\text{m}$  in Figure 3.9, it can be seen that there is a distinct window in which the bright signatures of reflected sunlight and thermal emissions are largely absent. Also present in this wavelength range are a large number of  $H_3^+$  emission lines (shown in Figure 3.8). Thus, in the research of this thesis the spectral bins used to extract  $H_3^+$  spectra have all come from this band of wavelengths as outside of this range the emissions threaten to overwhelm the  $H_3^+$  emissions and can be difficult to remove.

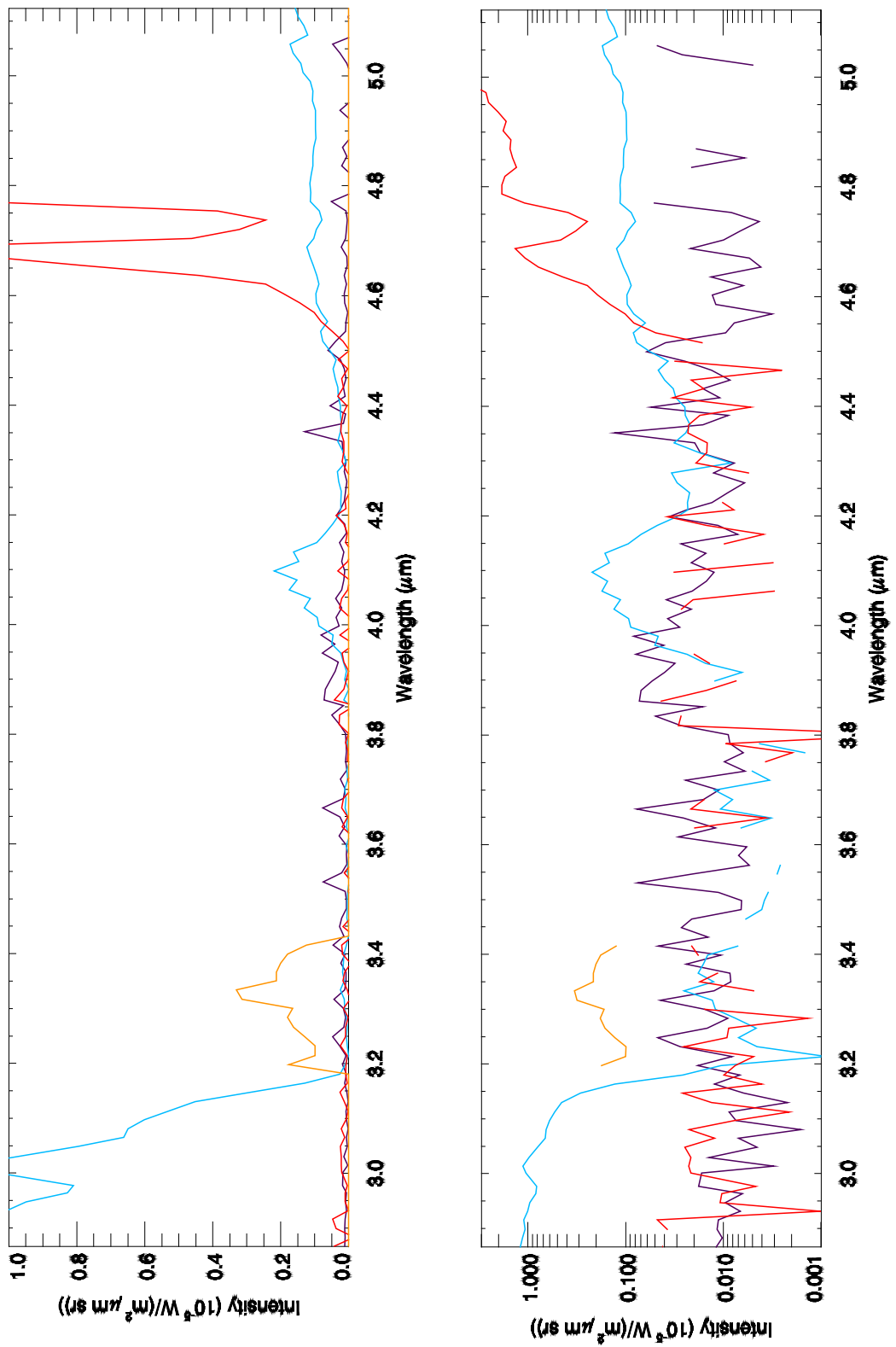


**Figure 3.9:** (on previous page) Two plots showing the same samples of spectra on both a normal scale (top) and a log scale (bottom). Each spectra was sampled to showcase the importance of selecting the right region to sample certain components. The reflected sunlight can be seen in the bright emission at the shorter wavelengths in the blue profile which was sampled from body of the planet on the dayside, between 06:30 and 10:00, of observation 2005-217T04\_55. The methane fluorescence signature, visible between 3.2 and 3.4  $\mu\text{m}$ , in the yellow profile, was also sampled from observation 2005-217T04\_55, on the dayside limb above the 1 bar level of the limb up to an altitude of 1000 km. The thermal emissions can be seen in the red profile which was sample on the night side, between 03:00 and 06:00, of Saturn in the observation 2007-160T11\_27 and 2007-160T04\_16, the tell-tale sign of this emission is the bright and dominant emission at longer wavelengths (greater than 4.6  $\mu\text{m}$ ). Lastly, the  $\text{H}_3^+$  emission was sampled from a sequence of observations (2007-160T13\_28, 2007-160T12\_40, 2007-160T08\_28, 2007-160T05\_04, 2007-160T04\_16) in the region between 300 and 1200 km above the 1 bar level at auroral and polar latitudes (greater than  $67^\circ$ ), this profile is shown in purple (after it has been cleaned from contributions). These plots also show there is a large difference in the relative brightness of each of these emission types. As demonstrated by the bottom panel, the reflected sunlight and thermal emission signatures are both at least an order of magnitude brighter than  $\text{H}_3^+$  emission. Note the data gaps in the profiles shown in the logarithmic plot (bottom panel) are bins which measured negative emission and were eliminated. These negative values happen due to the variation caused by the noise in the observations.

### Section 3.3: Poor data

The quality of VIMS data varies greatly from observation to observation. Figure 3.10 shows two examples of poor data that can cause problems when trying to analyse the emission of different spectral bins. As described in the figure caption, the observation in the left image is normally flagged as poor data due to the presence of emission intensity far outside the range of what could feasibly be expected in a normal VIMS observation (as a guiding example, the intensity of a pixel in the auroral regions would generally be expected to vary between 0.0 and  $4.0 \times 10^{-5} \text{ W m}^{-2} \mu\text{m}^{-1} \text{ sr}^{-1}$ ). Observations such as the one shown in the image on the right however, demonstrate a far more complex problem. Like the left image, it is possible that this observation suffered from a faulty subtraction of detector dark current, however this has not led to a pixel intensity that is outside of a feasible range of emission. Hence, observations like the one shown in the image on the right cannot be automatically removed. Worse still, these streaked artefacts are only present in a few spectral bins and hence will not show up in any image where a significant number of bins have been combined together. Thus it is important to always consider multiple spectral bins at once when selecting observations for inclusion in different studies. For smaller data sets this can be done by manual filtration (i.e. examining each observation individually) which was done for the study in Chapter 4. For larger data sets an automated filtration process (Chapter 5 and 6) is required which can identify artefacts such as those shown in Figure 3.10 (left) as the bad data in these streaks tend to contain intensities far outside the range normally expected ( $0-10 \times 10^{-5} \text{ W m}^{-2} \mu\text{m}^{-1} \text{ sr}^{-1}$ ), sometimes they even register as positive or negative infinities. For artefacts like those in Figure 3.10 (right), it is difficult to filter them automatically as their intensities fall within the normal range, however with the larger data sets in the broad scale statistical study of Chapters 5 and 6, these artefacts tend not to be an issue when averaged with the rest of the data. How these issues are resolved in this thesis is discussed in greater detail in Chapters 4-6.

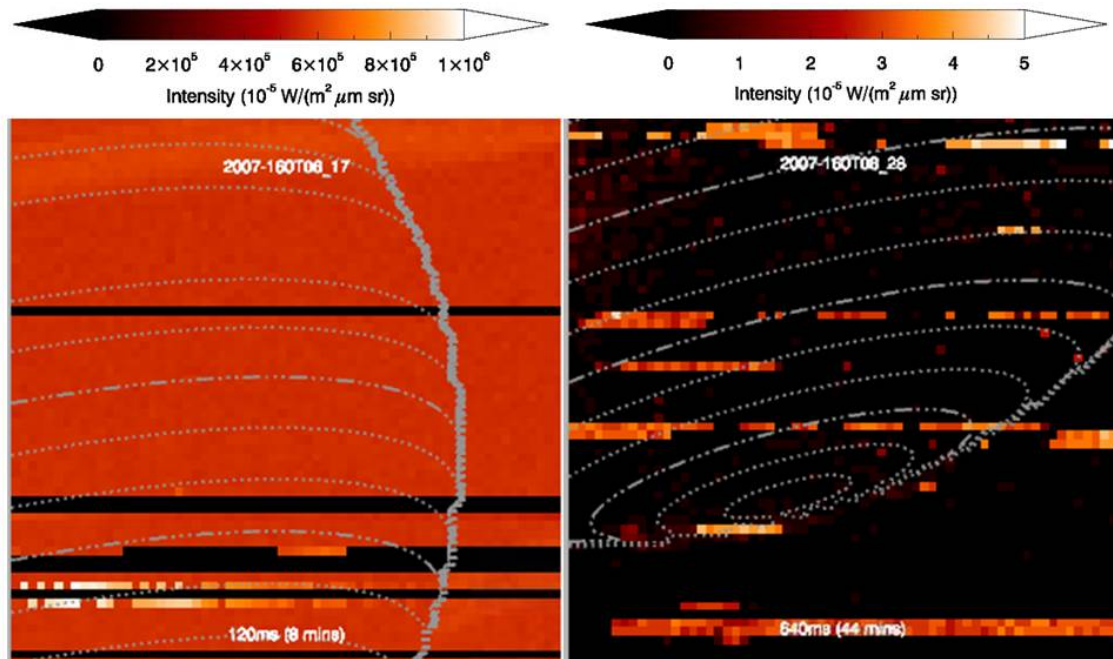


**Figure 3.10:** above are two examples of observations that have been classified as poor data with their corresponding colour scales shown above them. In the left image (2007-160T06\_17), there are three dark bands across the observation; these are the result of the presence of bad data, possibly sourced from a glitch in the detector dark current subtraction used in the calibration of systemic fluctuations described in Section 2.4. This artefact is present in all spectral bins and as such is immediately obvious. The right image (2007-160T08\_28) has suffered a similar problem though to a much lesser extent, as it has only affected specific bins and the resulting intensities are still within a nominally acceptable range. The image is displayed only in bin 181 (central  $\lambda = 3.86184 \mu\text{m}$ ), however if it were to be shown as a combination of a wider range of bins, the artefacts present in the above image would be obscured by the by other bins where it is not present, and thus these weaker artefacts tend to remain largely unknown prior to any data analysis as they are blended out. The reason for these affecting only some bins and not others is currently unknown.

## Section 3.4 Generating the backplanes and filtering the data

### Section 3.4.1 NASA navigational data

In order to analyse the observations, we require a reference frame that gives not only each observation, but each pixel within them a location with respect to Saturn (the position of which is shown in previous figures). This reference frame can then generate a pressure surface calculated from the orientation and trajectory of Cassini, a surface which can be used to spatially analyse the observations. What follows is a brief explanation on how this is done.

The pressure surface is generated from the pointing and spacecraft location data from the SPICE kernels (Section 2.5). This data is obtained from the Cassini Navigation team, who utilise an orbital model of Cassini's trajectory which is retroactively corrected with navigation data from the spacecraft. This produces a central position for the spacecraft as well as an orientation in the form of the SPICE kernels. Two of these kernels, the pointing and the position, are used to calculate the "Boresight" vector for the instrument payload pallet; the pallet is a cross shape and the boresight is therefore the line orthogonal to plane of the cross at its centre. The line of sight for the VIMS instrument can then be calculated using an offset from the main Boresight. Finally, from this vector, new vectors for the corners of each pixel can be calculated by considering the "viewing vector", the spacecraft location and orientation, the angular size of each pixel as well as the location of the pixel within the observation and finally the spacecraft motion (since each pixel is integrated over a period of time whilst Cassini is still progressing around its orbit). These calculations use a series of geometrical calculations and coordinate transformations to discern the values of multiple variables (which are collectively known as the backplane) for each pixel in an observation on an individual, case by case basis. Among these variables is the altitude, which is defined radially outwards from the centre of Saturn, where an altitude of 0 km is the altitude at the 1 bar pressure surface (also referred to as the 1 bar level). Section 3.4.2 details how we can use this variable to discern information about the distribution of  $\text{H}_3^+$  emission.

### Section 3.4.2 Filtering and purification of the data.

With a data bank of over fifteen thousand individual observation files it became necessary to find some way of automatically filtering the data for specific properties. Hence we improved upon a widget filter (a widget is a user interface with various fields that can be assigned values such as latitude or longitude, this interface then searches the database of observations for files that fit the specified ranges) to select files that matched the necessary criterion for any studies

that we have conducted as well as analysing them. The initial series of variables which could be filtered are listed below (note that each variable has either been annotated with [header] signifying that the variable comes from the file header, a list of information associated with each observation, or [SPICE] indicating that it is a variable calculated from the navigational data kernels (described in Section 2.5):

- File Directory Name [header] – this enables the selection of specific years and days from the Cassini campaign and can be used to manually select pre and post equinox (11<sup>th</sup> August 2009) observations.
- Integration time [header] – the amount of time the instrument takes to integrate the received emissions into a single pixel. The longer the integration time, the more light the detector has absorbed and thus – more often than not – the spectrum is cleaner and less prone to noise and variations. One drawback of longer integration times is the loss of temporal resolution (typically ranging from 10ms per pixel to around 1000 ms per pixel) due to the motion of the spacecraft and the planet below it. This variable is useful to control the degree of noise that a selected data set might contain.
- Spatial resolution [SPICE] – this is calculated according to where the spacecraft is located with reference to the planet; it is useful to constrain data sets to contain a specific spatial scale.
- Number of pixels [header] – each observation has a set number of pixels in the x (horizontal) and y (vertical) directions of an image. The VIMS instrument received upgrades to its software post launch that have enabled it to take a variety of image sizes in accordance with the needs of an observation campaign. Typically, images are  $64 \times 64$  pixels, but they can be any combination of 1, 12, 32 or 64 pixels in either dimension. The ability to filter out anything that is not  $64 \times 64$  pixels enables us to be more selective about observation types, and to remove observations that are not suitable for specific studies (a  $1 \times 12$  pixel observation is not generally suitable for altitudinal profiling). In this thesis we use only those observations with more than 32 pixels in either dimension in order to ensure the observations contain enough of the regions we want to sample (either the body or the limb of the planet).
- Latitude [SPICE] – utilises the maximum and minimum values contained within an observation to calculate if an observation contains pixels within a given latitude range. This is useful if a study requires analysis of say the north and south hemispheres separately.

It was deemed necessary to expand this list of variables so as to improve the versatility of the filtration process, especially when constructing the limb emission profiles. Hence, a further seven variables were added to the filter allowing for greater subtlety in the selection of data, they are listed below:

- Local Time [SPICE] – Calculated from the longitude after it has been corrected for sub-solar longitude, this variable allows for the distinction of local time sectors for study. This variable only applies to the local time on the planetary disk but not above the limb.
- Spacecraft Distance [SPICE] – This variable is a secondary method of selecting observations with a specific spatial scale. When resolution is less important, the spacecraft distance can be used to select observations in an approximate range of pixel spatial scale (e.g. a spacecraft distance of  $26 R_S$  will result in pixels that cover  $\sim 100\text{km}$  of altitude as compared to a distance of  $40 R_S$  which results in pixels that  $\sim 2000\text{km}$  altitude).
- Sub-Spacecraft Latitude [SPICE] – Also known as “Z angle”, this is the latitude of the spacecraft mapped down onto the planet. It is useful for the consideration of the alignment of the observations. It can give an indication as to whether or not the spacecraft is observing the limb at an oblique angle (which is particularly important for limb emission studies).
- Sub-Solar Latitude [SPICE] – This variable is similar to the sub spacecraft latitude, except with respect to the sun. This variable can be utilised to filter observations according to the position with respect to the Kronian equinox – this is especially important considering the influence solar irradiance has on the generation of plasma populations.
- Limb Latitude and Longitude [SPICE] – The latitude and longitude of the pixels above the limb of the planet. Note however that they are the latitudes and longitudes of the pixel mapped down to the limb along a radial line from the planetary centre and hence cannot describe the thickness of the observed layer of upper atmosphere.
- Altitude [SPICE] – Using the 1 bar pressure surface as the 0 km baseline, this variable increases radially outwards from the planet and is negative on the planetary disk. This variable is specifically for limb emission studies and is of great importance to this thesis. Its inclusion in the widget filter also ensures that observations actually contain, or contrarily do not contain, the planetary limb emission.

The following three chapters detail studies of the infrared main auroral oval of Saturn using both small and specific subsets of observations for the study in Chapter 4 as well as a large and

diverse set of data in the statistical study of Chapters 5 and 6. All of these require specific conditions for the observations that they analyse, which is why this widget was so important. It allowed for the automated filtration of data to quickly provide the necessary sets of observations relevant to each study. The original programs for this widget were constructed by Dr Tom Stallard and Dr Henrik Melin of the University of Leicester, and were further developed for this thesis through the inclusion of new variables and a new tool for analysing observations (described in Section 4.3.1).

## Chapter 4

### *The effects of alignment on the peak emission altitude*

The first research question of this thesis is whether the apparent peak emission altitude of the aurora is dominated by real altitude changes or through a line of sight bias effect. As will be explained in the following sections, a new technique designed to improve upon the method of Stallard et al. (2012a) was developed in the process of the analysing the effects of alignment on the altitudinal profile of the auroral IR emission.

#### Section 4.1 The altitudinal profiling in Stallard et al. (2012a)

In Stallard et al. (2012a), nine images taken in the same sequence of observations in 2006 by the Cassini VIMS instrument, yielded a peak auroral emission altitude at 1155 ( $\pm 25$ ) km above the 1 bar level. They used a histogram technique to collate the emission from multiple auroral observations into altitudinal bins, thereby producing an altitudinal profile. The selection of the observations required that the latitude of the auroral curtain be within 1.5 degrees of the planetary limb beneath it (pursuant to the measured variability in the latitude of the auroral oval as seen in Badman et al., 2011). To measure the alignment of the auroral curtain with the limb, the body  $\text{H}_3^+$  emission was considered. In each observation there is a visible arc of  $\text{H}_3^+$  auroral emission on the body of the planet; this was profiled with respect to latitude in order to measure the peak emission latitude of the auroral oval. Assuming the auroral oval to be circular, this latitude was then compared with the latitude of the limb auroral oval using a projected pressure surface that was 1000 km above the 1bar level. Thus Stallard et al. (2012a) had a measure of the auroral alignment. These measurements were completed using the NAIF SPICE (see Section 2.5) database to provide the relevant pressure surfaces and for the latitude of the body aurora, provide a latitudinal histogram of  $\text{H}_3^+$  emission, the peak emission latitude of which was ascertained by fitting this profile with a gaussian function and quadratic background.

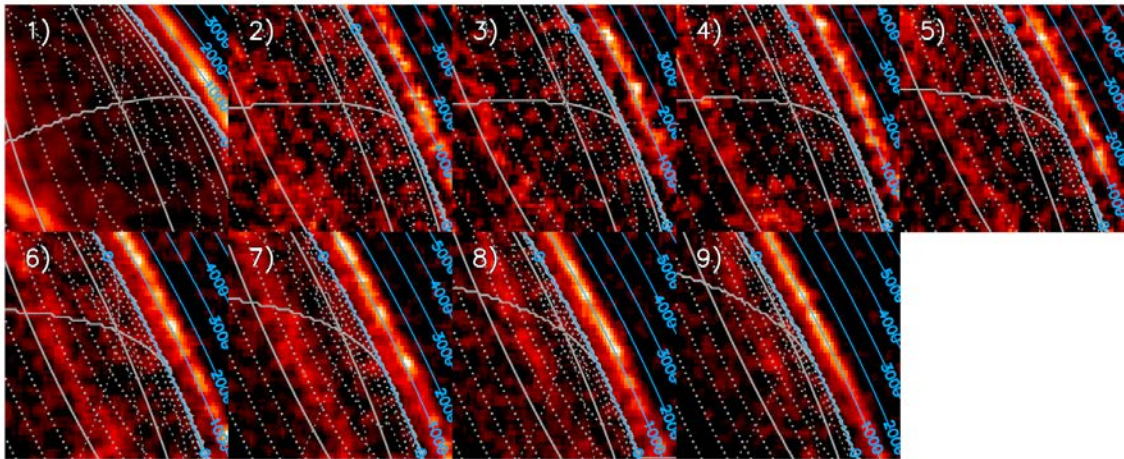


**Figure 4.1:** a sequence of nine observations of the southern auroral region taken between the 11<sup>th</sup> and 12<sup>th</sup> of October, 2006, from figure 1 (a-g) of Stallard et al. (2012a). In each observation the auroral emission can be seen above the 1 bar limb of the planet which has been marked by the white lines of latitude and local time. The aurorae in each of these observations were profiled in Stallard et al (2012a) using a histogram technique, which produced the combined altitudinal profile of  $H_3^+$  emission shown in Figure 4.2. Observations 2-5 were selected on the basis that the aurorae were within 1.5 degrees latitudinal alignment with the planetary limb beneath the auroral curtain.

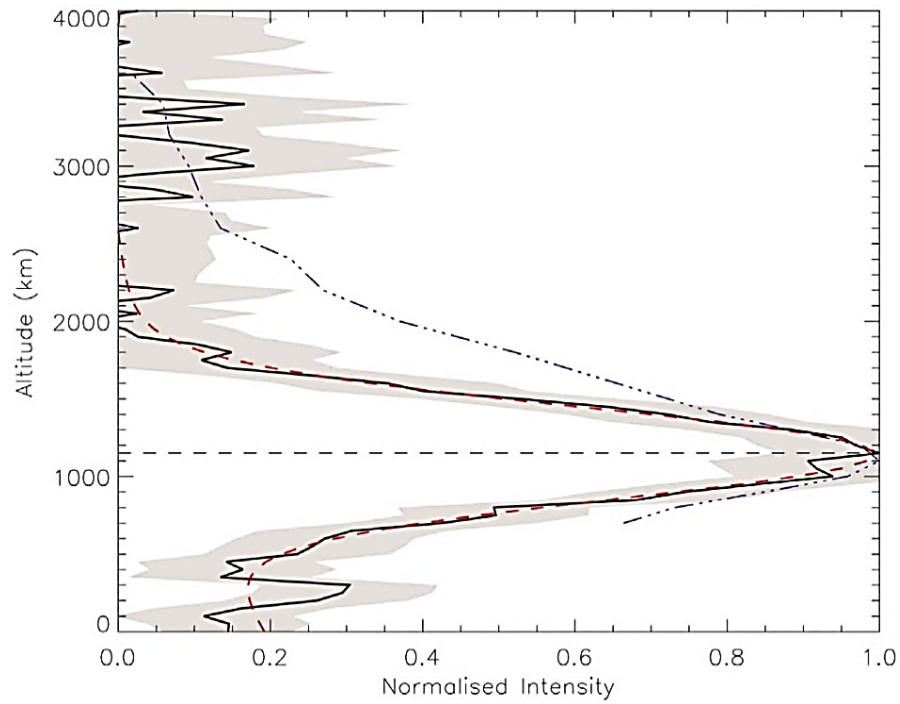


**Figure 4.2:** the altitudinal profile of  $\text{H}_3^+$  emission (the black solid line) from the combined auroral emissions of the observations 2-5 shown in Figure 4.1. The red dashed line is the gaussian fit combined with a quadratic background to the  $\text{H}_3^+$  emission profile, and yields a peak emission altitude of  $1155 (\pm 16)$  km with a full width half maximum of  $638 (\pm 19)$  km. The shaded grey region represents the uncertainty in the intensity. The purple dot-dashed line is the UV emission profile from Gerard et al. (2011).

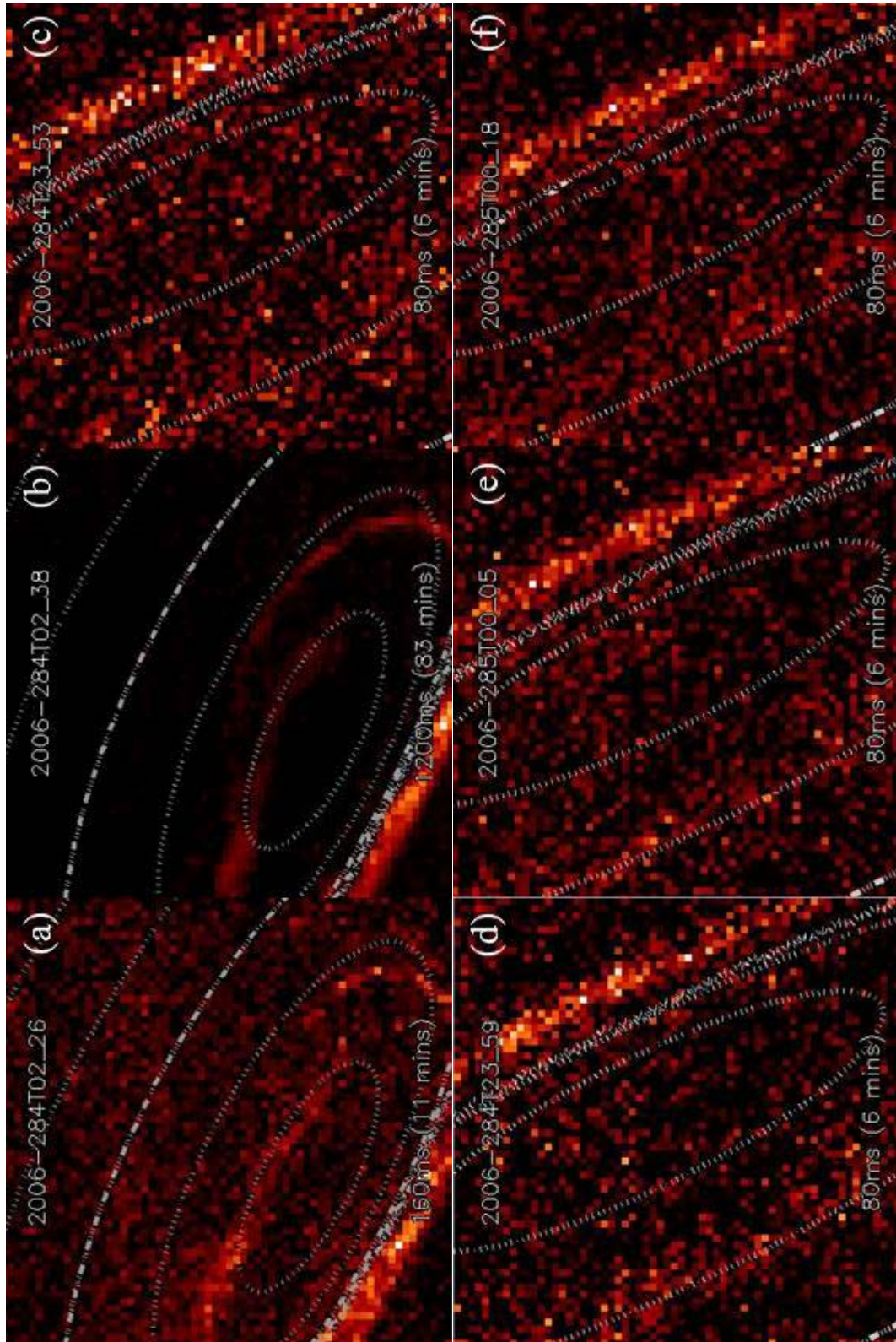
## Section 4.2 The data set

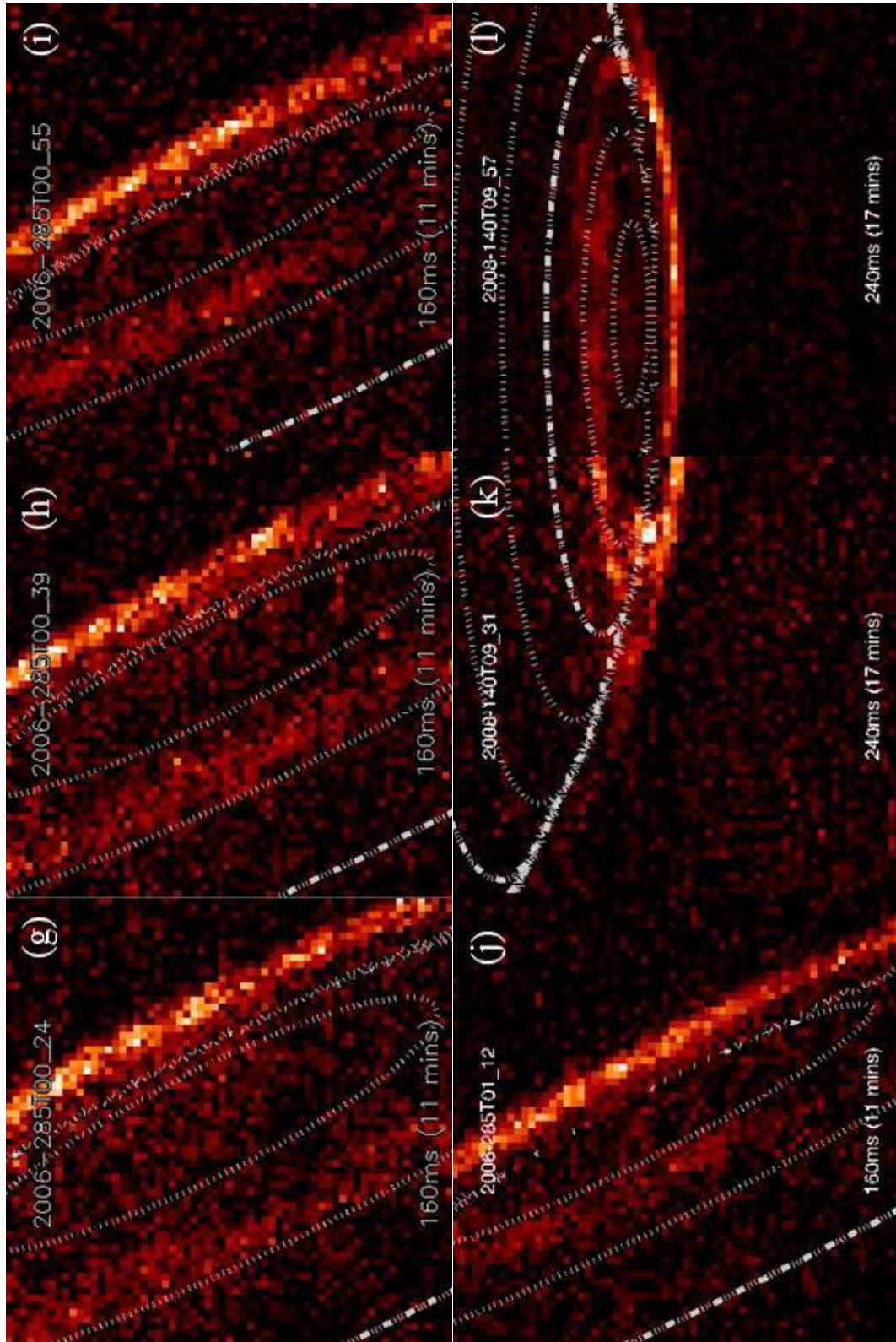
From a list of approximately 15,000 VIMS observations we used the filtering program described in Chapter 3 to narrow our data set to those candidates with likely auroral alignments (~250). The selection process used to find these observations consisted of a set of conditions that proximally matched the alignment of the data used in Stallard et al. (2012a), using a filter in conjunction with the NAIF spice navigational database to automatically sift through the observations yielding a list of suitable candidates. The conditions were as follows:

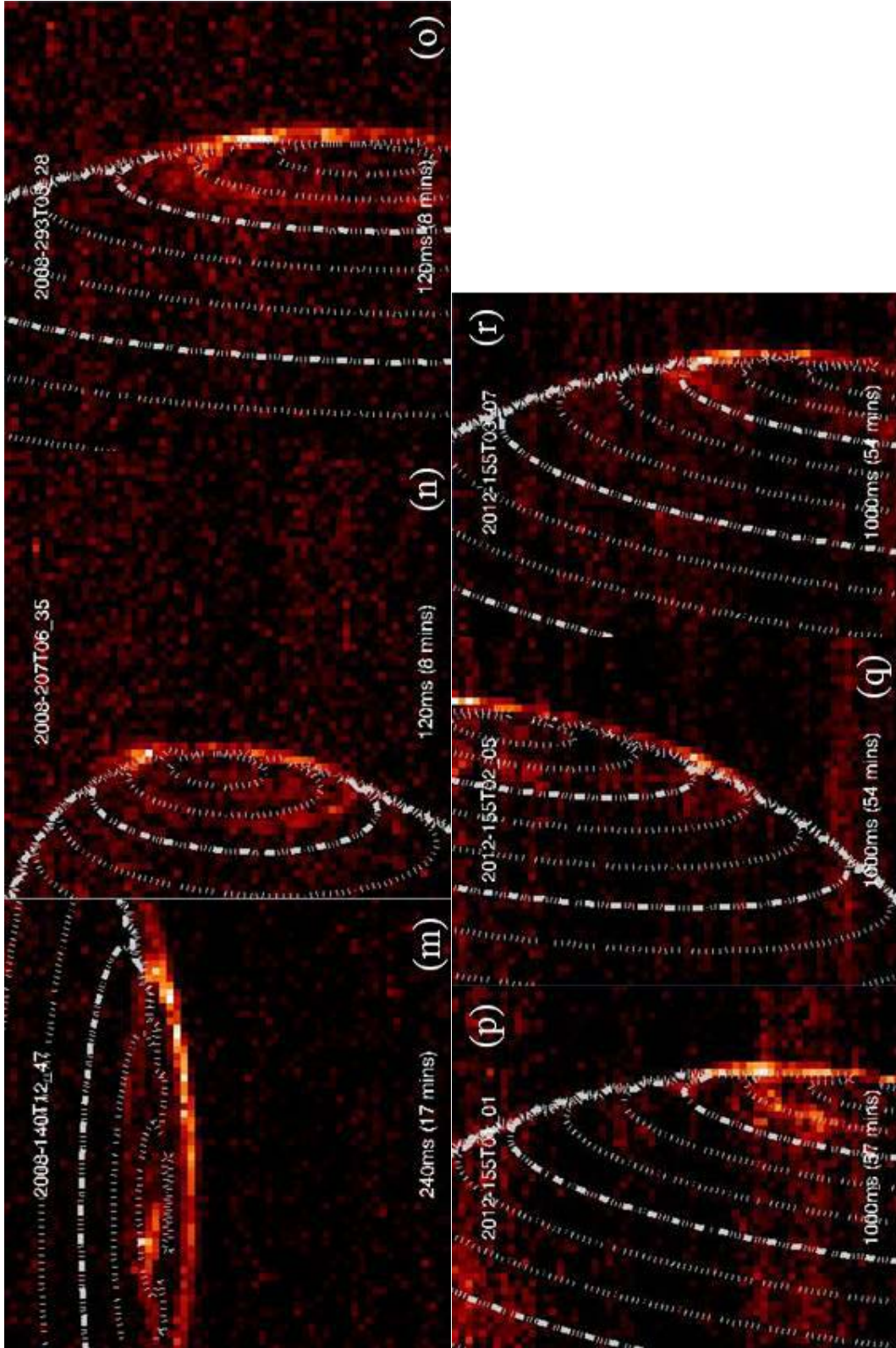
- The minimum integration time must be at least 75 milliseconds per pixel; this ensures that the image has a sufficiently large Signal to Noise (S/N) ratio.
- The minimum number of pixels in the x and y direction is 32; this was required to make certain that the observations included enough of the planet and the limb, should they be present, to observe the aurora at both these locations.
- The image must include the latitude range of 70° to 90° for either hemisphere and the limb latitude must be between 65° and 80°; without this limitation there would be no guarantee that an observation would contain the auroral regions and hence the auroral emission.
- The sub spacecraft angle must lie between 0° and 20°; in parallel with the rest of the conditions, this increases the probability that the auroral oval might be simultaneously observed on both the limb and the body of the planet in the same observation.

Further elimination was required in the consideration of the auroral morphology; in order for the techniques utilised in this research to function correctly it was necessary to collect only those images with an approximately circular aurora, as asymmetric aurorae would have a significantly variable range of latitudes on the main auroral oval, depending on which local time they were viewed at and thus could not be a reliable source of measurement of misalignment. Hence, only those observations that had a circular aurora where any deviations could be described as transpolar arcs were used (such features can be seen in Figure 4.3 (b) and (m) as the main oval is still contiguous however there is small extension of emission poleward of the main oval. A similar process was conducted with regard to analysis of the intensity profile across the body of Saturn. This process was completed by inspecting each observation individually for the necessary morphology as well as the integrity of the spectral bins as spatial filtering did in no way assure the prevention of poor quality observations as described in Chapter 3. The bins selected were centred on 3.39872, 3.51284, 3.64853, 4.18299 and 4.33280  $\mu\text{m}$ , with a bin width of  $\sim 0.016 \mu\text{m}$ . These bins were chosen for the fact that they contain strong

emission lines from  $H_3^+$  and weak emissions from other sources such as methane fluorescence and reflected sunlight. Despite a large number of observations meeting the alignment criterion, the majority of these files had to be rejected on the grounds that the uncertainties in their latitude and altitude measurements were too large. Hence, the data sample analysed consisted of twenty VIMS observations collected from the years 2006, 2008 and 2012. This is not sufficient to generate a broad scale statistical analysis of the auroral altitude; however it does offer a set of useful case studies.







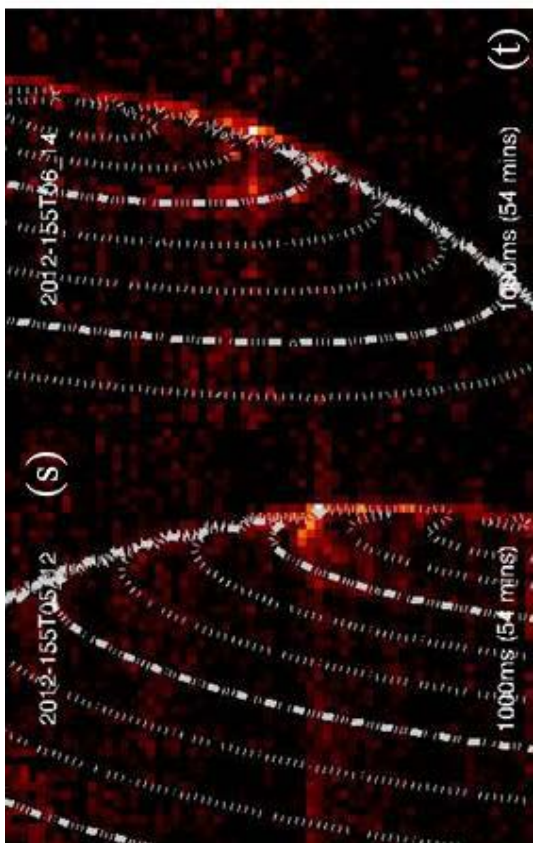
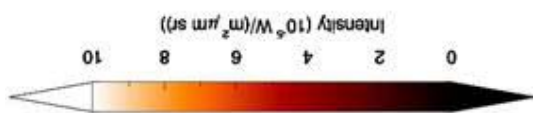


**Figure 4.3:** (shown on the previous page) The observations selected through the filtration process for having the correct viewing geometry and the presence of discernible auroral emissions, shown here, the observations have all undergone bin subtraction so as to remove reflected sunlight. Note that though (a) and (b) may appear to have spiral morphology, sampling the latitudinal profile in sub-sections of local time reveals that there is a faint arc of emission extending from the bright arc on the right around the planet to the rest of main. Whilst these two observations were borderline cases, they were accepted into the study thanks to this continuous profile. The observations (all of which are of the southern auroral oval) in this figure are as follows: (a) 2006-284T02\_26, (b) 2006-284T02\_38, (c) 2006-284T23\_53, (d) 2006-284T23\_59, (e) 2006-285T00\_05, (f) 2006-285T00\_18, (g) 2006-285T00\_24, (h) 2006-285T00\_39, (i) 2006-285T00\_55, (j) 2006-285T01\_12, (k) 2008-140T08\_31, (l) 2008-140T09\_57, (m) 2008-140T12\_47, (n) 2008-207T06\_35, (o) 2008-293T08\_28, (p) 2012-155T01\_04, (q) 2012-155T02\_05, (r) 2012-155T03\_07, (s) 2012-155T05\_12, (t) 2012-155T06\_14.

### Section 4.3 Calculating emission as a function of altitude

In order to get a good grasp of the effect that alignment of the aurora with the limb has on the altitudinal profile, it was necessary to measure the latitude of the auroral emission. The method for profiling the peak  $H_3^+$  emission altitude used by Stallard et al. (2012a) functioned by assigning the intensity of each selected limb pixel (a pixel with an altitude above 0km, and hence above the pressure surface reference frame) to the altitude at the centre of each pixel. This intensity was then added to the relevant altitudinal bin in the histogram, and with enough pixels it generated an accurate altitudinal emission profile. Whilst this method was highly effective for the study it was applied to (whereby 9 observations with high spatial resolution, 4 of which were combined to make one profile) it was found to be insufficient when used more widely as it provides a poor profile for both smaller numbers of pixels and observations with much lower spatial resolution. In other words, the histogram method was useful for an atypical observation sequence that was both unusually bright and had high resolution.

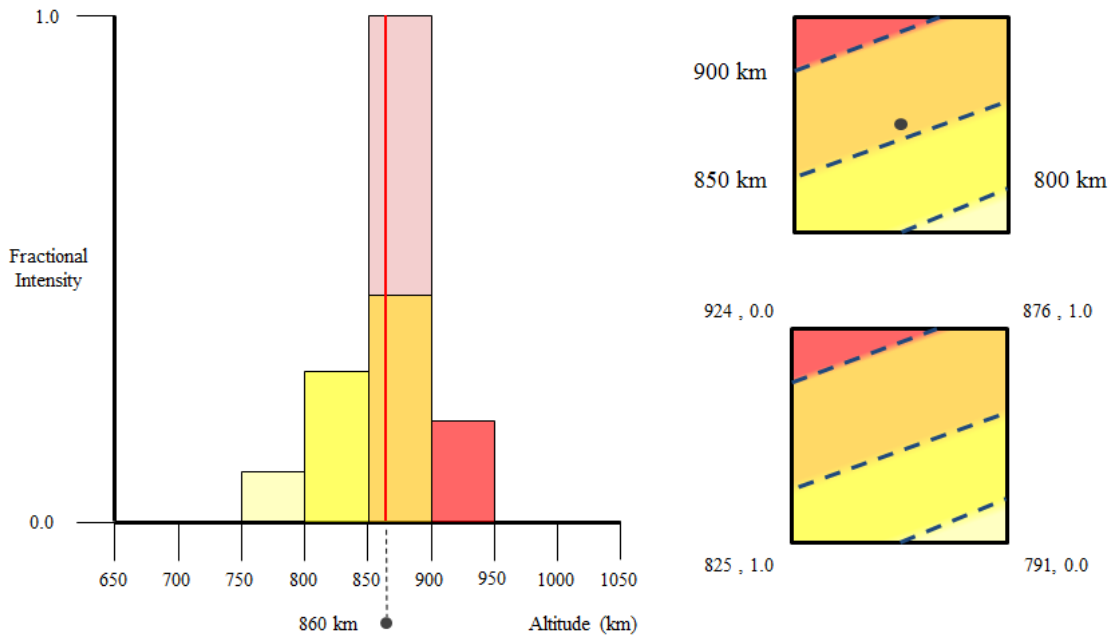


**Figure 4.4:** Each pixel (represented by the squares on the right) covers a range of altitudes (shown as a gradient of colours from light yellow to red, with each colour representing a bin that spans 50 km). In the original method from Stallard et al. (2012a), the intensity of the entire pixel is assigned to the altitude bin that contains the altitude of the central point of the pixel (marked in the upper square); all the emission is assigned to only one altitude bin (delineated by the solid red line), thus it assigns the emission covered by the entire pixel to only a portion of its area. The new method uses the altitude coordinates of the corners of the pixels with an artificial z coordinate (0 for the lowest and highest altitude and 1 for the remaining two corners), this is to enable the use of a polygon clipping procedure which calculates the altitudinal coverage as a fraction of 1.0 (hence the need for an artificial Z coordinate). This fractional area coverage allows the intensity of the pixel to be proportionately assigned to the actual altitudinal range that the pixel covers; as shown in the graph on the left.

Since the VIMS instrument does not have such “pin-point” resolution, the profiles for smaller groups of pixels are no longer reliable. To overcome this problem, a new method was devised that takes into account the full range of altitudes covered by each pixel. As shown in Figure 4.4, typically, this range of altitudes covered by a single pixel is much larger than the range of a single altitude bin for most observations. The program functions in an identical manner for both altitude and latitude, thus, in the following procedural description these two variables are directly interchangeable. As explained by Figure 4.4, for each pixel that is within the accepted range the program uses a polygon clipping procedure to calculate the “altitudinal area” of the

pixel from the values at the pixel's four corners. In this manner, the intensity is apportioned to the relevant altitudes in a manner that represents the real distribution covered by the pixel. This distribution is then projected onto a one dimensional array of altitudinal bins; the fractional intensities calculated by the polygon clipping procedure are assigned to the relevant altitudinal bin that covers their ranges. The fractional intensities are multiplied by the corresponding fractional area and added on top of each other in each altitude bin to produce the altitudinal emission profile (seen in black in Figure 4.5 (a)). This profile is subsequently divided by the total of the fractional area coverage in each bin (Figure 4.5 (b)) to produce an altitudinal emission profile (Figure 4.5 (c)) that is weighted towards pixels with either higher resolution or simply a better coverage of a particular altitudinal bin. In other words, the fractional intensities added to each altitudinal bin are weighted by the percentage of the pixels that represent, those that represent a greater percentage gain a greater weighting. The emission profile in Figure 4.5 (c) has been normalised to the maximum value in the profile to make it easier to compare with the old profile from the method of Stallard et al. (2012a), shown in red, which has also been normalised. When averaging the emission from multiple observations, we use take altitudinal profiles of each observation and multiply by the integration time of the observation they are sourced from, we then sum the profiles together and divide by the total integration time. This weights the final profile towards observations with a longer integration time and therefore a better S/N ratio.

So in essence, the new method is still a histogram process, but it takes into account the altitudinal coverage of each pixel rather than assuming a single value. As can be seen in Figure 4.5 (c), this new method also produces a significantly smoother plot when dealing with smaller numbers of pixels than the histogram method in Stallard et al. (2012a). So we see that when applied to smaller numbers of pixels the method of Stallard et al. (2012a) can lead to misleading profiles as shown in Figure 4.5 (c); the red profile has spikes of intensity where a pixel has been assigned to only one altitude, thus the profile is not continuous. The new method by contrast can cope with smaller pixel numbers and therefore is an ideal tool for the profiling of altitudinal and latitudinal profiling of the limb emission (whereby the number of pixels that are viable for study can often times be very small in number with each observation).

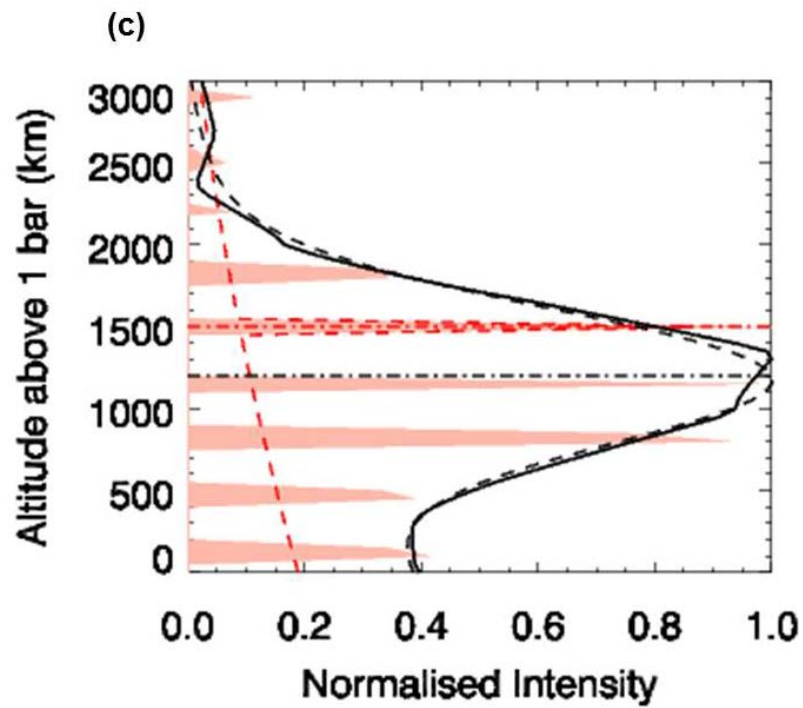
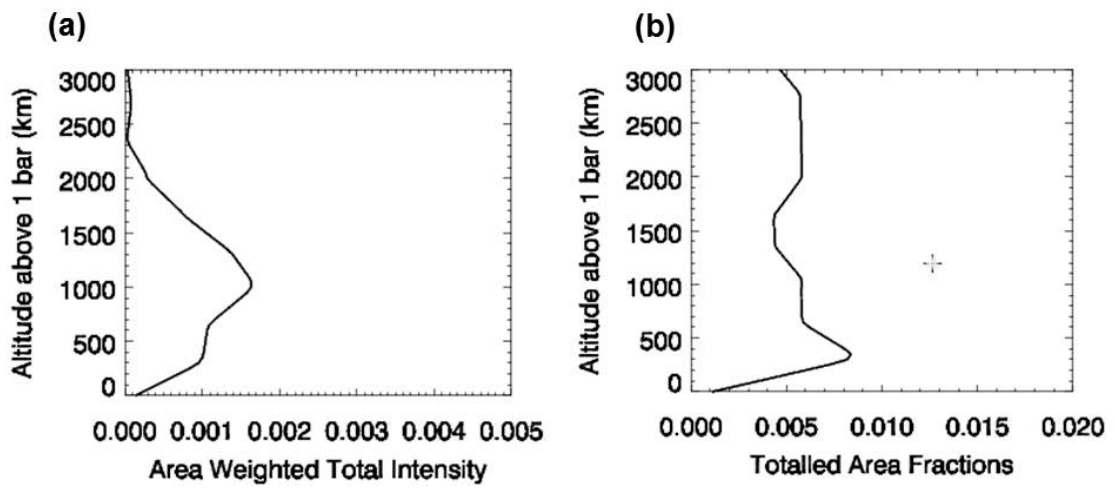


**Figure 4.5:** (shown on previous page) a series of different plots designed to further illustrate the difference between the old altitude profiling method from Stallard et al (2012a) and the new method developed for this thesis. First (a), is a plot of the intensities of each pixel multiplied the areas that pixels cover summed for each altitudinal spatial bin (hence “area weighted total intensities”). As each pixel is projected onto the altitude bins they add not only intensity by also their “fraction area coverage” to that bin, i.e. the percentage of the pixel which is covered the altitudinal range in a particular altitude bin. The total of these fractional areas for each altitudinal bin is shown in (b). Dividing the area weighted emission profile (a) by the total fractional area profile (b) we get the mean weighted intensity profile (c). This is the final output of the program and hence the new altitudinal emission profile (shown as the black solid line in c) which has a peak emission altitude measure by the Gaussian fit (dashed black line) of 1203 km as compared to the profile produced by the old method (red shaded region) where the Gaussian fit measures the peak emission altitude to be 1499 km above the 1 bar level.

#### Section 4.3.1 Sampling smaller regions

The new method allows us to sample a smaller number of pixels within individual observations without data gaps as the emission of the pixels is distributed over the full altitude range covered instead of one point, thereby enabling the analysis of intensity variations within a single image. Examples of this are shown in Figure 4.6 and 4.7; they contain altitude and latitude profiles that have been limited by limb latitude and local time, respectively. Note in particular for Figure 4.6, the histogram method from Stallard et al. (2012a) produces a highly discontinuous profile with a poor fit; this is due to the limited number of pixels contained in the selected limb latitude range, for which that histogram method was not designed. Hence, for studies that involve the examination of not only single observations but also specific sections within those observations, the new projection method has a strong advantage as a more appropriate profiling technique. The construction of this profiling program allowed for not only the study of profiles from individual observations, but also specifically selected areas within those observations (as shown in Figure 4.6 and 4.7).

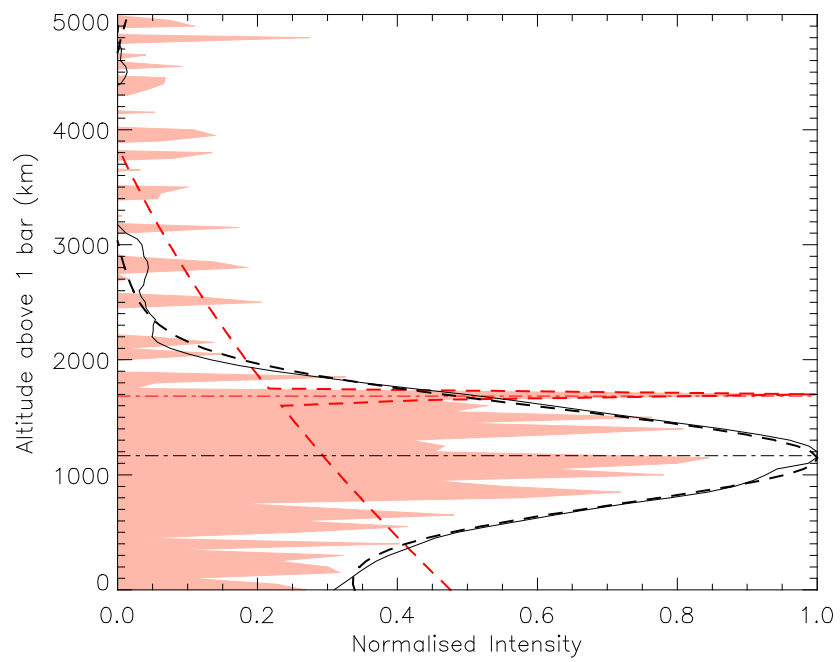
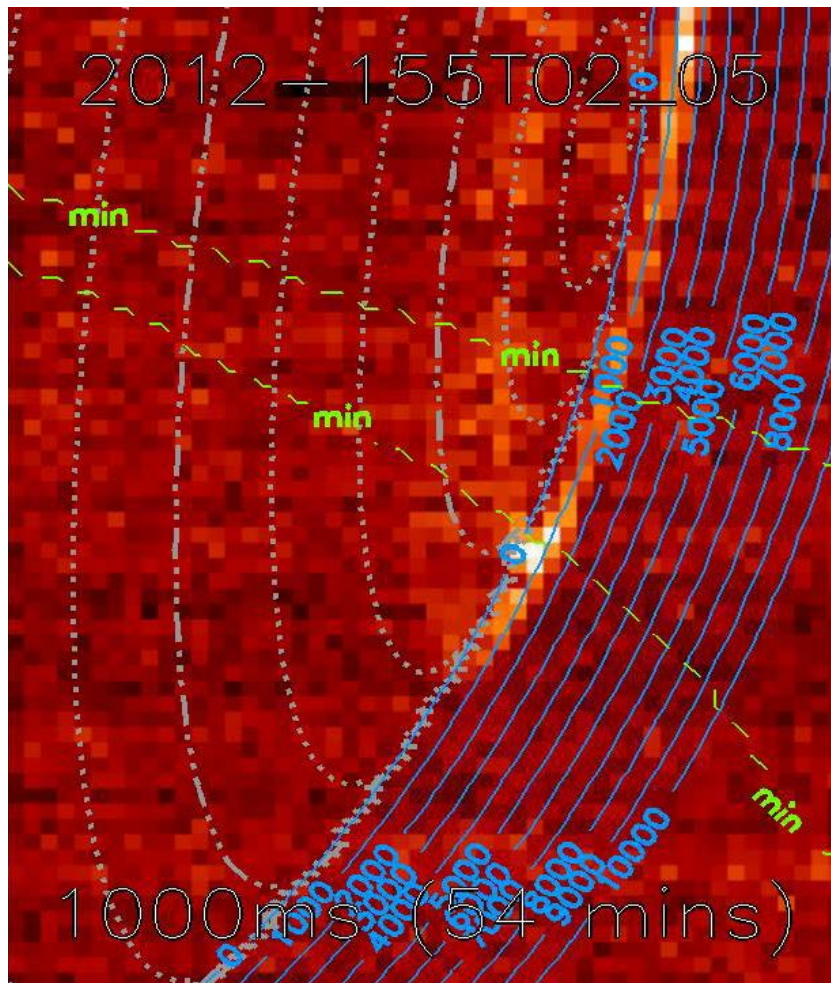


**Figure 4.6:** Shown on the left is an observation from 2012 day 155 at 02:05 UST, the blue solid lines mark lines of altitude, the dashed green lines mark the boundary of the selected area to be profiled; from -68 to -75 degrees of limb latitude. The grey dot-dash lines are the latitudinal contours of the 1 bar pressure surface. Shown at the bottom is the corresponding altitude profile for the region of the limb between the two green dashed lines in the left observation. As with Figure 4.5, the bottom plot shows the profile from the Stallard et al. (2012a) method in red (the data is shown as the red filled area, the Gaussian fit is shown by a dashed red line and the peak is marked by a horizontal red dot-dashed line) and the new method in black (the data is the solid black line and the Gaussian fit is the dashed black line, with the peak emission altitude marked by the black dot-dashed line).

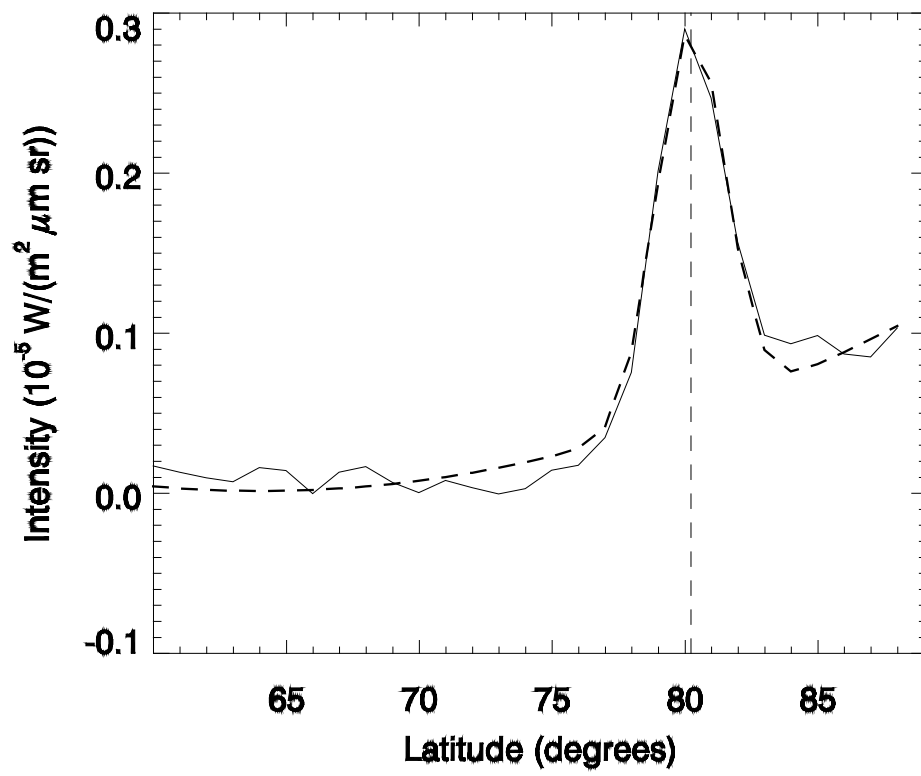
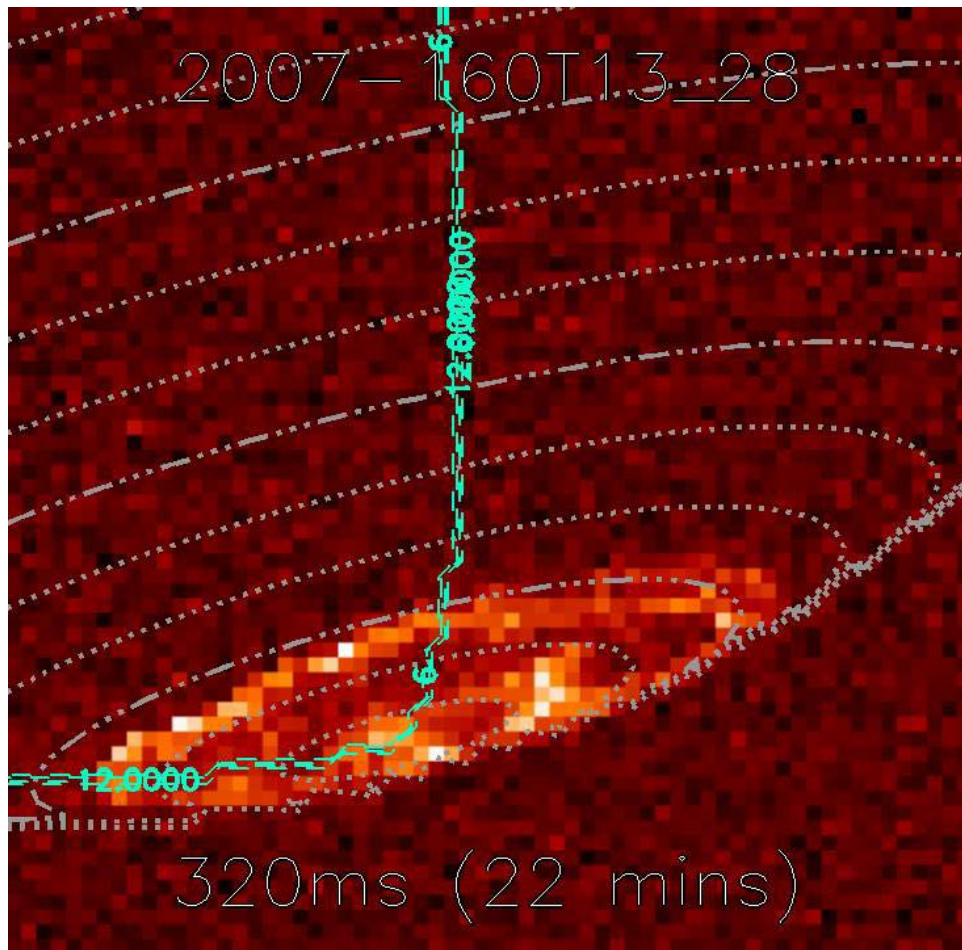


**Figure 4.7:** Shown on the previous page is an observation from day 160 of 2007 at 13:28 UST (top). The Blue dashed lines mark the limits of the selected region, their local times are 06:00 (the near vertical line) and 12:00 (the near horizontal line) Kronian Local time (corrected for solar azimuth). The dot-dashed lines are the contours of latitude. Shown at the bottom is the corresponding latitudinal emission profile for the region contained between the two blues lines. Note the significant intensity peak at around 80 degrees marking the main emission oval. The solid black line is the emission profile and the dashed line is a second order Gaussian fit, with the vertical dashed line being the position of the peak.

The ability to sample a smaller range of pixels and still derive an emission profile with sufficient accuracy lends a further advantage in that it allows for the measurement of variations in the peak emission altitude and latitude within each observation. By sampling across the body of the planet in steps of local time that are proportional to the local time coverage contained within the observation, we can sample the variance of the peak emission latitude across the body on the 1 bar pressure surface, which we have utilised to remove observations with significant variation in the latitude of the main auroral oval. Similarly, the variance in the peak emission altitude can be measured by sampling across smaller steps of the limb latitude (which, like the variability of local time, is divided into steps that are proportional to the limb latitude coverage). For observations where the auroral is spread across a large range of limb latitudes such as Figure 4.3 (j), the number of steps was on average 6-9, whereas those with smaller degrees of coverage such as Figure 4.3 (k) this number was closer to 3-5 steps. Although the new profiling technique affords the opportunity to sample smaller numbers of pixels within observations, there are still limits to what it can accomplish before the quality of the ensuing profiles degenerates beyond the realms of utility.

### Section 4.3.2 Measuring the alignment

The degree of misalignment was defined as the difference between the latitude of the aurorae on the body of the planet for a pressure surface projected 1000 km above the 1 bar level and the latitude of the limb at the 1 bar pressure surface beneath the limb auroral curtain. An overall profile of the entire visible body of the planet within the VIMS field of view (FOV) was measured to ascertain the average latitude of the main auroral oval on a 1 bar pressure surface, followed by profiles of individual sections generally of a scale of one to two hours of local time. The maximum and minimum altitudes and latitudes (from the individual segments) were used to produce the uncertainty ranges in the degree of misalignment seen in Figure 4.8 as well as a means of filtering observations that exceeded a particular uncertainty tolerance of  $\pm 4$  degrees latitude.

Measuring the variation of the peak emission latitude/altitude across the planet allows us to see the variation of the main auroral with latitude and local time, as well as the average of both properties across the entire range of the body/limb of the planet in the observation. It also helps identify if the natural variation in peak emission altitude is greater than the change caused by viewing geometry (alignment with the limb). Hence, for each file, the altitudinal emission profile was sampled above the 1 bar pressure surface, with a profile initially considered for the entire limb to obtain a general peak and further measurements of individual segments of limb altitude in order to observe the variation in peak emission altitude across the limb region. This provided a basis for uncertainty measurement and hence a constraint for eliminating files outside a range of error tolerance;  $\pm 250$  km for the peak emission altitude. Images were eliminated from the study if the variation of the measured peak emission latitudes exceeded a tolerance of  $\pm 4$  degrees or a variation of more than  $\pm 250$  km in the altitudinal profiles. The threshold of the latitudinal uncertainty and hence the uncertainty of the misalignment was chosen such that it encompassed the midnight offset from Badman et al. (2011) at least twice over to account for any sunward and anti-sunward shifts, the altitude uncertainty threshold range was chosen as to approximate the range of altitudes that have been measured in past studies and therefore allow for a consistent measurement of peak emission altitude whilst still leaving room for true altitudinal variance in the emission profiles. It should be noted that increasing the tolerance to levels any higher than this did not result in including more files being accepted until the tolerance was set to  $\pm 6$  degrees for the latitude. Observations with this difference between the body auroral latitude and the limb latitude tended to be taken at more equatorial sub spacecraft latitudes such that the peak emission altitude of the limb aurora is obscured by the limb (the peak emission of the limb aurora is below the planetary horizon in the observation). Hence, observations such as these only observe the emission above the peak

emission layer, therefore making the peak emission altitude impossible to measure. Taking each of the observations shown in Figure 4.3 we were able to analyse the effects of the alignment of the aurora with the limb on the observed peak emission altitude. The absolute magnitude of the differences in latitudes (planet body/limb) defined above as the degree of misalignment was used for the x axis in Figure 4.8, where the y axis is the peak emission altitude for each observation (with the associated variances explained above for uncertainty bars).

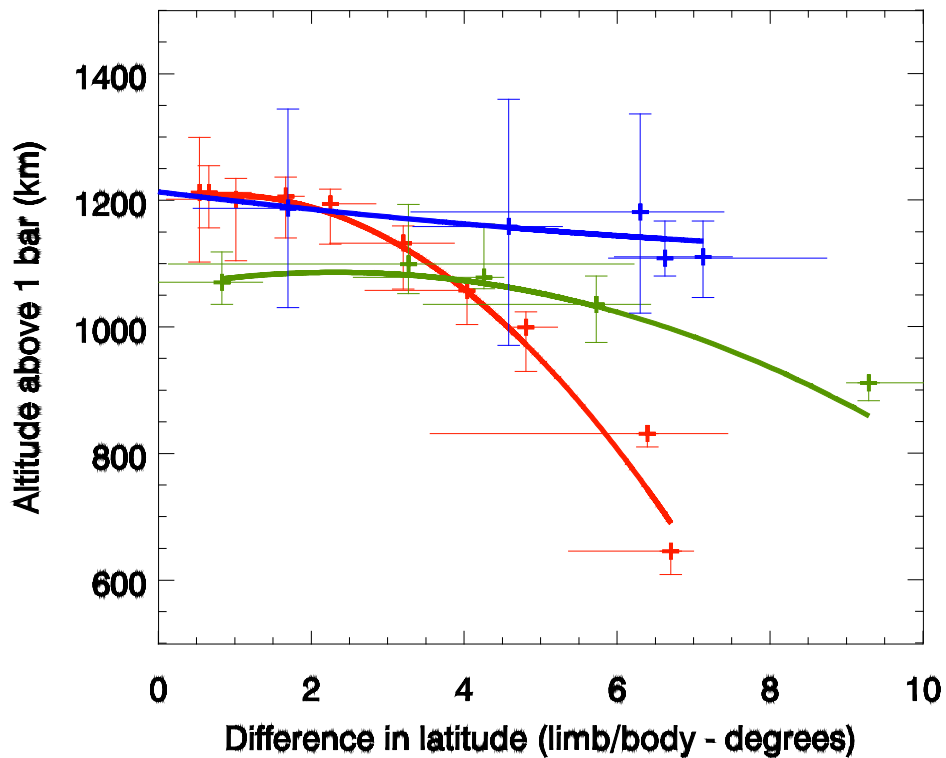


**Figure 4.8:** A scatter of plot of the peak emission altitude against the alignment of the aurora with the limb. The data set has been divided into years for this plot as this provides the greatest difference in the orbital geometry of the Cassini spacecraft which has changed significantly over the course of its mission. The year 2006 is shown in red, 2008 in green and 2012 in blue, as are their associated uncertainties and quadratic fits shown in the same relevant colours.

#### Section 4.4 Results

The correlation between the alignment of the auroral and the peak emission altitude can be seen in both Figures 4.8 and 4.9. For Figure 4.8, the data set has been split into the three different years from which the observations were taken. Note that the data from 2006 comes from only two consecutive days which may explain why this data set is the most strongly correlated since they all come from the same observing sequence; the viewing geometry is similar for all of them as they come from the same orbit of Cassini, however as the orbit progresses the alignment of aurora and limb changes producing the change in altitude. The other two years are less correlated insofar as they do not follow a parabolic curve quite as neatly as the 2006 observations; as may be surmised from Figure 4.3, these observations come from multiple points throughout their respective years and as such have varying degrees of alignment and spacecraft distance affecting their results. For each data set, a quadratic fitting procedure was used to establish what the peak emission altitude of the aurora would be if the curtain were perfectly aligned with the limb in an observation. This was done by taking the fit coefficients and substituting in a difference in latitude of zero degrees (the y axis intercept). For each of the three years we derive the following peak  $H_3^+$  emission altitudes in Table 4.1.

Year	Peak emission altitude
2006	$1197 \pm 52\text{km}$
2008	$1060 \pm 26\text{ km}$
2012	$1212 \pm 201\text{ km}$
All combined	$1215 \pm 119\text{ km}$
2006 – Stallard et al. (2012a)	$1155 \pm 25\text{ km}$

**Table 4.1:** The peak emission altitudes measured from the intercepts of the fits for each year in Figure 4.8 as well as all the data combined.

The uncertainties in these values of peak emission altitude (Table 4.1) came from applying the same quadratic fit to the sampled altitude plus and minus their respective altitudinal and latitudinal uncertainties. Putting all three data sets together produces a maximum altitude of  $1215 \pm 119\text{ km}$  when the degree of misalignment is zero; which compared to the peak emission altitude of Stallard et al (2012a)  $1155 \pm 25\text{ km}$  seems to be in agreement within their respective uncertainties. However, the uncertainty is significantly larger in this study than Stallard et al. (2012a) largely due to the data set from 2012. This is unsurprising, given that the space craft orientation for the 2012 data set is significantly different to 2006 and 2008 data sets; the sub

spacecraft latitudes for 2006 and 2008 was between 10 and 20 degrees, whereas for 2012 it ranged between 0 and 10 degrees. Furthermore, 2012 has the smallest number of observations with the largest uncertainties. If only the 2006 observations are considered, then the peak emission altitudes and associated uncertainties are much closer in magnitude to Stallard et al. (2012a). Despite peaking beyond the point of intercept (due to having fewer data points) the 2008 data set, shown in green in Figure 4.8, still has a discernible parabolic structure. Considering the uncertainty ranges shown on some of the observations, it is entirely possible that with more data, that the intercept of the fits and hence the aligned peak emission altitude could shift by a significant amount.

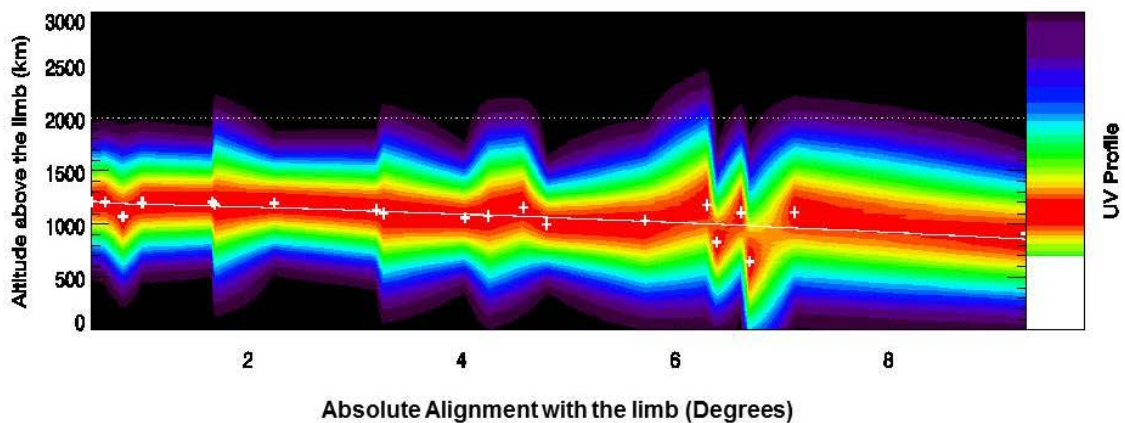


**Figure 4.9:** A scatter and contour plot of the altitude above the limb against the absolute alignment of each file. Each white cross marks the peak emission intensity altitude as shown in Figure 4.8; the contour plot is the Gaussian fit of the altitude intensity profile for each file. Red areas mark the maximum intensity and black areas mark the minimum intensity. The contours are set at intervals of 5 per cent of the maximum normalised intensity; i.e. black is 0%, dark purple is 5% increasing all the way to red which is 95% of the intensity. The UV profile from Gérard et al. (2009) is shown on the right for comparison. The solid white line marks the fit to the entire profile giving a peak altitude of 1215 km. The dotted white line marks the altitude of 2000 km above the limb to demonstrate that the IR profiles never extend any significant part of their signal above this altitude, which contrasts with the UV profile.

#### Section 4.4.1 The distribution of emission

Taking the results in Figure 4.8 a step further we can also look at how the distribution of emission with altitude changes with alignment. Each of the data points in Figure 4.8 corresponds to an altitudinal profile; these can be examined together as a series of contours as shown in Figure 4.9. As the degree of misalignment increases (the difference between the latitude of the aurora on the body of the planet and the latitude of the limb) the peak emission altitude decreases. The change of altitude with misalignment is gradual over the collective data set, but clearly consistent which indicates that much of the variation of the peak emission altitude is due to misalignment of the aurora and limb in an observation.

To analyse and compare the IR emission with the UV, Figure 4.9 shows the peak emission altitude as white crosses for each observation against the corresponding degree of misalignment. The coloured contours in the background show the normalised Gaussian fits (divided by the maximum intensity value so the profile is expressed as a fraction of 1) from each observation's overall altitudinal profile, with red marking the region of greatest intensity. On the right hand side is a contour plot of the UV profile (from the peak emission upwards) from Gérard et al. (2009) which has been similarly normalised.

From Figure 4.9 it can be seen that though there are some variations in the peak emission altitude from natural altitudinal fluctuations in the  $H_3^+$  emission, the majority of the change in altitude is dominated by the degree of misalignment of the aurora in the observation. When comparing the IR profiles to the UV profile (Gérard et al., 2009) in Figure 4.9, it becomes immediately apparent that though their peaks are well aligned, the long tail of emission above this altitude drops at a much faster rate in the IR profile than the UV. This effect can also be seen in Figure 4.10, the intensity is almost zero when it reaches an altitude of 2000 km, however the UV profile extends beyond this point as can be seen in Figure 4.9. However, there are points in the series of IR profiles where the peak emission altitudes almost seem to be aligned with those of the UV profile. This may suggest that despite the collocation of peak emission altitude (explained in Section 1.4 of Chapter 1), the emission processes for both the IR aurora and UV aurora are exhibiting different behaviours at higher altitudes; this will be discussed in Section 4.5.

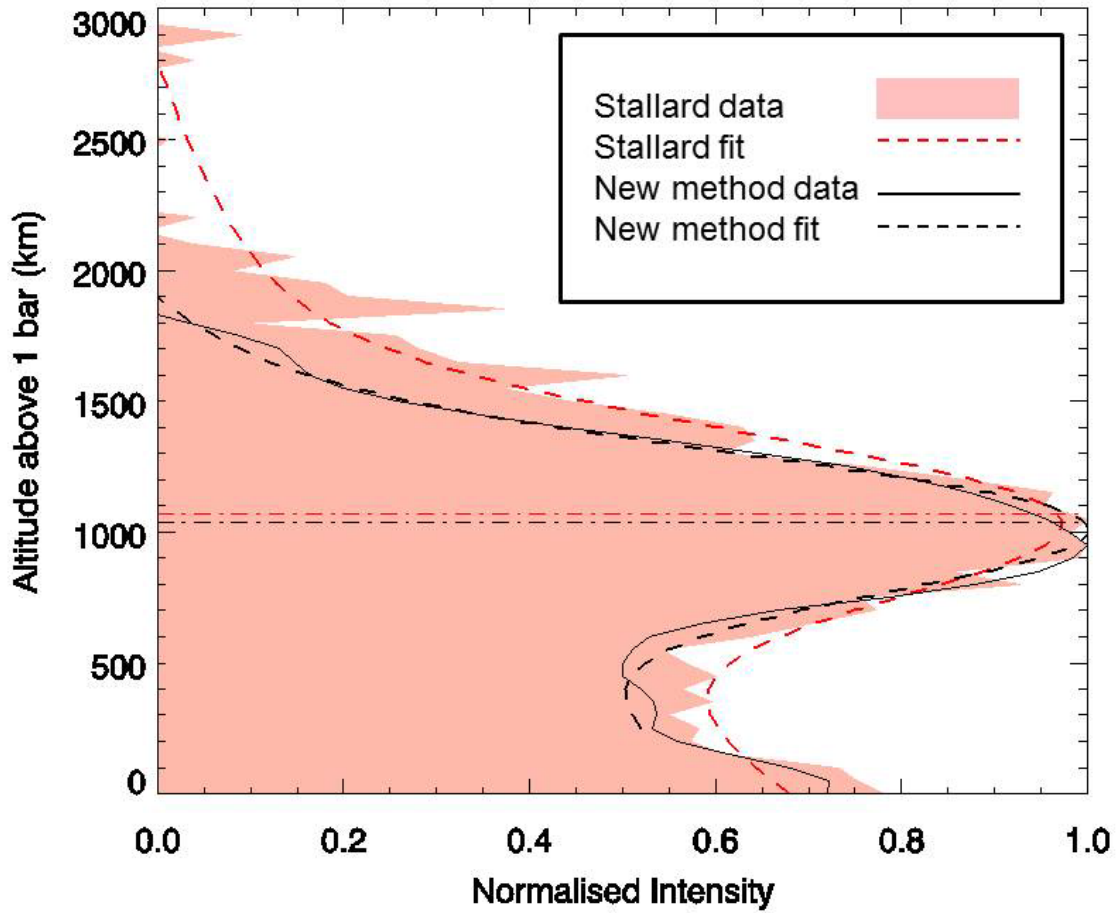


**Figure 4.10:** Normalised altitudinal profiles generated from the auroral emission above the 1 bar limb for observations with a degree of misalignment that is less than  $4^\circ$ : 2006-284T23:53, 2006-284T23:59, 2006-285T00:05, 2006-285T00:18, 2006-285T00:24, 2006-285T00:39, 2008-140T09:57, 2008-140T12:47 and 2012-155T06:14. From the collective auroral profiles we find that the method from Stallard et al. (2012) provides a peak emission altitude of 1069 km with a FWHM of 732 km (the resultant profile was too noisy to obtain a convergent fit in the uncertainty calculations) and our method provides a peak emission altitude of  $1031 \pm 1$  km with a FWHM of  $523 \pm 1$  km. Note the increase in intensity in the range of 0-200km, this is caused by auroral emissions that wrap around the limb onto the body of the planet (see Figure 4.3 observations k-t).

## Section 4.5 Discussion

Strong assurances in the validity of the technique developed for this study is provided in Figure 4.10 which provides a comparison with the technique of Stallard et al. (2012a). There are two profiles, one created from the technique used in Stallard et al. (2012a) shown as the red with a gaussian fit shown by the red dashed line. The other was made using the technique detailed in this Chapter, the data for which is shown by the black solid line and a gaussian fit by the black dashed line. The emission was selected from pixels between 0 and 5000 km above the limb. The emission profiles of each observation were multiplied by the integration time and added together with the others; this enabled a weighted mean profile to be constructed by dividing by the final profile by the total integration time at the end of the process. In Stallard et al. (2012a) they used multiple observations to generate an altitudinal profile and hence derive a peak emission altitude. The same process has been applied here, except the image selection was this time limited to observations with less than a 4 degree misalignment of the auroral oval with the limb. The altitudinal emission profiles from both the new method presented here and the old method of Stallard et al. (2012a) are presented for comparison in Figure 4.10. Encouragingly, both techniques yield very similar profiles, although the new method (shown in black) clearly shows a much improved S/N ratio. As the old technique places the intensity of an entire pixel in one altitudinal bin, it is more vulnerable to the noise and variability within the data (as it would not take many pixels of strong intensity to preferentially brighten one bin over others). It is thought that this effect is responsible for the spikes in the emission in the red profile. In contrast the black profile from the newer technique is less vulnerable to this problem as the emission is more widely distributed and hence yields a smoother profile with a more accurate peak emission altitude.

All of the peak emission altitudes in the individual quadratic fits for each year as well as the general fit all lie well within range of the measurements of Stallard et al. (2012a) for the IR emission as well as the 900-1300 km range of Gerard et al. (2009) of the UV emission. It is useful to consider the key result of the aligned peak emission altitude  $1215 \pm 119$  km as a ceiling value. The peak emission altitudes were derived from the intercept of the Gaussian fits with the y axis in Figure 4.8; hence they are estimated to be the altitude of the aurorae when there is no misalignment, thus the emission is thought to be directly above the limb. As such, it is thought the above altitude is the maximum possible with the provided error range. Note that we will be using this result for comparison in Chapter 5 when considering line of sight corrections.

The observed variations in altitude are dominated by the alignment of Cassini with the aurorae on the limb and body as shown in both Figure 4.8 and 4.9. This fits with what was initially

predicted. However, a further conclusion that has been drawn from the data is that the IR altitudinal emission profile consistently drops off in intensity much faster than the UV profile, declining to a small fraction of its peak intensity at 2000 km. This may suggest that the emission processes for both the IR aurora and UV aurora are exhibiting different behaviours with altitude.

One suggested explanation for this is that the scale heights of the diatomic hydrogen molecule and the monatomic hydrogen atom are significantly different such that at a high enough altitude, the mechanism which produces  $H_3^+$  (which is highly reliant on the presence of a molecular hydrogen population) may drop off with the decrease in density of  $H_2$ . The source of UV emission is  $H_2$  and H and thus the UV emission would experience no such drop off in intensity. As was discussed in Chapter 1, another explanation was posited by Miller et al. (2010). The emission of the IR aurorae is also dependent on the thermalisation of the  $H_3^+$  population with the surrounding atmosphere as well as non-local thermal equilibrium effects (Melin et al., 2005, Tao et al., 2011). As the altitude increases, the atmosphere becomes more rarefied and hence the collisions required for thermalisation become increasingly scarce. Thus, the necessary mechanism for the IR emission becomes depleted. In this respect, the  $H_3^+$  is still being produced at higher altitudes, but the low density and thus lack of energy transfer inhibits transitions and hence creates a steady drop off in the intensity profile.

Though the IR emission profile does seem to decrease at a significantly faster rate than the UV profile from Gerard et al. (2009) it is still true that the peak emission intensities for both spectral types are strongly collocated, which is in agreement with Melin et al. (2011) and Stallard et al. (2012a). It is subsequently possible therefore to infer that peak emission layer of both the UV and IR auroral ovals are produced by the same population of precipitating electrons and that the differences of the profiles outside of the peak emission region are the result of the differences in their respective production mechanisms. As explained in Chapter 1, the UV emission process requires less energy than the IR emission process; the IR process requires precipitating electrons with more than 13.6 eV of energy for the ionisation of  $H_2$  and the subsequent chemical reaction, the UV emission however, does not. Given that the depth to which electrons can precipitate depends on their energy (with higher energy electrons able to sustain multiple collisions as compared to low energy electrons) there will be an altitude at which the electrons are no longer sufficiently energetic to trigger the  $H_3^+$  reaction and therefore IR emission, however they are still able to stimulate UV emission. Thus the UV emission would be sustained at altitudes where the IR emission is not.

This study has examined sets of observations from three different years, and has shown that variations in the peak emission altitude of the aurora can be mainly put down to the line of sight

bias engendered by different viewing geometries. Whilst this evidence is very conclusive, it still comes from a relatively small data set with only 20 observations taken of only the southern aurora. As such, this study is limited in its ability to say that the relationship between the peak emission altitude and the degree of misalignment is the statistically average behaviour of the main auroral oval since we do not have a measure of how our observations relate to the average auroral conditions. Like Stallard et al. (2012a) we have selected a group of observations with bright auroral ovals in pursuit of consistent and accurate altitudinal profiles of  $\text{H}_3^+$  emission, but we do not know if the conditions in these observations are representative of most aurora at Saturn. Though this does not harm the validity of our results it does show the apparent need for a broad scale statistical study to examine the average properties of the aurora as a basis for comparison.

An assumption that has not been explicitly stated thus far is that the auroral curtain is a thin layer of constant thickness with altitude. Whilst this study has examined the effects of the alignment of the auroral curtain with the limb on the peak emission altitude, it has not considered the potential for the variation of thickness with altitude. A region where the curtain is thicker would appear brighter due to a greater number of  $\text{H}_3^+$  molecules emitting along the line of sight; even if the emission per molecule was weak in this thick region, the layer would still appear bright due to the sheer number of emissions. Though this study has shown the correlation between the variation of the peak emission altitude and the degree of aurora/limb alignment, it cannot differentiate between a peak emission layer that is caused by a high number density, a wider distribution of the auroral curtain or a high atmospheric temperature triggering bright emissions. To do this we would require altitudinal temperature and density measurements as well as a measure of the latitudinal breadth (the thickness) of the auroral curtain. Unfortunately, as this study has only used 20 observations, the data density and hence the S/N ratios is insufficient to measure these temperatures or densities. In Chapter 1 we described how these properties are intrinsically important to understanding the dynamics and behaviour of the atmosphere of Saturn as well as the interaction of the magnetosphere with the ionosphere. If this study had included more observations contributing to the altitudinal profile, it is possible that the S/N ratio of the result would be high enough that for the first time, the altitudinal structure of temperature and density could be measured for Saturn. Dealing with this issue and providing a broader statistical measurement of the properties of intensity, temperature and density is the subject of the Chapters 5 and 6 as described below.

The next two chapters will detail an extensive statistical study of the IR aurora that encompasses more than 500 observations from the VIMS instrument. One very pressing issue of such a study is that observations with perfect alignments are few and far between (as demonstrated by both the study detailed in this chapter and Stallard et al., 2012a) which means

that a broad scale statistical study would require many observations with widely varying degrees of alignment. Under such circumstances, it is very difficult to control the observer bias that is engendered from sampling such a diverse range of viewing geometries. One of the primary aims of this statistical study was to derive temperatures and densities from the combined spectra, due to the low spectral resolution of the VIMS instrument it was necessary obtain a data set large enough to provide the necessary spectral fidelity and high enough S/N ratio for such calculations. Hence, in this a study the alignment of the observations was not the strongest consideration as doing so would come at the cost of spatial fidelity of the resultant maps (the data set would be too narrow). Thus, the study of the effects of alignment in this chapter provided a much needed touchstone with regard to the altitudinal profile of intensity and hence broadened the scientific result that could be derived from the statistical study of Chapters 5 and 6.

## Chapter 5

### *Intensity mapping of the infrared aurorae*

#### 5.1 The aims of a statistical auroral study

One of the fundamental aims of this thesis, laid out in Chapter 1, is to utilise the large dataset of observations taken by the VIMS instrument in order to produce a statistical study of the long term average morphology of Saturn's infrared aurorae. Attaining a detailed analysis of such data would yield several products of scientific value. The first, discussed in this chapter, is to identify the average conditions of the aurorae; the average altitudes and latitudes of the peak emission in each hemisphere. This information would provide a "standard candle" for comparison with specific case studies, both past and future. Furthermore, it allows us to place variations of the auroral conditions into better context. For example, if the auroral oval presents what may be described as unusual morphology or if, say, the magnetosphere is compressed and the main auroral oval moves to higher latitudes, having a measurement of the average conditions would enable a comparison that showed how far removed from the average these conditions are. As the distribution of  $\text{H}_3^+$  emission with altitude is dependent on the energy of precipitating electrons and the altitudinal temperature profile of the atmosphere, a temporally statistical study of the altitudinal profiles of the  $\text{H}_3^+$  emission would by way of inference provide insight on these features when used as a constraint in models of the ionosphere. With sufficient spectral fidelity, these observations will allow us to produce measurements of temperatures and densities; as detailed in Chapter 6.

Previous studies of Saturn's aurorae have naturally focused on the column integrated properties of the aurora using remote observations of the aurora, mapped in latitude and local time. Those that utilised VIMS and UVIS observations, as well as radio occultations, have either mapped the aurora in latitude and local time, or focused on altitude in isolation. Most of these observations have been case studies which are limited in scope with regard to ascertaining the average structure of the aurorae, and even those that take a statistical approach (such as Badman et al., 2011) tend to use small subsets of bright auroral images. Hence, the process of projecting the limb emissions from a large number of observations confers two significant advantages over past studies. First is the opportunity to study the altitudinal structure of the aurorae at different locations on the planet, by mapping it in three dimensions. Second, we can measure the average brightness of the aurora across a large number of observations.

One of the simplest methods for generating a three dimensional image of an object is to observe it from multiple vantage points and then combine those images using their respective viewing geometries to create a three dimensional representation of said object. Unfortunately, this is not possible for Saturn as the only vantage point in orbit is the VIMS instrument. As such, one of the key obstacles of this study was how to generate a three dimensional projection of the observations with only this single view point, given that we could not make a complete measure of how much of the limb atmosphere is intersected by the VIMS line of sight. The reason this is important is that the limb latitudes and local time given by the NAIF SPICE database for each pixel are the latitudes and local times projected out from the limb of the planet; the limb of the planet does not simply consist of a thin slice of the atmosphere but rather a wedge consisting of a series of atmospheric layers.

In order to select a large number of observations from the VIMS database, we need to filter for the necessary viewing geometry. However, as was demonstrated in Chapter 3, there are some observations in the VIMS database that have corrupted data or artefacts within them that would skew a statistical study. The more extreme of these observations, which are generally the most common, are easy to filter out. There are a select few observations where these aberrations have intensities of a similar order of magnitude to the real emissions from the planet, and as such these observations are much harder to deal with, however, as they are small in number compared to the entirety of the data set, the influence of their fainter artefacts is dampened by the average of all the observations. This is discussed further in Section 5.2.

In Chapter 4, we concluded that changes in the apparent peak emission altitude of the aurora are dominated by line of sight bias. Hence, we assume that the peak emission altitude should be relatively constant and so we can correct for the line of sight bias as described in Section 5.5.1. This assumption enables us to use a larger number of observations which would not normally be considered in auroral studies due to their poor alignment thereby improve our statistical study by increasing the amount of data available.

Conducting a statistical study over a large timescale using VIMS data has another key vulnerability; the issue of the shift in the central wavelength of the spectral bins with time. As the central wavelength of each spectral bin shifts, the observed intensities of emission from  $H_3^+$  as well as other emission sources change within them. This is problematic as the process for extraction  $H_3^+$  emission from the observations using the bin subtraction technique is different for each year; the amount of light a spectral bin registers will change for each of these emission lines, which means that the numerical factor derived from matching the intensities of two bins near the equator will also change with time. Given the reliance of temperature calculations on

spectral fidelity, this issue serves to add a complexity to the study which must be handled with some delicacy. This issue is dealt with in Section 5.3.2.

## 5.2 The observations

Whilst the observations with the necessary spacecraft viewing geometry for the study of Chapter 4 are few and far between, there are a very large number of observations that have been taken from more equatorial sub-spacecraft latitudes (between 15° north and south) that contain the auroral oval on the limb of the planet. As with the study in Chapter 4, we needed to filter the database of VIMS observations for these viewing geometries. In selecting observations we filtered the database using a set of criterion. The first is that the integration time had to be greater than 100 ms to ensure a reasonable signal to noise ratio (S/N). Second, the observations had to be free of ‘corruption’ which can occur either due to a fault in the detector dark current subtraction or stray light entering the instrument (these would produce obviously unrealistic values for the intensity and so were rejected). Each observation must contain the planetary body and limb with altitudes above the limb reaching higher than 5000 km (this was required for background noise subtraction). Lastly, the viewing geometry of the Cassini spacecraft was limited to observations that were taken from spacecraft distances of less than 27 Rs; it was determined the spatial resolution of individual pixels became too large beyond this point such that one pixel could cover a range of altitudes greater than 500 km and is therefore unable to provide a detailed altitudinal structure of the  $\text{H}_3^+$  emission. As can be seen in Figure 5.1, the spacecraft distances extend out to a maximum of 40 Saturn radii (Rs) and an approximate minimum of 5 Rs. A further point of interest in Figure 5.1 is that many of the observations are grouped together in the same orbits as they are from the same observing sequences; this signifies that the data is clustered both spatially and temporally. This does however raise the issue of line of sight bias, as the emission would be assigned to a lower altitude than is realistic. To resolve this, we employ an onion shell model similar to that of Lystrup et al. (2008) to the combined emissions from the entire data set, the implementation of which is described in Section 5.5.1.

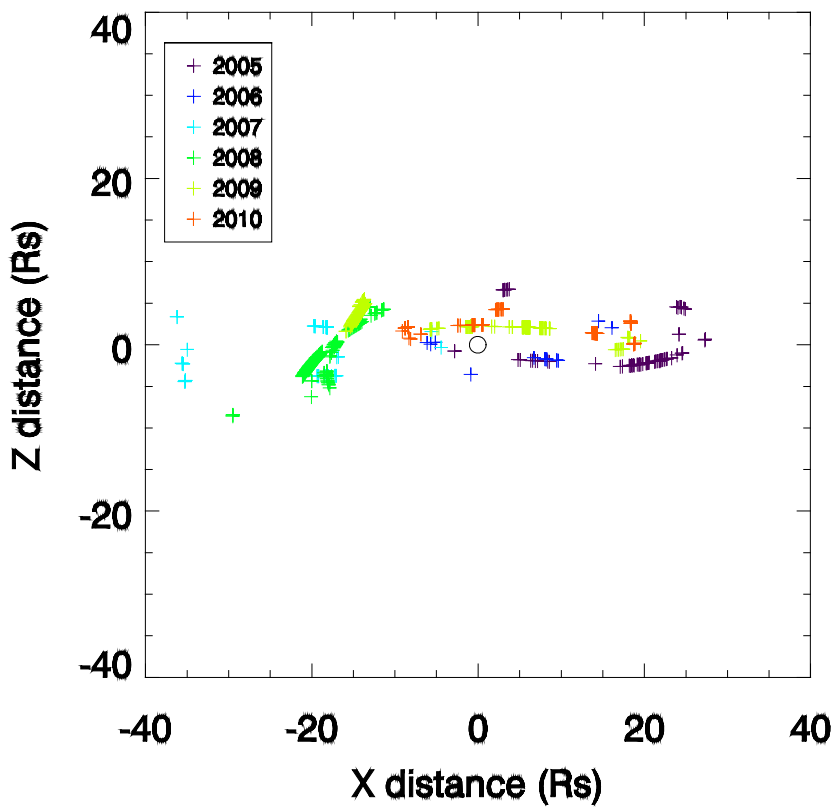
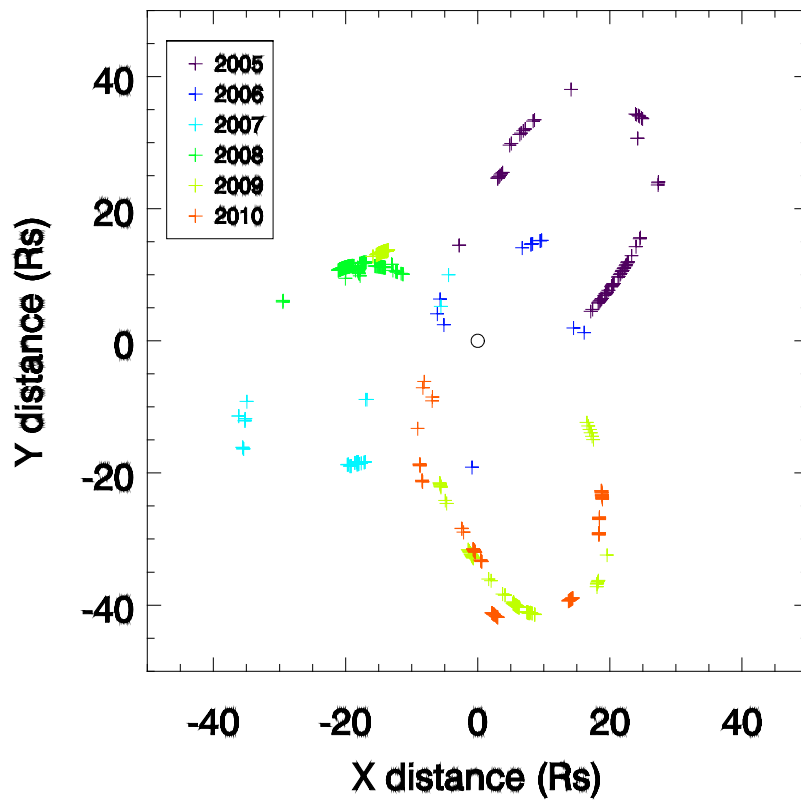


**Figure 5.1:** (shown on previous page) Two plots displaying the spacecraft locations of all the observations considered for this study. The first plot (top) shows of the spacecraft location in the x-y plane (where y is in planet-sun axis and x is the perpendicular axis lying in the equatorial planet) for the observations used in this study and the second plot (bottom) is the same plot but in the x-z plane (where z is normal to the ecliptic plane, perpendicular to both x and y). This also displays the local time coverage contained within this study.

Year	Number of Files
2005	79
2006	11
2007	42
2008	159
2009	150
2010	70

**Table 5.1:** a table showing the distribution of observations across the different years included in this study. The number of observations used is dependent on orbital geometries; 2008 and 2009 had a larger number of observations from equatorial sub-spacecraft latitudes.

### 5.3 The projection process

In Chapter 4 we have seen the workings of a projection process which creates altitudinal profiles of intensity using a poly-clipping procedure. This process was the starting point for the projection technique described in this section. This new projection process was not only applied to altitude, but also to the dimensions of latitude and local time. As described in Section 5.1, the major challenges of this study arise from creating a series of programs that automate the process of eliminating a wide range of issues with the VIMS observations without the need for a user to investigate each and every observation individually. In this Section we explain how this new technique functions, starting with automatically isolating the emission above the limb (pixels above the 1 bar level) and examining the coverage of each pixel in this region using a polygon clipping procedure as described in Section 5.3.1 and 5.3.1.1 respectively. Once this emission is isolated the second step, described in Section 5.2, was to examine the intensity of the emission in these pixels to ensure that no artefacts (pixels with emission corrupted by instrument error) are included in the study; the intensity of such pixels would threaten to overpower the other pixels that contribute to the same region of the three dimensional grid. This step also incorporates the subtraction of background noise from the sampled emission. As was demonstrated in Chapter 4, there is very little  $H_3^+$  emission beyond 2000 km above the 1 bar level, as such, sampling the region above this altitude confers the opportunity to sample the background noise level of the observation and subsequently remove it. The range of 3000 km of altitude was deemed sufficient to sample an average of the background noise level which we remove from all pixels in order to improve the S/N ratio. These two procedures (artefact elimination and background subtraction) are explained in Section 5.3.2. Once all of the pixels in the selected region have been filtered and the background noise has been removed, the last step is to combine their emissions in a grid of latitudes, altitudes and local times to produce the maps of intensity; this is described in Section 5.3.3.

#### 5.3.1 Selecting the pixels

The procedure that generated the profile shown in Chapter 4 utilised a polygon clipping procedure, whereby we calculate the full altitudinal coverage of each pixel. This was done using the NAIF SPICE data to obtain the altitudes at the corner of each pixel which were subsequently projected onto a grid of altitudes; the elements that were encompassed by the area were then assigned the appropriate proportion of the pixel's emission, thereby splitting each pixel across a range of altitudes representative of the pixel's dimensions. Figure 5.2 demonstrates that this principle was similarly applied to the dimensions of both limb latitude and limb longitude in order to create a three dimensional projection of the emission above the

limb from 511 observations. Each observation was projected onto a grid of altitude, latitude and longitude for a range of spectral bins, thereby creating three dimensional maps for the spectral bins listed in Section 5.3.4. With each observation, the measured intensities were multiplied by the observation integration time and added to the maps, once all the observations were collated together, each element of the maps were divided by their total integration time to produce a mean weighted average intensity with a preference for longer integration times. This ensured the reduction of the S/N ratio.

The initial set up required creating two grids for the projection, the first was a grid of latitudes and local times (180 by 390 elements; encompassing  $-90^{\circ}$  to  $90^{\circ}$  in bins of  $1^{\circ}$  latitude and  $0^{\circ}$  to  $360^{\circ}$  in bins of  $1^{\circ}$  local time with the extra 30 included as some observations cross the midday boundary – noon was defined as  $0^{\circ}$ ) and the second was a grid of latitudes and altitudes (180 by 500 elements; the latitude is binned in the same manner as the first grid and the each altitude bin covers a range of 10km leading to a coverage of 0-5000km above the 1 bar level).

The first step for projecting an observation was to isolate the emission above the limb. This is done using the limb longitude, local time and altitude parts of the back plane at the 1 bar level. The values of these variables at the corner of each pixel are used in much the same way as the projection technique in Chapter 4 uses altitude, the difference being that because each grid is a map of two variables, we can use the values at the corner each pixel as co-ordinates. These co-ordinates are fed to the polygon clipping procedure which ascertains which elements of the relevant grid are encompassed by the pixel that is currently being processed.

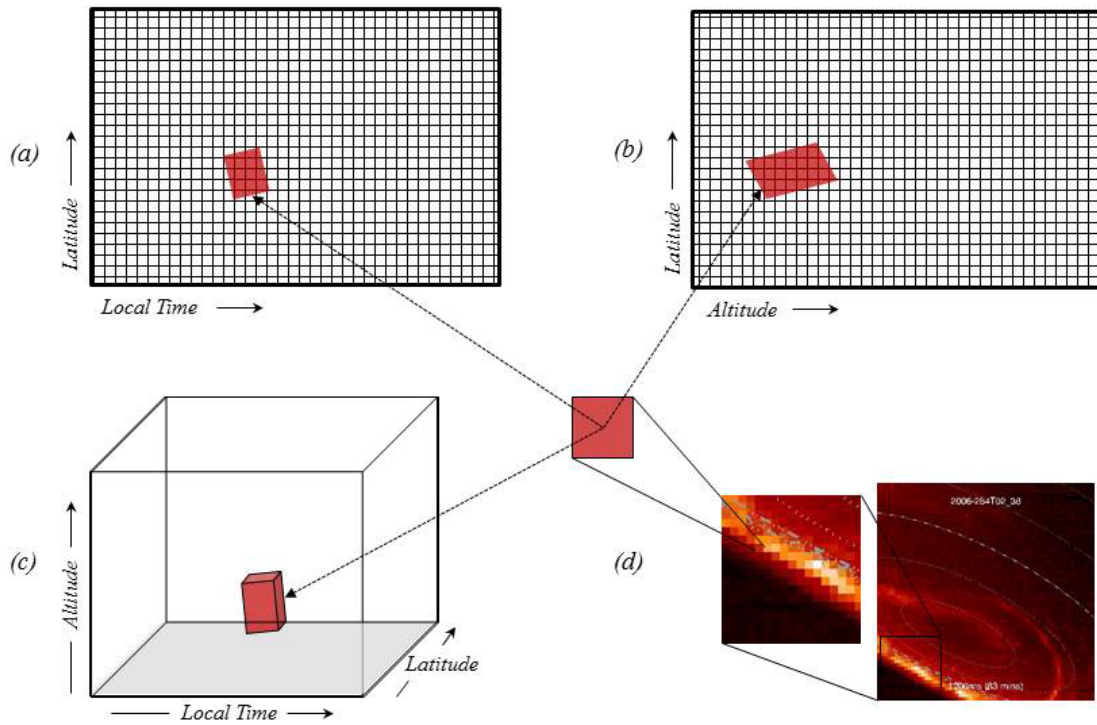


**Figure 5.2:** A pixel is selected from the observations (d), each corner of this pixel has an associated latitude, local time and altitude which serve as co-ordinates for the spatial grids of latitude/local-time (a) and latitude/altitude (b). For each element that the pixel touches, the program calculates what fraction of the pixel's total area on that grid is coincident with the area represented by the element. The number derived from this fraction is used to determine how much of the pixel's emission is assigned to that particular element in the grid. Cross correlating these grids produces a distributed volume of emission shown in the cube (c). Each element of this grid encompassed the dimensional range of  $1^\circ$  of latitude by  $1^\circ$  of longitude by 10 km of altitude.

#### 5.3.1.1 The polygon clipping procedure 3D

The projection process essentially functions by calculating what fraction of the pixel an element in a grid covers, then assigning to that element the fractional portion of the pixel's emission. To do this, the procedure follows the steps outlined below:

1. A polygon clipping procedure analyses how much of a pixel's designated area is coincident with the spatial bins in the grid.
2. The ratio of this area for each spatial bin or element is compared to the total area of the pixel; this factor dictates what fraction of the emission from the pixel will be assigned to that particular spatial bin.
3. Once these fractions are calculated for both grids for an individual pixel, the grids are then cross correlated by multiplying their elements together to produce a three dimensional cube where the only region with values will be the volume covered by the pixel.
4. This volume of fractions is then multiplied by the intensity of emission of the pixel's different spectral bins and the integration time of the pixel which is cumulatively added to a three dimensional array (of latitude, local time and altitude) with every other pixel that has been projected.
5. The integration time is included so that when all pixels in all observations have been included, each element of the three dimensional array can be divided by the total integration time of all the pixels that have contributed to it and in doing so produce a mean intensity for that element, weighted by integration time. The pixels with longer integration times have better S/N ratios and as such provide better spectral fidelity; hence we weighted the mean in favour of longer integration times.
6. The "wrap around" in local time at the midnight boundary is accounted for by adding the extra 30 bins (360-390°) are added to the first 30 bins (0-30°) for both the intensity-integration time grid and the integration time grid. Without this, the program would get confused and assign a pixel to all local times in the latitudinal band covered by the pixel thereby miscalculating the area.

### 5.3.1.2 The spreading functions

In the early development of this technique it was swiftly realised that the process could not initially account for the depth of the atmosphere along the line of sight (due to only having one vantage point). In other words, the limb latitude and longitude variables do not account for the variation of latitude or longitude along the instrumental line of sight. To give an example, if an observation of the equator were taken at an equatorial sub spacecraft latitude, then the longitude on the limb would only vary along the line of sight. However, since the limb longitude is measured by projecting the 1 bar level outwards, a pixel on the equator would measure the true variation of latitude but only register a single longitude for all of its corners. Conversely, if we were to consider the same point on the equator but from a polar sub spacecraft latitude, it would be the latitude that would be constant and the longitude that varied (as latitude would change along the line of sight whereas the longitude would change perpendicular to the line of sight). To counter this, we examined the variation of the body latitude and longitude (local time) close to the limb in representative observations we determined the average variation of these properties across the limb. For longitude it was found that the variation was a minimum of 5 degrees at the equator increasing to a maximum of approximately 10 degrees at the poles (where the meridians converge) for an observation at equatorial sub-spacecraft latitudes (which is typical of the observations used in this study). Similarly, the latitude the variation was found to be on average 5 degrees at the poles when viewed from equatorial sub-spacecraft latitudes. Hence, we required a “spreading function” that would give these values of latitude and longitude at their respective locations and viewing geometries; i.e. they needed to be a function of both sub-spacecraft latitude and limb latitude with yield the numbers above for latitude and longitude under the same observing conditions. Given the near spherical geometry of the planet, it was assumed that the change of these variables could be approximated as trigonometric functions. The longitudinal spreading included a sin term of the limb latitude as this would be a maximum at the poles and minimum at the equator. It also included a cos term of the sub spacecraft latitude as equatorial observations would have the greatest variation of longitude along the line of sight and so must be a maxima and a minima when the sub spacecraft latitude is polar. In order to ensure that this would provide a value of  $10^\circ$  for a polar limb latitude and  $5^\circ$  for an equatorial limb latitude as viewed from the equator, both the sin and cos terms were multiplied by a factor of 5 as can be seen in equation 5.1 (the variables of which are defined in Figure 5.3).

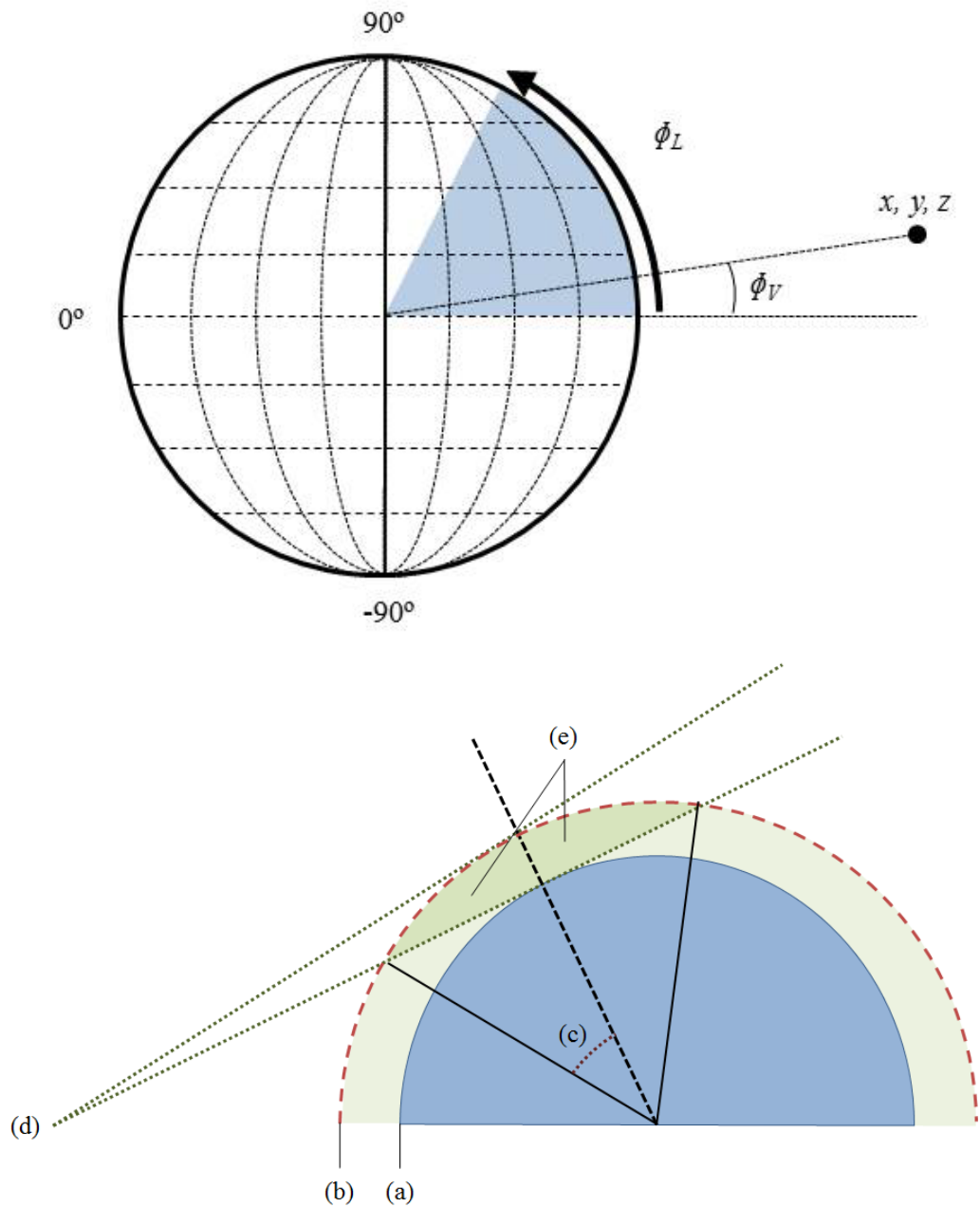


**Figure 5.3:** (shown on previous page) (top) The spreading of the longitudes was determined by two variables, the latitude of the pixel on the limb  $\phi_L$  and the sub spacecraft latitude of Cassini at the time of observation  $\phi_V$ , as seen from point  $(x, y, z)$ . The horizontal dashed lines are meridians of latitude, with zero degrees at the equator,  $90^\circ$  at the northern pole and  $-90^\circ$  at the southern. (bottom) a diagram to demonstrate that the line of sight of the VIMS instrument at point (d) is actually viewing a broad volume of atmosphere (e) between the 1 bar level at altitude (a) and the edge of the atmosphere at altitude (b). As a result, the emissions which would normally be assigned just to the dotted black line need to be spread out by angle (c) to encompass the volume of atmosphere contained by the line of sight of the instrument observing at point (d).

$$\textit{Longitude spread} = \textit{Abs}(5 \sin \phi_L) + \textit{Abs}(5 \cos \phi_V). \quad (5.1)$$

A similar process was instigated for latitude values which were calculated using equation 5.2 (variables are defined in Figure 5.3);

$$\textit{Latitude spread} = \textit{Abs}(5 \sin \phi_V), \quad (5.2)$$

though this was only a function of the sub-spacecraft latitude as unlike the meridians of longitude, the lines of latitude do not converge and hence the only way for the variation of the latitude along the instrumental line of sight to change is by altering the sub spacecraft latitude. Once this spreading had been calculated for each pixel, the process then examined the maximum and minimum latitudes and longitudes, assessing it in comparison with the calculated spread and selecting the larger of the two. Without this spreading calculation, there would have been many instances of the projection process assigning all of the emission observed in a pixel to unrealistically thin slices of atmosphere.



### 5.3.2 Pixel filtration and noise reduction

In order to prevent the introduction of anomalous data it was further necessary to introduce a limit on the intensity of any given pixel before putting it through the projection process. This limit was set to  $\pm 5.0 \times 10^{-5} \text{ W m}^{-2} \mu\text{m}^{-1} \text{ sr}^{-1}$  as this was found to be reasonably in excess of the maximum possible auroral intensity, but smaller than most anomalies born from file corruption or faulty instrumental detector dark current subtraction processes. As described in Chapter 2, every VIMS observation has a built in subtraction process designed to remove the effects of residual currents and internal IR emissions of the VIMS instrument from the observation. To improve the S/N further, it was necessary to remove noise from the observations by means of a second background subtraction. This entailed examining the emission at altitudes greater than 4000km above the 1bar level (a region which should ostensibly be devoid of  $\text{H}_3^+$  emission) and subsequently using the mean of the emission above this level as a measure of the noise to be subtracted from the emission in the regions below. This was performed on a row by row basis as this is the most common orientation of such striations, as shown in Figure 5.4; by subtracting the background noise from rows that contain these artefacts, the entire row of pixels would often be eliminated as their newly subtracted emissions would be pushed outside of the range of  $\pm 5.0 \times 10^{-5} \text{ W m}^{-2} \mu\text{m}^{-1} \text{ sr}^{-1}$  thereby removing many of the artefacts from our maps of intensity.

A final condition that had to be adhered to was the elimination of any pixels that encroached on the rings. The rings of Saturn have quite a strong reflectance and as such can outshine other emissions, whilst it is true that the rings can only seriously affect the more equatorial latitudes, it was still necessary to remove them as they would typically be a great deal brighter than even the aurora. Using the SPICE algorithm it was possible to run a geometrical calculation to show which pixels had coverage of the rings. This number, where present, served as a flag which could be used to automatically remove the relevant pixels.

### 5.3.3 Projection into three dimensions – making the maps

After measuring each eligible pixel's spatial coverage as well as removing the background noise, we were then able to combine them all into maps. As described in Section 5.3.1.1, we create two maps, one of pixel intensity multiple by integration and another simply of integration time. It is at this point in the process that we were able to divide the former by the latter to produce maps of weight mean intensity. When viewed as a latitude-altitude map summed over all longitudes, as is shown in Figure 5.5, it can be seen that this technique has ample coverage and data density for producing intensity maps of the same dimensions (insofar as it covers a wide range of latitudes and altitudes). It is notable that there are a few data gaps in Figure 5.6

(represented by the white regions) between the equatorial latitudes of  $15^\circ$  south and north as well as polar latitudes greater than  $80^\circ$  north. The absence of data at the equatorial latitudes was caused by an automated filter set to reject any pixels that covered the rings in order to remove any light that might be reflected from them. The polar latitudes in the north lack coverage due to the alignment of the observations in this region not covering that area.

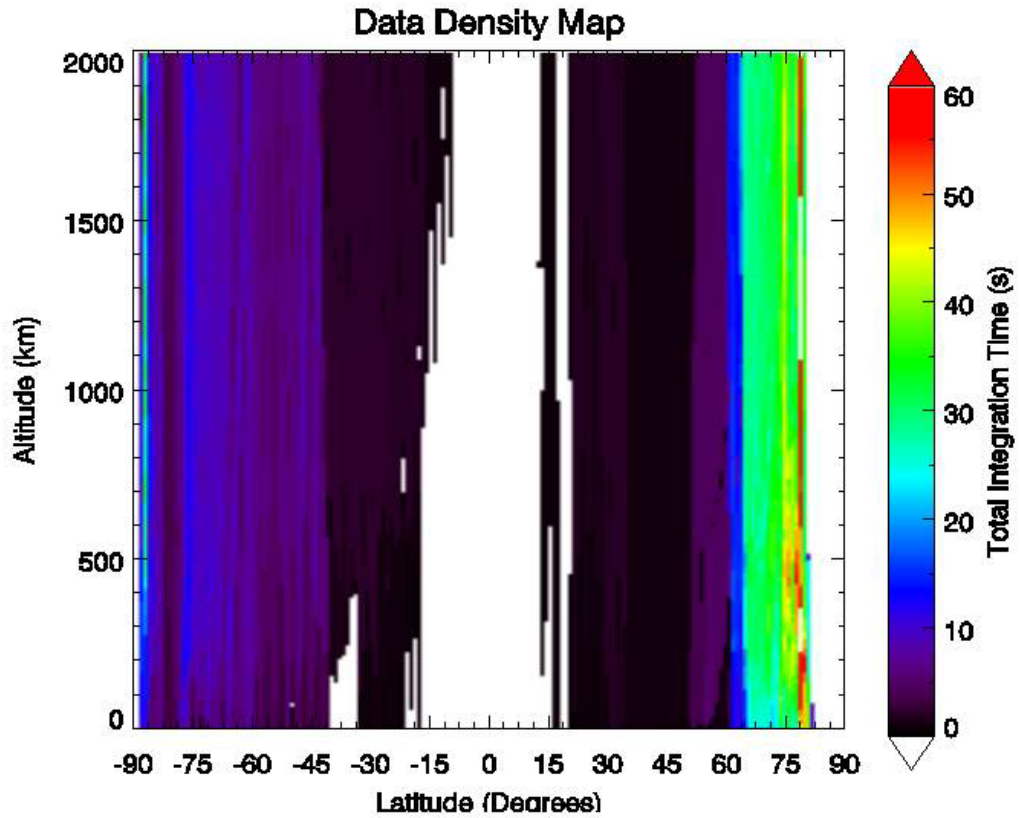


**Figure 5.5:** A latitude-altitude map of data density measured in terms of the total integration time of all contributing observations summed over all longitudes. It very clearly demonstrates the difference in data density between the northern and southern auroral regions as well as the absence of data at lower latitudes (due to the ring elimination process).

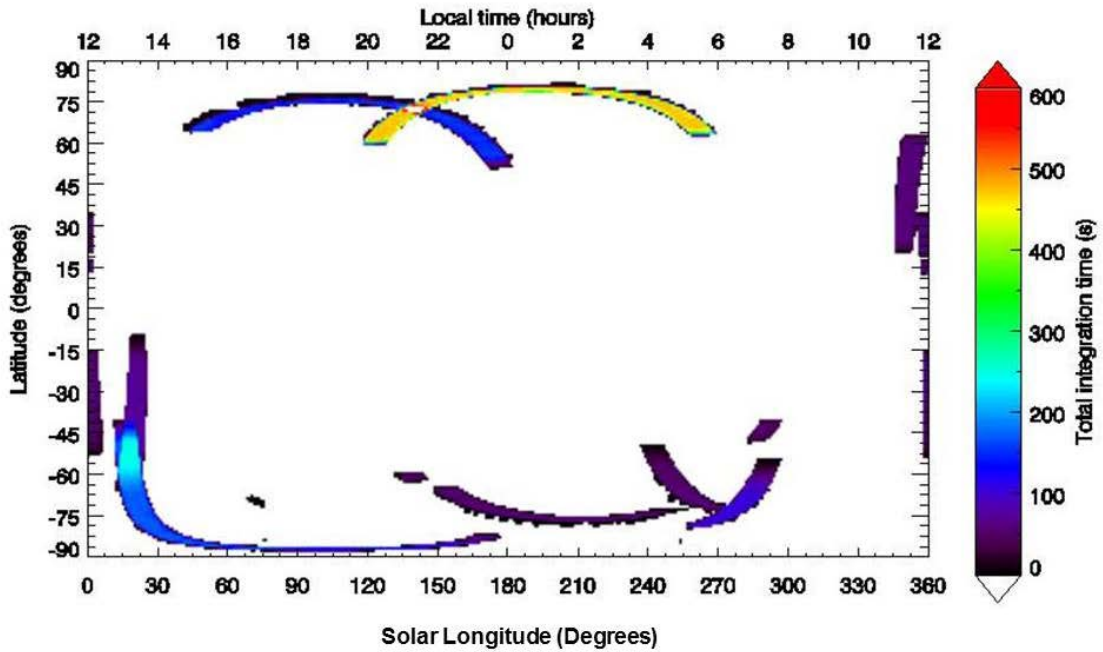


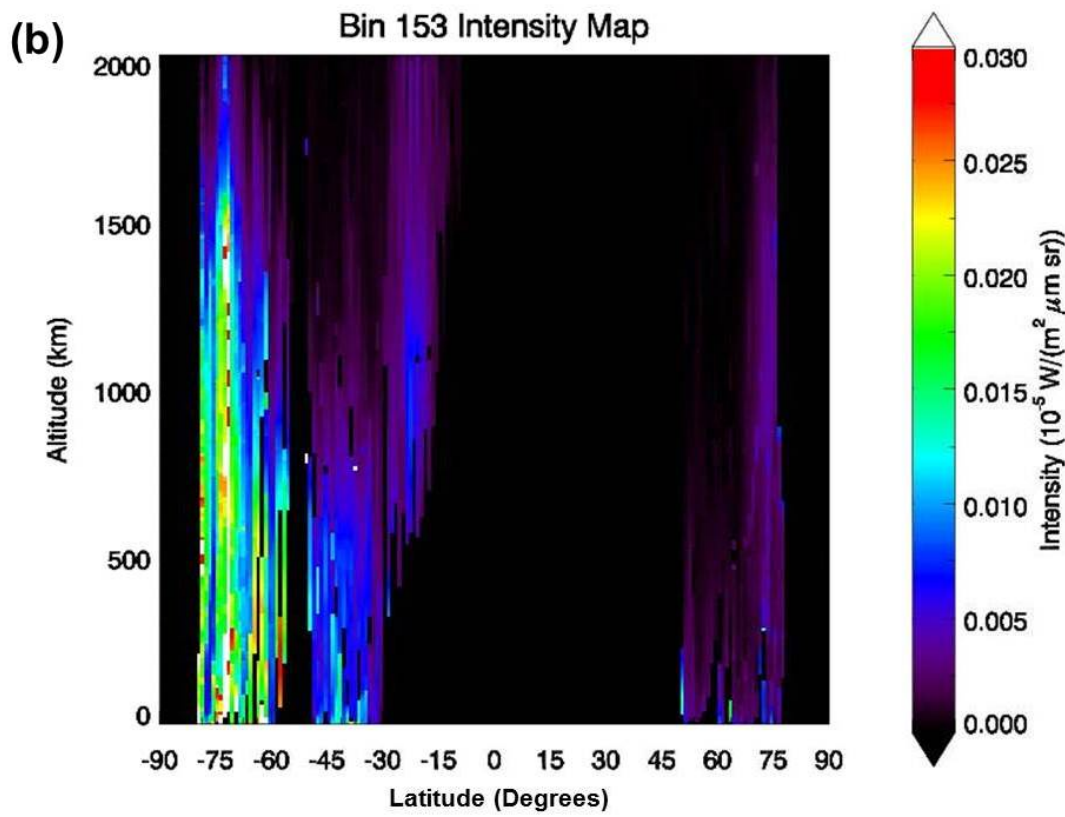
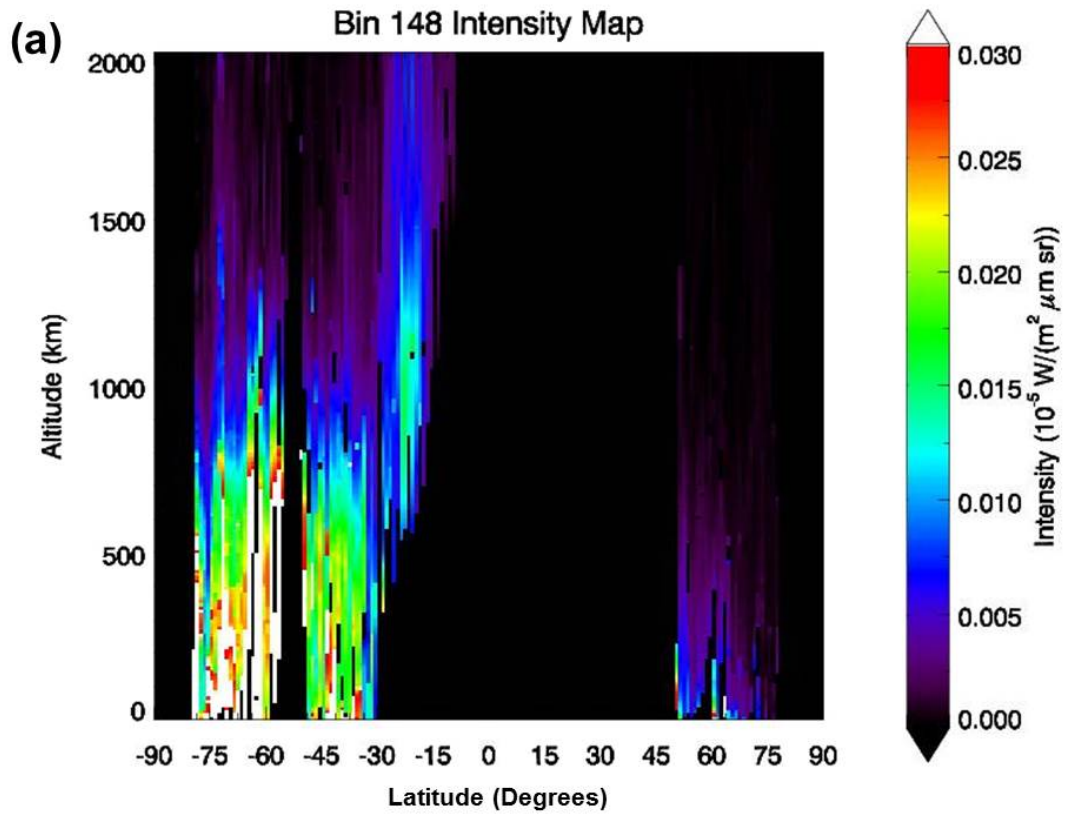
**Figure 5.6:** A latitude-longitude (local time) map in local time coordinates (summed over an altitude range of 0-5000km) of total integration time. This map shows the coverage for the entire data set used in this study. Note that midnight is in the centre (180 degrees/0 hrs) and noon is at either end of the plot (0/360 degrees/12 hrs).

Although the original intention was to create a three dimensional projection of emission over latitude, altitude and longitude, it was decided that the emission should be averaged over all longitudes and presented as two dimensional maps of only latitude and altitude (as is seen in Figure 5.8) given the local time coverage of Figure 5.6. Unfortunately, even with a data set containing 511 observations, the local time coverage is still too poor to derive any meaningful information with respect to this dimension. The reason behind the lack of local time coverage is that many of the observations are clustered in specific orbits from the same observing sequences, when Cassini was in the range of orbital geometries required for this study as can be seen in Figure 5.1. This does mean that this study will contain some local time bias as when examining Figure 5.6 in detail, we see that the northern aurora has been sampled between local times of 14:00 and 06:00 with the greatest data density lying between 20:00 and 06:00, whereas the southern aurora has been sampled between 12:00 and 06:00, with the greatest data density lying between 13:00 and 00:00. Unfortunately there is a complete lack of data in the auroral regions for the regions between 06:00, through noon to 14:00 in the north, and between 08:00 and 12:00 in the south; hence, it was not possible to feasibly derive any useful information regarding longitudinal variations. As such, all maps shown in subsequent sections of this Chapter are latitude-altitude maps with intensities which have been averaged using a mean weighting of integration time; each bin of longitude contained an intensity multiplied by an

integration time, thus the mean weighting was done by summing these values across all longitudes and then dividing by the total integration time for the same latitudinal meridian. As explained in Chapter 1, the auroral oval is dynamic both in its location (expansion and contraction) and its shape (varying between an oval and a spiral). Due to the loss of the dimension of local time we will not be able to examine the global morphology of the oval; we can however examine the average latitudinal and altitudinal location of the aurora.

#### 5.3.4 Extraction of the $H_3^+$ emission

Once the maps were complete it was also necessary to perform a subtraction of any emission that was not identifiably  $H_3^+$  emission so that the aurorae could be isolated. This was done by pairing each “auroral” bin (defined as such by the fact that they contain strong  $H_3^+$  emission lines) with a “background” bin that has similar broad scale spectral characteristics, but containing no bright auroral emission lines. The auroral bins used were 153, 160, 165, 168, 183, 184, 185, 186, 187, 189, 200 and 209 whereas the background bins used were 148, 162, 167, 170, 190, 202 and 207 (refer to Table 3.1 for wavelength ranges of these bins). In order to ensure that the extraneous light from reflected sunlight and thermal emissions from deep within the planet were sufficiently eliminated, each background bin was scaled by an empirically determined factor and then subtracted from its paired auroral bin. These subtraction factors were determined by considering the emission at equatorial latitudes in the completed maps for each year, where  $H_3^+$  emission would be too weak for VIMS to detect, to isolate the background sources (such as reflected sunlight and thermal emissions from other species). The background bin emission was then scaled to the auroral bin as necessary until these background emissions matched in both bins. This process had to be done on a year by year basis in order to account for the wavelength shift observed within VIMS data over this period (as explained in Section 2.1). To enable this year by year subtraction of the spectral bins, the data set was split into individual years with each set being projected separately; this was significantly more time efficient than performing the subtraction on each observation. The success of this process can be observed in Figure 5.7, where the bin pair auroral 153 and background 148 are shown, along with bin 153 after the subtraction has been performed for the combined years that have contributed to it. Strikingly, it can be seen that the aurora has been successfully isolated here in the south (the sample of observations used here did not have much coverage of the northern hemisphere which is why there is no auroral emission present in this region).



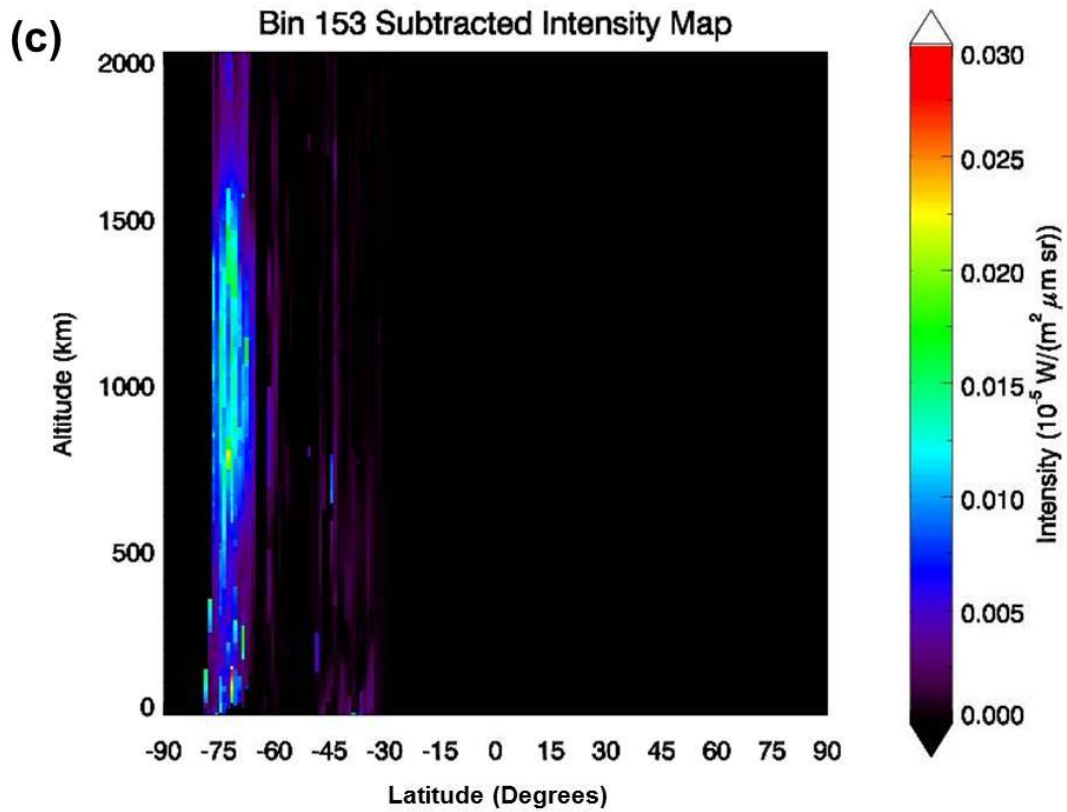


**Figure 5.7:** To demonstrate the efficacy of the subtraction process, shown here are three plots latitude-altitude maps of intensity for bin 148 (a), bin 153 (b) and bin 153 after the subtraction process (c). This is a result of combining a sample of observations from all years which were used to test the projection process' functionality without consuming too much in the way of virtual memory or time. What is immediately apparent about these maps is the contrast between bin 153 before the subtraction (b) and after (c), in that the main emission source that has been left behind is the  $H_3^+$  aurorae.

## 5.4 Results

### 5.4.1 The intensity map

After the  $H_3^+$  emission had been extracted for each auroral spectral bin, the auroral bins were all combined to form the first product of the projection process, shown in Figure 5.8, a latitude-altitude map of  $H_3^+$  emission. To improve the S/N ratio the intensities were averaged into larger spatial bins; for the auroral regions (60-90° in each hemisphere) where the  $H_3^+$  emission is brighter the spatial bins were of dimensions 2° latitude by 50 km altitude, for the non-auroral regions (-60° to 60°) where the  $H_3^+$  emission is weak the spatial bins were of dimensions 30° latitude by 500 km altitude. The scaled sizes of these new spatial bins were chosen so as to balance the S/N ratio with spatial resolution; the larger numbers of spatial bins averaged together produce a better S/N ratio at the cost of spatial resolution.

Figure 5.8 shows both the northern and southern auroral ovals as regions of stronger intensity between latitudes of 70 and 80 degrees in each respective hemisphere, with the southern aurora being brighter than the north. There is extensive emission present at altitudes between 0 and 500 km above the 1 bar level, which has been attributed to the fact that none of the data input for this map has been corrected for the line of sight bias examined in Chapter 4. This is resolved in Section 5.5.1 which details the application of the onion skin model.

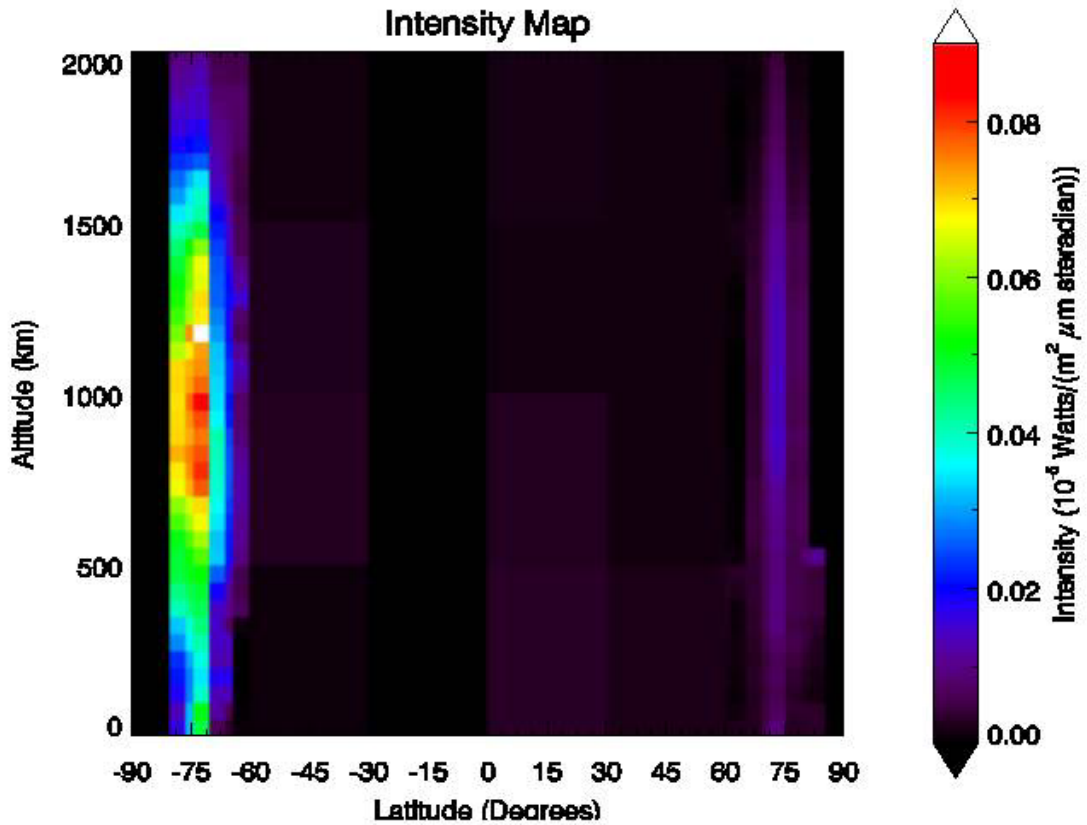


**Figure 5.8:** A latitude-altitude map of the intensity of  $H_3^+$  emission summed over the bins 153, 160, 165, 168, 183, 184, 185, 186, 187, 189, 200 and 209 as observed by Cassini VIMS after background subtraction as described in Section 2.4 for the files listed in Table 1. The intensities have been differentially binned according to latitude. At latitudes greater than 60 degrees the bins are 2 degrees of latitude by 50 km of altitude, the remaining equatorial latitudes are binned into 30 degrees of latitude and 500 km of altitude. This re-binning was performed by taking the average of the original bins over the spatial range of the new ones. The auroral regions have smaller bins as the S/N in these regions is far higher than the lower latitudes. Even with such large spatial bins, VIMS was unable to detect any discernible  $H_3^+$  emission beyond the background noise level.

The non-auroral regions (especially from 30° to 60°) show some  $H_3^+$  emission, though it is weak and variable in intensity. This variability is unsurprising considering the distribution of the data density in this region as shown in Figure 5.5 and 5.6; the auroral regions show high data density whereas the non-auroral have a much lower density. The  $H_3^+$  emissions in this region already very weak, and hence the S/N ratio is much lower as compared to the auroral regions. Given the distribution of the number of observations in each year shown in Table 5.1, it is apparent there are far more observations before the 11<sup>th</sup> August 2009 equinox than after. As a result, the observations of the northern aurorae have on average had much less exposure to solar irradiance in comparison to the southern aurorae, leading to a reduced ionisation rate from Solar EUV photons as well as a lower temperature from the smaller solar heat input. As noted in O'Donoghue et al. (2014) there is also a north-south asymmetry in the magnetic field strength and hence an asymmetry in the heating rate, with the southern auroral region being an average 56 K hotter than the northern auroral region. O'Donoghue et al. (2014) also found that field asymmetry means the particle precipitation and hence ionisation in the south is distributed over a greater latitudinal range than the north. Thus, not only would there be a smaller  $H_3^+$  population in the north (over the latitude range 70-80° that we sampled), but the ambient temperature would mean that there would be few  $H_3^+$  molecules occupying excited states due to the lower temperature, thus yielding a significantly lower intensity of emission.

#### 5.4.2 Testing the Gaussian fits

To analyse the aurorae in Figure 5.8 (as described in the following section) we used Gaussian fits to the intensity profiles of latitude and altitude. These fits were used to measure the peak emission latitude and altitude with associated uncertainties. To calculate these uncertainties, we used a technique to test the stability of these Gaussian fits derived from a similar method used in Stallard et al. (2012a). This method essentially takes the intensity and its Gaussian fit, and increases the noise in the intensity profile to see if the Gaussian fit will select a new peak emission using the following steps:

1. A profile of a size with the data set is created and populated with random numbers between -1 and 1; each element of this array is then multiplied by the standard deviation of the emission above 4000 km (in other words the amount of noise in the map).
2. The “noise profile” of step 1 is added to the original intensity profile and a new Gaussian fit is performed.
3. The peak emission altitude/latitude of this new fit as well as the FWHM is recorded.
4. Steps 1-3 are repeated iteratively 10,000 times to generate a decent statistical population.
5. The standard deviation of the all peak emission altitudes and FWHM measured is then taken as the uncertainty in these respective values.

### 5.4.3 Altitude and latitude profiles of $H_3^+$ emission

In this section we discuss altitudinal and latitudinal profiles of the map of  $H_3^+$  emission in Figure 5.8. For the altitudinal profiles, both aurorae were sampled between the latitudes of 70 and 80 degrees in their respective hemisphere. As shown in Figure 5.9 the south has a peak emission altitude of  $953 \pm 1$  km with a FWHM of  $440 \pm 3$  km and the north has a peak emission altitude of  $1059 \pm 1$  km with a FWHM of  $500 \pm 1$  km; both of these altitudes are a little lower than previous measurements, but well within range of the findings of Stallard et al. (2012), Gerard et al. (2009) and the results of Chapter 4 after considering their respective error ranges. Note that the uncertainties are derived from repeated gaussian fitting (chosen as it closely matches the shape of the altitudinal intensity profile) of the intensity profile with random variations of the standard deviation of the noise sampled between 3000 and 5000 km above the 1 bar level. Closer inspection of their maximum intensities reveals that whilst the southern aurora peaks at  $0.22 \times 10^{-5} \text{ W m}^{-2} \mu\text{m}^{-1} \text{ sr}^{-1}$ , the northern aurora peaks at  $0.04 \times 10^{-5} \text{ W m}^{-2} \mu\text{m}^{-1} \text{ sr}^{-1}$ . There is a precedent for the southern oval being brighter as O'Donoghue et al. (2016) found it to be a factor of 1.3 times brighter than the north. The ratio found here however is 5.5 for the peak emission intensities with an average ratio of 5.9 for the altitudinal intensity profiles overall. The causes for such a difference will be discussed in Section 5.6.

After summing the emission over an altitude range of 500-1500 km above the 1 bar level, we find that both the northern and southern aurora have a peak  $H_3^+$  emission intensity at a latitude of  $74 \pm 1$  degrees as shown in Figure 5.10. The spread over which this occurs however is substantially different. For the north the full width half maximum (FWHM) is  $3 \pm 1$  degrees whereas the south has a FWHM of  $5 \pm 2$  degrees. This indicates that the south has either a larger variation in latitude for the auroral oval, or that the southern oval is wider than the north. This result is concurrent with the both latitudinal offset between the day and night side aurora and the difference in latitudinal coverage of the north and south auroral ovals as measured in Badman et al. (2011). Given that the auroral morphology shifts between an oval and spiral, it is possible that the observations of the southern aurora contain a wider variety of auroral morphologies and therefore the measurements of the southern aurora are spread over a wider latitudinal range. Alternatively, it could also be due to the north-south magnetic field asymmetry leading to broad particle precipitation in the south as compare to the north (O'Donoghue et al., 2014). Without a measure of the auroral emission with respect to local time, it is impossible to discern which is true in this study.

Outside of the auroral regions, we note that there is some emission equatorward of  $60^\circ$  in both hemispheres. This emission reaches a peak intensity of approximately  $1.0 \times 10^{-5} \text{ W m}^{-2} \mu\text{m}^{-1} \text{ sr}^{-1}$  in both hemispheres. On examining the spectral bins individually in these regions we find that

this emission is mostly thermal emissions and reflected sunlight that has escaped the bin subtraction; there may be  $H_3^+$  emission in this region, but it does not provide a clear spectral signature as compared to the auroral emissions.

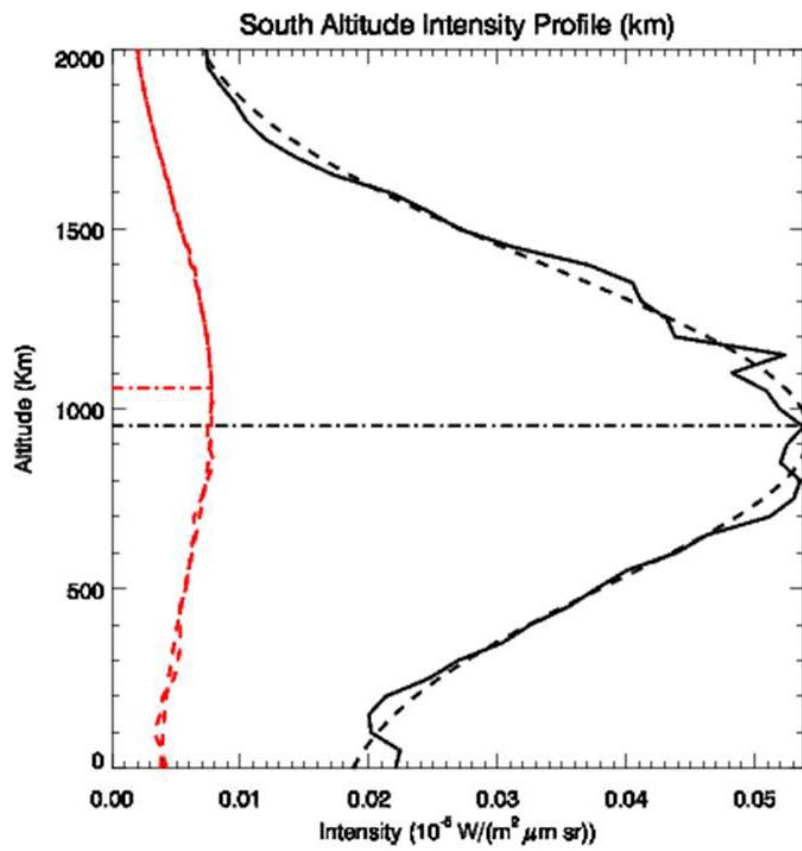
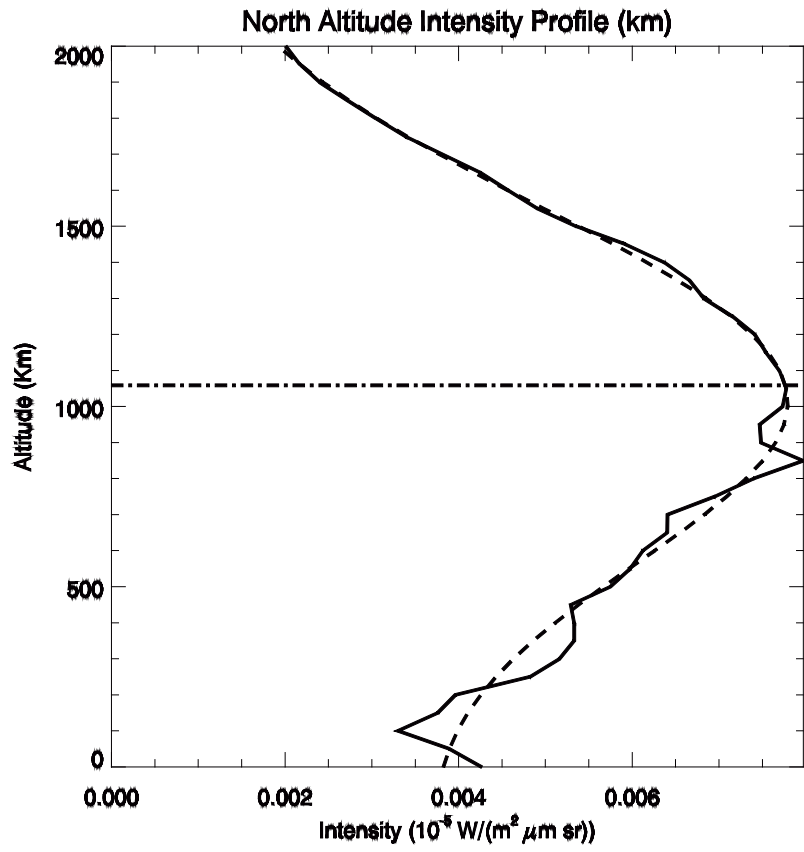


**Figure 5.9:** (shown on previous page) Two plots showing the altitudinal intensity profile sample between 70 and 80 north (top) and 70 and 80 south (bottom). The peak emission altitudes are  $1059 \pm 1$  km with a FWHM of  $500 \pm 1$  km and  $952 \pm 1$  km with a FWHM of  $440 \pm 3$  km for the north and south gaussian fits respectively. The altitudes of these peak emission intensities is marked by the black dot dashed line in each plot, with the northern profile repeated in the bottom plot shown in red for comparison.

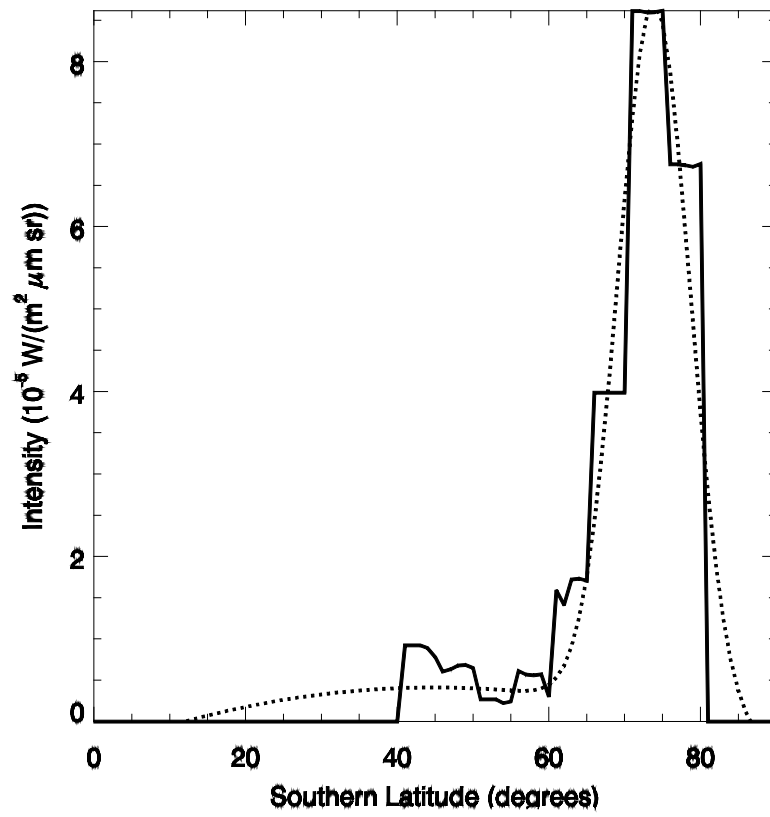
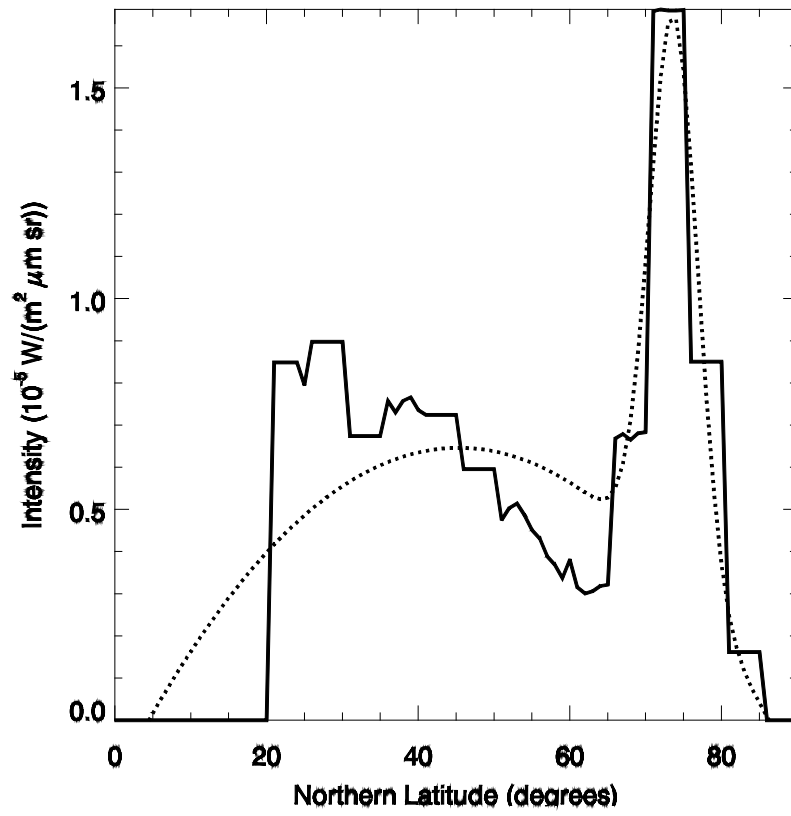


**Figure 5.10:** (on previous page) The variation of total intensity with latitude for both the northern hemisphere (top) and the southern (bottom). The intensity was summed between an altitude of 500 and 1500 km above the 1 bar level.

### 5.5.1 The shell subtraction model

Though efforts were made to ensure that no corrupted observations were included, very little heed was paid to the fact that every observation of the auroral emission has been taken through multiple layers of the upper atmosphere that intercept the line of sight of the VIMS instrument. Hence, it was necessary to augment the maps in order to redistribute the emission to present a more accurate and representative altitudinal profile of the  $H_3^+$  emission. As explained in Chapter 1, we do not expect the  $H_3^+$  emission to extend down to regions lower than the homopause due to the presence of the hydrocarbon species. We augment the altitudinal  $H_3^+$  emission profiles using a shell subtraction model akin to that which is presented in Lystrup et al. (2008) and portrayed in Figure 5.11. Using this shell model we were able to run line of sight calculations that could recursively subtract the emission from upper layers from those below based on the geometry of the latitude-altitude bins and the longitudinal depth that would be associated with each bin in turn. The results of running these calculations were two-fold. First was that the emission was redistributed yielding altitudinal intensity profiles of similar form to the aligned profile of Chapter 4. The second was that it also became possible to produce a measurement of the  $H_3^+$  column density for each spatial bin in the auroral regions, by converting the number density profile into a volumetric density and summing over altitude as will be described in Chapter 6. One significant detractor of this technique is that it has amplified the influence of the noise in the upper reaches of the atmosphere (3000-5000 km above the 1 bar level) where the S/N ratio is significantly poorer as can be seen in Figure 5.12; particular in comparison to the S/N ratio in the peak auroral emission layer at approximately 1000 km.

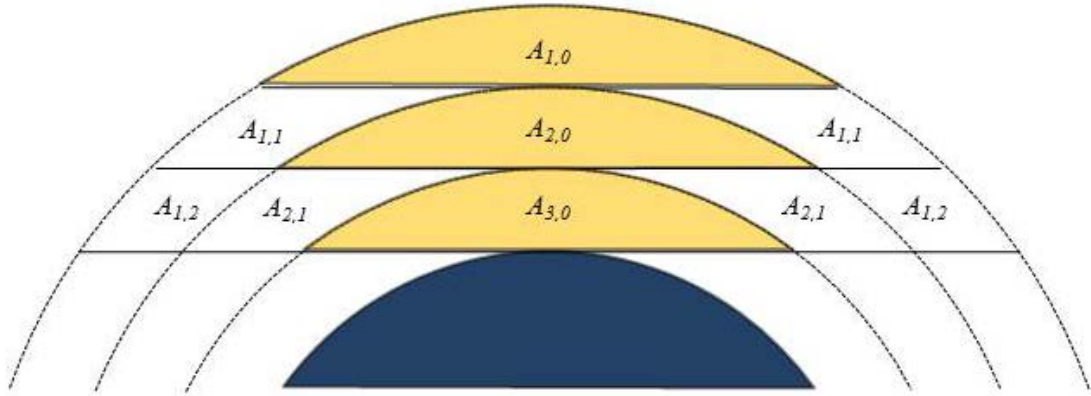


**Figure 5.11:** We calculate the volume of each altitudinal layer along that line of sight and thereby remove the contribution of emission from the upper layers of the atmosphere from the lower layers via a method similar to that used in Lystrup et al. (2008). To begin with, we used the outermost layer shown above as  $A_{1,0}$ ,  $A_{1,1}$  and  $A_{1,2}$ .  $A_{1,1}$  and  $A_{1,2}$  are the contributions of layer  $A_1$  to the lower layers  $A_2$  and  $A_3$  respectively. Using the ratio of the regions  $A_{1,1}$  and  $A_{1,0}$  we calculated the fraction of emission from layer  $A_1$  that has contributed to layer  $A_2$  by applying the ratio the intensity of emission in region  $A_{1,0}$  to give the intensity in  $A_{1,1}$ , and subsequently subtracting it from the intensity in region  $A_{2,0}$ , leaving only the emission from  $A_{2,0}$  remaining. This is repeated recursively with each layer starting from an altitude of 2000 km down to the 1 bar level (shown in dark blue). Ultimately, the result of this process is to only leave behind the emission from the regions labelled  $A_{x,0}$  in each layer.

### 5.5.2 Line of Sight corrected intensity profiles

After the application of the shell model, the intensity profiles for both the northern and southern aurorae are found to be radically changed, as can be seen in Figure 5.12. The first and greatest difference is that the peak emission intensity has shifted to higher altitudes in both hemispheres. Before the application of the onion skin model the peak emission altitude for the north is  $1059 \pm 1$  km with a FWHM of  $500 \pm 1$  km and south is  $953 \pm 1$  km with a FWHM of  $440 \pm 3$  km. As the northern profile is in strong agreement with the aligned profile, we surmise that the disparity in the peak emission altitudes is due to a poorer average alignment of the aurora with the limb in the south as compared to the north. Much like the altitudinal intensity profiles in Stallard et al. (2012) and Gérard et al. (2009), these profiles assume that the auroral curtain is aligned with the limb. To remove this assumption we applied the shell subtraction model yielding a revised altitude of  $1225 \pm 193$  km for the south and  $1333 \pm 152$  km for the north. We note that the shell subtraction process entirely removes the emission below 500 km as was expected as well as significantly increasing the peak  $H_3^+$  emission altitude. Considering these new peak altitudes in the context of Figure 5.12 where the fitted peak altitude at perfect alignment is  $1219 \pm 119$  km, we surmise that the true peak  $H_3^+$  emission altitude is much closer to 1200 km than was previously believed.

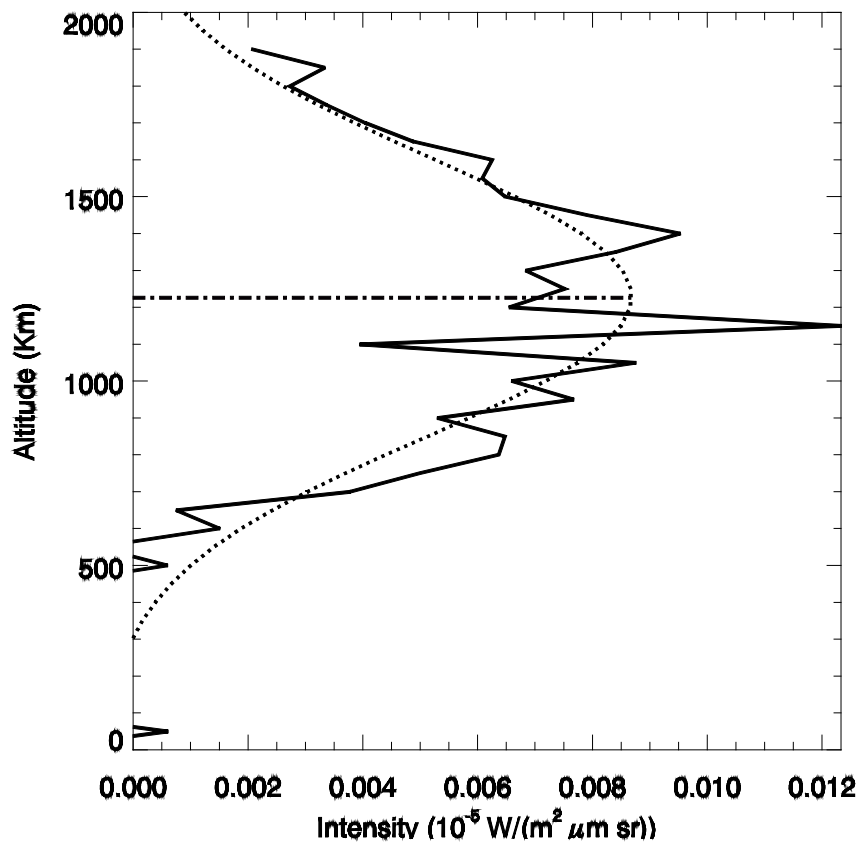
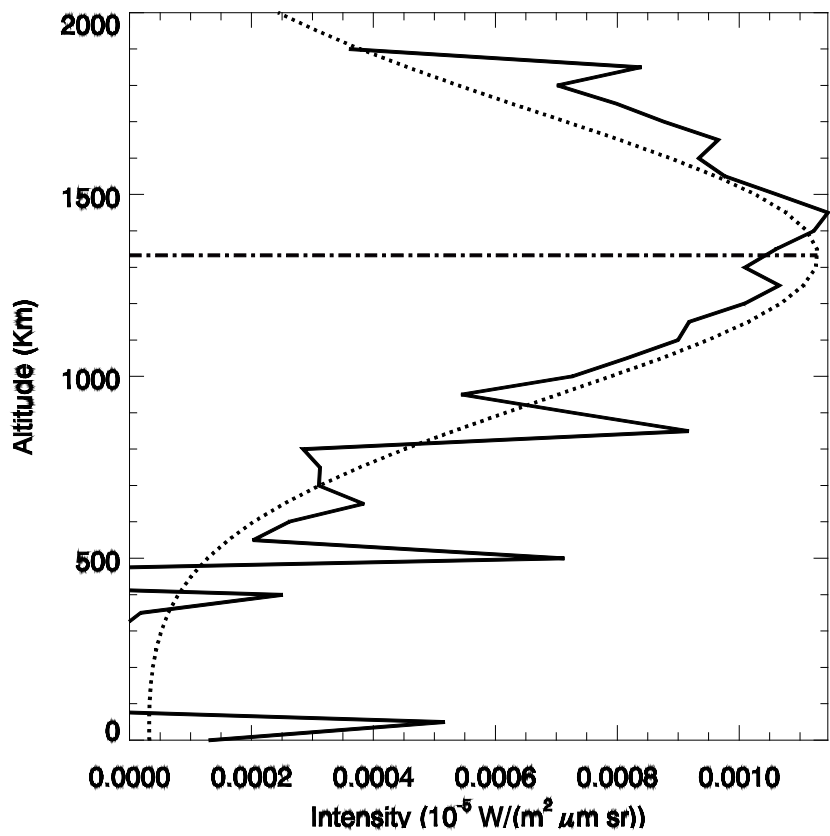


**Figure 5.12:** (shown on previous page) Altitudinal density (top) and intensity (bottom) profiles of the northern (top row) and southern (bottom row) aurorae, rescaled using a recursive shell subtraction technique. The corrected peak emission altitudes are  $1333 \pm 152$  km with a FWHM of  $391 \pm 51$  km for the north and  $1225 \pm 193$  km with a FWHM of  $379 \pm 65$  km for the south.

It is noted that the influence of noise has increase in both intensity profiles, as can be surmised from the spikes of emission in the profiles of Figure 5.12. This noise was responsible for the fact that an uncertainty estimate could not be derived from the peak emission altitude of the northern profile when using a Gaussian fit with six terms (equations 5.3 and 5.4).

$$z = \frac{x-A_1}{A_2} \quad (5.3)$$

$$f(x) = A_0 e^{\frac{-z^2}{2}} + A_3 + A_4 x + A_5 x^2, \quad (5.4)$$

where  $x$  is the variable of the fit and  $A_n$  are the fit coefficients. Any attempt to test the stability of the fit immediately forced it to shift to one of the spikes instead of the peak emission of the profile. Hence, for the northern profile we use a Gaussian fit with only three terms (equation 5.5) to provide; this was stable enough to yield an uncertainty estimate.

$$f(x) = A_0 e^{\frac{-z^2}{2}} \quad (5.5)$$

## Section 5.6 Discussion

We present here the first ever latitude-altitude map of  $\text{H}_3^+$  emission intensity. Upon examining the first results shown in Section 5.4, before any shell subtraction has been applied, it can be seen that the peak emission altitudes are very similar to those of Stallard et al (2012a) and other published literature that have not used any form of line of sight corrections. As was to be reasonably expected, once the shell subtraction model had been applied, the peak emission altitude increased for both hemispheres, though more so for the north than the south. This suggests that many measurements of the peak emission altitude have been consistently underestimating the true altitude of the emission as was the conclusion of Chapter 4. The differences in these altitudes and the reasons behind them are discussed in Section 5.6.1.

### Section 5.6.1 The north-south asymmetry

In Chapter 1 we described the influences on the auroral morphology and intensity; these included the energy of the precipitating electrons, the ambient temperature of the atmosphere and the loss mechanisms of  $\text{H}_3^+$ . In this study we observe that the peak emission altitude is notably higher in the north than the south, and brighter in the south than the north, after line of sight correction has been applied. This must be due to a difference in the mechanisms that generate and destroy  $\text{H}_3^+$  emission. The reason for this could be due to an observation bias such that we have observed each hemisphere under different magnetosphere/atmospheric conditions such as “the south was observed during periods of high energy particle precipitation as compared to the north”. Since the depth to which electrons penetrate depends on their energy, this would explain why the southern aurora has a greater intensity and peaks at a lower altitude than the northern. However, it is also possible that this difference is not the result of observation bias but rather it is the long term average behaviour for the aurorae.

It has previously been observed in Dougherty et al. (2005) that there is an interhemispheric magnetic field asymmetry. O’Donoghue et al. (2014) calculated the magnetic field strength for the north and south auroral ionosphere (1000 km above the 1 bar level) and found that the northern magnetic field is 1.2 times stronger than the conjugate region in the south. With a lower magnetic field strength in the south, O’Donoghue et al. (2014) found that the joule and ion drag heating rate as well the latitudinal range of particle precipitation would be greater in the south as it would cover a larger area. This would explain why we observe that the northern auroral oval is dimmer and narrower than the south, as predicted in Badman et al. (2011) and observed the UV observations in Nichols et al. (2009).

If the difference in peak emission altitude is not due to observation bias then it is possible that the average energy of the precipitating electrons is higher for the south than the north, though

there is no observational precedent for this. Since the depth to which electrons penetrate is dependent on electron energy, it may suggest that the altitude difference is the result of higher energy electrons in the south penetrating deeper. Further, it should be noted however that a deeper penetration depth (lower peak emission altitude) also means a greater ambient  $H_2$  population and therefore an increased production rate of  $H_3^+$ ; this in turn would increase the emission intensity due to a larger  $H_3^+$  density in the south (this is investigated in Chapter 6). Further contributions to this ion density difference could also arise from the fact that the data has been sampled from the years 2005 to 2010, where the north has passed from autumn through winter to spring, which could result in a difference in the photo-ionisation rate from insolation. O'Donoghue et al. (2014) modelled this effect using STIM from which they found that the increased insolation leads to a larger  $H_2^+$  population due a greater influx of solar photons and therefore an increase in the  $H_3^+$  population.

After the shell subtraction had been applied, it was noted that there is a significant increase in the strength of the noise; there are sharp peaks in emission at various points throughout the altitudinal profiles. This is likely due to the propagation of noise down through the profile as each upper layer is recursively subtracted from the lower layers. Whilst this does not prevent the Gaussian fitting procedure from producing a peak emission altitude, it does increase the influence of the noise for the altitudinal emission profiles as reflected by the larger uncertainty ranges ( $1333 \pm 152$  km for the north and  $1225 \pm 193$  km for the south). However, given that these uncertainty ranges are similar to those of Chapter 4,  $1215 \pm 119$  km, we find the uncertainty ranges to be acceptable.

### Section 5.6.2 Comparisons to other measurements and models

Comparing the new altitude from the southern shell subtracted profile to the aligned peak emission altitude Chapter 4 we find strong agreement for the southern aurora; we measure a peak emission altitude of  $1225 \pm 193$  km for this study compared with  $1215 \pm 119$  km. As the data of Chapter 4 was all collected from observations of the south, we cannot directly compare these measurements with north ( $1333 \pm 152$  km). One concern that was raised in Section 4.5 was that we had no measure of the thickness of the auroral curtain or its variation with altitude. Upon examining the map Figure 5.8, it can be seen that there is significant variation with altitude, with the widest point coinciding with the peak emission altitude, however, we do not know if this distribution is caused by a local time variation (as we have averaged over all local times), a temporal variation (the auroral oval shifting in latitude in response to changes in the magnetosphere) or because it is the true latitudinal distribution of the aurora. What can surmised however, is that the observed auroral emission in the map is widest where it is

brightest, and decreases in width with altitude in either direction. Assuming that the difference in peak emission altitude for the north and south is not due to observation bias, this means that the peak emission layer of the aurorae are consistently produced by the same energy of electrons in each respective hemisphere regardless of auroral morphology (as the electrons must penetrate to the same depth irrespective of the compression or expansion of the main auroral oval).

Aside from the altitudinal intensity profile of Stallard et al. (2012a) and the profile presented in Chapter 4, we can also compare our altitudinal profiles of this Chapter to the model of Tao et al. (2011). In their paper, Tao et al. (2011) modelled the altitudinal density profile of  $H_3^+$  as well as the volume emission rate for the fundamental transition line at  $3.95299 \mu\text{m}$ . We cannot directly compare the intensity of this line in the model to our data (as VIMS cannot resolve a single line as explained in Chapter 3) nor can we use the spectral bin that contains this line (185) on its own as the S/N ratio prevents altitudinal profiles of a single bin from surviving the shell subtraction process (the noise quickly accumulates and destroys the profile). We can however use the altitudinal profiles in Figure 5.12 on the basis of comparing the distribution of emission. This comparison can be seen in Figure 5.14, which shows the profiles of Figure 5.12 and the altitudinal emission profile derived from the volume emission rate of  $H_3$  with a precipitating electron energy of 10 keV shown in Figure 5.13 (b); the energy of the electrons that produce the main auroral oval has been measured to be in the range of 10-18 keV (Gerard et al., 2009).

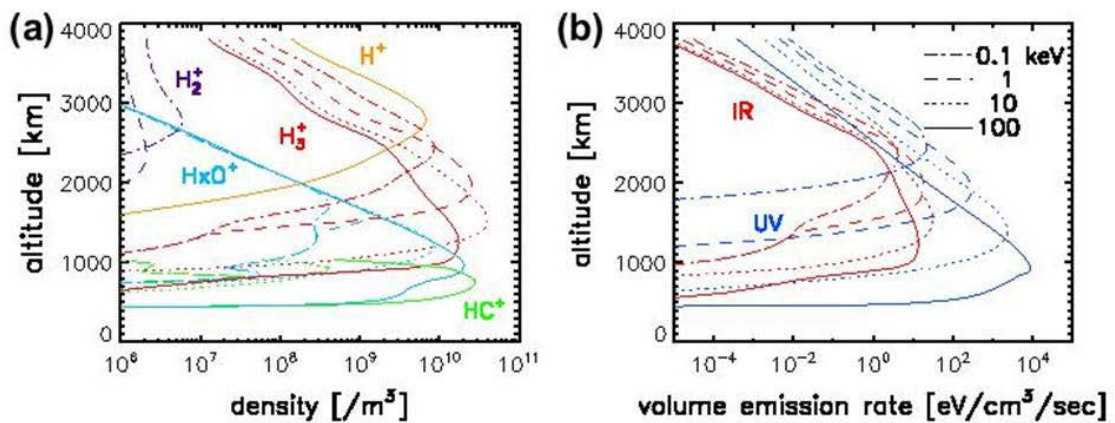


**Figure 5.13:** Figure 8 of Tao et al. (2011) showing the altitudinal density profiles (a) of the species  $HC^+$  (green),  $H_xO^+$  (light blue),  $H_3^+$  (red),  $H_2^+$  (purple) and  $H^+$  (yellow) as well as the volume emission rates with altitude (b) for the IR (red) and the UV (blue) generated by precipitating electrons a various energies: 0.1 keV (dot dashed lines), 1 keV (dashed lines), 10 keV (dotted lines) and 100 keV (solid lines).

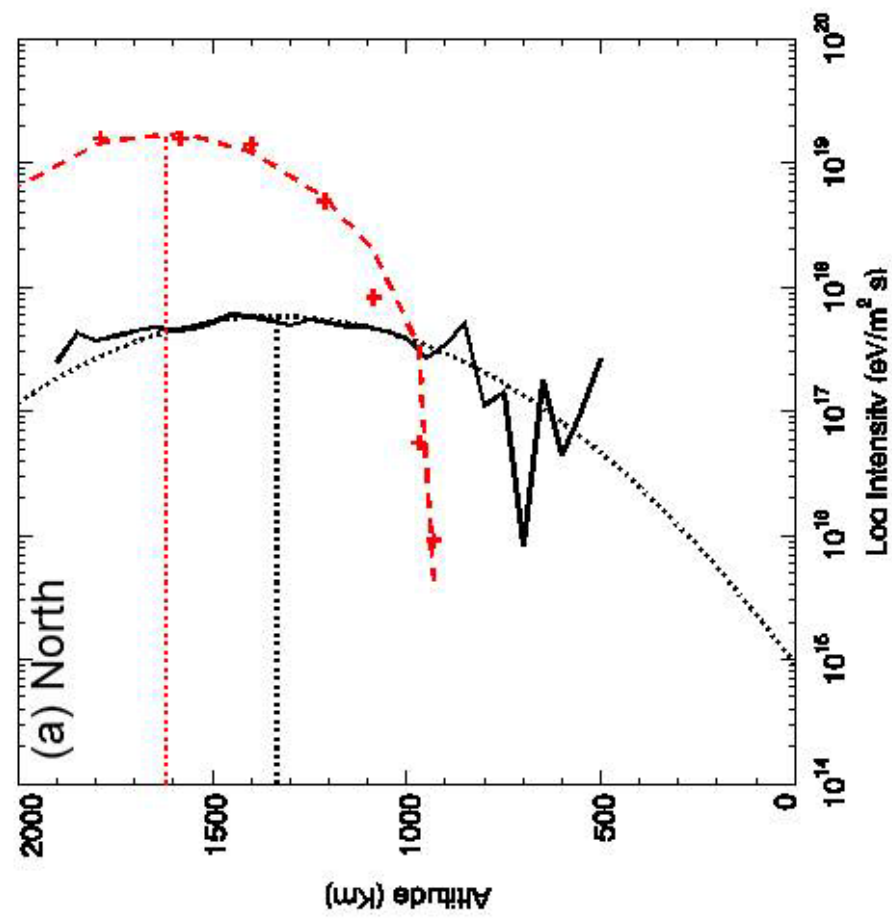
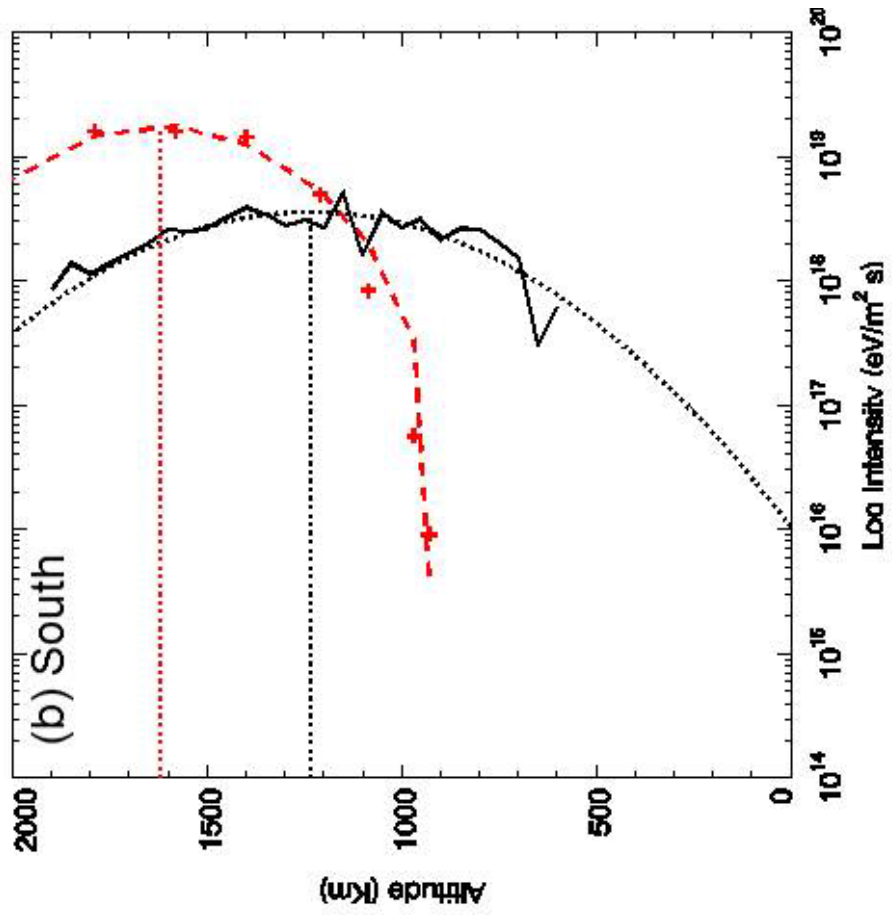


**Figure 5.14:** The shell subtracted altitudinal intensity profile (solid black line) for the North (a) and the South (b) as well as their associated Gaussian fits (black dotted curve) in comparison to the modelled altitudinal  $H_3^+$  emission profile (red crosses) of Figure 8 (b) of Tao et al. (2011) and the associated Gaussian fit (red dashed line) for a precipitating electron energy of 10 keV. The horizontal black dotted line marks the peak emission altitude measured by the Gaussian fits for the Northern (1333 km) and Southern (1225 km) shell subtracted intensity profiles, likewise the red dotted line is the peak emission altitude (1620 km) of the Tao et al. (2011) profile. Note that unlike the other altitudinal plots, the units of intensity are shown here as  $eV m^{-2} s^{-1}$  for the Tao et al. (2011) profile (red) and  $eV m^{-2} s^{-1} \mu m^{-1}$  for the shell subtracted profile (black) on a logarithmic scale; the original units of the Tao et al. (2011) was  $eV cm^{-3} s^{-1}$  in comparison to the units of  $W m^{-2} \mu m^{-1} sr^{-1}$  from the shell subtracted profile. We cannot remove the unit of  $\mu m^{-1}$  from the shell subtracted profile as it is made of intensities from multiple spectral bins instead of the single emission line in Tao et al. (2011).

It is immediately apparent in Figure 5.14 that the model of Tao et al. (2011) is a great deal brighter, by around an order of magnitude, than the average intensity of the  $H_3^+$  aurora measured in this study. Further, the emission profile of Tao et al. (2011) yields a peak emission altitude that is around 300 km higher than those measured from our Northern and Southern altitudinal auroral profiles. Given that the shell subtracted profile in black consists of multiple spectral lines compared to the Tao et al. (2011) profile in red which modelled a single transition line, we surmise that the intensities from this model ( $0.053 \times 10^{-5} W m^{-2} sr^{-1}$ ) are likely much higher than the average. Without first measuring temperatures and densities from our measured  $H_3^+$  intensities, it is difficult to say whether or not Tao et al. (2011) underestimated the temperatures, overestimated the  $H_3^+$  densities or a combination of the two. However, based on the difference in peak emission altitude, either the aurora we observe is produced by a population of electrons with a higher energy, such as the 100 keV electron precipitation as modelled in Figure 5.13 and 5.14, or Tao et al. (2011) modelled densities and emission rates for conditions that we have not observed. This will be explored in the next chapter where we calculate these temperatures and densities and examine their implications with respect to the intensity profiles of this chapter.

## Chapter 6

### *Temperatures and densities of the infrared aurorae*

#### Section 6.1 The challenges of temperature and density analysis

Detailed in Section 1.2.6 and Section 1.2.7 of Chapter 1 are various studies of the temperature and density of  $\text{H}_3^+$  at Saturn. Many of these studies analysed what is defined as the column temperatures and densities using telescope data, which is to say they analysed a column of  $\text{H}_3^+$  emission integrated over a range of altitudes to produce a column temperature and density and as such have lost any measure of altitudinal structure. There have been two Voyager radio occultations which provided an altitudinal temperature structure for the troposphere and stratosphere (Lindal et al., 1985, Lindal, 1992), but these have been limited to one location in one time frame and thus do not provide statistical measurements. Koskinen et al. (2013, 2015) used Cassini UVIS occultations for multiple latitudes, though these studies largely focused on the exosphere (over 1800 km above the 1 bar level for Koskinen et al., 2013, and 1600-1900km for Koskinen et al., 2015). Koskinen et al. (2015) did model altitudinal neutral temperature profiles based on a group of stellar occultations; however these profiles were based only on exospheric measurements of the neutral atmosphere at 20° north. As such, the study in this thesis is the first of its kind, in that it can provide information on the altitudinal structure of temperature and density within the ionosphere of Saturn. Measurements of the temperature structure of the atmosphere are an intrinsic component to understanding the dynamics of the thermosphere and the transit of energy throughout the magnetosphere-ionosphere system. The results of this study and the analysis of the structure we find are covered from Section 6.5 onwards.

As discussed in Chapter 5, one of the great challenges in measuring the temperature from VIMS observations is obtaining a high enough S/N ratio to produce a clear spectrum. The variation of the emission spectrum of  $\text{H}_3^+$  with temperature is a very well understood process that has been calculated from *ab initio* modelling of the structure of  $\text{H}_3^+$ , and measured empirically thereafter; as described in Section 6.2. One widely used technique for measuring the temperature based on these spectra is to take the ratio of two particular  $\text{H}_3^+$  emission lines and then compare this with a model of how the ratio of these two lines changes with temperature. This requires two very strong and stable emission lines with a low level of uncertainty, a high S/N ratio and a clear separation in their respective energy states. With ground based instrumentation, where the spectral resolution (up to 100,000) is much higher and can therefore facilitate the extraction of

particular  $\text{H}_3^+$  emission lines with relative ease. In contrast VIMS has a much lower spectral resolution ( $\sim 400$ ), to the point where individual  $\text{H}_3^+$  emission lines cannot be resolved (as described in Chapter 3). To measure temperatures from VIMS data requires an understanding of how the emissive behaviour of  $\text{H}_3^+$  changes with temperature, but also how the VIMS instrument would observe this change; the technique for managing this issue is described in Section 6.3. This challenge is further complicated by the gradual shift in the central wavelength of VIMS spectral bins that has been occurring throughout the duration of the Cassini mission. The method for dealing with this is detailed in Section 6.4.

In the past column integrated densities (column density from here on) have been measured by first considering the temperature of the observed  $\text{H}_3^+$  population and using this to derive the emission per molecule using a model of  $\text{H}_3^+$  emissions. The measured total intensity is then divided by the emission of a single molecule to provide column density, but these measurements cannot provide information on altitudinal structure. With the altitudinal profiles of both intensity and temperature it is possible to apply the same technique described above to the VIMS data to produce values for  $\text{H}_3^+$  density. However, once again there is another set of challenges that must be overcome. As covered in Section 6.5, the first issue is also a problem that plagued the temperature measurements; VIMS's inability to resolve individual spectral lines. To calculate the  $\text{H}_3^+$  density we must first know the intensity of emission per molecule for the given temperature of our observed  $\text{H}_3^+$  population. Hence, we model the emissive behaviour of a single  $\text{H}_3^+$  molecule as would be viewed by the VIMS instrument for the same spectral range used in the intensity map, then divide the latter by the former to give the density. The second challenge was to model the atmosphere in order to allow us to calculate the volumetric densities, here we utilised the shell model described in Section 5.5.1. This is discussed in greater detail in Section 6.7 and 6.8.

The last part of this chapter, Section 6.9, covers the pressure and number density scale height of  $\text{H}_3^+$ . This property is of interest as it can allow for the comparison of the number density scale heights measured from the observed intensities and densities to those derived from the temperatures based on the emission spectra. The scale height tells us how fast the number density or pressure of a particular species should decline with altitude due to redistribution by gravity, so if the pressure scale height measured from the altitudinal intensity and density profiles matches the pressure scale height measured from the temperature, then  $\text{H}_3^+$  is redistributed by gravity (and vice versa).

## Section 6.2 The partition function

The partition function is an equation that defines the statistical properties of a system in thermal dynamic equilibrium. They consist of system variables such as temperature, volume and pressure and can give system aggregate variables such as total energy. The first partition function derived from explicitly calculated values for  $\text{H}_3^+$  was published in Neale and Tennyson (1995). This work was further developed by Miller et al. (2013) and we use here their polynomial fit of a partition function derived and measured for  $\text{H}_3^+$  as shown in equations 6.1-6.3. The equation used for the direct calculation of the partition function is shown in equation 6.1 as well as the polynomial fit in equation 6.2 which is used to approximate equation 6.1 for the sake of computing expedience, of which the associated constants  $A_N$  are shown in Table 6.1.

$$Z(T) = \sum_i g_i(2J_i + 1)\exp(-E_i/kT) \quad (6.1)$$

$$Z(T) = \sum_n A_n T^n \quad (6.2)$$

Where  $g_i$  and  $J_i$  are the nuclear spin degeneracy and the angular momentum of energy level  $i$  respectively,  $E_i$  is the energy of said level at temperature  $T$  and  $k$  is the Boltzmann constant ( $1.38 \times 10^{-23} \text{ m}^2 \text{ kg s}^{-2} \text{ K}^{-1}$ ). This partition function can then be used in conjunction with equation 6.3 which calculated the number of particles at energy level  $i$  and equation 6.4 which calculated the intensity of a given transition line for a single  $\text{H}_3^+$  molecule to produce equation 6.5 which does the same but for an entire population of  $\text{H}_3^+$  at a given temperature.

$$N_i = \frac{N}{Z(T)} (2J + 1)g_{ns}\exp\left[-\frac{E_i}{kT}\right] \quad (6.3)$$

Where  $N_i$  is the fraction of the total number of molecules  $N$  that are at energy level  $i$ ,  $Z(T)$  is the temperature dependent partition function,  $J$  is the rotational angular momentum for energy level  $i$ ,  $g_{ns}$  is the spin weighting associated with the ortho and para symmetry states,  $E_i$  is the energy of level  $i$ .

$$I(\omega_{if}) = hc\omega_{if} \quad (6.4)$$

$$I(T) = \frac{N \times g_{ns}(2J+1)hc\omega_{if}A_{if}}{4\pi Z(T)} \exp\left[-\frac{hc\omega_i}{kT}\right]. \quad (6.5)$$

Where  $\omega_{if}$  is the wavenumber ( $\text{cm}^{-1}$ ) of the transition from a higher energy level  $i$  to a lower energy level  $f$ ,  $h$  is Planck's constant,  $c$  is the speed of light and  $A_{if}$  is the Einstein transition coefficient of spontaneous emission. This equation for emission intensity (6.5) calculates the theoretical emission intensity of a specific transition of a population of  $\text{H}_3^+$  molecules of size  $N$  from a higher energy state  $i$  to a lower energy state  $f$ .

Applicable Temperature Range:	100-1800 K
$A_0$	-1.11391
$A_1$	+0.0581076
$A_2$	+0.000302967
$A_3$	$-2.87324 \times 10^{-7}$
$A_4$	$+2.31119 \times 10^{-10}$
$A_5$	$-7.15895 \times 10^{-14}$
$A_6$	$+1.00150 \times 10^{-17}$

**Table 6.1:** The fit coefficients used in Miller et al. (2010) for equation 6.2.

### Section 6.3 Generating model spectra

Using the partition function and line model outlined in the previous section it is possible to create model spectra for the use of calculating temperatures. The technique of using the ratio of two spectral lines to determine the temperature functions so well because of the change in emissive behaviour demonstrated in Figure 6.1. There are two spectra shown, one for a population at 400 K and another at a temperature of 600 K. Whilst all emission lines change significantly with temperature (by an order of magnitude over this temperature range), when normalised to the brightest line, as can be seen in Figure 6.1, there are some emission lines that brighten significantly more than the brightest line and others that brighten by a similar amount. This is due to the different energies required to fill each of the energy states associated with the emission lines. The VIMS instrument is incapable of resolving individual emission lines (Chapters 2 and 3), hence, Figure 6.2 shows a broad  $H_3^+$  emission spectrum as would be observed by VIMS for 400 K (black) and 600 K (red) with the ratio of the two spectra shown in blue. The ratio of these two profiles (blue) is there to demonstrate that as with the emission lines, some bins change more than others and that this change is significant enough to be able to provide temperature measurements in a consistent manner, provided there is a high enough S/N ratio.

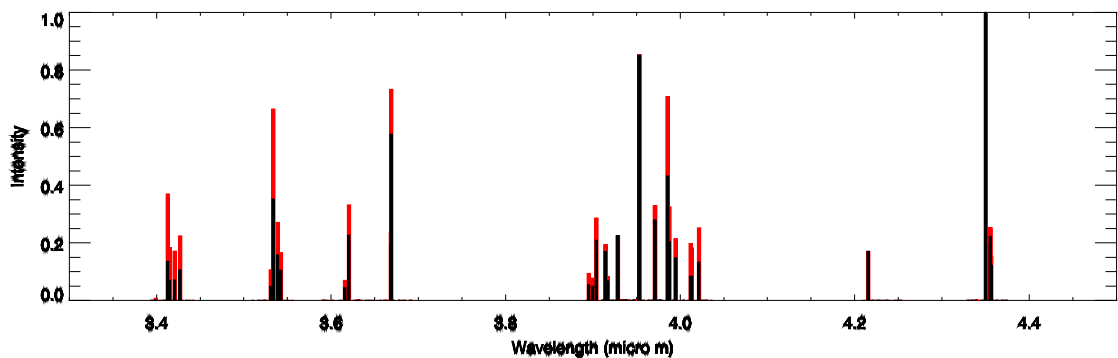


**Figure 6.1:** A model  $H_3^+$  spectrum between 3.0 and 4.5  $\mu\text{m}$  at 400 K in black and 600 K in red, using the line emission line list of Neale et al. (1996); normalised to the maximum intensity for the purpose of clarity.

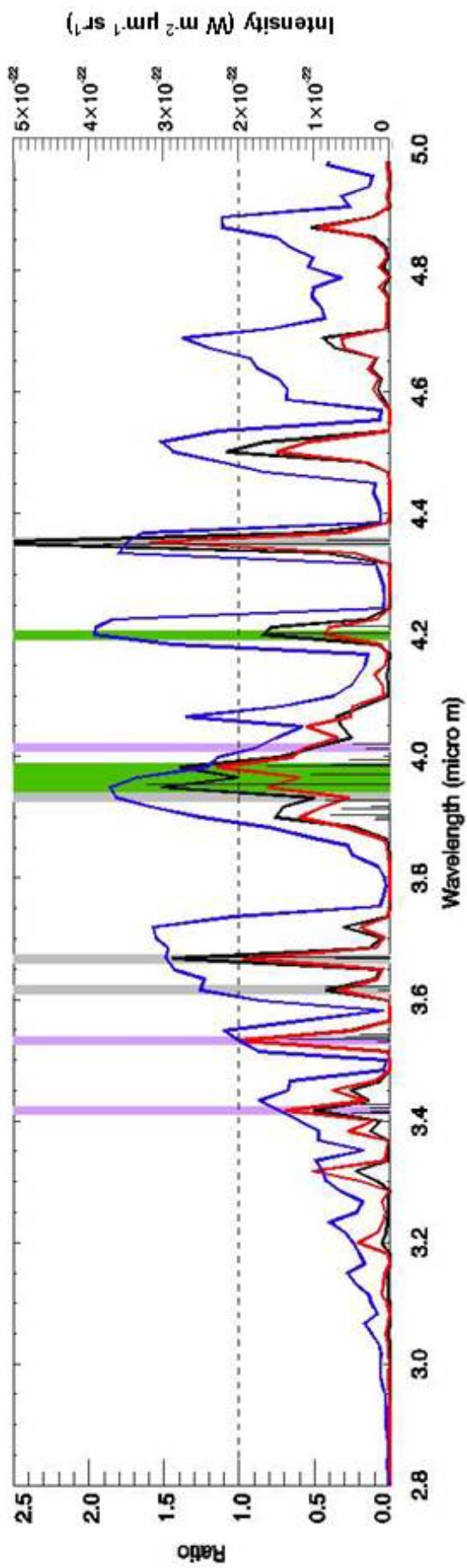


**Figure 6.2:** (shown on previous page) A modelled spectrum of  $H_3^+$  emission as resolved by the VIMS instrument at two different temperatures; 400K shown in red and 600K shown in black (scaled to the right hand axis of intensity). The blue line is the ratio of these two profiles (scaled to the left hand axis marked 'ratio'). This plot was used to determine which groups of spectral bins would be appropriate in the use of calculating the temperature of the  $H_3^+$  population. Two groups of VIMS spectral bins were selected based on two specific criteria; the first group highlighted in green were selected on the basis that the emission lines they encompassed change significantly with temperature and the second group highlighted in purple do not change significantly with temperature (relative to the brightest emission line). Thus, the ratio of these two groups is highly sensitive to temperature changes and can therefore deliver a more accurate temperature measurement. The bins highlighted in grey are those which were included in the  $H_3^+$  intensity projection process but have not been used for the purpose of temperature calculation.

#### 6.4 Calculating temperatures

In Section 6.1, we described the requirements for measuring temperatures from  $\text{H}_3^+$  emission spectra. Among these requirements is the need for two bright and stable emission lines. Unlike ground-based instruments however, VIMS does not have a high enough spectral resolution to resolve individual  $\text{H}_3^+$  emission lines, but instead has spectral bins that each contain several emission lines. Another challenge is that  $\text{H}_3^+$  emission at Saturn as seen by VIMS is quite weak; so the primary concern in this instance was to improve the S/N ratio. This was achieved by selecting two groups of spectral bins (shown in Figure 6.2) to perform this ratio in order to maximise the sampled  $\text{H}_3^+$  emission. Hence the process shown here utilises the ratio of multiple wavelength bins sorted into two groups. To select which bins were most suitable for this temperature calculation, we modelled how the emission would change with temperature for several of VIMS spectral bin combinations. Two groups were then derived from this, as is shown in Figure 6.2. All emission lines will increase in intensity with temperature as the number of molecules in excited states increases. However, the extent of this increase is different for each emission line and as such there is a relationship between the temperature and the ratio of different emission lines, or in this case, groups of emission lines. To ensure the greatest sensitivity to temperature, the bins were selected such that the first group had a much greater rate of change in intensity with temperature as compared to the second. The first group consisted of bins 153, 160, 165 and 189 (shown in green in Figure 6.2) and the second consisted of bins 184, 185 and 186 (shown in purple in Figure 6.2). Initially the second group also contained bin 200, however it was discovered that the intensity of this was relatively unstable in observations, possibly due to the overlap with the thermal emissions in this wavelength region. These two groups of bins produced the strongest variation of bin group ratio with temperature, thereby improving the accuracy of the subsequent temperature calculations. Thus, we can use the ratio of these two spectral bin groups to derive a temperature.

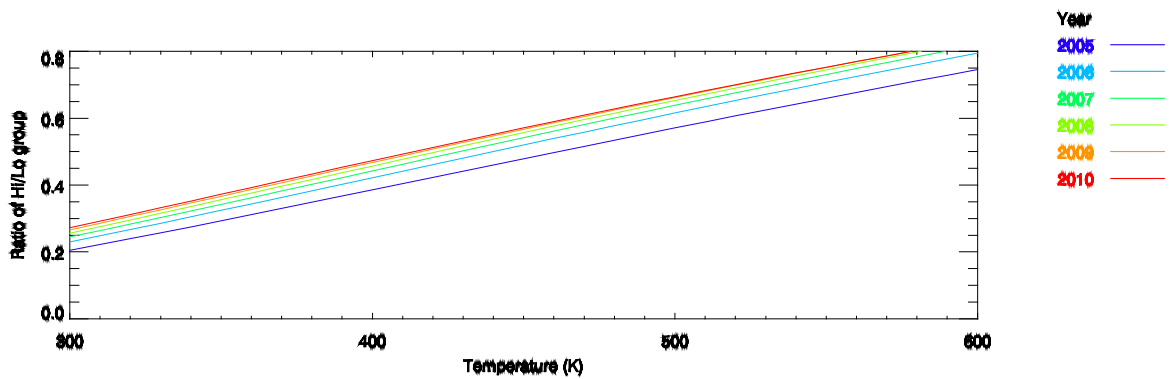


**Figure 6.3:** The temperature-bin ratio profile modelled for a range of years; from 2005 in blue, transitioning to 2010 in red. This quite clearly demonstrates the importance of the VIMS wavelength shift with time, especially when combining observations from multiple years. It signifies that spectrally speaking, each year must be treated differently.

### Section 6.5 The wavelength shift

To address the wavelength shift (explained in Chapter 3), whereby the central wavelength of each spectral bin has been shifting each year, we calculated the variation of the ratio with temperature for each year from which observations were taken (so as to account for the wavelength shift). The different profiles for each year are shown in Figure 6.3, varying from 2005 in blue through to 2010 in red. It is clear from Figure 6.3 that the wavelength shift has a significant effect on temperature calculations and hence, correcting for it was a critical necessity. As each element of the latitude altitude map would have a different contribution of observations from each year, it was necessary to incorporate this spectral shift on an element by element basis to create the latitude-altitude map of temperature. This process involved calculating the total integration time of each year that contributed to each projected latitude-altitude bin, then using these to take a weighted mean of the aforementioned temperature-ratio profiles. In other words, for a given element, each ratio-temperature profile from Figure 6.3 was multiplied by the total integration time of each year that had contributed to it; these profiles were subsequently summed together and divided by the total integration to give the weighted mean profile. This was repeated for each spatial bin in the latitude-altitude maps individually as each of them has different levels of contribution from different years.

## Section 6.6 Results: temperature maps and profiles

To reduce noise, the original map of intensity was resampled from spatial bins of 1 degree of latitude by 10 km of altitude to 5 degrees of latitude by 50 km of altitude for the polar regions (60-90° latitude in both hemispheres), and 30 degrees of latitude by 500 km for the lower latitudes (-60° to 60° latitude. The reason for the significantly larger bin sizes at lower latitudes is the self-evident lack of significant emission in the region enclosed between 60 degrees north and 60 degrees south (as shown in Figure 5.8).

Using the technique detailed in Section 6.4 we have calculated a map of temperature shown in Figure 6.4 from two maps of  $H_3^+$  emission intensity containing groups of spectral bins as described in Section 6.4. The auroral regions are clearly shown as areas of higher temperature, with a distinct cut off at 60 degrees in each hemisphere. This may be due to the fact that the intensity emission has dropped off sharply as can be seen in Figure 5.8. At latitudes less than 60 degrees the intensity of the emission is very weak and the S/N ratio very poor, as such we averaged the emission between 60 degrees latitude north and south in bins of 30 degrees by 500 km. This was done to reduce the S/N ratio and thereby derive some temperature measurements. The only non-auroral region that we were able to calculate temperatures for was between 30 and 60 degrees north which show up as regions of purple in Figure 6.4, and provided an average temperature and associated uncertainty range (expressed as super- and sub script numbers) of  $287^{+82}_{-22}$  K between 500 and 1500 km above the 1 bar level (the derivation of the uncertainties used the same method as the auroral regions as described below). This may be the result of  $H_3^+$  emission or it could also be a coincidence caused by the noise; the emission is very weak in the region 30-60° north so it is difficult to be certain which of these is the case. For the rest of the latitudes, between 30 degrees north and 60 degrees south, the intensity of the  $H_3^+$  is very weak to the point of being indistinguishable from the noise, hence any temperature measurements from this region are meaningless (essentially they are trying to measure the temperature of an  $H_3^+$  population that VIMS is unable to spectrally resolve). In this region we measured only infeasible temperatures which were greater than 800 K (the maximum observed temperature from Festou and Atreya, 1983) in some places and less than 0 K in others; and have thus been set to zero. This issue also affected the regions closest to the poles, where in the south the sampled emission was too weak derive a meaningful temperature measurement and in the north, this region was not sampled in our study (these regions are both black in Figure 6.4).

The auroral temperatures have been sampled and averaged over 10 to 20 degrees co-latitude, the resultant altitudinal profiles are shown for the north and south in Figure 6.5. The south has a temperature of 470 K at the 1 bar level (though as we shall see, this value must be treated very carefully), increasing to 600 K by 1500 km, with an average temperature between 1000 km and

1500 km of  $585^{+6}_{-29}$  K. In contrast the north has a temperature of 570 K at the 1 bar level and decreases slowly with altitude, averaging at  $549^{+34}_{-12}$  K between the altitudes of 1000 and 1500 km above the 1 bar level. The uncertainty in the ratios were derived using the standard deviation of the emission above 2000 km and between the latitude limits of 10 to 20 degrees co-latitude for both groups of spectral bins. This was passed through the “ratio-matching” process as a percentage error to calculate the uncertainty in the temperature profile, yielding the red shaded region in Figure 6.5. In the region of the auroral peak emission layer, this uncertainty amounts on average to approximately  $\pm 20$  K for both the north and south auroral regions. As the altitude increases the error margin for the temperature profile increases (Figure 6.5), this is due to the fact the emission is weaker at higher altitudes and so the S/N worsens. This effect is notably more pronounced in the south as compared north; in spite of the south having a far brighter intensity, it also only has approximately a quarter of the data density possessed by the north, as such the signal to noise ratio for the south is intrinsically worse by comparison.

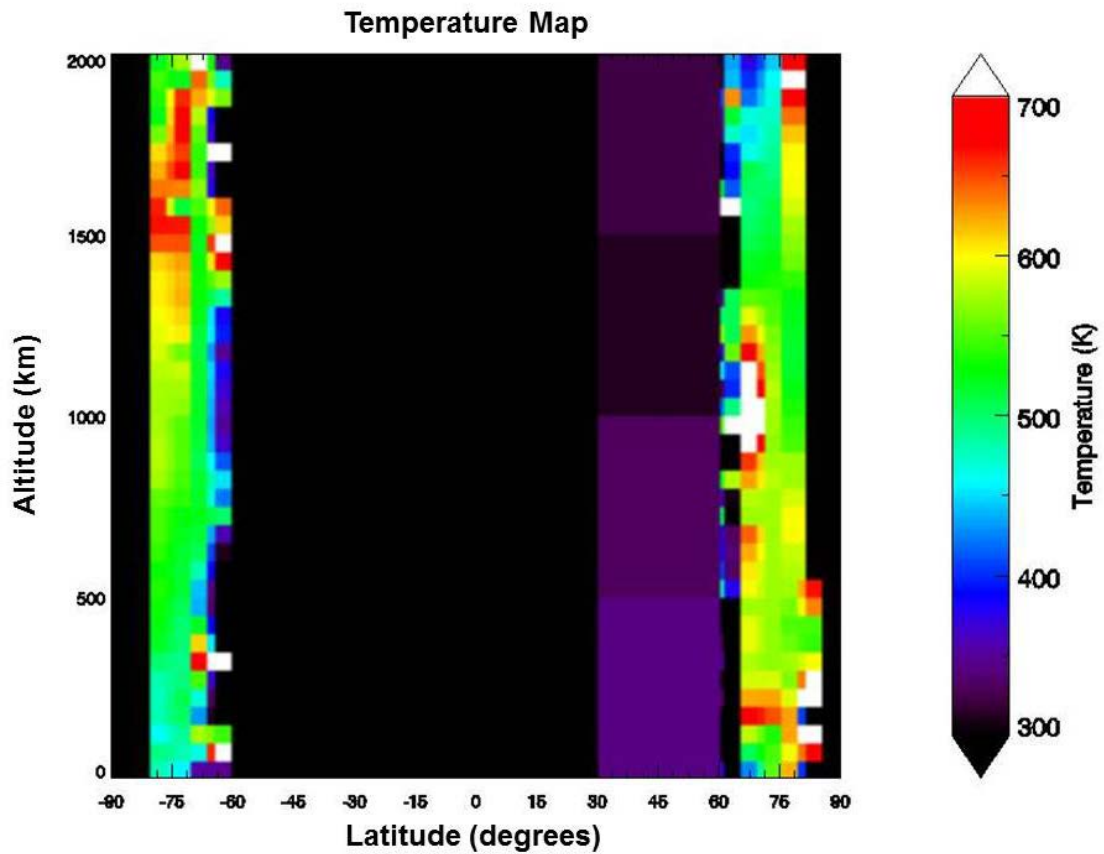
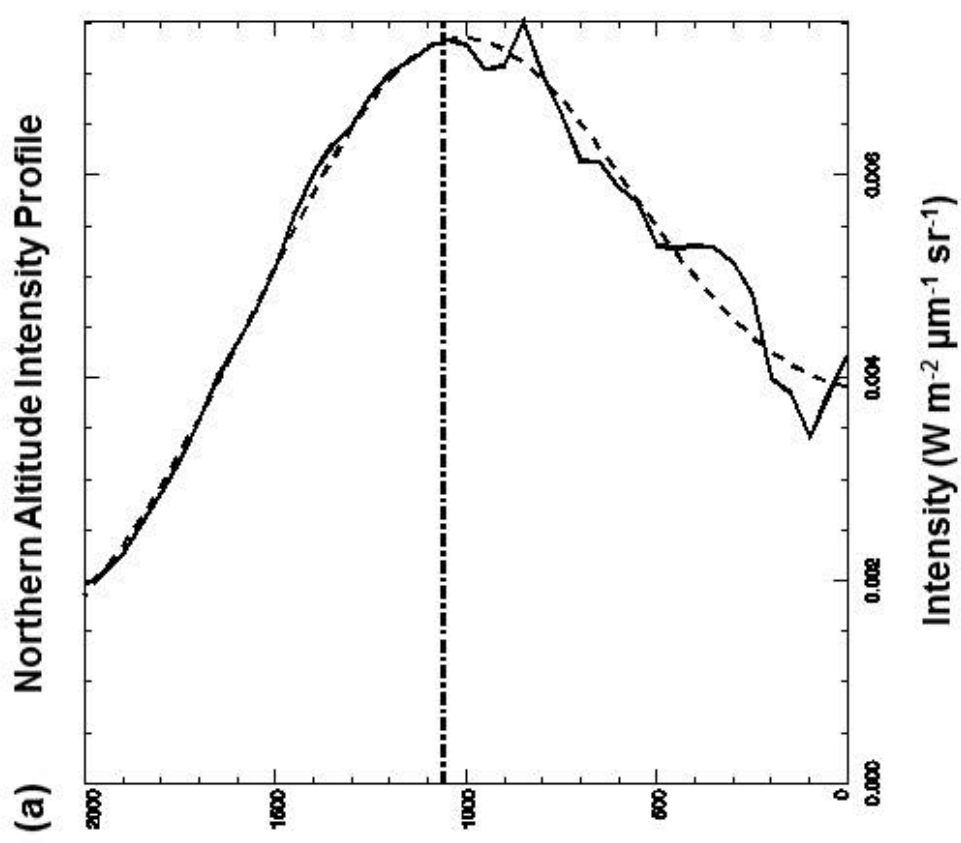
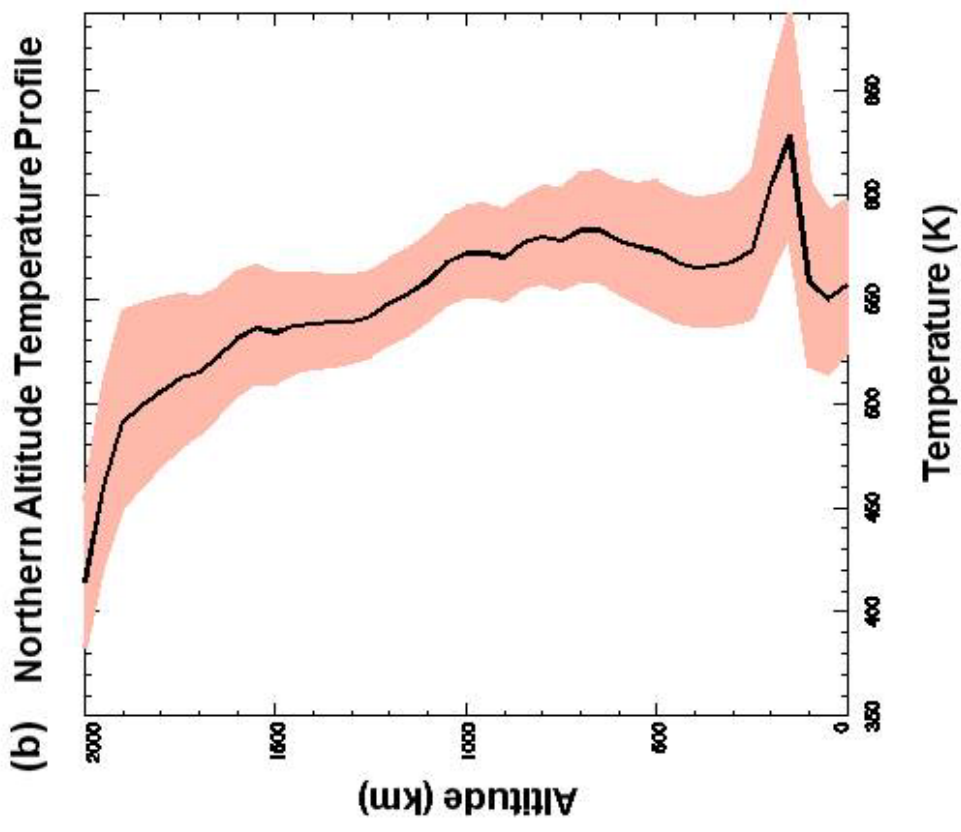
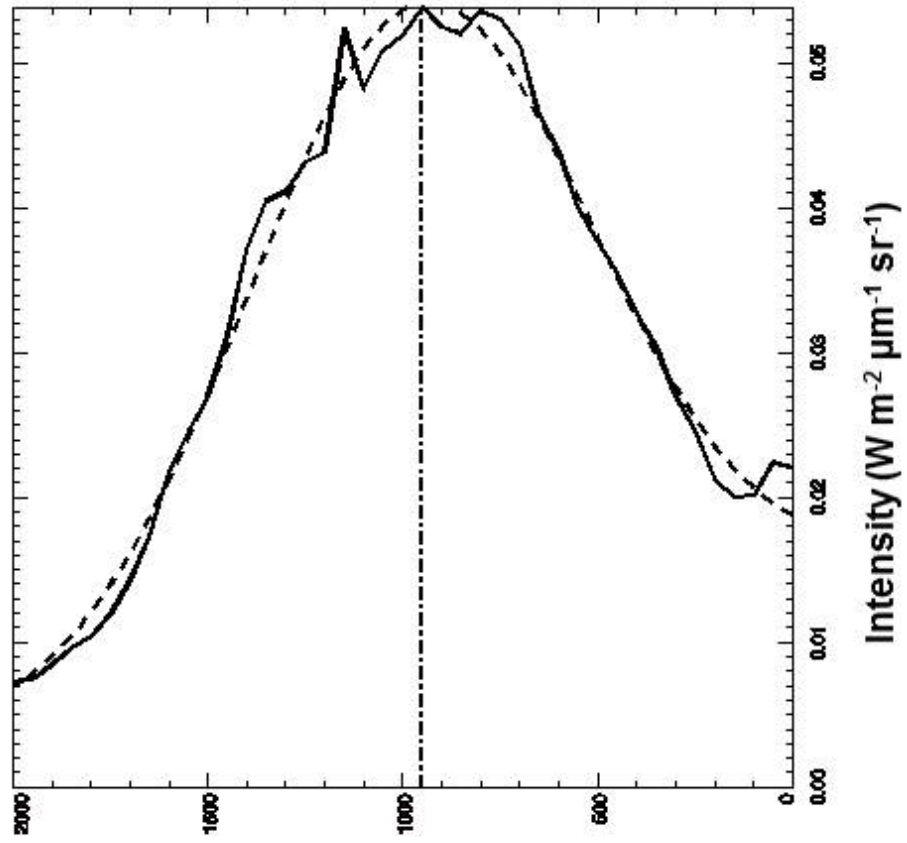


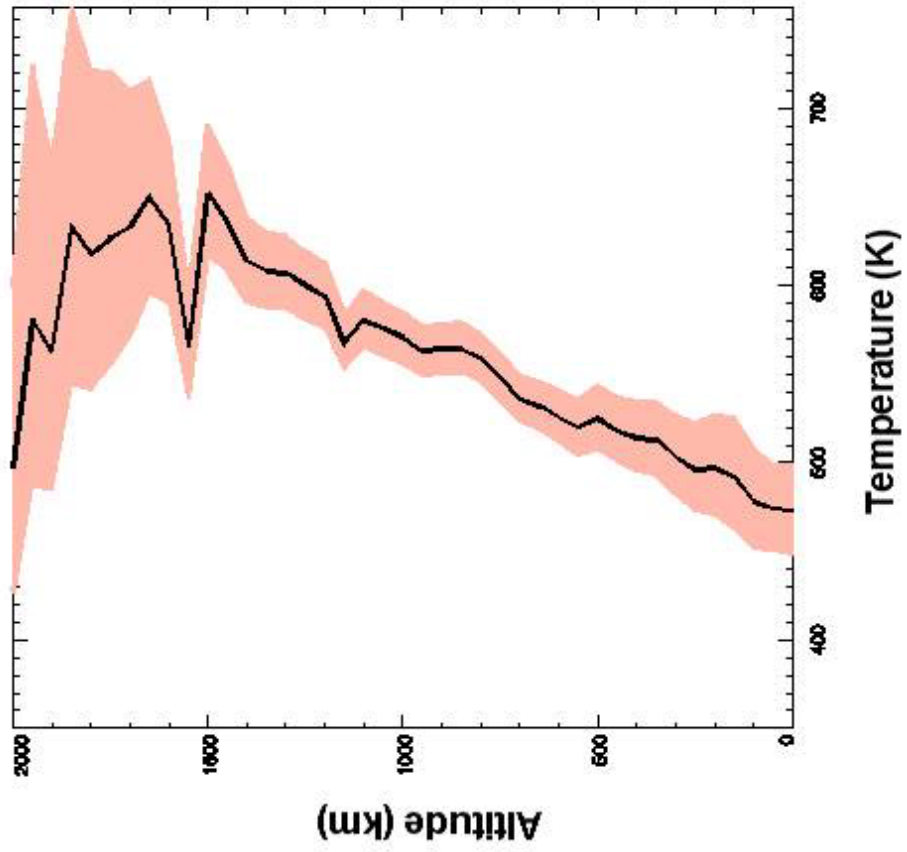
**Figure 6.4:** A latitude-altitude map of  $H_3^+$  temperature averaged derived for each spatial bin averaged across all longitudes and time (years). Due to the difference in data density, the polar regions (area of latitude of 60 degrees or more) has been binned into a grid size of 2 degrees of latitude by 50 km of altitude. The remaining “low latitude” region has been binned into a grid size of 30 degrees by 500 km in an effort to obtain useful information on this area. Unfortunately, even at so large a grid size, most of the emission collected from the lower latitudes is entirely insufficient to produce credible results (they produced unrealistic temperatures that were either excessively small - near or below zero kelvin - or large – several thousand kelvin). The region of 30-60 north was the only non-auroral latitude range that produced realistic temperatures.



(c) Southern Altitude Intensity Profile



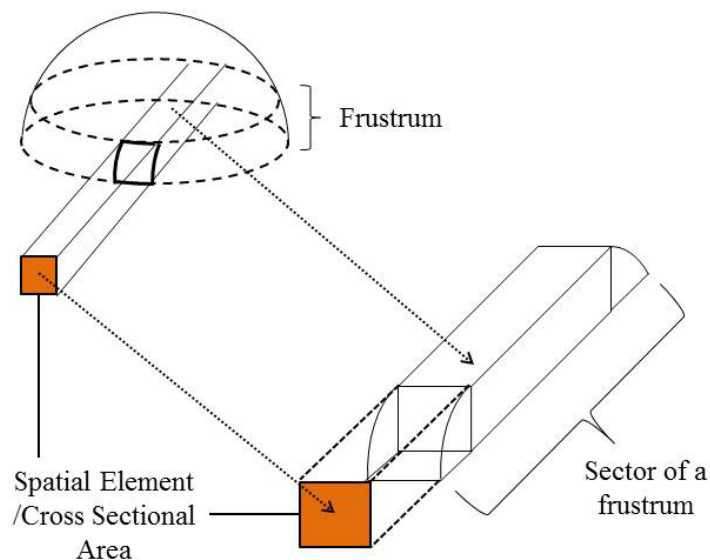
(d) Southern Altitude Temperature Profile



**Figure 6.5:** Altitudinal  $H_3^+$  intensity profiles from Chapter 5 (a and c) and temperature profiles (b and d) of the same regions for the Northern (a and b) and Southern (c and d) aurora. The red shaded regions denote the uncertainty in the temperature as measured from the noise in the intensities of the spectral bins used.

## 6.7 Calculating Densities

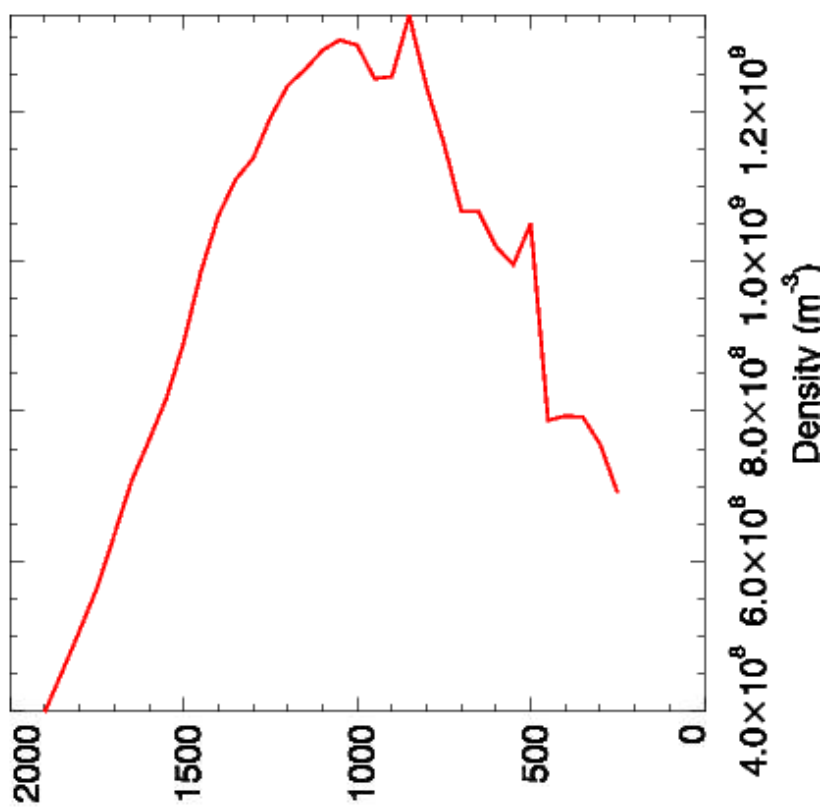
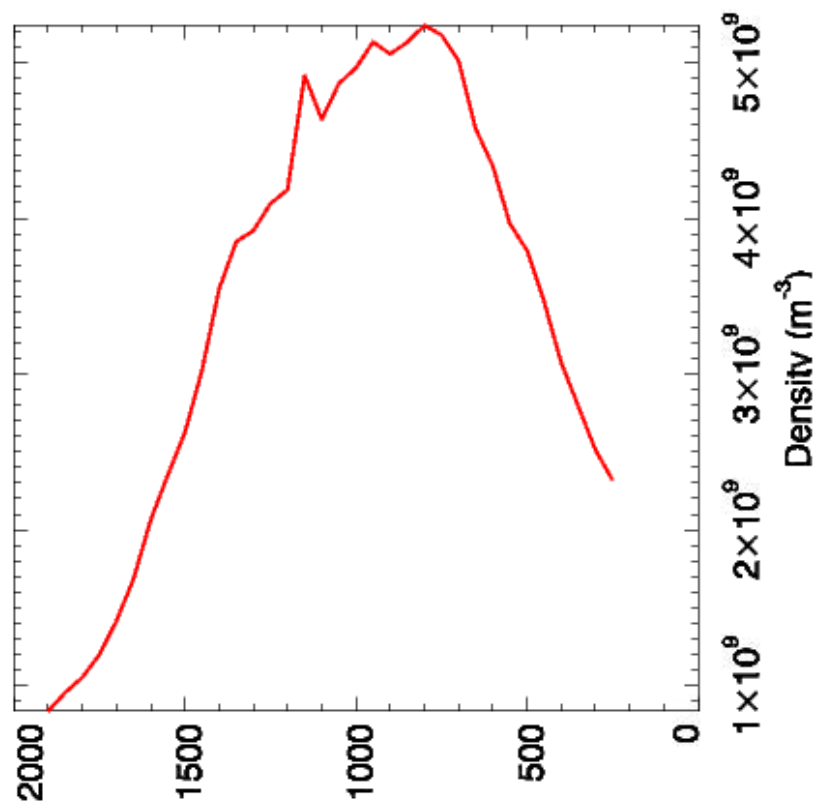
Having calculated the temperature it was then possible to derive the density of  $\text{H}_3^+$ . This was done using the intensities from our maps in conjunction with a model of  $\text{H}_3^+$  emission at the temperatures derived for the same spatial regions. With each spectral bin that is used, a gaussian is applied to the calculated emission of each spectral line to ensure that the resultant emission matches that which would be resolved by the VIMS instrument. Summing these variables over the spectral range used (specifically the bins contained within the maps) provides the emission of a single molecule at the measured temperature, thus dividing the total emission of each element of the map by this energy yields the ion density for that region. Due to the size of the uncertainties across the temperature profiles that are shown in Section 6.6, it was necessary to use an average temperature taken from the region 1000-1500 km above the 1 bar level. Though the ideal scenario would have been to use the temperature profile verbatim, it was found to produce densities that became nonsensical due to the noise in the data.



**Figure 6.6:** A diagram of the cross sectional area of frustum created by the intersect of a spatial bin from Figure 5.8 with the shells  $A_{1,2}$ ,  $A_{2,1}$  and  $A_{3,0}$  in Figure 5.11.

Since the maps of intensity have been summed over all longitudes and each spatial bin in the map has only two dimensions (latitude and altitude), the initial calculate densities were column densities ( $\text{m}^{-2}$ ) instead of volumetric densities ( $\text{m}^{-3}$ ). In Section 5.5.1 we discussed a shell model of the atmosphere used to correct the intensity profiles, here we use this to represent each element of the latitude-altitude as the cross sectional area of the sector of a frustum as viewed from one end (Figure 6.6). This cross sectional area of the frustum sector corresponds to the total emission from the entire volume of the frustum sector, and hence allows us to convert to volumetric densities ( $\text{m}^{-3}$ ) as shown in Figure 6.7. Note that the column densities we measure

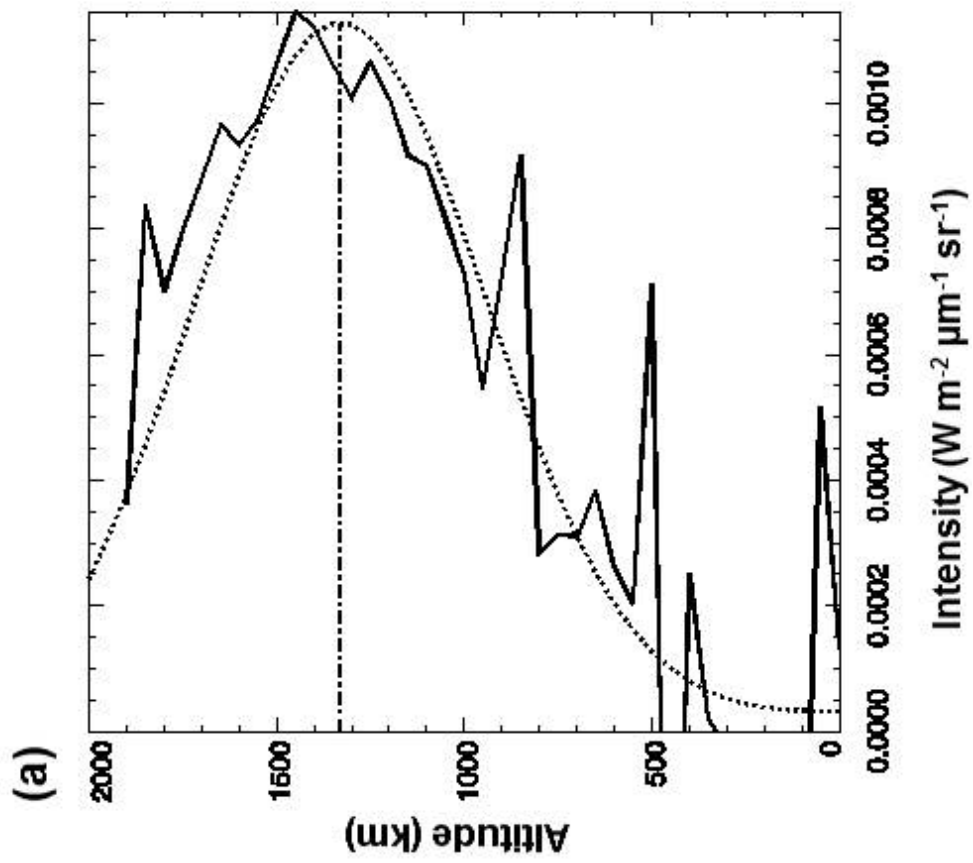
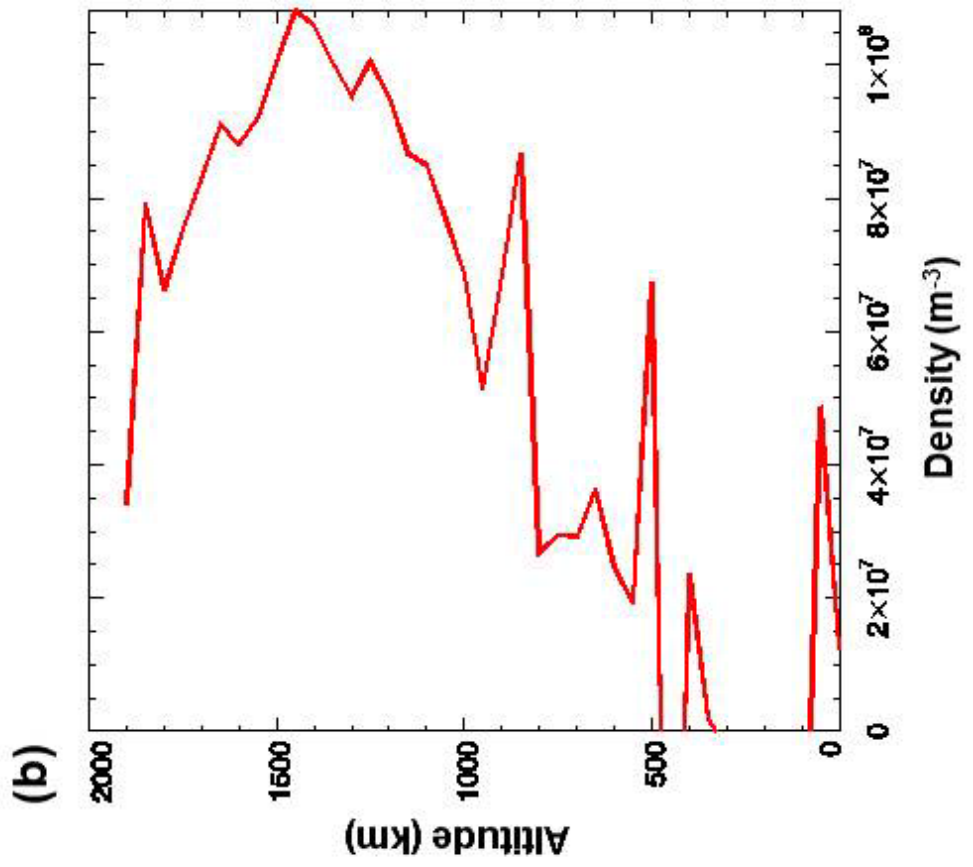
here are for a line of sight which is perpendicular to the auroral curtain, unlike ground based nadir observations which have a line of sight that passed down through the curtain (which we approximate here as being parallel to the auroral curtain). The column densities measured here can be converted to a “nadir” (as seen from directly above) column density by taking our altitudinal volumetric density profiles, then summing these volumetric densities over all altitudes. In this manner, we derive a column density of  $6.2_{-0.3}^{+0.4} \times 10^{15} \text{ m}^{-2}$  ( $T_{H_3^+} = 585 \text{ K}$ ) for the southern auroral profile and  $1.6_{-0.9}^{+3.6} \times 10^{15} \text{ m}^{-2}$  ( $T_{H_3^+} = 549 \text{ K}$ ) for the north. These Figures were based on temperatures averaged between 1000 and 1500 km for the main, maximum and minimum temperature profiles of both hemispheres (as given in Section 6.5). This compares favourably with previous measurements  $7.7 \pm 2.3 \times 10^{15} \text{ m}^{-2}$  for the north and  $1.5 \pm 0.7 \times 10^{15} \text{ m}^{-2}$  for the south from O’Donoghue et al. (2016) and  $7 \pm 1 \times 10^{15} \text{ m}^{-2}$  for the south from Melin et al. (2011). The difference in these column densities would indicate a higher ionisation rate in the southern auroral regions as compared to the north.



**Figure 6.7:** (see and rotate previous page 90° clockwise) Altitudinal volumetric  $\text{H}_3^+$  density profiles of the northern aurora (left) and southern aurora (right) where the temperature used to derive the emission per molecule is taken as the average temperature between 1000 and 1500 km above the 1 bar pressure surface.

#### Section 6.8 Line of sight corrected density profiles

In this Section, we apply the density calculation to the shell subtracted intensity profiles of Figure 5.12. The results of this are shown in Figure 6.8, where it is immediately apparent that unlike the originals, these rescaled profiles display significant noise with the shell subtraction process introducing errors into the data; much in the same as the shell subtracted intensity profiles of Figure 5.12 which have been shown again in Figure 6.8 for comparison. However, in spite of this fact, the process has removed the emission and  $\text{H}_3^+$  populations below 500 km as well has shifted the peak emission and density layers up to an altitude of  $1225 \pm 193$  km for the south and  $1333 \pm 152$  km for the north. As the shell subtraction process propagated an increase in S/N ratio throughout each shell with successive iterations, in this Section we have used the average temperature between 1000 and 1500 km above the 1 bar level. Due to the use of a constant temperature, the resultant altitudinal density profiles (Figure 6.7 and 6.8) have the same shape as the altitudinal intensity profiles that they correspond to. However, these altitudinal density profiles are the first measurement of the variation of  $\text{H}_3^+$  density with altitude, further, they are also the first altitudinal profiles that have been corrected for line of sight bias.



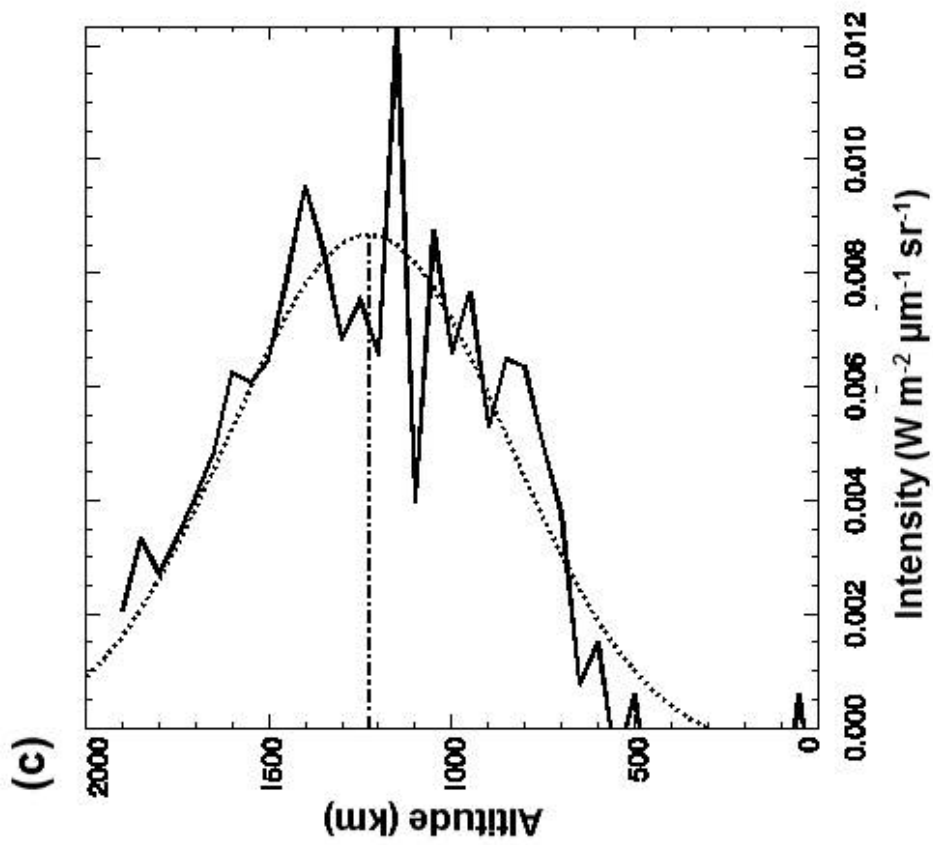
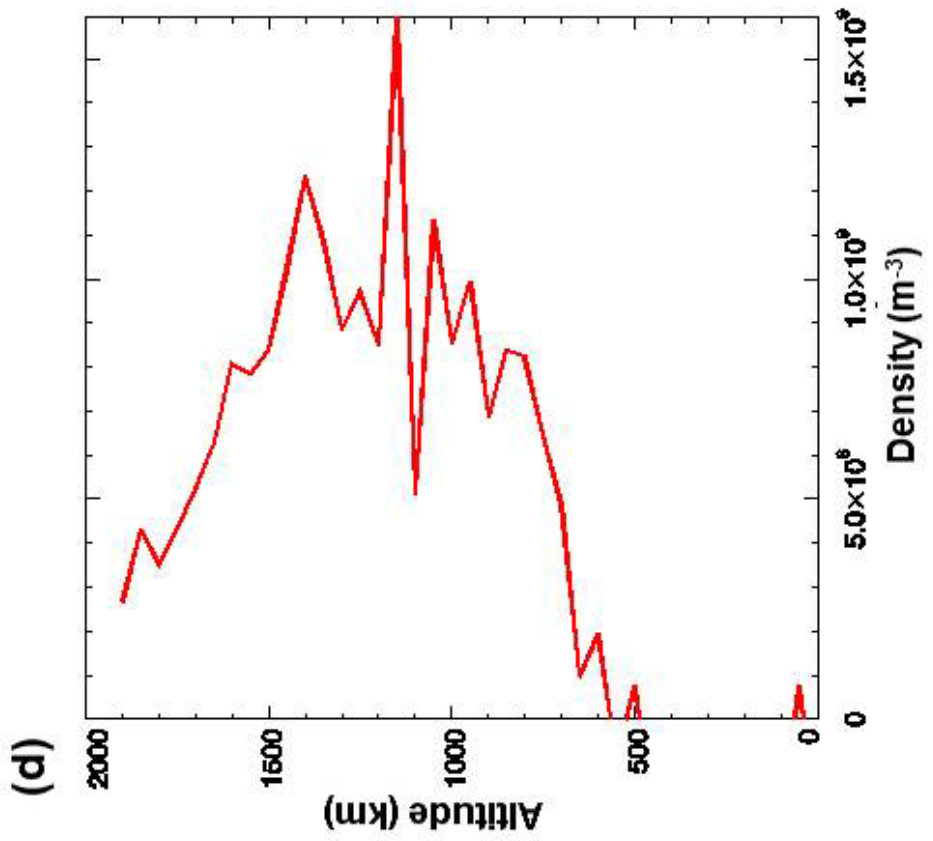


**Figure 6.8:** (previous two pages) Altitudinal intensity (a and c) profiles from Figure 5.12 and their corresponding volumetric density (b and d) profiles of the northern (a and b) and southern (c and d) aurorae rescaled using a recursive shell subtraction technique. The peak emission altitudes are  $1333 \pm 152$  km with a FWHM of  $391 \pm 51$  km for the north and  $1225 \pm 193$  km with a FWHM of  $379 \pm 65$  km for the south.

### Section 6.9 The scale height

One of the aspects of the altitudinal intensity profiles noted in both Stallard et al. (2012a) and Chapter 4 of this thesis is the difference between the altitudinal distribution of the IR and UV emission. A suggested explanation for this was the difference between the scale heights of  $H_2$  and  $H$ , in other words the distance over which each respective population is reduced by a factor of  $1/e$ . In this Section we derive the pressure scale height of  $H_3^+$  from both the temperature measurements and the density measurements. If these values match then it signifies that the  $H_3^+$  population is being redistributed by gravity, whereas if they do not match then the  $H_3^+$  altitudinal distribution that we observe is instead controlled by the  $H_3^+$  production and loss mechanisms.

In Schunk and Nagy (2000) a distinction is made for the scale heights of major and minor ions. Major ions are defined as having a density comparable to the electron density such that they are important to maintaining charge neutrality, whereas minor ions have a density much less than that of the  $e^-$  population and hence have a negligible contribution to charge neutrality. In Figure 1.9 we see that from Galand et al. (2011) the electron number density for the southern auroral region ( $78^\circ$  S) in the region of 1000-1500 km above the 1 bar level is of the order of  $10^4$ - $10^5$   $\text{cm}^{-3}$ , which can also be expressed as  $10^{10}$ - $10^{11}$   $\text{m}^{-3}$ . In Figure 6.8 we see that our maximum number density for  $H_3^+$  in either hemisphere is of the order of  $10^8$ - $10^9$   $\text{m}^{-3}$ . Hence we assume here that  $H_3^+$  is a minor ion and use the pressure scale as defined in equation 6.6 assuming a constant temperature (which is the same as the pressure scale height derived in Section 1.2.1) for the altitude range 1000-1500 km. We use the average  $H_3^+$  temperature for this altitude range from Figure 6.5;  $549^{+34}_{-12}$  K for the north and  $585^{+6}_{-29}$  K for the south.

$$H = \frac{kT}{Mg} \quad (6.6)$$

Where  $H$  is the distance over which the pressure changes by a factor of  $1/e$  (in km),  $k$  is the Boltzmann constant,  $T$  is the temperature (K),  $M$  is the molecular mass (which for  $H_3^+$  is  $5.0149 \times 10^{-27}$  kg) and  $g$  is the gravitational field strength of Saturn (assumed to be constant  $9.0 \text{ N.kg}^{-1}$ ). By substituting in the average temperatures and their associated uncertainties into equation 6.6

we derive the pressure scale heights, which for the north is  $144_{-7}^{+10}$  km and for the south is  $154_{-15}^{+3}$  km.

We measure the number density scale height by considering the peak altitudinal  $H_3^+$  density and distance over which the altitudinal density profile falls to a value that is  $1/e$  smaller than this peak. By performing a linear fit of this region for the shell subtracted altitudinal density profiles we find the number density scale heights. These were then be converted into pressure scale heights (assuming the same constant temperature for the north and south) using equation 6.7 (from Schunk and Nagy, 2000).

$$\frac{1}{H} = \frac{1}{H_p} - \frac{1}{T}, \quad (6.7)$$

where  $H_p$  is the number density scale height. From this we find the pressure scale heights to be  $212_{-5}^{+2}$  km for the north and  $181_{-1}^{+2}$  km for the south. The uncertainty estimates came from substituting in the maximum and minimum temperature uncertainties into equation 6.7. These results are summarised in Table 6.2.

Hemisphere	Temperature derived pressure scale height	Density derived pressure scale height
North	$144_{-7}^{+10}$ km	$212_{-5}^{+2}$ km
South	$154_{-15}^{+3}$ km	$181_{-1}^{+2}$ km

**Table 6.2:** A summary of the pressure scale heights as derived from the average temperature between 1000-1500 km and from the density profiles of Figure 6.5 (above the peak density).

## Section 6.10 Discussion

To summarise our key results, we find the altitudinal structure of the temperature profiles to be different for the northern and southern aurorae, but that both aurorae consistently have temperatures in excess of 500 K. In considering the average temperature between 500 and 1500 km above the 1 bar level, we find the southern aurora is on average hotter than the north by 36 K. The temperature range for peak emission layer of both auroral regions averages around  $580 \pm 20$  K. We find the northern and southern aurorae to have different variations of temperature with altitude as shown in Figure 6.5; the south begins at 530 K at 500 km above the 1 bar level and increases to 600 K by 1500 km with an average temperature between 1000 km and 1500 km of  $585^{+6}_{-29}$  K, whereas the north has a temperature of 570 K at 500 km and decreases slowly with altitude, averaging at  $549^{+34}_{-12}$  K between the altitudes of 1000 and 1500 km above the 1 bar level. From these temperatures and intensity profiles we calculate a nadir column density of  $6.2^{+0.4}_{-0.3} \times 10^{15} \text{ m}^{-2}$  for the southern aurora and  $1.6^{+3.6}_{-0.9} \times 10^{15} \text{ m}^{-2}$  for the northern aurora. In terms of the shape of the profile we find the peak  $\text{H}_3^+$  densities are coincident with the peak emission altitudes with a cut off at 500 km above the 1 bar level (as shown in Figure 6.8); this is due to the fact that we used a constant temperature in the calculation of the density profiles.

As suggested in Chapter 5, this could also be attributed to a bias in the observations whereby the southern aurora has been sampled during times of greater particle precipitation and more intense auroral activity as compared to the north. However, in consideration of the results of O'Donoghue et al. (2014) and (2016) as discussed in Chapter 5 and briefly in Section 6.6, it seems very likely that the difference in intensity, temperature and density of the northern and southern auroral ovals is due to a physical cause. In both O'Donoghue et al. (2014) and (2016) they measure the southern auroral oval to be brighter and hotter than the north and attributed this to the north-south asymmetry in the magnetic field strength leading to an overall greater total heating rate and a broader latitudinal range of particle precipitation in the south. With a higher overall heating rate there is an increase in the ambient temperature of the atmosphere and therefore an increase in  $\text{H}_3^+$  emission intensity. A further contributing factor is that the majority of the observations used in this study were taken before the 2009 equinox; this means that the south has received a greater influx of solar irradiance on average than the north, though this contribution to the ion density would be small compared to the magnetic field asymmetry. Therefore the south will have had a higher average ionisation rate than the north over the latitudinal range that we have sampled for the aurorae (70-80°), a fact which is reflected in the difference in the column densities,  $6.2^{+0.4}_{-0.3} \times 10^{15} \text{ m}^{-2}$  for the southern auroral profile and

$1.6_{-0.9}^{+3.6} \times 10^{15} \text{ m}^{-2}$  for the northern. The combination of these factors accounts for the difference in  $\text{H}_3^+$  emission intensity between the two hemispheres.

### Section 6.10.1 $\text{H}_3^+$ temperature comparisons

Comparing the altitudinal temperature profiles in Figure 6.5 with the models in Moore et al. (2009) in Figure 6.9 and Tao et al. (2011) in Figure 6.11, it is apparent that there does not seem to be a single shape to the profile for both hemispheres. Some measurements of the upper atmosphere suggest that the neutral temperature profile should remain relatively constant (Hubbard et al., 1997, Smith et al., 1983), as is seen in the northern  $\text{H}_3^+$  temperature profile (within uncertainties). Models such as Moore et al. (2009) show that the  $\text{H}_3^+$  temperature profile should increase through the thermosphere from the 1 bar level for about 1000 km (at low to mid latitudes), at which point the temperature plateaus in the exosphere. Likewise, Tao et al. (2011) also suggest this varying temperature  $\text{H}_3^+$  structure (for auroral latitudes), which we observe in the southern auroral  $\text{H}_3^+$  temperature profile, though the profile does not completely level off, the rate of increase is certainly curbed, and given the uncertainty range at higher altitudes, it is possible for the temperature to remain relatively constant across the exospheric range depicted in Moore et al. (2009) and Tao et al. (2011). With the temperature changing relatively little with altitude above the thermosphere (above the peak emission altitude), we conclude that the variation in  $\text{H}_3^+$  emission intensity in this region as seen in Chapter 5 is dominated by the population density of  $\text{H}_3^+$  and therefore the production/destruction rates which are governed by atmospheric density and particle precipitation.

On comparing the average temperature over the range of 1000-1500 km above the 1 bar level with previous studies, we find that our temperature measurements are consistently higher; O'Donoghue (2016) measured an average of 404 K for the northern dayside aurora and 460 K for the southern dayside aurora, Melin et al. (2007) measured an average auroral temperature (for both north and south) of  $\sim 400 \pm 50$  K. However, there are higher measurements such as in O'Donoghue et al. (2016) where individual observations of the main oval temperature reached  $583 \pm 54$  K,  $506 \pm 58$  K and  $501 \pm 48$  K. These studies focus on smaller sets of observations at specific local times compared to this study where we use the long term average of 511 observations averaged over all local times. Whilst our study does incorporate the local times observed in Melin et al. (2007) and O'Donoghue et al. (2016), it is possible that the global average has led to higher  $\text{H}_3^+$  temperatures measurements;  $549_{-12}^{+34}$  K for the north and  $585_{-29}^{+6}$  K for the south. In other words, localised  $\text{H}_3^+$  temperatures may be lower on local scales, but the global average is closer to our measurements which we interpret as the long term

average. With better local time coverage, it would be possible to measure the temperature variation with respect to local time. With this profile, it may be possible that we would observe similar temperatures to O'Donoghue et al. (2016) and Melin et al. (2007) on local scales.

### Section 6.10.2 H<sub>3</sub><sup>+</sup> density comparisons

Here we compare our shell subtracted density altitude profiles with the models of Tao et al. (2011) shown in Figure 6.9 and Moore et al. (2009) in Figure 6.11. We have used their H<sub>3</sub><sup>+</sup> density profiles modelled for 10 keV electrons as the primary energy range of electrons that generate the UV aurora has been estimated at 10-18 keV (Gerard et al., 2009). For this energy range, the modelled altitudinal density profile from Tao et al. (2011) does show a similar shape and distribution to our observed profile (Figure 6.12), however we measure H<sub>3</sub><sup>+</sup> densities that are much lower than their model suggests; the peak H<sub>3</sub><sup>+</sup> density in the southern aurora is measured at  $1.59 \times 10^9 \text{ m}^{-3}$  and the north is  $1.08 \times 10^8 \text{ m}^{-3}$  as compared to the modelled peaks which are of the order of magnitude of  $10^{10} \text{ m}^{-3}$ . We account for this difference by considering the fact that our measured intensities are smaller than the intensity used in the in Tao et al. (2011) as demonstrated in Chapter 5. Further, our measured temperatures are higher by approximately 100 K which increases the emission per molecule and therefore reduces our observed densities. As can be seen in Figure 6.12 there is also a disparity in the altitudes of our measured densities and those modelled in Tao et al. (2011), which peaks at roughly 1600 km above the 1 bar level. Given that the ion density profiles in this model were not constrained by ion density measurements, their model may not have a realistic input for the interaction of the precipitating electrons with the thermosphere such that ion populations peak at a higher altitude. It would be an interesting future development to see what results their model would produce given the constraints on intensity, density and temperature from our observations.

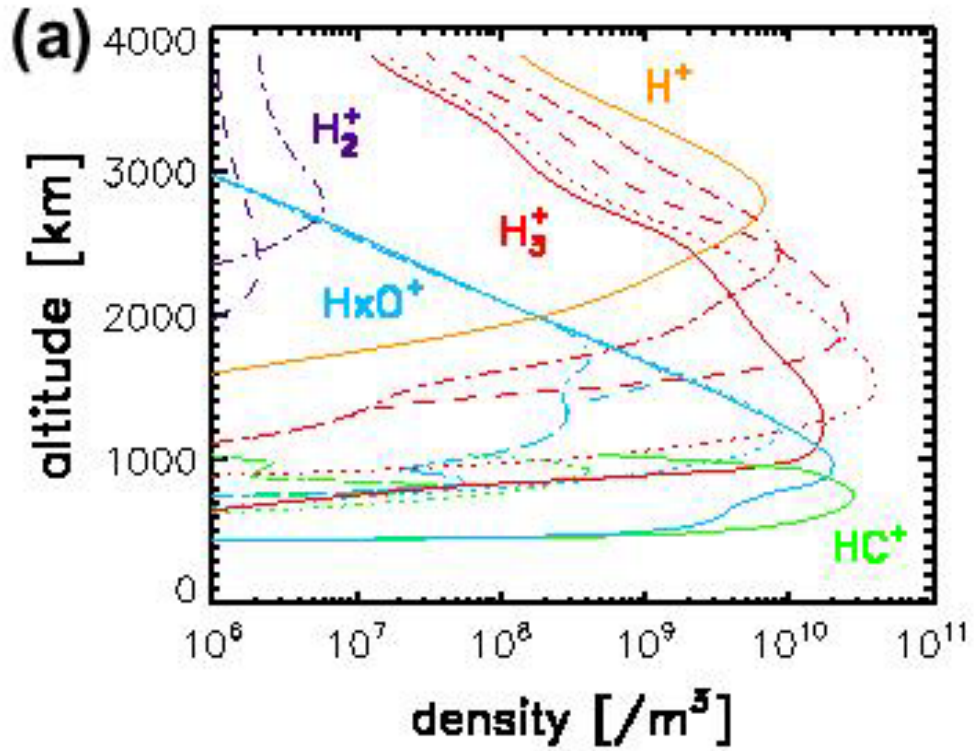


**Figure 6.9:** Figure 8 (a) from Tao et al. (2011) showing the altitudinal density profiles (a) of the species  $\text{HC}^+$  (green),  $\text{H}_x\text{O}^+$  (light blue),  $\text{H}_3^+$  (red),  $\text{H}_2^+$  (purple) and  $\text{H}^+$  (yellow) generated by precipitating electrons a various energies: 0.1 keV (dot dashed lines), 1 keV (dashed lines), 10 keV (dotted lines) and 100 keV (solid lines).

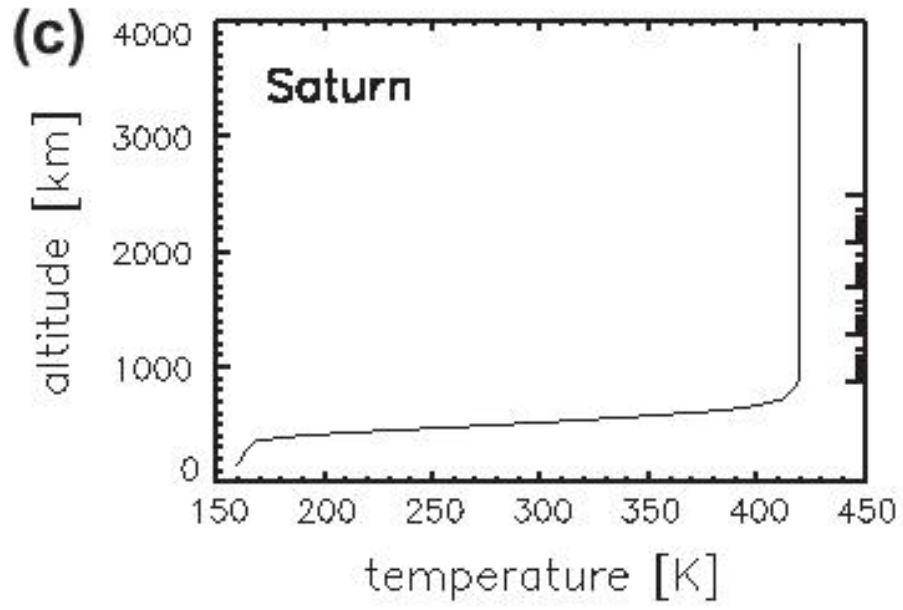


**Figure 6.10:** Figure (c) from Tao et al. (2011) showing the high latitude neutral temperature model of Gerard et al (2009).

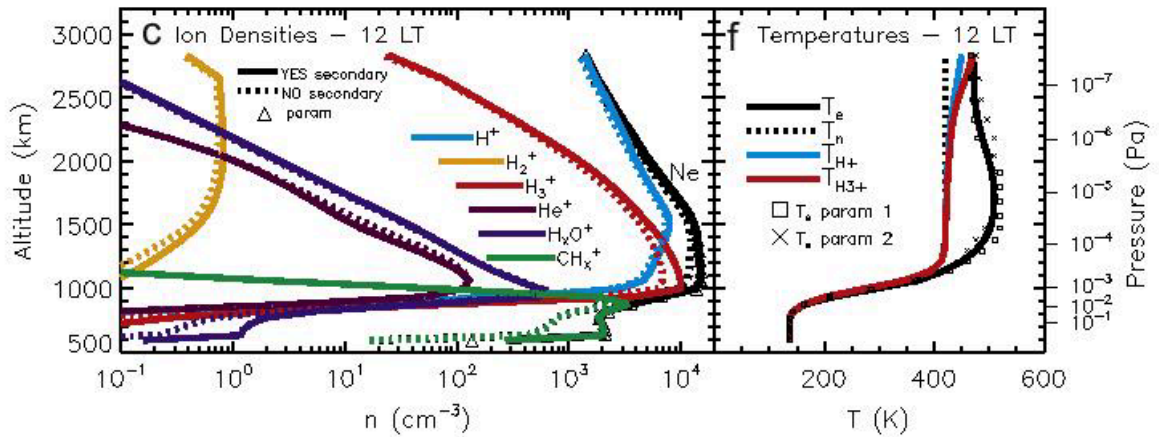


**Figure 6.11:** Figure 1 of Moore et al. (2009) the results from the Saturn Thermosphere Ionosphere Model for  $30^\circ$  N using TIMED/SEE solar maximum conditions during the Saturn equinox. (c) Ion and electron densities at local noon. Solid curves represent calculations that have accounted for secondary production, while dotted curves represent calculations that have not. Triangles give the electron densities that result from the parameterizations of the secondary production rates. (f) Ion and electron temperatures at local noon. The cross and square symbols correspond to electron temperatures that have been derived using the two different parameterizations of the electron heating rates. For the full version of this Figure, please refer to Figure 1.6 in Chapter 1. This model assumed a temperature profile that was consistent with observed temperature measurements

The model of Moore et al. (2009) is shown above in Figure 6.11. The densities of  $\text{H}_3^+$  calculated from this model (the blue line in Figure 6.12) are generally much higher than our measured auroral densities. We do not, however, observe significant  $\text{H}_3^+$  emission at the latitude of the model profile of Moore et al. (2009). The only non-auroral region that we were able to calculate temperatures for was between 30 and 60 degrees north which show up as regions of purple in Figure 6.4, and provided an average temperature of  $287^{+82}_{-22}$  K for the altitude range of 500-1500 km above the 1 bar level. Whilst this is northward of the region modelled by Moore et al. (2009), this temperature does lie in the middle of the temperature range for the same altitudinal region in Figure 6.11. Comparing their modelled  $\text{H}_3^+$  densities to our auroral densities it would seem that Moore et al. (2009) have overestimated the ionisation rate. The model focuses on the ionisation rate from Solar EUV photons and secondary electrons, but not particle precipitation, which suggests that the modelled densities are higher than what we would measure for the same latitudinal regions; were this possible. On the other hand, the modelled densities of Moore et al. (2009) were for solar maximum conditions during the equinox of 2002 whereas our observations have come from a period of solar minimum (2005-2010), during which time the energy influx of solar photons may have been insufficient to generate the

population seen in their model. It would be possible to distinguish between these two explanations by using observations taken during solar maximum conditions. Alternatively, this model could be run for the 2009 equinox which occurred during a solar minimum.

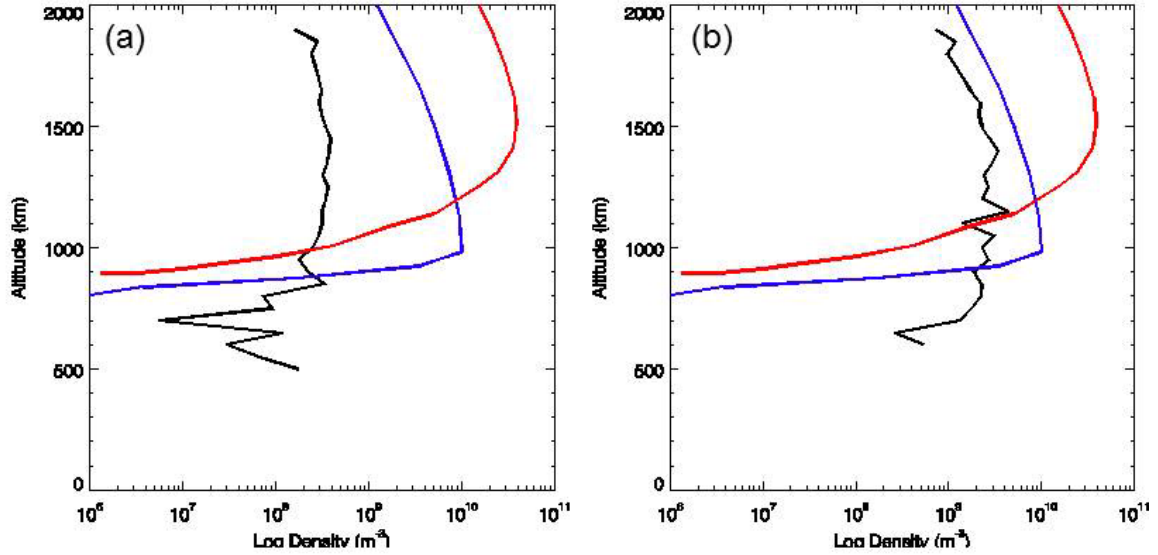


**Figure 6.12:** The shell subtracted altitudinal  $H_3^+$  density profile (black) for the north (a) and south (b) shown in comparison with the altitudinal density profile of Tao et al. (2011) modelled for 78° south (red) and Moore et al. (2009) modelled for 30° north (blue).

### Section 6.10.3 The effect of scale height

When comparing the scale heights calculated from equation 6.6 ( $134_{-2}^{+1}$  km for the north and  $135_{-2}^{+9}$  km for the south), to those measured from the altitudinal density profiles using a linear fit of the densities above the peak emission altitude and equation 6.7 ( $212_{-5}^{+2}$  km for the north and  $181_{-1}^{+2}$  km for the south), we find significant differences. The pressure scale height from equation 6.6 only considers the effects of gravity, mass and temperature. However, the  $H_3^+$  population is dependent on the key components of its production mechanism; the population density of  $H_2$  as well as the energy and amount of electron particle precipitation as described in Chapter 1. Given that the pressure scale height calculated from the  $H_3^+$  temperatures are not the same as the pressure scale heights measured from the distribution of  $H_3^+$  density (i.e. the pressure scale height derived from the rate at which the density decreases is greater than that predicted by the temperature derived pressure scale height), we conclude that the distribution of  $H_3^+$  is governed by its production and loss mechanisms.

# Chapter 7

## *Conclusions and future developments*

In this thesis we examine the properties of  $\text{H}_3^+$  infrared aurorae of Saturn as viewed by the VIMS instrument aboard Cassini. We have conducted two studies, the findings of which are detailed in the sections below. This is followed by an outline of how the research of this thesis could be further developed and applied, not only for Saturn's infrared aurora but also Jupiter.

### Section 7.1 The effect of limb alignment on peak emission altitude

In Chapter 4 we discussed a study of the peak emission altitude of the  $\text{H}_3^+$  infrared aurorae. This work followed on from Stallard et al. (2012a), which examined 9 observations that were assumed to be aligned with the limb, yielding a peak emission altitude of  $1155 \pm 25$  km above the 1 bar level. In light of this work, we developed a technique for profiling the altitudinal distribution of the auroral emissions and subsequently applied this technique to measure the effects of viewing geometry on the measured peak emission altitude for 20 different observations of the southern auroral oval. Analysis of the alignment and altitudinal distribution of emission revealed that the viewing geometry engenders a line of sight bias that dominates the variation in the peak emission altitude (as opposed to actual variation in the location of the peak emission). By applying a fit to the peak emission altitudes and their associated degrees of alignment, we determined that an auroral curtain that was perfectly aligned with the limb of the planet would have a peak emission altitude of  $1219 \pm 119$  km.

### Section 7.2 Intensities

Further developments were made in the profiling technique of Chapter 4 such that we were able to map the emission above the limb of 511 observations, providing a more statistical approach to analysing the aurora with respect to both latitude and altitude (Chapter 5). When the auroral regions were sampled between  $70^\circ$  and  $80^\circ$  latitude for each hemisphere we found a peak emission altitude of  $1333 \pm 152$  km for the north and  $1225 \pm 193$  km for the south. Comparing the new peak emission altitude from the southern altitude profile to the aligned peak emission altitude ( $1215 \pm 119$  km) of Chapter 4, we found strong agreement between the two. Though peak emission latitude of both the northern and southern auroral ovals was found to be  $74^\circ \pm 1^\circ$ ,

the latitudinal distribution of emission was broader in the south than the north (the FWHM of the northern latitudinal fit is  $3^\circ \pm 1^\circ$  as compared to  $5^\circ \pm 2^\circ$  for the south). We also noted that the intensity of the southern aurora is on average  $\sim 5$  times brighter than the north. We explore this further in Section 7.5.

When compared to Tao et al. (2011), we found their model altitudinal emission profile is a great deal brighter, by around an order of magnitude, than the average intensity of the  $H_3^+$  aurora measured in this study. Further, the emission profile of Tao et al. (2011) yielded a peak emission altitude that is around 300 km higher than both those measured from our northern and southern altitudinal auroral profiles. Given that our altitudinal intensity profiles consisted of multiple spectra lines compared to the Tao et al. (2011) which modelled a single transition line, we surmised that the intensities from this model ( $0.053 \times 10^{-5} \text{ W m}^{-2} \text{ sr}^{-1}$ ) were likely much higher than the average. To ascertain why this would be, we derived temperatures and densities.

### Section 7.3 Temperatures

Melin et al. (2007) measured temperatures of  $380 \pm 70 \text{ K}$  and  $420 \pm 50 \text{ K}$  in the southern main auroral oval and the remaining southward Polar Regions respectively from multiple observing campaigns using the spectrometer CGS4 at the United Kingdom Infrared Telescope (UKIRT). O'Donoghue et al. (2016) used the ground based 10m W. M. Keck telescope to observe the regions of the aurorae in both the north and the south simultaneously in April of 2013. Their average measurements of the temperature yielded  $404 \pm 13 \text{ K}$  for the northern dayside and  $460 \pm 17 \text{ K}$  for the southern dayside. Koskinen et al. (2015) used a wide variety of stellar and solar occultations taken between the years 2004 and 2015 and measured the exospheric temperatures to be in the range of 380 – 590 K. As described in Section 1.4.5, the consensus of these measurements and several others besides is that the temperature of the aurora generally lies in the range of 400-600 K. Using the spectra contained in our latitude-altitude intensity maps we were able to derive the first ever altitudinal temperature profiles for both auroral regions for our data set. We found the northern and southern aurorae to have different variations of temperature with altitude as shown in Figure 6.5; the south began at 530 K at 500 km above the 1 bar level and increases to 600 K by 1500 km with an average temperature between 1000 km and 1500 km of  $585 \pm_{29}^6 \text{ K}$ , whereas the north had a temperature of 570 K at 500 km and decreased slowly with altitude, averaging at  $549 \pm_{12}^{34} \text{ K}$  between the altitudes of 1000 and 1500 km above the 1 bar level. The altitudinal structure of the temperature profiles was found to be different for the northern and southern aurorae however; both aurorae consistently have temperatures in the range of prior measurements.

We found that our temperatures were significantly higher than the estimated temperatures used in the model of Tao et al. (2011) and Moore et al. (2010). These models show that the temperature profile should increase from the 1 bar level for about 1000 km, at which point the temperature plateaus. We observe this temperature structure in the southern auroral temperature profile, though the profile does not completely level off, the rate of increase is certainly curbed, and given the error range at higher altitudes, it is possible for the temperature to remain relatively constant across the range depicted in Moore et al. (2009) and Tao et al. (2011). The northern profile however seemed to remain almost constant with altitude. This difference in structure may be due to line of sight bias as these temperatures are derived from non-shell subtracted intensity profiles. Alternatively, it could be a real structural difference. The only way to distinguish between these answers for our study would be to add more data; perhaps by adding Cassini VIMS observations from the years 2011 to 2017, such the S/N ratio of the shell subtracted intensity profiles is good enough to derive temperatures. With the relative stability of the temperature with altitude, we conclude that the variation in  $\text{H}_3^+$  emission intensity as seen in Chapter 5 is dominated by the population density of  $\text{H}_3^+$  and therefore the production/destruction rates which are governed by atmospheric density and particle precipitation.

#### Section 7.4 Densities

Aside from the density profiles presented in this thesis, as of writing there are currently no known measurements of the altitudinal structure of  $\text{H}_3^+$  density in the auroral regions. Previous measurements of the density of  $\text{H}_3^+$  have been expressed in terms of the column density; the number of  $\text{H}_3^+$  molecules along the line of sight in an area of observation. O'Donoghue et al. (2016) measured the column densities to be  $7.7 \pm 2.3 \times 10^{15} \text{ m}^{-2}$  for the northern dayside and  $1.5 \pm 0.7 \times 10^{15} \text{ m}^{-2}$  for the southern dayside. In contrast Melin et al. (2011) measured a higher southern auroral column density of  $7 \pm 1 \times 10^{15} \text{ m}^{-2}$  in 2008, which suggest some margin of variability in the auroral ion column density. These were case studies of small number of observations and as such are limited in their ability to constrain the average density of  $\text{H}_3^+$  in the auroral regions. Hence, using our intensity and temperature measurements of Section 7.2 and 7.3 we calculated altitudinal density profiles. When summed over all altitudes we measure a nadir column density of  $6.2_{-0.3}^{+0.4} \times 10^{15} \text{ m}^{-2}$  for the southern aurora and  $1.6_{-0.9}^{+3.6} \times 10^{15} \text{ m}^{-2}$  for the northern aurora. In terms of the shape of the profile we found the peak  $\text{H}_3^+$  densities are coincident with the peak emission altitudes with a cut off in the  $\text{H}_3^+$  population at 500 km above the 1 bar level (as shown in Figure 6.8); this is due to the fact that we used a constant temperature in the calculation of the density profiles.

Comparing our measured density altitude profiles with the model of Tao et al. (2011) for 10 keV electrons, there was a similarity shape and distribution to our observed profiles, however we measured  $\text{H}_3^+$  densities that were much lower than their model suggests; our peak  $\text{H}_3^+$  density in the southern aurora was measured at  $1.59 \times 10^9 \text{ m}^{-3}$  and the north is  $1.08 \times 10^8 \text{ m}^{-3}$  as compared to the modelled peaks which are of the order of magnitude of  $10^{10} \text{ m}^{-3}$ . We accounted for this difference by considering the fact that our measured intensities are smaller than those of Tao et al. (2011) as demonstrated in Chapter 5. Further, our measured temperatures were higher by approximately 100 K which increases the emission per molecule and therefore reduced our observed densities. There is also a disparity in the altitudes of our measured densities and those modelled in Tao et al. (2011), which peaks at roughly 1600 km above the 1 bar level. Given that the ion density profiles in this model were not constrained by ion density measurements (which we measure here for  $\text{H}_3^+$ ), their model may not have a realistic input for the interaction of the precipitating electrons with the thermosphere such that ion populations peak at a higher altitude.

#### Section 7.5 North – South asymmetry

In comparing our observed properties of the northern and southern aurorae, we find a distinct asymmetry such that the southern aurora is hotter, brighter and more dense than the northern aurora. This has been observed before, as in O'Donoghue et al. (2016), where the southern auroral oval was found to be brighter and hotter than the north, which was attributed to the north-south asymmetry in the magnetic field strength and the resultant difference in heating rates as the lower heating rate in the north also means a lower energy input for the excitation of  $\text{H}_3^+$ . O'Donoghue et al. (2014) also observed a temperature asymmetry with the southern auroral region being 56 K hotter than the north, a difference which they attributed to the inverse relationship between the thermospheric heating rate (joule heating and ion drag) and the magnetic field strength. In considering the average temperature between 500 and 1500 km above the 1 bar level, we find the southern aurora is on average hotter than the north by 36 K, which would partly help explain the difference in brightness (Section 7.1) as the higher temperature would lead to a brighter auroral emission in the south. It should be noted however that a higher altitude also means a lower ambient  $\text{H}_2$  population and therefore a lower reaction rate for the production of  $\text{H}_3^+$ . Using the STIM model O'Donoghue et al. (2014) also noted that the north-south magnetic field asymmetry leads to a wider latitudinal distribution of particle precipitation and hence ionisation in the southern auroral region. This is reflected by the wider distribution of intensity in the latitudinal profile of emission for the south as compared to the north. Thus, when comparing the same latitudinal ranges (70-80°) in both hemispheres, the southern aurora has a higher  $\text{H}_3^+$  density overall. Further, the data has been sampled from the

years 2005 to 2010 where the North has passed from autumn through winter to spring, which could engender a seasonal temperature difference as well as a difference in the photo-ionisation rate from insolation. This explains why we found the northern auroral oval to be dimmer and narrower than the south, a result which is in agreement with the UV observations of Nichols et al. (2009) and was predicted in Badman et al. (2011). We conclude that the southern aurora must have a higher average ionisation rate (over the latitude range 70-80°) than the north as the column densities derived from our altitudinal profiles are  $6.2_{-0.3}^{+0.4} \times 10^{15} \text{ m}^{-2}$  for the southern auroral profile and  $1.6_{-0.9}^{+3.6} \times 10^{15} \text{ m}^{-2}$  for the northern.

### Section 7.6 Pressure scale height and $\text{H}_3^+$ altitudinal structure

In Chapter 6 we also examined the scale height of  $\text{H}_3^+$  (the distance over which the population density is reduced by a factor of e). We find that the pressure scale heights derived from the average temperature of the aurorae do not match those derived from their respective altitudinal density profiles. Hence, we conclude that the distribution of  $\text{H}_3^+$  with altitude is dominated by its production and loss mechanisms.

### Section 7.7 Future developments

In this thesis we have presented the results of a statistical analysis of the aurora for 511 observations. This study has produced completely new and scientifically valuable results which can be used to greatly improve our understanding of the aurora of Saturn and subsequently the systems connected to it, such as the neutral upper atmosphere and the magnetosphere; as will be discussed in Section 7.7.3. However, this is by no means the end of what our projection technique can provide; rather it is only the beginning of the program's full potential.

#### Section 7.7.1 Mapping the body emissions

This thesis has largely focused on the limb emission however there is still a wealth of body emission that could still be analysed using the technique from our statistical study in Chapter 5 and 6. The projection technique which we developed for our intensity maps could be adapted to focus only on the latitude and local time on the body, and in doing so provide a global map of emission. Initial tests of this idea were attempted however the data set of this thesis was insufficient to achieve global coverage. In studying region above the limb, we avoided the emissions from deeper in the atmosphere, however, on the body of the planet these emissions

cannot be avoided and therefore require new subtraction factors for each year (i.e. we could not simply use those calculated for the limb emissions). Due to time constraints, we were unable to complete this new line of investigation, though it has great potential. Not only could it provide analysis of the local time/latitude variation of the aurorae in both hemispheres, with enough data and a high enough S/N ratio these global maps could potentially observe the average effects of the ring rain on the upper atmosphere as first observed by O'Donoghue et al. (2013).

#### Section 7.7.2 Broadening the data set

The observations used in the statistical study of Chapters 5 and 6 spanned the years 2005 to 2010. There are, however, many more years-worth of data that have subsequently been collected since, and there shall more thereafter until the end of the Cassini mission. Were the appropriate observations from these more recent years to be included in our study, we would be able to determine the properties of the aurora with even greater accuracy (via an improved S/N ratio). Furthermore, with a larger data set, it is possible that we would achieve full planetary coverage, such that we would be able to analyse the auroral emission with respect to local time. Further, splitting the data set into pre and post equinox groups would potentially provide insight into the seasonal variations in the aurora (or lack thereof).

#### Section 7.7.3 Constraining models

One issue that Tao et al. (2011) faced for their model was the absence of altitudinal observations of the temperature and density structure of  $H_3^+$ . Now that we have these measurements from our statistical study, it would be very valuable to see what new results the model of Tao et al. (2011) would produce based on our altitudinal profiles of these properties. Further, with an increase in the size of the data set (Section 7.7.1) it is possible that the S/N ratio of non auroral latitudes would improve. These regions, which we have mostly ignored due to the lack of measurable  $H_3^+$  emission, would become viable areas for analysis and hence direct comparison with models of the upper atmosphere closer to the equator such as Moore et al. (2009). Should this work for all latitudes (both auroral and non auroral alike) we would then have a measure of the global variation of the temperature and  $H_3^+$  population in the thermosphere of Saturn. The temperature measurements would be invaluable for modelling the global circulation and energy distribution.

## Bibliography

- Achilleos, N., Miller, S., Tennyson, J., Aylward, A.D., Mueller-Wodarg, I., and Rees, D., (1998) “*JIM: A time-dependent, three-dimensional model of Jupiter’s thermosphere and ionosphere*”. *Journal of Geophysical Research*, doi:10.1029/20089–20112
- Andre, N., Blanc, M., Maurice, S., et al. (2008). “*Identification of Saturn’s magnetospheric regions and associated plasma processes: Synopsis of Cassini observations during orbit insertion*”, *Reviews of Geophysics*, 46, doi:10.1029/2007RG000238.
- Arridge, C. S., Russell, C.T., Khurana, K.K., Achilleos, N., Andre, N., Rymer, A. M., Dougherty, M. K. and Coates, A. J. (2007), “*The mass of Saturn’s magnetodisc: Cassini observations*”, *Geophys. Res. Lett.*, 34, L09108, doi:10.1029/2006GL028921.
- Badman, S. V., Achilleos, N., Baines, K. H., Brown, R. H., Bunce, E. J., Dougherty, M. K., Melin, H., Nichols, J. D., Stallard, T. (2011), “*Location of Saturn’s northern infrared aurora determined from Cassini VIMS images*”, *Geophys. Res. Lett.*, 38, L03102, doi:10.1029/2010GL046193.
- Badman, S.V., Branduardi-Raymont, G., Galand, M., Hess, S.L.G., Krupp, N., Lamy, L., Melin, H. & Tao, C., (2015), “*Auroral processes at the giant planets: energy deposition, emission mechanisms, morphology and spectra*”, *Space Science Reviews*, vol 187, no. 1-4, pp. 99-179., 10.1007/s11214-014-0042-x
- Badman, S.V., Cowley, S.W.H., (2007), “*Significance of Dungey-cycle flows in Jupiter’s and Saturn’s magnetospheres and their identification on closed equatorial field lines.*”, *Ann. Geophys.* **25**, 941–951, doi:10.5194/angeo-25-941-2007
- Baines, K. H., et al., 2005. “*The atmospheres of Saturn and Titan in the near-infrared: First results of 37 Cassini/VIMS.*”, *Earth, Moon, and Planets*, 96, 119–147, doi:10.1007/s11038-005-9058-2.
- Belenkaya, E.S., Cowley, S.W.H., Nichols, J.D., Blokhina, M.S., Kalegaev, V.V., (2011), “*Magnetospheric mapping of the dayside UV auroral oval at Saturn using simultaneous HST images, Cassini IMF data, and a global magnetic field model.*”, *Ann. Geophys.* 29, 1233–1246 (2011). doi:10.5194/angeo-29-1233-2011

Boudouridis, A., Zesta, E., Lyons, R., Anderson, P. C., Lummerzheim, D., (2003), “*Effect of solar wind pressure pulses on the size and strength of the auroral oval*”, J. Geophys. Res., 108(A4), 8012, doi:10.1029/2002JA009373

Brown, R.H., Baines, K.H., Bellucci, G., Bibring, J-P., Buratti, B.J., Capaccioni, F., Cerroni, P., Clark, R.N., Coradini, A., Cruikshank, D.P., Drossart, P., Formisano, V., Jaumann, R., Langevin, Y., Matson, D.L., Mccord, T.B., Mennella, V., Miller, E., Nelson, R.M., Nicholson, P.D., Sicardy, B., Sotin, C., (2004), “*The Cassini Visual and Infrared Mapping Spectrometer (VIMS) investigation*”, Space Science Review, Volume 115:111-168

Brown, Private communication – The wavelength shift

Bunce, E. J., Arridge, C. S., Clarke, J. T., Coates, A. J., Cowley, S. W. H., Dougherty, M. K., Gérard, J.-C., Grodent, D., Hansen, K. C., Nichols, J. D., Southwood, D. J., Talboys, D. L., (2008) “*Origin of Saturn’s aurora: simultaneous observations by Cassini and the Hubble Space Telescope*”, JGR, VOL. 113, A09209, doi:10.1029/2008JA013257, 2008

Bunce, E. J. (2012), “*Origins of Saturn’s auroral emissions and their relationship to large-scale magnetosphere dynamics, in Auroral Phenomenology and Magnetospheric Processes: Earth and Other Planets*”, Geophys. Monogr. Ser., vol. 197, 397–410, AGU, Washington, D. C., doi:10.1029/2011GM001191.

Clarke, J.T., Grodent, D., Cowley, S.W.H., Bunce, E.J., Zarka, P., Connerney, J.E.P., Satoh, T., (2004), “*Jupiter’s aurora*”, in Jupiter: The Planet, Satellites and Magnetosphere, pp. 639–670

Clarke, J.T., Gérard, J.-C., Grodent, D., Wannawichian, S., Gustin, J., Connerney, J., Crary, F., Dougherty, M., Kurth, W., Cowley, S.W.H., Bunce, E.J., Hill, T., Kim, J., (2005), “*Morphological differences between Saturn’s ultraviolet aurorae and those of Earth and Jupiter.*”, Nature 433(7027), 717–719, doi:10.1038/nature03331

Clarke, J. T., Nichols, J., Gérard, J.-C., Grodent, D., Hansen, K.C., Kurth, W., Gladstone, G.R., Duval, J., Wannawichian, S., Bunce, E., Cowley, S.W.H., Crary, F., Dougherty, M., Lamy, L., Mitchell, D., Pryor, W., Retherford, K., Stallard, T., Zieger, B., Zarka, P., Cecconi, B., (2009), “*Response of Jupiter’s and Saturn’s auroral activity to the solar wind*”, J. Geophys. Res., 114, A05210, doi:10.1029/2008JA013694.

Connerney, J. E. P., (1986), “*Magnetic connection for Saturn’s rings and atmosphere.*”, Geophys. Res. Lett. 13, 773–776

- Connerney, J.E.P. and Waite, J.H., (1984), “*New model of Saturn’s ionosphere with an influx of water from the rings.*”, *Nature* 312(5990), 136–138
- Cowley, S. W. H., Balogh, A., Dougherty, M. K., Dunlop, M. W., Edwards, T. M., Forsyth, R. J., Laxton, N. F., Staines, K. (1996), “*Plasma flow in the jovian magnetosphere and related magnetic effects: Ulysses observations*”, *J. Geophys. Res.*, 101, 15 197– 15 210
- Cowley, S.W.H., and Bunce, E. J., (2003), “*Corotation-driven magnetosphere-ionosphere coupling currents in Saturn’s magnetosphere and their relation to the auroras*”, *Ann. Geophys.*, 21(8), 1691–1707
- Cowley, S.W.H., Bunce, E.J., O’Rourke, J.M., (2004). “*A simple quantitative model of plasma flows and currents in Saturn’s polar ionosphere*”. *J. Geophys. Res.* 109, A05212. <http://dx.doi.org/10.1029/2003JA010375>.
- Cowley, S.W.H., Badman, S.V., Bunce, E.J., Clarke, J.T. Gérard, J.-C., Grodent, D., Jackman, C.M., Milan, S.E., Yeoman, T.K., (2005), “*Reconnection in a rotation-dominated magnetosphere and its relation to Saturn’s auroral dynamics.*”, *J. Geophys. Res.* 110(A2), doi:10.1029/2004JA010796
- Cowley, S.W.H., Arridge, C.S., Bunce, E.J., Clarke, J.T., Coates, A.J., Dougherty, M.K., Gérard, J.-C., Grodent, D., Nichols, J.D., Talboys, D.L., (2008), “*Auroral current systems in Saturn’s magnetosphere: Comparison of theoretical models with Cassini and HST observations.*”, *Ann. Geophys.* 26(9), 2613–2630
- Cravens, T.E., (1987), “*Vibrationally excited molecular hydrogen in the upper atmosphere of Jupiter.*”, *J. Geophys. Res.* 92, 11083–11100, doi:10.1029/JA092iA10p11083
- Dougherty, M.K., Achilleos, N., Andre, N., Arridge, C., Balogh, A., Bertucci, C., Butron, M.E., Cowley, S.W.H., Erdos, G., Giamperi, G., Klassmeir, K-H., Khurana, K.K., Leisner, J., Neubauer, F.M., Russell, C.T., Smith, E.J., Southwood, D.J., Tsurutani, B.T. (2005), “*Cassini Magnetometer Observations during Saturn Orbit Insertion*”, *Science*, 307, 1266–1270.
- Drossart, P., Fouchet, T., Crovisier, J., Lellouch, E., Encrenaz, T., Feuchtgruber, H., Champion, J.P., (1999), “*Fluorescence in the 3 micron bands of methane on Jupiter and Saturn from ISO/SWS observations, in The Universe as Seen by ISO*”, *Eur. Space Agency Spec. Publ.*, ESA SP-427, 169 – 172.
- Dungey, J.W., (1963), “*The structure of the exosphere or adventures in velocity space*”, in *Geophysics, the Earth’s Environment*, p. 503

- Fegley, B. Jr. and Prinn, R.G., (1985), “*Equilibrium and non-equilibrium chemistry of Saturn’s atmosphere: Implications for observability of PH<sub>3</sub>, N<sub>2</sub>, CO and GeH<sub>4</sub>*”, *Astrophys. J.*, 299, 1067-1078
- Festou, M.C., Atreya, S.K., (1983), “*Voyager ultraviolet 1738 stellar occultation measurements of the composition 1739 and thermal profiles of the Saturnian upper 1740 atmosphere.*”, *Geophys. Res. Lett.*, 9, 1147–1150, doi:10.1029/GL009i010p01147.
- Fletcher, L. N., Irwin, P. G. J., Teanby, N. A., Orton, G. S., Parrish, P. D., de Kok, R., Howett, C., Calcutt, S. B., Bowles, N., Taylor, F. W., (2007), “*Characterising Saturn’s vertical temperature structure from Cassini/CIRS.*”, *Icarus*, Volume 189, Issue 2, p. 457-478, doi:10.1016/j.icarus.2007.02.006
- Fletcher, L.N., Greathouse, T.K., Moses, J.I, Guerlet, S., West, R.A., (2016), “*Saturn’s Seasonal Atmosphere: Temperatures, Clouds and Composition*”, in *Saturn in the 21st Century*, Chapter 10, Cambridge University Press, accepted (<http://arxiv.org/abs/1510.05690>)
- Flower, D., (1990), “*Molecular collisions in the interstellar medium*”. Cambridge University Press
- Galand, M., Moore, L., Charnay, B., Müller-Wodarg,, I., Mendillo, M., (2009), “*Solar primary and secondary ionization at Saturn.*”, *J. Geophys. Res.* 114, doi:10.1029/2008JA013981
- Galand, M., Moore, L., Müller-Wodarg, I., Mendillo, M., Miller, S., (2011), “*Response of Saturn’s auroral ionosphere to electron precipitation: Electron density, electron temperature, and electrical conductivity.*”, *J. Geophys. Res.* 116, 9306, doi:10.1029/2010JA016412
- Geballe, T. R., Jagod, M. F., Oka, T. (1993), “*Detection of H<sub>3</sub><sup>+</sup> emission lines in Saturn*”, *Astrophys. J.*, 408, L109.
- Gérard, J.-C., Singh, V., (1982), “*A model of energy deposition of energetic electrons and EUV emission in the Jovian and Saturnian atmospheres and implications.*”, *J. Geophys. Res.* 87, 4525–4532, doi:10.1029/JA087iA06p04525
- Gérard, J.-C., Bonfond, B., Gustin, J., Grodent, D., Clarke, J. T., Bisikalo, D., Shematovich, V., (2009), “*Altitude of Saturn’s aurora and its implications for the characteristic energy of precipitated electrons*”, *Geophys. Res. Lett.*, 36, L02202, doi:10.1029/2008GL036554.
- Gosling, J. T., and Pizzo, V. J., (1999), “*Formation and Evolution of Corotating Interaction Regions and their Three Dimensional Structure*”, *Space Sci. Rev.*, 89, 21–52, doi:10.1023/A:1005291711900.

- Gombosi, T.I., Armstrong, T.P., Arridge, C.S., Khurana, K.K., Krimigis, S.M., Krupp, N. Persoon, A.M., Thomsen, M.F. (2009), “*Saturn’s magnetospheric configuration*”, Saturn from Cassini-Huygens, Springer Netherlands. pp. 203-256. doi:10.1007/978-1-4020-9217-6\_11
- Grodent, D., (2015), “*A brief review of Ultraviolet emissions on giant planets*”, Space Sci. Rev., vol 187, issue 1, pg 23-50, DOI:10/1007/s11214-014-0052-8
- Guerlet, S., Fouchet, T., Bezard, B., et al., (2009), “*Vertical and meridional distribution of ethane, acetylene and propane in Saturn’s stratosphere from CIRS/Cassini limb observations.*” Icarus, 203, 214{232.
- Gustin, J., Bonfond, B., Grodent, D., Gérard, J.-C., (2012), “*Conversion from HST ACS and STIS auroral counts into brightness, precipitated power, and radiated power for H<sub>2</sub> giant planets*”, J. Geophys. Res., 117, A07316, doi:10.1029/2012JA017607.
- Gustin, J., Gérard, J.-C., Grodent, D., Gladstone, G.R., Clarke, J.T., Pryor, W.R., Dols, V., Bonfond, B., Radioti, A., Lamy, L., Ajello, J.M., (2013), “*Effects of methane on giant planet’s UV emissions and implications for the auroral characteristics*”, Journal of Molecular Spectroscopy, 291, 108–117, doi:10.1016/j.jms.2013.03.010
- Guillot, T., Gautier, D., (2015), *Giant Planets*, Treatise on Geophysics, 2nd Edition 00 1–42
- Hansen, C.J., Esposito, L., Stewart, A.I.F., Colwell, J., Hendrix, A., Pryor, W., Shemansky, D., West, R., (2006), “*Enceladus’ water vapor plume.*”, Science 311, 1422–1425, doi:10.1126/science.1121254
- Herbert, F., Schneider, N.M., Dessler, A.J., (2008), “*New description of Io’s cold plasma torus*”, JGR, 113, A01208, doi:10.1029/2007JA012555
- Hill, T.W., (1979), “*Inertial limit on corotation.*”, J. Geophys. Res. 84, 6554–6558, doi:10.1029/JA084iA11p06554
- Kim, Y.H., Fox, J.L., (1994), “*The chemistry of hydrocarbon ions in the Jovian ionosphere.*”, Icarus 112, 310–325, doi:10.1006/icar.1994.1186
- Kimura, T., Badman, S. V., Tao, C., Yoshioka, K., Murakami, G., Yamazaki, A., Tsuchiya, F., Bonfond, B., Steffl, A. J., Masters, A. et al, (2015), “*Transient Internally-driven Aurora at Jupiter Discovered by Hisaki and the Hubble Space Telescope*”, Geophys. Res. Lett., doi:10.1002/2015GL063272
- Kivelson, M. G. and Russell, C. T., (1995), “*Introduction to space physics.*”, Cambridge University Press

- Kliore, A.J., Nagy, A.F., Marouf, E.A., Anabtawi, A., Barbinis, E., Fleischman, D.U., Kahan, D.S. (2009), “*Mid latitude and high-latitude electron density profiles in the ionosphere of Saturn obtained by Cassini radio occultation observations.*”, *J. Geophys. Res.*, 114, 4315 (2009). doi:10.1029/2008JA013900
- Koskinen, T. T., Sandel, B. R., Yelle, R. V., Capalbo, F. J., Holsclaw, G. M., McClintock, W. E., Edgington, S., (2013), “*The density and temperature structure near the exobase of Saturn from Cassini UVIS solar occultations.*”, *Icarus*, 226(2), 1318-1330. 10.1016/j.icarus.2013.07.037Appendices
- Koskinen, T.T., Sandel, B.R., Yelle, R.V., Strobel, D.F., Müller-Wodarg, I.C.F., Erwin, J., (2015), “*Saturn’s variable thermosphere from Cassini/UVIS occultations.*”, *Icarus*, 260, 174-189, doi: 10.1016/j.icarus.2015.07.008
- Krimigis, S. M., et al. (2004), “*Magnetosphere Imaging Instrument (MIMI) on the Cassini mission to Saturn/Titan.*”, *Space Sci. Rev.*, 114, 233 – 329, doi:10.1007/s11214-004-1410-8.
- Krimigis, S. M., Sergis, N., Mitchell, D.G., Hamilton, D.C., Krupp, N., (2007), “*A dynamic, rotating ring current around Saturn.*”, *Nature*, 450, 1050 – 1053, doi:10.1038/nature06425.
- Lamy, L., Prangé, R., Pryor, W., Gustin, J., Badman, S.V., Melin, H., Stallard, T., Mitchell, D.G., Brandt, P.C., (2013), “*Multispectral diagnosis of Saturn’s aurorae throughout a planetary rotation.*”, *J. Geophys. Res. Space Physics*, 118, 4817–4843, doi:10.1002/jgra.50404
- Lystrup, M. B., Miller, S., Dello Russo, N., Vervack Jr., R. J., Stallard, T., (2008), “*First vertical ion density profile in Jupiter’s auroral atmosphere: Direct observations using the Keck II telescope*”, *Astrophys. J.*, 677, 790–797, doi:10.1086/529509.
- Majeed, T., McConnell, J.C., (1991), “*The upper ionospheres of Jupiter and Saturn.*”, *Planet. Space Sci.*, 39, 1715–1732, doi:10.1016/0032-0633(91)90031-5
- Mauk, B.H., Hamilton, D.C., Hill, T.W. et al., (2009). “*Fundamental Plasma Processes in Saturn’s Magnetosphere*”, *Saturn from Cassini–Huygens*, Springer Netherlands. pp. 281–331. doi:10.1007/978-1-4020-9217-6\_11
- McConnell, J.C., Holberg, J.B., Smith, G.R., Sandel, B.R., Shemansky, D.E., Broadfoot, A.L., (1982), “*A new look at the ionosphere of Jupiter in light of the UVS occultation results.*”, *Planet. Space Sci.* **30**, 151–167, doi:10.1016/0032-0633(82)90086-1

- Melin, H., Miller, S., Stallard, T., Trafton, L.M., Geballe, T.R., (2007), “*Variability in the  $H_3^+$  emission of Saturn: Consequences for ionisation rates and temperature*”, *Icarus*, 186, 234–241, doi:10.1016/j.icarus.2006.08.014.
- Melin, H., Shemansky, D.E., Liu, X., (2009), “*The distribution of atomic hydrogen and oxygen in the magnetosphere of Saturn*”, *Planet. Space Sci.*, 57(14–15), 1743–1753.
- Melin, H., Stallard, T., Miller, S., Gustin, J., Galand, M., Badman, S.V., Pryor, W.R., O’Donoghue, J., Brown, R.H., Baines, K.H., (2011), “*Simultaneous Cassini VIMS and UVIS observations of Saturn’s southern aurora: Comparing emissions from H,  $H_2$  and  $H_3^+$  at a high spatial resolution*”, *Geophys. Res. Lett.*, 38, L15203, doi:10.1029/2011GL048457.
- Mendillo, M., Moore, L., Clarke, J., Mueller-Wodarg, I., Kurth, W.S., Kaiser, M.L., (2005), “*Effects of ring shadowing on the detection of electrostatic discharges at Saturn*”, *Geophys.Res.Lett.*32, L05107.
- Miller, S., Joseph, R.D., Tennyson, J., (1990), “*Infrared emissions of  $H_3^+$  in the atmosphere of Jupiter in the 2.1 and 4.0 micron region.*”, *Astrophys. J. Lett.* 360, 55–58, doi:10.1086/185811
- Miller, S., Lam, H.A., Tennyson, J., (1994). “*What astronomy has learned from observations of  $H_3^+$ .*” *Can. J. Phys.* 72, 760–771.
- Miller, S., Achilleos, N., Ballester, G.E., Geballe, T.R., Joseph, R.D., Prangé, R., Rego, D., Stallard, T., Tennyson, J., Trafton, L.M., Waite Jr., J.H., (2000), “*The role of  $H_3^+$  in planetary atmospheres*”, *Philos. Trans. R. Soc. A Math. Phys. Eng. Sci.*, 358, 2485–2502.
- Miller, S., Stallard, T., Melin, H., Tennyson, J., (2010), “ *$H_3^+$  cooling in planetary atmospheres*”, *Faraday Discuss.*, 147, 283–291, doi:10.1039/c004152c
- Miller, S., Stallard, T.S., Tennyson, J., Melin, H., (2013), “*Cooling by  $H_3^+$  emission*”, *Journal of Physical Chemistry*, 117(39), DOI: 10.1021/jp312468b
- Moore, L., Nagy, A.F., Kliore, A.J., Mueller-Wodarg, I., Richardson, J.D., Mendillo, M., (2006), “*Cassini radio occultations of Saturn’s ionosphere: model comparisons using a constant water flux*”, *Geophys.Res.Lett.*33, L22202.
- Moore, L., Mendillo, M., (2007), “*Are depletions in Saturn’s ionosphere caused by explosive surges of water from Enceladus?*”, *Geophys.Res.Lett.*34, L12202.
- Moore, L., Galand, M., Mueller-Wodarg, I., Yelle, R.V., Mendillo, M., (2008), “*Plasma temperatures in Saturn’s ionosphere*”, *J. Geophys. Res.*, 113, A10306, doi:10.1029/2008JA013373

- Moore, L., Galand, M., Mueller-Wodarg, I., Mendillo, M., (2009), “*Response of Saturn's ionosphere to solar radiation: Testing parameterizations for thermal electron heating and secondary ionization processes*”, *Planetary and Space Science*, Vol 57, 1699-1705, doi:10.1016/j.pss.2009.05.001
- Moore, L., Müller-Wodarg, I., Galand, M., Kliore, A., Mendillo, M., (2010), “*Latitudinal variations in Saturn's ionosphere: Cassini measurements and model comparisons.*”, *J. Geophys. Res.*, 115, 11317, doi:10.1029/2010JA015692
- Moses, J.I., Bass, S.F., (2000), “*The effects of external material on the chemistry and structure of Saturn's ionosphere.*”, *J. Geophys. Res.*, 105, 7013–7052, doi:10.1029/1999JE001172
- Müller-Wodarg, I., Mendillo, M., Yelle, R.V., Aylward, A.D., (2006), “*A global circulation model of Saturn's thermosphere*”, *Icarus*, Vol 180, 147-160, doi:10.1016/j.icarus.2005.09.002
- Müller-Wodarg, I., Moore, L., Mendillo, M., (2012), “*Magnetosphere–atmosphere coupling at Saturn: Response of thermosphere and ionosphere to steady state polar forcing*”, *Icarus*, 221(2), doi:10.1016/j.icarus.2012.08.034
- Nagy, A.F., Kliore, A.J., Mendillo, M., Miller, S., Moore, L., Moses, J.I., Müller-Wodarg, I., Shemansky, D.E., (2009), “*Upper atmosphere and ionosphere of Saturn*”, in *Saturn from Cassini-Huygens*, Springer Netherlands. pp. 181-202
- Neale, L., Miller, S., Tennyson, J., (1996) “*Spectroscopic properties of the  $H_3^+$  molecule: a new calculated line list*”, *Astrophysical Journal*, 464, 516-520
- Nichols, J., Cowley, S., (2004), “*Magnetosphere-ionosphere coupling currents in Jupiter's middle magnetosphere: Effect of precipitation-induced enhancement of the ionospheric Pedersen conductivity*”, *Ann. Geophys.*, S., 1799–1827, doi:10.5194/angeo-22-1799-2004
- Nichols, J.D., Clarke, J.T., Cowley, S.W.H., Duval, J., Farmer, A.J., Gérard, J.-C., Grodent, D., Wannawichian, S., (2008), “*Oscillation of Saturn's southern auroral oval*”, *J. Geophys. Res.*, 113, A11205, doi:10.1029/2008JA013444.
- Nichols, J.D., Badman, S.V., Baines, K.H., Brown, R.H., Bunce, E.J., Clarke, J.T., Cowley, S.W.H., Crary, F.J., Gerard, J.-C., Grocott, A., Grodent, D., Kurth, W.S., Melin, H., Mitchell, D.G., Pryor, W.R., Stallard, T.S., (2014), “*Dynamic auroral storms on Saturn as observed by the Hubble Space Telescope*”, *Geophys. Res. Lett.*, 41(10), 3323–3330, doi: 10.1002/2014GL060186.

- O'Donoghue, J., Stallard, T.S., Melin, H., Jones, G.H., Cowley, S.W.H., Miller, S., Baines, K.H., Blake, J.S.D., (2013), "*The domination of Saturn's low latitude ionosphere by ring 'rain'*", *Nature*, vol 496, 193-195, doi:10.1038/nature12049
- O'Donoghue, J., Stallard, T.S., Melin, H., Cowley, S.W.H., Badman, S.V., Moore, L., Miller, S., Tao, C., Baines, K.H., Blake, J.S.D., (2014), "*Conjugate observations of Saturn's northern and southern aurorae*", *Icarus*, Vol 229, 214-220, doi:10.1016/j.icarus.2013.11.009
- O'Donoghue, J., Melin, H., Stallard, T.S., Provan, G., Moore, L., Badman, S.V., Cowley, S.W.H., Baines, K.H., Miller, S., Blake, J.S.D., (2016), "*Ground-based observations of Saturn's auroral ionosphere over three days: Trends in  $H_3^+$  temperature, density and emission with Saturn local time and planetary period oscillation*", *Icarus*, Volume 263, Pages 44–55, doi:10.1016/j.icarus.2015.04.018
- Oka, T., (1992), "*The infrared spectrum of  $H_3^+$  in laboratory and space plasmas*", *Rev. Mod. Phys.*, 64, 1141-1149
- Pan, F.-S. and Oka, T., (1986), "*Calculated forbidden rotational spectra of  $H_3^+$* ", *The Astrophysical Journal*, 305, 518–525
- Pryor, R.W. et al (2011), "*The auroral footprint of Enceladus on Saturn*", *Nature*, Vol 472, 331-333, doi:10.1038/nature09928
- Radioti, A., Grodent, D., Gérard, J.-C., Milan, S.E., Bonfond, B., Gustin, J., Pryor, W.R., (2011), "*Bifurcations of the main auroral ring at Saturn: Ionospheric signatures of consecutive reconnection events at the magnetopause*", *J. Geophys. Res.*, 116, doi:10.1029/2011JA016661
- Radioti, A., Lystrup, M., Bonfond, B., Gérard, J.-C., (2013), "*Jupiter's aurora in ultraviolet and infrared: Simultaneous observations with the Hubble space telescope and the NASA infrared telescope facility*", *J. Geophys. Res.*, 118(5), 2286–2295, doi:10.1002/jgra.50245
- Russel, C.T., (1993), "*Planetary Magnetospheres*", *Rep. Prog. Phys.* 56, 687-732
- Schunk, R.W. and Nagy, A.F., (2000), "*Ionospheres: physics, plasma physics and chemistry*", Cambridge University Press
- Shemansky, D. E. and Liu, X., (2012), "*Saturn upper atmospheric structure from Cassini EUV/FUV occultations*", *Can. J. Phys.*, 90, 817–831, doi: 10.1139/p2012-036
- Southwood, D.J. and Kivelson, M.G., (2007), "*Saturnian magnetospheric dynamics: Elucidation of a camshaft model*", *J. Geophys. Res.* 112, A12222, doi: 10.1029/2007JA012254

- Smith, G. R., Shemansky, D. E., Holberg, J. B., Broadfoot, A. L., Sandel, B. R., McConnell, J. C., (1983), “*Saturn’s upper atmosphere from the Voyager 2 EUV solar and stellar occultations*”, J. Geophys. Res., 88, 8667–8678
- Smith, H.T., Johnson, R.E., Perry, M.E., Mitchell, D.G., McNutt, R.L., Young, D.T., (2010), “*Enceladus plume variability and the neutral gas densities in Saturn’s magnetosphere*”, J. Geophys. Res., 115, A10252, doi:10.1029/2009JA015184.
- Stallard, T., Miller, S., Melin, H., Lystrup, M., Cowley, S.W.H., Bunce, E.J., Achilleos, N., Dougherty, M., (2008), “*Jovian like aurorae on Saturn*”, Nature, 453(7198), 1083–1085 doi:10.1038/nature07077
- Stallard, T., Melin, H., Cowley, S.W.H., Miller, S., Lystrup, M.B., (2010), “*Location and magnetospheric mapping of Saturn’s mid-latitude infrared auroral oval*”, Astrophys. J. Lett., 722, 85–89, doi:10.1088/2041-8205/722/1/L85
- Stallard, T., Melin, H., Miller, S., Badman, S., Brown, R., Baines, K. (2012a), “*Peak emission altitude of Saturn’s  $H_3^+$  aurora*”, Geophys. Res. Lett., VOL. 39, L15103, doi:10.1029/2012GL052806
- Stallard, T., Masters, A., Miller, S., Melin, H., Bunce, E.J., Arridge, C.S., Achilleos, N., Dougherty, M.K., Cowley, S.W.H., (2012b) “*Saturn’s auroral/polar  $H_3^+$  infrared emission: The effect of solar wind compression*”, J. Geophys. Res., 117, 12302 doi:10.1029/2012JA018201
- Tao, C., and Fujimoto, M. (2011), “*UV and IR auroral emission model for the outer planets: Jupiter and Saturn comparison*”, Icarus, 213, 581–592, doi:10.1016/j.icarus.2011.04.001.
- Tao, C., Badman, S.V., Fujimoto, M., (2013), “*Characteristic time scales of UV and IR auroral emissions at Jupiter and Saturn and their possible observable effects*”, in Proc. of the 12th Symposium on Planetary Science (TERRAPUB, Japan, 2013)
- Vasyliunas, V.M., (1983), “*Plasma distribution and flow*”, in *Physics of the Jovian Magnetosphere*, Cambridge University Press, Cambridge, pp. 395–453
- West, R. A., Baines, K. H., Karkoschka, E., et al. (2009), “*Clouds and Aerosols in Saturn’s Atmosphere*”, in Saturn from Cassini-Huygens. Springer. Chap. 7, pages 161-179.
- Wilson, R.J., et al., (2008), “*Cassini plasma spectrometer thermal ion measurements in Saturn’s inner magnetosphere*”, J. Geophys. Res., 113, A12218, doi:10.1029/2008JA013486